



MINISTÉRIO DA CIÊNCIA E TECNOLOGIA

INSTITUTO NACIONAL DE PESQUISAS ESPACIAIS

sid.inpe.br/mtc-m21b/2015/02.27.16.58-TDI

HILDCAA-RELATED EFFECTS RECORDED IN MIDDLE-LOW LATITUDE MAGNETOMETERS

Binod Adhikari

Doctorate Thesis of the Graduate Course in Space Geophysics, supervised by Drs. Ezequiel Echer, Odim Mendes Junior, and Margarete Oliveira Domingues, approved on February 24, 2015.

URL of the original document:

<<http://urlib.net/8JMKD3MGP3W34P/3J3GH78>>

INPE

São José dos Campos

2015

PUBLISHED BY:

Instituto Nacional de Pesquisas Espaciais - INPE

Gabinete do Diretor (GB)

Serviço de Informação e Documentação (SID)

Caixa Postal 515 - CEP 12.245-970

São José dos Campos - SP - Brasil

Tel.:(012) 3208-6923/6921

Fax: (012) 3208-6919

E-mail: pubtc@sid.inpe.br

**COMMISSION OF BOARD OF PUBLISHING AND PRESERVATION
OF INPE INTELLECTUAL PRODUCTION (DE/DIR-544):****Chairperson:**

Marciana Leite Ribeiro - Serviço de Informação e Documentação (SID)

Members:

Dr. Gerald Jean Francis Banon - Coordenação Observação da Terra (OBT)

Dr. Amauri Silva Montes - Coordenação Engenharia e Tecnologia Espaciais (ETE)

Dr. André de Castro Milone - Coordenação Ciências Espaciais e Atmosféricas
(CEA)

Dr. Joaquim José Barroso de Castro - Centro de Tecnologias Espaciais (CTE)

Dr. Manoel Alonso Gan - Centro de Previsão de Tempo e Estudos Climáticos
(CPT)

Dr^a Maria do Carmo de Andrade Nono - Conselho de Pós-Graduação

Dr. Plínio Carlos Alvalá - Centro de Ciência do Sistema Terrestre (CST)

DIGITAL LIBRARY:

Dr. Gerald Jean Francis Banon - Coordenação de Observação da Terra (OBT)

Clayton Martins Pereira - Serviço de Informação e Documentação (SID)

DOCUMENT REVIEW:

Simone Angélica Del Ducca Barbedo - Serviço de Informação e Documentação
(SID)

Yolanda Ribeiro da Silva Souza - Serviço de Informação e Documentação (SID)

ELECTRONIC EDITING:

Marcelo de Castro Pazos - Serviço de Informação e Documentação (SID)

André Luis Dias Fernandes - Serviço de Informação e Documentação (SID)



MINISTÉRIO DA CIÊNCIA E TECNOLOGIA

INSTITUTO NACIONAL DE PESQUISAS ESPACIAIS

sid.inpe.br/mtc-m21b/2015/02.27.16.58-TDI

HILDCAA-RELATED EFFECTS RECORDED IN MIDDLE-LOW LATITUDE MAGNETOMETERS

Binod Adhikari

Doctorate Thesis of the Graduate Course in Space Geophysics, supervised by Drs. Ezequiel Echer, Odim Mendes Junior, and Margarete Oliveira Domingues, approved on February 24, 2015.

URL of the original document:

<<http://urlib.net/8JMKD3MGP3W34P/3J3GH78>>

INPE

São José dos Campos

2015

Cataloging in Publication Data

Adhikari, Binod.

Ad42h HILDCAA-related effects recorded in middle-low latitude magnetometers / Binod Adhikari. – São José dos Campos : INPE, 2015.

xxxiv + 242 p. ; (sid.inpe.br/mtc-m21b/2015/02.27.16.58-TDI)

Thesis (Doctorate in Space Geophysics) – Instituto Nacional de Pesquisas Espaciais, São José dos Campos, 2015.

Guiding : Drs. Ezequiel Echer, Odim Mendes Junior, and Margarete Oliveira Domingues.

1. HILDCAA. 2. Geomagnetic storm. 3. Geomagnetic sub-storm. 4. Space electrodynamics. 5. Magnetosphere. I.Title.

CDU 530.388.8:523.4-852



Esta obra foi licenciada sob uma Licença [Creative Commons Atribuição-NãoComercial 3.0 Não Adaptada](https://creativecommons.org/licenses/by-nc/3.0/).

This work is licensed under a [Creative Commons Attribution-NonCommercial 3.0 Unported License](https://creativecommons.org/licenses/by-nc/3.0/).

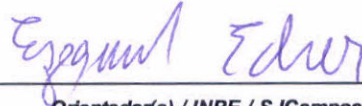
Aprovado (a) pela Banca Examinadora
em cumprimento ao requisito exigido para
obtenção do Título de **Doutor(a)** em
**Geofísica Espacial/Ciências do Ambiente
Solar-Terrestre**

Dr. Polinaya Muralikrishna



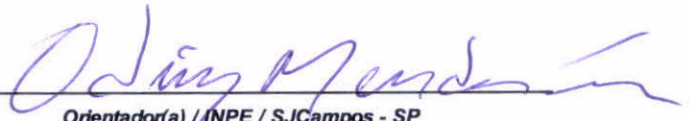
Presidente / INPE / São José dos Campos - SP

Dr. Ezequiel Echer



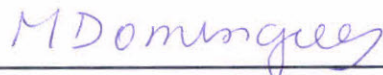
Orientador(a) / INPE / SJC Campos - SP

Dr. Odim Mendes Junior



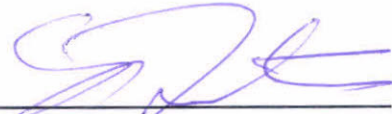
Orientador(a) / INPE / SJC Campos - SP

Dra. Margarete Oliveira Domingues



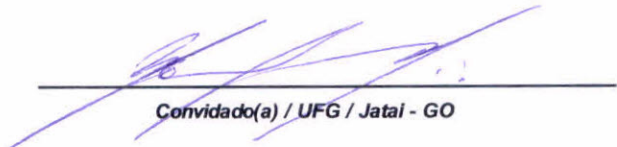
Orientador(a) / INPE / SJC Campos - SP

Dr. Severino Luiz Guimarães Dutra



Membro da Banca / INPE / SJC Campos - SP

Dr. Maurício José Alves Bolzam



Convidado(a) / UFG / Jataí - GO

Dra. Marisa Roberto



Convidado(a) / ITA/DCTA / São José dos Campos - SP

Este trabalho foi aprovado por:

() maioria simples

(X) unanimidade

Aluno (a): **Binod Adhikari**

São José dos Campos, 24 de Fevereiro de 2015

*This thesis is dedicated to the memory of my father,
Bashu Dev Adhikari.
I miss him every day, his words of inspiration and
encouragement in pursuit of excellence, still linger on.*

ACKNOWLEDGEMENTS

I would like to express my sincere gratitude to my supervisors Dr. Odim Mendes (Space Physics), Dr. Margarete Oliveira Domingues (Applied Mathematics) and Dr. Ezequiel Echer (Space Physics) for their continuous support in my PhD research with their immense knowledge, patience, kindness as well as motivation. Their scientific ideas, logical way of thinking, and enthusiasm have been greatly supportive to me with a great value. I would like to thank them for being such the great Supervisors and wonderful human beings. Every single discussion with them about the research was greatly valued to me and will be helpful for my future career.

It is my honor to say, without any doubt that without them, I would not be the physicist that I am today.

My sincere thanks to Prof. Dr. Carl-Gunne Falthammar, Professor Emeritus of Plasma Physics in the Royal Institute of Technology, for his continuous suggestions, motivation and encouragement. I am grateful to Dr. Rajkumar Hajra, Dr. Arian Ojeda Gonzalez, Dr. Daiki Koga, Dra. Aline De Lucas, Dr. Pramod Lamichhane, Dr. Sanjaya Poudel, Dra. Rashmi Rawat and Dra. Flavia Cardoso for their suggestions, encouragement and help in my research activities.

My sincere gratitude goes to our graduation program coordinators (CEA-INPE, 2011-2015): Dr. Alisson dal Lago, Dr. Polinaya Muralikrishna and Dr. Maria Virginia Alves. I am thankful to many Professors, fellow students and the administrative staff at INPE. I owe sincere thanks to Eng. V. E. Menconni and the helpdesk team members for their help and support in various software and in the preparation of various programs. Also, I would like to thank OMNI and INTERMAGNET science team members for the datasets used in this work. In addition to them, it is my honor to remember my dearest friends Baburam Tiwari, Oluwasegun Folarin-Jonah, Carlos Roberto Braga, Paulo Ricardo Jauer, Marcos Vinicius Dias Silveira, Vitor Moura, Anna Karina and Muller Moreira Souza Lopes for their help and friendship during the course work.

I would like to thank INPE, GES and CEA for their support in this PhD project. Also CAPES and CNPq (Grants 312246/2013-7 and 140568/2013-1) for financial support. I cannot forget all Brazilian people who made me feel at home in this country.

Finally, I am forever grateful to all members of my family especially my mother Radha Devi Adhikari and my wife Anjana Mishra Adhikari, without their continuous support and encouragement, I would never have been able to achieve my goals.

ABSTRACT

Disturbances of the geomagnetic field are caused by enhanced solar wind-magnetosphere electrodynamic coupling process. The principal cause of geomagnetic disturbance is the magnetic reconnection between the southward directed interplanetary magnetic field component and the northward directed magnetopause field, that establishes an electrodynamic coupling between the solar wind plasma and magnetosphere. In general, this coupling is controlled by dominant structures emanating from the sun like sporadic coronal mass ejections (CMEs) and their interplanetary counterparts (ICMEs), around the solar maximum, and by corotating high-speed streams, including corotating interaction region (CIR), in the descending and minimum phases of solar cycle. These high speed streams are embedded with highly fluctuating Alfvén waves, which produce phenomena called HILDCAA events (high-intensity, long duration, continuous AE activity). This study investigates magnetic records from middle-low latitude geomagnetic observatories during HILDCAA periods. To this purpose, three primary conditions of the interplanetary space are considered: HILDCAA (i) not preceded by magnetic storm, (ii) preceded by storm generated by CIR, and (iii) preceded by storm generated by ICME. A fourth case is considered as a background condition: a geomagnetically quiet interval. As methodology of analysis, wavelet techniques to study multi-scale features of the HILDCAA events were explored in this work. The signal analysis techniques are composed by continuous wavelet transform, discrete wavelet transform, cross correlation using wavelet, and the usual modulus cross correlation. Complementarily, an evaluation on the field aligned currents (FAC) are considered in the investigation. Besides this, we estimate the polar cap potential (PCP) and merging electric field (E_y), and examine the role of PCP and geomagnetic AL index to monitor geomagnetic activity generated by geoeffective solar wind parameters during HILDCAAs. Thus, this work contributes to extend the understanding of HILDCAA events at higher latitudes to disturbances occurring at middle-low latitudes. There are magnetic effects related to the occurrence of HILDCAA even at middle-low latitudes.

Keywords: HILDCAA. Geomagnetic storm. Geomagnetic substorm. Space Electrodynamics. Magnetosphere.

EFEITOS RELACIONADOS A EVENTOS *HILDCAA* REGISTRADOS EM MAGNETÔMETROS DE MÉDIA E BAIXA LATITUDES

RESUMO

Perturbações do campo magnético da Terra são causadas por intensificação de um processo de acoplamento eletrodinâmico entre o vento solar e a magnetosfera. A causa principal das perturbações geomagnéticas é a reconexão magnética entre o campo magnético interplanetário com orientação para o sul e o campo magnético da Terra orientado para o norte, que estabelecem um acoplamento eletrodinâmico entre o plasma do vento solar e a magnetosfera. Em geral, esse acoplamento é controlado por estruturas dominantes emanadas do Sol como ejeções de matéria coronal (CMEs) e suas contrapartes interplanetárias (ICMES), em torno do máximo solar, e por feixes de alta velocidade corrotantes, incluindo regiões corrotantes de interação (CIR), nas fases descendente e de mínimo do ciclo solar. Esses feixes de alta velocidade portam ondas alfvênicas com intensa flutuação dos parâmetros físicos do plasma, que produzem os fenômenos de atividade AE continuada de alta intensidade e de longa duração, denominados eventos HILDCAA (high-intensity, long duration, continuous AE activity). Este estudo investiga os registros magnéticos obtidos de observatórios geomagnéticos durante períodos de HILDCAA. Para esse propósito, três condições fundamentais do espaço interplanetário são consideradas: HILDCAA (i) não precedida de tempestade geomagnética; (ii) precedida por tempestade gerada por CIR; e (iii) precedida por tempestade gerada por ICME. Um quarto caso é considerado como uma condição de ambiente de fundo: um intervalo geomagneticamente calmo. Como metodologia de análises, técnicas wavelets para estudar características multiescalas dos eventos HILDCAAs são exploradas neste trabalho. As técnicas de análises de sinais são compostas pela transformada wavelet contínua, transformada wavelet discreta, correlação cruzada usando wavelet, e a usual correlação cruzada das intensidades dos sinais. De maneira complementar, uma avaliação das correntes elétricas alinhadas com o campo geomagnético são consideradas na investigação. Além disso, estimamos o potencial na região polar (polar cap potential, PCP) e o campo elétrico resultante da reconexão magnética (E_y), e examinamos o papel do PCP e do índice geomagnético AL para monitorar a atividade geomagnética produzida pelos parâmetros solares geofetivos durante os eventos HILDCAAs. Assim, este trabalho contribuiu para estender a compreensão dos eventos HILDCAAs de altas latitudes para distúrbios ocorrendo em médias e baixas latitudes. Há efeitos magnéticos relacionados a ocorrências de HILDCAAs mesmo em baixas e médias latitudes.

Palavras-chave: HILDCAA. Tempestade geomagnética. Subtempestade geomagnética. Eletrodinâmica Espacial. Magnetosfera.

LIST OF FIGURES

	<u>Page</u>
2.1 Artist's depiction of solar wind particles interacting with the Earth's magnetosphere	8
2.2 Schematic of a Coronal Mass Ejection (ICME)	10
2.3 X-ray image of the Sun	11
2.4 Drawing of the corona as it appeared to Tempel at Torreblanca, Spain during the total solar eclipse of 18 July 1860 that may be the first register of a CME	12
2.5 A schematic view of a Corotating Interaction Region (CIR)	15
2.6 Current systems in the cross section of Earth's magnetosphere.	22
3.1 The relation between XYZ-HDZ components of the magnetic field vector in three coordinate systems: Cartesian, polar, and spherical.	32
3.2 Locations of currently operating geomagnetic observatories.	34
3.3 From top to bottom, the panels show variations of H-component (nT) at the observatories GUAM, ABG, VSS, KAK, THL along with the geomagnetic indices SYM-H (nT), ASY-H (nT) and AE (nT) respectively during the HILDCAA event on 20-23 April, 2003. The green line represents the average quietest day variation, the black line represents the disturbed day variation and the red horizontal arrow in the AE panel indicates the HILDCAA interval.	35
3.4 A HILDCAA interval detected on March 11, 1998, starting about 4:00h to 18:00h. From top to bottom are the 1 min average AU and AL indices, the AE index and Dst	37
3.5 Distribution of AE(12) observatories.	37
3.6 Distribution of the Dst Observatories.	39
3.7 From top to bottom, the panels represent the variations of interplanetary electric field (E_y in mV/m), merging electric field (E_m in mV/m), polar cap potential (PCV in kv), and geomagnetic index PC(mV/m) and AL(nT) for the non-storm HILDCAA event. The HILDCAA interval is marked by red horizontal arrow in AL panel. It occurs during 20-23 April, 2003.	41
3.8 The relationship between the ecliptic reference systems (GSE) and the magnetosphere reference systems (GSM)	42

3.9	From top to bottom, variations of solar wind temperature (T_{sw} in 10^4 K), speed (V_{sw} in km/s), plasma density (N_{sw} in cm^{-3}), IMF magnitude (B_0 in nT), B_y (nT), B_z (nT), SYM-H(nT) and AE(nT). The HILDCAA interval is marked by red horizontal arrow in AE panel. It occurs during April 20-23, 2003.	43
4.1	Time-frequency plane representation $t \times \xi$ in the wavelet context. [Source: Mendes et al. (2005)].	50
4.2	Scalogram for ΔH -component from VSS observatory during HILDCAA event on April 20-23, 2003.	51
4.3	From top to bottom, the panels represent the correlation of IMF- B_z with ΔH -component from geomagnetic stations GUAM, ABG, VSS, KAK and THULE during the HILDCAA event on 20-23 April, 2003.	53
4.4	Daubechies Wavelet coefficients d^j (for $j= 1,2,3,\dots,7$) for ΔH -component from VSS observatory during HILDCAA event occurred on 20-23, April 2003. The red color identify where the HILDCAA events occurs.	58
5.1	From (a) to (d), variations of solar wind temperature (T_{sw} in 10^4 K), speed (V_{sw} in km/s), plasma density (N_{sw} in cm^{-3}), IMF magnitude (B_0 in nT), B_y (nT), B_z (nT), SYM-H(nT) and AE(nT) during (a) quiet period (QUIET) from 18-21 July 2006 and HILDCAA events on (b) 20-23 April 20-23 2003 (NON), (c) 12-15 February 2004 (CIR), and (d) 15-18 May 2005 (ICME). The HILDCAA intervals are marked by red horizontal arrow in AE panel.	65
5.2	Scalograms for IMF- B_z during (a) quiet period (QUIET) from 18-21 July 2006 and HILDCAA events on (b) 20-23 April 20-23 2003 (NON), (c) 12-15 February 2004 (CIR), and (d) 15-18 May 2005 (ICME). For a better highlight, the representation of energy in this scalogram is showed after an application of a \log_2 function.	67
5.3	Scalograms for AE index during (a) quiet period (QUIET) from 18-21 July 2006 and HILDCAA events on (b) 20-23 April 2003 (NON), (c) 12-15 February 2004 (CIR), and (d) 15-18 May 2005 (ICME).	68
5.4	Details of the scalograms for AE index during quiet (QUIET) period from 18-21 July 2006. The range is modified to highlight very weak variations.	69
5.5	Global wavelet spectrum for (a) IMF- B_z and (b) AE index during quiet and HILDCAAs periods. Where the red line represents quiet, the orange line represents non-storm HILDCAA, the green line represents HILDCAA preceded by CIR-storm and the blue line represents HILDCAA preceded by ICME-storm.	69

5.6	The squared Daubechies Wavelet coefficients $(d^j)^2$ (for $j= 1,2,3,\dots,7$) for IMF-Bz during during (a) quiet period (QUIET) from 18-21 July 2006 and HILDCAA events on (b) 20-23 April 2003 (NON), (c) 12-15 February 2004 (CIR), and (d) 15-18 May 2005 (ICME). The red color identifies where the HILDCAA event is happening.	74
5.7	Daubechies Wavelet coefficients d^j (for $j= 1,2,3,\dots,7$) for geomagnetic index AE during during (a) quiet period (QUIET) from 18-21 July 2006 and HILDCAA events on (b) 20-23 April 2003 (NON), (c) 12-15 February 2004 (CIR), and (d) 15-18 May 2005 (ICME). The red color identifies where the HILDCAA event is happening.	75
5.8	Wavelet modulus cross correlation of IMF-Bz with AE index during (a) quiet period (QUIET) from 18-21 July 2006 and HILDCAA events on (b) 20-23 April 2003 (NON), (c) 12-15 February 2004 (CIR), and (d) 15-18 May 2005 (ICME).	76
5.9	From top to bottom, the panels represent variations in solar wind pressure (Psw in nPa), IEF(E_y in mV/m), Akasofu parameter (ϵ in 10^{11} watts), first correction (ϵ^* in 10^{11} watts) and the second correction (ϵ^{**} in 10^{11} watts) during (a) quiet period (QUIET) from 18-21 July 2006 and HILDCAA events on (b) 20-23 April 2003 (NON), (c) 12-15 February 2004 (CIR), and (d) 15-18 May 2005 (ICME). The HILDCAA interval is marked by red horizontal arrow in ϵ^{**} panel.	77
5.10	From top to bottom, the panels represent variations in solar wind pressure (Psw in nPa), IEF(E_y in mV/m), Akasofu parameter (ϵ in 10^{11} watts), first correction (ϵ^* in 10^{11} watts) and second correction (ϵ^{**} in 10^{11} watts) during (a) quiet period (QUIET) from 18-21 July 2006 and HILDCAA events on (b) 20-23 April 2003 (NON), (c) 12-15 February 2004 (CIR), and (d) 15-18 May 2005 (ICME). The HILDCAA interval is marked by red horizontal arrow in ϵ^{**} panel.	78
5.11	Cross-correlation of Akasofu parameter (ϵ), first correction (ϵ^*) and second correction (ϵ^{**}) with SYM-H index during (a) quiet period from 18-21 July 2006 and HILDCAA events on (b) 20-23 April 2003 (c) 12-15 February 2004 and (d) 15-18 May 2005.	79

5.12	From top to bottom, the panels show variations of H-component (nT) at the observatories TAM, CTA, HON, VSS along with the geomagnetic indices SYM-H (nT), ASY-H (nT) and AE (nT) respectively during the HILDCAA event on 20-23 April 2003. The green line represents the average quietest day variation, the black line represents the disturbed day variation and the red horizontal arrow in AE panel indicates the HILDCAA interval.	84
5.13	From top to bottom, the panels represent the variation of ΔH signatures from TAM, CTA, HON, VSS and geomagnetic indices SYM-H (nT), ASY-H (nT) and AE (nT) during HILDCAA event during 20-23 April 2003. The red horizontal arrow in AE panel represents the HILDCAA interval.	85
5.14	Scalograms for ΔH -component from (a) TAM (b) CTA (c) HON and (d) VSS during HILDCAA event on April 20-23, 2003.	87
5.15	Daubechies Wavelet coefficients d^j (for $j= 1,2,3,\dots,7$) for ΔH -component from TAM (left) and CTA (right) during HILDCAA event occurred on 20-23 April 2003. The red color identifies where the HILDCAA events is happening.	88
5.16	Daubechies Wavelet coefficients d^j (for $j= 1,2,3,\dots,7$) for ΔH -component from HON (left) and VSS (right) during HILDCAA event occurred on 20-23 April 2003. The red color identifies where the HILDCAA events is happening.	89
5.17	From top to bottom, the panels represent the correlation of IMF-Bz with H component from geomagnetic observatories TAM, CTA, HON and VSS during the HILDCAA event on 20-23 April 2003.	90
5.18	From top to bottom, the panels show variations of H-component (nT) at the observatories TAM, CTA, HON, VSS along with the geomagnetic indices SYM-H (nT), ASY-H (nT) and AE (nT) respectively during the HILDCAA event on 12-15 February 2004. The green line represents the average quietest day variation, the black line represents the disturbed day variation and the red horizontal arrow in AE panel indicates the HILDCAA interval.	92
5.19	From top to bottom, the panels represent the variation of ΔH signatures from TAM, CTA, HON, VSS and geomagnetic indices SYM-H (nT), ASY-H (nT) and AE (nT) during HILDCAA event during 12-15 February 2004. The red horizontal arrow in AE panel represents the HILDCAA interval.	93

5.20	Scalograms for ΔH -component from (a) TAM (b) CTA (c) HON and (d) VSS during the HILDCAA event on 12-15 February 2004.	94
5.21	Daubechies Wavelet coefficients d^j (for $j= 1,2,3,\dots,7$) for ΔH -component from TAM (left) and CTA (right) during HILDCAA event occurred on 12-15 February 2004. The red color identifies where the HILDCAA events is happening.	95
5.22	Daubechies Wavelet coefficients d^j (for $j= 1,2,3,\dots,7$) for ΔH -component from HON (left) and VSS (right) during HILDCAA event occurred on 12-15 February 2004. The red color identifies where the HILDCAA events is happening.	96
5.23	From top to bottom, the panels represent the correlation of IMF-Bz with ΔH -component from geomagnetic observatories TAM, CTA, HON and VSS during the HILDCAA event on 12-15 February 2004.	97
5.24	From top to bottom, the panels show variations of H-component (nT) at the observatories TAM, CTA, HON, VSS along with the geomagnetic indices SYM-H (nT), ASY-H (nT) and AE (nT) respectively during the HILDCAA event on 15-18 May 2005. The green line represents the average quietest day variation, the black line represents the disturbed day variation and the red horizontal arrow in AE panel indicates the HILDCAA interval.	99
5.25	From top to bottom, the panels represent the variation of ΔH signatures from TAM, CTA, HON, VSS and geomagnetic indices SYM-H (nT), ASY-H (nT) and AE (nT) during HILDCAA event during 15-18 May 2005. The red horizontal arrow in AE panel represents the HILDCAA interval.	100
5.26	Scalograms for ΔH -component from (a) TAM (b) CTA (c) HON and (d) VSS during HILDCAA event on 15-18 May 2005.	101
5.27	Daubechies Wavelet coefficients d^j (for $j= 1,2,3,\dots,7$) for ΔH -component from TAM (left) and CTA (right) during HILDCAA event occurred on 15-18 May 2005. The red color identifies where the HILDCAA events is happening.	102
5.28	Daubechies Wavelet coefficients d^j (for $j= 1,2,3,\dots,7$) for ΔH -component from HON (left) and VSS (right) during HILDCAA event occurred on 15-18 May 2005. The red color identifies where the HILDCAA events is happening.	103
5.29	From top to bottom, the panels represent the correlation of IMF-Bz with ΔH -component from geomagnetic observatories TAM, CTA, HON and VSS during the HILDCAA event on 15-18 May 2005.	104

5.30	From top to bottom, the panels show variations of H-component (nT) at the observatories TAM, CTA, HON, VSS along with the geomagnetic indices SYM-H (nT), ASY-H (nT) and AE (nT) respectively during quiet periods from 18 to 21 July, 2006.	106
5.31	Scalograms for ΔH -component from (a) TAM (b) CTA (c) HON and (d) VSS during quiet periods from 18 to 21 July, 2006.	107
5.32	Daubechies Wavelet coefficients d^j (for $j= 1,2,3,\dots,7$) for ΔH -component from TAM (left) and CTA (right) during during quiet periods from 18 to 21 July, 2006.	108
5.33	Daubechies Wavelet coefficients d^j (for $j= 1,2,3,\dots,7$) for ΔH -component from HON (left) and VSS (right) during quiet periods from 18 to 21 July, 2006.	108
5.34	From top to bottom, the panels represent the correlation of IMF-Bz with H component from geomagnetic observatories TAM, CTA, HON and VSS during quiet periods from 18 to 21 July, 2006.	109
5.35	From top to bottom, the panels show variations of H-component (nT) at the observatories GUAM, ABG, VSS, KAK, THL along with the geomagnetic indices SYM-H (nT), ASY-H (nT) and AE (nT) respectively during the HILDCAA event on 20-23 April 2003. The green line represents the average quietest day variation, the black line represents the disturbed day variation and the red horizontal arrow in AE panel indicates the HILDCAA interval.	114
5.36	From top to bottom, the panels represent the variation of ΔH signatures from GUAM, ABG, VSS, KAK, THL and geomagnetic indices SYM-H (nT), ASY-H (nT) and AE (nT) during HILDCAA event during 20-23 April 2003. The red horizontal arrow in AE panel represents the HILDCAA interval.	115
5.37	Scalograms for ΔH -component from (a) GUA (b) ABG (c) VSS and (d) KAK during HILDCAA event on April 20-23, 2003.	116
5.38	Scalogram for ΔH -component from THL observatory during HILDCAA event on April 20-23, 2003.	117
5.39	Daubechies Wavelet coefficients d^j (for $j= 1,2,3,\dots,7$) for ΔH -component from GUAM (left) and ABG (right) observatories during HILDCAA event occurred on 20-23, April 2003. The red color identifies where the HILDCAA events is happening.	119

5.40	Daubechies Wavelet coefficients d^j (for $j= 1,2,3,\dots,7$) for ΔH -component from VSS (left) and KAK (right) observatories during HILDCAA event occurred on 20-23, April 2003. The red color identifies where the HILDCAA events are happening.	120
5.41	Daubechies Wavelet coefficients d^j (for $j= 1,2,3,\dots,7$) for ΔH -component from THL observatory during HILDCAA event occurred on 20-23, April 2003. The red color identifies where the HILDCAA events are happening.	121
5.42	From top to bottom, the panels represent the correlation of IMF-Bz with ΔH -component from geomagnetic observatories GUAM, ABG, VSS, KAK and THULE during the HILDCAA event on 20-23 April 2003.	122
5.43	From top to bottom, the panels show variations of H-component (nT) at the observatories GUAM, ABG, VSS, KAK, THL along with the geomagnetic indices SYM-H (nT), ASY-H (nT) and AE (nT) respectively during the HILDCAA event on 12-15 February 2004. The green line represents the average quietest day variation, the black line represents the disturbed day variation and the red horizontal arrow in AE panel indicates the HILDCAA interval.	124
5.44	From top to bottom, the panels represent the variation of ΔH signatures from GUAM, ABG, VSS, KAK, THL and geomagnetic indices SYM-H (nT), ASY-H (nT) and AE (nT) during HILDCAA event during 12-15 February 2004. The red horizontal arrow in AE panel represents the HILDCAA interval.	125
5.45	Scalograms for ΔH -component from (a) GUA (b) ABG (c) VSS and (d) KAK during HILDCAA event on 12-15 February 2004.	126
5.46	Scalogram for ΔH -component from THL observatory during HILDCAA event on 12-15 February 2004.	127
5.47	Daubechies Wavelet coefficients d^j (for $j= 1,2,3,\dots,7$) for ΔH -component from GUAM (left) and ABG (right) observatories during HILDCAA event occurred on 12-15 February 2004. The red color identifies where the HILDCAA events is happening.	128
5.48	Daubechies Wavelet coefficients d^j (for $j= 1,2,3,\dots,7$) for ΔH -component from VSS (left) and KAK (right) observatories during HILDCAA event occurred on 12-15 February 2004. The red color identifies where the HILDCAA events are happening.	129
5.49	Daubechies Wavelet coefficients d^j (for $j= 1,2,3,\dots,7$) for ΔH -component from THL observatory during HILDCAA event occurred on 12-15 February 2004. The red color identifies where the HILDCAA events are happening.	130

5.50	From top to bottom, the panels represent the correlation of IMF-Bz with H component from geomagnetic observatories GUAM, ABG, VSS, KAK and THULE during the HILDCAA event on 12-15 February 2004.	131
5.51	From top to bottom, the panels show variations of H-component (nT) at the observatories GUAM, ABG, VSS, KAK, THL along with the geomagnetic indices SYM-H (nT), ASY-H (nT) and AE (nT) respectively during the HILDCAA event on 15-18 May 2005. The green line represents the average quietest day variation, the black line represents the disturbed day variation and the red horizontal arrow in AE panel indicates the HILDCAA interval.	133
5.52	From top to bottom, the panels represent the variation of ΔH signatures from GUAM, ABG, VSS, KAK, THL and geomagnetic indices SYM-H (nT), ASY-H (nT) and AE (nT) during HILDCAA event during 15-18 May 2005. The red horizontal arrow in AE panel represents the HILDCAA interval.	134
5.53	Scalograms for ΔH -component from (a) GUA (b) ABG (c) VSS and (d) KAK during HILDCAA event on 15-18 May 2005.	135
5.54	Scalogram for ΔH -component from THL observatory during HILDCAA event on 15-18 May 2005.	136
5.55	Daubechies Wavelet coefficients d^j (for $j= 1,2,3,\dots,7$) for ΔH -component from GUAM (left) and ABG (right) observatories during HILDCAA event occurred on 15-18 May 2005. The red color identifies where the HILDCAA events is happening.	136
5.56	Daubechies Wavelet coefficients d^j (for $j= 1,2,3,\dots,7$) for ΔH -component from VSS (left) and KAK (right) observatories during HILDCAA event occurred on 15-18 May 2005. The red color identifies where the HILDCAA events is happening.	137
5.57	Daubechies Wavelet coefficients d^j (for $j= 1,2,3,\dots,7$) for ΔH -component from THL observatory during HILDCAA event occurred on 15-18 May 2005. The red color identifies where the HILDCAA events is happening.	138
5.58	From top to bottom, the panels represent the correlation of IMF-Bz with ΔH -component from geomagnetic observatories GUAM, ABG, VSS, KAK and THULE during the HILDCAA event on 15-18 May 2005.	139
5.59	From top to bottom, the panels show variations of H-component (nT) at the observatories GUAM, ABG, VSS, KAK, THL along with the geomagnetic indices SYM-H (nT), ASY-H (nT) and AE (nT) respectively during quiet periods from 18 to 21 July, 2006.	140

5.60	Scalograms for ΔH -component from (a) GUA (b) ABG (c) VSS and (d) KAK during quiet periods from 18 to 21 July, 2006.	141
5.61	Scalogram for ΔH -component from THL observatory during quiet periods from 18 to 21 July, 2006.	142
5.62	Daubechies Wavelet coefficients d^j (for $j= 1,2,3,\dots,7$) for ΔH -component from GUAM (left) and ABG (right) observatories during quiet periods from 18 to 21 July, 2006.	142
5.63	Daubechies Wavelet coefficients d^j (for $j= 1,2,3,\dots,7$) for ΔH -component from VSS (left) and KAK (right) observatories during quiet periods from 18 to 21 July, 2006.	143
5.64	Daubechies Wavelet coefficients d^j (for $j= 1,2,3,\dots,7$) for ΔH -component from THL observatory during quiet periods from 18 to 21 July, 2006.	144
5.65	From top to bottom, the panels represent the correlation of IMF-Bz with H component from geomagnetic observatories GUAM, ABG, VSS, KAK and THULE during quiet periods from 18 to 21 July, 2006.	145
5.66	From top to bottom, the panels show variations of H-component (nT) at the observatories ISK, GNA, TRW, GUI along with the geomagnetic indices SYM-H (nT), ASY-H (nT) and AE (nT) respectively during the HILDCAA event on 20-23 April, 2003. The green line represents the average quietest day variation, the black line represents the disturbed day variation and the red horizontal arrow in AE panel indicates the HILDCAA interval.	150
5.67	From top to bottom, the panels represent the variation of ΔH signatures from ISK, GNA, TRW, GUI and geomagnetic indices SYM-H (nT), ASY-H (nT) and AE (nT) during HILDCAA event during 20-23 April, 2003. The red horizontal arrow in AE panel represents the HILDCAA interval.	152
5.68	Scalograms for ΔH -component from (a) ISK (b) GNA (c) TRW and (d) GUI during HILDCAA event on 20-23 April 2003.	153
5.69	Daubechies Wavelet coefficients d^j (for $j= 1,2,3,\dots,7$) for ΔH -component from ISK (left) and GNA (right) during HILDCAA event occurred on 20-23 April, 2003. The red color identifies where the HILDCAA events is happening.	155
5.70	Daubechies Wavelet coefficients d^j (for $j= 1,2,3,\dots,7$) for ΔH -component from TRW (left) and GUI (right) during HILDCAA event occurred on 20-23 April, 2003. The red color identifies where the HILDCAA events is happening.	156

5.71	From top to bottom, the panels represent the correlation of IMF-Bz with ΔH -component from geomagnetic observatories ISK, GNA TRW and GUI during the HILDCAA event on 20-23 April, 2003.	157
5.72	From top to bottom, the panels show variations of H-component (nT) at the observatories ISK, GNA, TRW, GUI along with the geomagnetic indices SYM-H (nT), ASY-H (nT) and AE (nT) respectively during the HILDCAA event on 12-15 February 2004. The green line represents the average quietest day variation, the black line represents the disturbed day variation and the red horizontal arrow in AE panel indicates the HILDCAA interval.	159
5.73	From top to bottom, the panels represent the variation of ΔH signatures from ISK, GNA, TRW, GUI and geomagnetic indices SYM-H (nT), ASY-H (nT) and AE (nT) during HILDCAA event during 12-15 February 2004. The red horizontal arrow in AE panel represents the HILDCAA interval.	160
5.74	Scalograms for ΔH -component from (a) ISK (b) GNA (c) TRW and (d) GUI during HILDCAA event on 12-15 February 2004.	161
5.75	Daubechies Wavelet coefficients d^j (for $j= 1,2,3,\dots,7$) for ΔH -component from ISK (left) and GNA (right) during HILDCAA event occurred on 12-15 February 2004. The red color identifies where the HILDCAA events is happening.	162
5.76	Daubechies Wavelet coefficients d^j (for $j= 1,2,3,\dots,7$) for ΔH -component from TRW (left) and GUI (right) during HILDCAA event occurred on 12-15 February 2004. The red color identifies where the HILDCAA events is happening.	163
5.77	From top to bottom, the panels represent the correlation of IMF-Bz with ΔH -component from geomagnetic observatories ISK, GNA TRW and GUI during the HILDCAA event on 12-15 February 2004.	164
5.78	From top to bottom, the panels show variations of H-component (nT) at the observatories ISK, GNA, TRW, GUI along with the geomagnetic indices SYM-H (nT), ASY-H (nT) and AE (nT) respectively during the HILDCAA event on 15-18 May 2005. The green line represents the average quietest day variation, the black line represents the disturbed day variation and the red horizontal arrow in AE panel indicates the HILDCAA interval.	166

5.79	From top to bottom, the panels represent the variation of ΔH signatures from ISK, GNA, TRW, GUI and geomagnetic indices SYM-H (nT), ASY-H (nT) and AE (nT) during HILDCAA event during 15-18 May 2005. The red horizontal arrow in AE panel represents the HILDCAA interval.	167
5.80	Scalograms for ΔH -component from (a) ISK (b) GNA (c) TRW and (d) GUI during HILDCAA event on 15-18 May 2005.	168
5.81	Daubechies Wavelet coefficients d^j (for $j= 1,2,3,\dots,7$) for H-component from ISK (left) and GNA (right) during HILDCAA event occurred on 15-18 May 2005. The red color identifies where the HILDCAA events is happening.	169
5.82	Daubechies Wavelet coefficients d^j (for $j= 1,2,3,\dots,7$) for H-component from TRW (left) and GUI (right) during HILDCAA event occurred on 15-18 May 2005. The red color identifies where the HILDCAA events is happening.	169
5.83	From top to bottom, the panels represent the correlation of IMF-Bz with ΔH -component from geomagnetic observatories ISK, GNA TRW and GUI during the HILDCAA event on 15-18 May 2005.	170
5.84	From top to bottom, the panels show variations of H-component (nT) at the observatories ISK, GNA, TRW, GUI along with the geomagnetic indices SYM-H (nT), ASY-H (nT) and AE (nT) respectively during quiet periods from 18 to 21 July, 2006.	172
5.85	Scalograms for ΔH -component from (a) ISK (b) GNA (c) TRW and (d) GUI during quiet periods from 18 to 21 July, 2006.	173
5.86	Daubechies Wavelet coefficients d^j (for $j= 1,2,3,\dots,7$) for ΔH -component from ISK (left) and GNA (right) during quiet periods from 18 to 21 July, 2006.	173
5.87	Daubechies Wavelet coefficients d^j (for $j= 1,2,3,\dots,7$) for ΔH -component from TRW (left) and GUI (right) during quiet periods from 18 to 21 July, 2006.	174
5.88	From top to bottom, the panels represent the correlation of IMF-Bz with ΔH -component from geomagnetic observatories ISK, GNA TRW and GUI during quiet periods from 18 to 21 July, 2006.	174
5.89	From top to bottom, the panels represent Field Aligned Current density (J_{\parallel} in μAm^{-2}), Interplanetary Electric Field (E_y in mV/m), Declination (ΔD in nT) and Horizontal (ΔH in nT) components of geomagnetic field as recorded at Vassouras for the non-storm HILDCAA event. The HILDCAA interval is marked by red horizontal arrows in ΔH panel. It occurs during 20-23 April 2003.	177

5.90	Scalograms for FAC (left) and ΔD (right) during HILDCAA event on 20-23 April 2003.	178
5.91	Daubechies wavelet coefficients d^j (for $j= 1, 2, 3, \dots 7$) ΔD during HILDCAA event occurred on 20-23, April 2003. The red color identify where the HILDCAA events are happening.	179
5.92	From top to bottom, the panels represent the correlation of FAC and ΔD with the components of interplanetary magnetic field (B_y and B_z) during the HILDCAA event on 20-23 April 2003.	180
5.93	Cross-correlation of FAC and E_y with ΔD during the HILDCAA event on 20-23 April 2003. Where blue, green and red lines represent the cross-correlation for $FAC - E_y$, $E_y - \Delta D$ and $FAC - \Delta D$ respectively.	181
5.94	From top to bottom, the panels represent Field Aligned Current density (J_{\parallel} in $\mu A m^{-2}$), Interplanetary Electric Field (E_y in mV/m), Declination (ΔD in nT) and Horizontal (ΔH in nT) components of geomagnetic field as recorded at Vassouras for the non-storm HILDCAA event. The HILDCAA interval is marked by red horizontal arrow in ΔH panel. It occurs during 12-15 February 2004.	182
5.95	Scalograms for FAC (left) and ΔD (right) during HILDCAA event on 12-15 February 2004.	183
5.96	Daubechies wavelet coefficients d^j (for $j= 1, 2, 3, \dots 7$) for ΔD during HILDCAA event occurred on 12-15 February, 2004. The red color identifies where the HILDCAA events are happening.	184
5.97	From top to bottom, the panels represent the correlation of FAC and ΔD with the components of interplanetary magnetic field (B_y and B_z) during the HILDCAA event on 12-15 February 2004.	185
5.98	Cross-correlation of FAC and E_y with ΔD during the HILDCAA event on 12-15 February 2004. Where blue, green and red lines represent the cross-correlation for $FAC - E_y$, $E_y - \Delta D$ and $FAC - \Delta D$ respectively . . .	185
5.99	From top to bottom, the panels represent Field Aligned Current density (J_{\parallel} in $\mu A m^{-2}$), Interplanetary Electric Field (E_y in mV/m), Declination (ΔD in nT) and Horizontal (ΔH in nT) components of geomagnetic field as recorded at Vassouras for the non-storm HILDCAA event. The HILDCAA interval is marked by red horizontal arrow in ΔH panel. It occurs during 15-18 May 2005.	186
5.100	Scalograms for FAC (left) and ΔD (right) during HILDCAA event on 15-18 May 2005.	187

5.101	Daubechies wavelet coefficients d^j (for $j= 1, 2, 3, \dots 7$) for ΔD during HILDCAA event occurred on 15-18 May 2005. The red color identify where the HILDCAA events are happening.	188
5.102	From top to bottom, the panels represent the correlation of FAC and ΔD with the components of interplanetary magnetic field (B_y and B_z) during the HILDCAA event on 15-18 May 2005.	189
5.103	Cross-correlation of FAC and E_y with ΔD during the HILDCAA event on 15-18 May 2005. Where blue, green and red lines represent the cross-correlation for $FAC - E_y$, $E_y - \Delta D$ and $FAC - \Delta D$ respectively	189
5.104	From top to bottom, the panels represent Field Aligned Current density (J_{\parallel} in $\mu A m^{-2}$), Interplanetary Electric Field (E_y in mV/m), Declination (ΔD in nT) and Horizontal (ΔH in nT) components of geomagnetic field as recorded at Vassouras during quiet periods from 18 to 21 July 2006.	190
5.105	Scalograms for FAC (left) and ΔD (right) during quiet periods from 18 to 21 July 2006.	191
5.106	Daubechies wavelet coefficients d^j (for $j= 1, 2, 3, \dots 7$) ΔD during quiet periods from 18 to 21 July 2006.	191
5.107	From top to bottom, the panels represent the correlation of FAC and ΔD with the components of interplanetary magnetic field (B_y and B_z) during quiet periods from 18 to 21 July 2006.	192
5.108	Cross-correlation of FAC and E_y with ΔD during quiet periods from 18 to 21 July 2006. Where blue, green and red lines represent the cross-correlation for $FAC - E_y$, $E_y - \Delta D$ and $FAC - \Delta D$ respectively	192
5.109	From top to bottom, the panels represent the variations of interplanetary electric field (E_y in mV/m), merging electric field (E_m in mV/m), polar cap potential (PCV in kV), and geomagnetic index $PC(mV/m)$ and $AL(nT)$ for the non-storm HILDCAA event. The HILDCAA interval is marked by red horizontal arrow in AL panel. It occurs during 20-23 April 2003.	196
5.110	Scalograms for AL (left) and PCI (right) during HILDCAA event on 20-23 April 2003.	197
5.111	Daubechies Wavelet coefficients d^j (for $j= 1,2,3,\dots,7$) for AL (left) and PC (right) indices during HILDCAA event occurred on 20-23 April 2003. The red color identifies where the HILDCAA events are happening.	198

5.112	(Left panel) Cross correlation between PCI and AL (black line), PCI and SYM-H (red line), E_y and PCI (blue line) and B_z and PCI (pink line). (right Panel) Cross correlation between PCV and AL (black line), PCV and SYM-H (red line), E_y and PCV (blue line) and B_z and PCV (pink line) for the HILDCAA event on 20-23 April 2003.	199
5.113	From top to bottom, the panels represent the variations of interplanetary electric field (E_y in mV/m), merging electric field (E_m in mV/m), polar cap potential (PCV in kv), and geomagnetic index PC(mV/m) and AL(nT) for the non-storm HILDCAA event. The HILDCAA interval is marked by red horizontal arrow in AL panel. It occurs during 12-15 February 2004.	201
5.114	Scalograms for AL (left) and PCI (right) during HILDCAA event on 12-15 February 2004.	201
5.115	Daubechies Wavelet coefficients d^j (for $j= 1,2,3,\dots,7$) for AL (left) and PC (right) indices during HILDCAA event occurred on 12-15 February 2004. The red color identifies where the HILDCAA events are happening.	202
5.116	(left panel)Cross correlation between PCI and AL (black line), PCI and SYM-H (red line), E_y and PCI (blue line) and B_z and PCI (pink line). (right panel) Cross correlation between PCV and AL (black line), PCV and SYM-H (red line), E_y and PCV (blue line) and B_z and PCV (pink line) for the HILDCAA event on 12-15 February 2004.	203
5.117	From top to bottom, the panels represent the variations of interplanetary electric field (E_y in mV/m), merging electric field (E_m in mV/m), polar cap potential (PCV in kv), and geomagnetic index PC(mV/m) and AL(nT) for the non-storm HILDCAA event. The HILDCAA interval is marked by red horizontal arrow in AL panel. It occurs during 15-18 May 2005.	205
5.118	Scalograms for AL (left) and PCI (right) during HILDCAA event on 15-18 May 2005.	205
5.119	Daubechies Wavelet coefficients d^j (for $j= 1,2,3,\dots,7$) for AL (left) and PC (right) indices during HILDCAA event occurred on 15-18 May 2005. The red color identifies where the HILDCAA events are happening.	206
5.120	(Left panel)Cross correlation between PCI and AL (black line), PCI and SYM-H (red line), E_y and PCI (blue line) and B_z and PCI (pink line). (right panel) Cross correlation between PCV and AL (black line), PCV and SYM-H (red line), E_y and PCV (blue line) and B_z and PCV (pink line) during HILDCAA event occurred on 15-18 May 2005.	207

5.121	From top to bottom, the panels represent the variations of interplanetary electric field (E_y in mV/m), merging electric field (E_m in mV/m), polar cap potential (PCV in kv), and geomagnetic index PC(mV/m) and AL(nT) during the quiet periods from 18-21 July 2006.	208
5.122	Scalograms for AL (left) and PCI (right) during the quiet periods from 18-21 July 2006.	209
5.123	Daubechies Wavelet coefficients d^j (for $j= 1,2,3,\dots,7$) for AL (left) and PC (right) indices during the quiet periods from 18-21 July 2006.	209
5.124	(Left panel) Cross correlation between PCI and AL (black line), PCI and SYM-H (red line), E_y and PCI (blue line) and B_z and PCI (pink line). (right panel) Cross correlation between PCV and AL (black line), PCV and SYM-H (red line), E_y and PCV (blue line) and B_z and PCV (pink line) during the quiet periods from 18-21 July 2006.	210

LIST OF TABLES

	<u>Page</u>
3.1 Geomagnetic observatories (organized by latitude)	33
3.2 Geomagnetic observatories (organized by longitude)	33
3.3 Selection of HILDCAA events	44
5.1 Average values of ϵ , ϵ^* and ϵ^{**} during HILDCAAs and quiet periods . . .	72
5.2 Average values of AL, PCI, PCV and Em during HILDCAAs and quiet-day interval	211
5.3 Cross-correlation coefficient for PCI with AL, SYM-H, Ey and Bz only for HILDCAAs interval	211
5.4 Cross-correlation coefficient for PCV with AL, SYM-H, Ey and Bz only for HILDCAAs interval	211

LIST OF ABBREVIATIONS

ABG	–	Alibag
ACE	–	Advanced Composition Explorer
AE	–	Auroral Electrojet
AL	–	Westward Auroral Electrojet
AU	–	Astronomal Union
CIRs	–	Corotating Interaction Regions
CME	–	Coronal Mass Ejection
CPCP	–	Cross Polar Cap Potential
CTA	–	Charters Towers
CWT	–	Continuous Wavelet Transform
Dst	–	Disturbance Storm Time Index
DWT	–	Discrete Wavelet Transform
FACs	–	Field Aligned Currents
FFT	–	Fast Fourier Transform
FT	–	Fourier Transform
GNA	–	Gnangara
GSE	–	Geocentric Solar Ecliptic Coordinate System
GSM	–	Geocentric Solar Magnetospheric Coordinate System
GUA	–	Guam
GUI	–	Guimar-Tenerife
HCS	–	Hemispheric Current Sheet
HON	–	Honolulu
IAGA	–	International Association of Geomagnetism and Aeronomy
ICMEs	–	Interplanetary Coronal Mass Ejections
IEF	–	Interplanetary Electric Field
IMF	–	Interplanetary Magnetic Field
IMP-8	–	Interplanetary Monitoring Platform-8
IPS	–	Interplanetary Shocks
ISK	–	Istanbul
KAK	–	Kakioka
L1	–	Lagrange Point Number 1
LASCO	–	Large Angle And Spectrometric Coronagraph
LT	–	Local Time
MC	–	Magnetic Cloud
MCs	–	Magnetic Clouds
MLT	–	Magnetic Local Time
MR	–	MultiResolution
NS	–	Noth to the South
OSO	–	Orbiting Solar Observatory
PCI	–	Polar Cap Index

PCV	–	Polar Cap Potential
RE	–	Earth Radius
SB	–	Sector Boundary
SECCHI	–	Sun-Earth Connection Coronal And Helispheric Investigation
SI	–	Sudden Impulse
SOHO	–	Solar And Helispheric Observatory
Sq	–	Solar quiet
SSC	–	Sudden Storm Sommcement
STEREO	–	Solar TERrestrial RELations Observatory
SW	–	Solar Wind
TAM	–	Tammanrasset
THL	–	Thule
TIDs	–	Travelling Ionospheric Disturbances
TRW	–	Trelew
UT	–	Universal Time
UVI	–	Ultra Violet Image
VSS	–	Vassouras
WFT	–	Window Fourier Transform
WIND	–	Comprehensive Solar Wind Laboratory

CONTENTS

	<u>Page</u>
1 INTRODUCTION	1
2 PHENOMENOLOGY ON GEOMAGNETIC DISTURBANCES	7
2.1 Effects of geomagnetic activity	7
2.2 Solar maximum	8
2.3 Solar minimum	10
2.4 Different Interplanetary structures	11
2.4.1 Solar Coronal Mass Ejections	11
2.4.2 ICMEs	12
2.4.3 Magnetic Clouds	13
2.4.4 Interplanetary Shocks(IS)	13
2.4.5 Corotating Interaction Regions(CIRs)	14
2.4.6 Heliospheric Current Sheet (HCS)	15
2.5 Alfvén Waves	16
2.6 Geomagnetic Disturbances	17
2.6.1 Geomagnetic Storms	17
2.6.2 Substorms	18
2.6.3 HILDCAAs	18
2.6.4 Solar quiet variation of geomagnetic field	20
2.7 Magnetospheric Current Systems	21
2.7.1 Magnetopause current	21
2.7.2 Tail current	22
2.7.3 Ring current	23
2.7.4 Field aligned currents	24
2.8 Polar Cap Potential	25
2.9 Akasofu's parameter and solar wind energy	27
3 DATASETS	31
3.1 Ground based observations	31
3.1.1 Geomagnetic field	31
3.2 Geomagnetic indices	34
3.2.1 The K and Kp Index	35
3.2.2 The AE Index	36

3.2.3	The Dst Index	38
3.2.4	The Polar Cap Index	38
3.3	Space based observations	40
3.4	Events to be analyzed	44
4	METHODOLOGIES FOR SIGNAL ANALYSIS	45
4.1	From Fourier to Wavelet Analysis	45
4.1.1	Continuous Wavelet Transform (CWT)	49
4.1.2	Discrete Wavelet Transform (DWT)	54
5	RESULTS AND DISCUSSIONS	59
5.1	Characterization of HILDCAAs	59
5.2	Magnetic effects during HILDCAAs recorded from low latitudes geomagnetic observatories	82
5.3	Geomagnetic signatures recorded at different longitudinal observatories during HILDCAAs.	112
5.4	The effects of HILDCAAs recorded from mid latitudes geomagnetic observatories	149
5.5	Study of field aligned current (FAC) with D-component (east-west) and interplanetary electric field (E_y) during three different HILDCAA events	176
5.6	Estimation of Polar Cap Potential (PCV) and Merging electric field (E_m) during HILDCAAs	195
6	CONCLUSIONS	213
6.1	Perspectives for future work:	214
	REFERENCES	217

1 INTRODUCTION

The structure of the Earth is composed of a thin outer crust, a silicate mantle, an outer core and an inner core. These structures can be defined by either their chemical or their rheological (deformation and flow of matter) properties. Both temperature and pressure increase with depth within the Earth. The estimated temperature of the core mantle boundary is 4800 K. That is hot enough for the outer core to exist in a liquid state. However, the inner core, composed mostly of iron and a small percentage of lighter elements, is solid because of its high/elevated pressure. Due to the Earth's rotation and convection, the outer core is in constant motion, in which the convection is driven by the upward motion of the light elements as the heavier elements freeze onto the inner core. Several sources contribute to produce the magnetic field of the Earth (OLSEN et al., 2010). However, the actual process by which the magnetic field produced is extremely complex. Many of the parameters required for a complete solution of the mathematical equations describing the problem are poorly known. Nevertheless, the basic concepts to generate magnetic field on the Earth are: there must be a conducting fluid, enough energy to cause the fluid to move with sufficient speed with appropriate flow pattern, and a seed magnetic field. In the outer core of the Earth, all these conditions are met, in which the convective motion is coupled with the Earth's rotation and produces the appropriate flow pattern. This flow of liquid iron generates electric currents, which in turn produce magnetic fields. Charged metals passing through these fields go on to create electric currents of their own, and so the cycle continues. This self-sustaining process is known as the geodynamo (CHAPMAN; BARTELS, 1962; MCELHINNY, 1973). The magnetic field of the Earth is also contributed by electric currents in the ionosphere and magnetosphere. On average, their contribution is relatively weak, a few percent of the total field at ground during geomagnetic quiet conditions. These external currents cause geomagnetic disturbances (CHAPMAN; BARTELS, 1962).

The principal cause of geomagnetic disturbance is the magnetic reconnection between southward interplanetary magnetic field (IMF) and Earth's dayside northward magnetic fields, which establishes an electrodynamic coupling between the solar plasma and the magnetosphere (DUNGEY, 1961; GONZALEZ et al., 1994). In the Earth's magnetosphere, several plasma regions are affected and strong modifications are generated in the systems of electrical currents, during the occurrence of geomagnetic storms. The mechanisms for such modifications are associated with intensifications in the current systems which increased auroral ionospheric currents at high and mid-latitudes, and by enhancements in the ring current at lower lati-

tudes (TSURUTANI; GONZALEZ, 1997). All these mechanisms for the energy transfer processes are related to solar activities. The activities of the sun are believed to be driven by energy release from the solar magnetic field (KIVELSON; RUSSEL, 1995). The amount of solar activity on the Sun is not constant, and is closely related to the typical number of sunspots that are visible. The number of sunspots and the levels of solar activity vary within a 11- year period known as the solar cycle. The solar sources of the geomagnetic disturbances are known to have various interplanetary manifestations like coronal mass ejection (ICMEs), magnetic clouds, co-rotating interaction region (CIR) and other interplanetary structures like interplanetary shocks (IPS), heliospheric current sheet (HCS) and sector boundary (SB) (WEI et al., 2003; GONZALEZ et al., 1999; KLEIN; BURLAGA, 1982). These structures in the interplanetary medium, which often proves to be hostile conditions to technological systems, are controlled by the activity of the Sun, from which a constant flow of particles and magnetic field under special conditions may transfer energy and particles into the Earth's magnetosphere. If magnetic effects are considered, the middle latitudes are dominated by the ring current, while the low latitudes are also affected significantly by a system of ionospheric electrojet. These current systems are the manifestations for geomagnetic disturbances: storms and substorms (KAMIDE et al., 1998). The field-aligned currents provide a link between high and low-latitude currents and contribute to increase the complexity of these current systems. Other current systems are also present in the boundary and tail of the magnetosphere and ionosphere. They may also contribute to produce geomagnetic disturbances. The main effects of these current systems are especially seen on the horizontal component of the Earth magnetic field observed in geomagnetic middle-low latitude (HARGREAVES, 1992). In disturbed conditions, the modification in magnetospheric and ionospheric current systems is caused by the mechanisms of viscous interaction (AXFORD; HINES, 1961), magnetic reconnection (DUNGEY, 1961) and resonant wave-particle interaction (TSURUTANI; THORNE, 1982). The main cause associated with these mechanisms is the intensification in the current systems mainly in the equatorial ring current. During the enhancement of equatorial ring current, hot ions are injected into the inner magnetosphere. As the hot ions are injected into the inner magnetosphere, the geometry of the geomagnetic field causes them to drift around the Earth, forming a westward ring current (O'BRIEN; MCPHERRON, 2000; MENDES et al., 2005). The ring current results of linear and nonlinear processes. The injection of charged particles and their magnetic effects may be approximated as a linear process. On the other hand, the trapping mechanism and consequently the resulting ring current intensity may not be approximated as a linear process. It depends on the history of the

cross tail potential difference. This effect will limit the efficiency of the linear prediction functions of the ring current from the solar wind parameters (TAKAHASHI et al., 1990). The understanding of ring current state is a necessity to forecast the magnetic field in the magnetosphere. The magnetic field variations produced by the ring current decrease the magnetic field on the Earth surface. Then, these variations are measured by the Dst index (SUGIURA, 1964; SUGIURA; KAMEI, 1991). The Dst index represents the longest commonly used measure of the state of the ring current (BAKER, 1998). In general, a geomagnetic storm includes a significant ring current that develops over a few hours and then recovers over several days (KAMIDE et al., 1998). If the southward oriented Bz component of IMF interconnects with the earth magnetic field and is sustained for enough time, it will be the necessary condition for the development of a geomagnetic storm (GONZALEZ et al., 1994; GONZALEZ et al., 1999; KAMIDE et al., 1998). The Bz with intensities higher than 10 nT and sustained for at least 3 hours is sufficient to cause an intense geomagnetic storm (Dst < -100 nT) (GONZALEZ; TSURUTANI, 1987).

During the descending and minimum solar cycle phases, coronal holes occur more often. From these coronal holes, high speed streams emanate with the velocities much higher than typical solar wind velocities. The difference of the velocities between high and slow co-rotating streams forms an interface region, known as Corotating Interaction Regions (CIRs), in the interplanetary medium. These high speed streams are embedded with highly fluctuating Alfvén waves. Generally, geomagnetic storms caused by high speed streams have moderate intensity because of high fluctuations in the southward oriented Bz-component of the interplanetary magnetic field (IMF). When the fluctuations in IMF (Bz) diminish, the storm starts its long recovery phase. This long magnetic storm recovery phase is seen simultaneously with intense and continuous auroral activity and known as HILDCAA (High Intensity Long Duration Continuous AE Activity) (TSURUTANI; GONZALEZ, 1987; TSURUTANI et al., 2004; GUARNIERI et al., 2006; HAJRA et al., 2013; HAJRA et al., 2014a; HAJRA et al., 2014b). The auroral activity can be measured by the AE index, which monitors the horizontal component of the disturbed magnetic field in the auroral zone (ROSTOKER, 1972; DAVIS T. N. AND SUGIURA, 1966). During the HILDCAA events –hereafter HILDCAAs –, the AE index is expected to reach over 1000 nT at least once and never occurs below 200 nT for periods longer than two hours at a time. These conditions should last at least two days and should occur outside the main phase of geomagnetic storms. At this time, the AE index showed an intense and continuous activity. These criteria were chosen arbitrarily to ensure the presence of high intensity and long duration activity (TSURUTANI; GONZALEZ, 1987). If an

event does not match one or more criteria, still there is a possibility that the physical processes are similar to those found during HILDCAAs (TSURUTANI et al., 2004). Some major research projects done on HILDCAAs are summarized below.

Gonzalez et al. (1994) studied the difference between magnetic storms, substorms and HILDCAAs, in terms of AE and Dst indices and IMF z-component. They found that a modest southward IMF lasting about one hour is a sufficient condition for a substorm. Similarly, a modest southward IMF is also a sufficient condition for HILDCAAs occurrence but an intense magnetic storm takes place under large amplitude IMF Bz and sustained duration. They also pointed out that the IMF Bz with intensity higher than -10 nT and sustained for at least 3 hours is sufficient to cause an intense geomagnetic storm ($Dst < -100$ nT) (GONZALEZ; TSURUTANI, 1987). The known mechanisms for the decay of injected particles in the radiation belt, wave-particle interactions, Coulomb scattering and Joule heating, have time scales of hours to fraction of days (DAGLIS et al., 1999). But these mechanisms cannot explain the recovery phases of magnetic storms that last as long as days or weeks.

Initially Tsurutani and Gonzalez (1987) observed that the source of high intense auroral activity is an intermittent magnetic reconnection between southward component of interplanetary Alfvén wave fluctuations with magnetopause magnetic fields. Tsurutani et al. (1990) found that Alfvén wave intervals were present over 60 percentage of the time and the southward component of the Alfvén waves were well correlated with AE index with a time lag of 43 min. Later the studies of (TSURUTANI et al., 2004) provided new information. Similarly, Alves et al. (2006) showed that one third of the CIR events observed near Earth are geoeffective followed by moderate magnetic activity ($Dst < -50$ nT).

Soraas et al. (2004) studied the evidence for particle injection as the cause of Dst reduction during HILDCAA events. They found that Dst and AE indices are in good correspondence with ring current particle injections during a magnetic storm. They also showed that HILDCAA events are associated with injection of protons into the outer portion of the ring current (the regions between $L = 4 R_E$ and $L = 5.6 R_E$), where R_E is the Earth radius. This indicates that a slow decay in the Dst index is not related to other magnetospheric current systems. This shows that when the injection occurs during a storm recovery phase, there is a delay in the Dst recovery, which can maintain negative values for long intervals. Tsurutani et al. (1995) studied the injections of particles during substorms and proposed that consecutive injections caused by substorms were related to the prolonged Dst recovery during

HILDCAAs. Similarly, Tsurutani et al. (2004) observed the relationship between *AE* and *AL* indices and substorm onsets using auroral images from POLAR Ultraviolet Imager (UVI). In this observation, they found no correlation between substorms and *AE/AL* intensifications. They suggested that substorm expansion phases can occur simultaneously during HILDCAAs, and the repetitive particle injections were caused by enhanced inward convection due to dawn-to-dusk electric fields during southward intervals of the Alfvén wave trains. Lee et al. (2006) suggested that substorms are related to successive northward turnings of Alfvén waves during HILDCAA phenomena. It means that the repetitive feature of substorms are related to high-speed streams which are triggered by the IMF. This shows that substorms are responsible for plasma sheet particles motion toward the inner magnetosphere in which the particle injections associated with substorm onsets may contribute to long Dst recovery times. On the other hand, the occurrence of repetitive southward intervals of the Alfvénic IMF is also another mechanism for enhanced earthward convection. Hence, substorms and enhanced convection impelled by highly fluctuating Alfvén waves within high speed streams may play an important role in HILDCAA events (KIM et al., 2008). HILDCAAs can occur after ICME storms as well as CIR storms or without occurrence of any storms (GUARNIERI et al., 2006; HAJRA et al., 2013). Hajra et al. (2013) studied the number of 133 AE events satisfying the HILDCAA criteria suggested by Tsurutani and Gonzalez (1987) and found that 94 % were associated with interplanetary CIRs/HSSs. The remaining 6 % occurred after the passage of ICMEs. Hajra et al. (2014a) studied the energetics of the solar wind-magnetosphere-ionosphere system during HILDCAA events for solar cycle 23 (from 1995 through 2008). For all events, they found that the average energy transferred to the magnetospheric/ionospheric system was $6.3 \times 10^{16} J$, and the ram kinetic energy of the incident solar wind was $7.1 \times 10^{18} J$. They also studied the coupling efficiency for individual HILDCAA events and found that it varied between 0.3% and 2.8%, with an average value of 0.9%. More details about HILDCAAs can be found in Gonzalez and Tsurutani (1987), Guarnieri et al. (2006), Sobral et al. (2006), Koga et al. (2011), Hajra et al. (2013), Hajra et al. (2014a) and Hajra et al. (2014b).

The main objective of this work is to analyze middle-low latitudes geomagnetic signatures recorded during HILDCAA events, whose results are a significant contribution to the area of Space Physics. Thus, to obtain a comprehensive view, several fundamental interplanetary conditions that can be connected with those occurrences will be examined. Besides these, significant elements of the electrodynamic coupling between incident solar plasma and the magnetosphere-ionosphere system will be also taken into account in this investigation: the field aligned currents, the polar cap po-

tential, and merging electric field (E_m) during the same events. The importance of this study is that, although a subtle phenomenon, HILDCAA events through mainly modifications of electrical currents affect the environment of the Earth and are related to geomagnetic disturbances. The understanding of the magnetic manifestation outside the auroral region during those kinds of phenomena could contribute to a better diagnosis of effects and interconnection among parts of the magnetosphere system. This work extends the studies from high latitude to middle-low latitude and complements the analyses on this area of the space sciences. The analyses use wavelet transform methodology by its skill to deal with non-stationary time series, its time-scale localization, and its multiscale property.

The earlier introduction has attempted to describe briefly the general interplanetary phenomena that could produce geoeffectiveness. HILDCAAs can be interpreted as a different type of geomagnetic disturbance besides activities of geomagnetic storms and substorms. This thesis consists of five chapters, divided according to our concept to better understand the present study. Chapter 2 discusses the theoretical development related to HILDCAAs and its geomagnetic impacts. Chapter 3 describes the interplanetary data and the ground magnetometer data used for HILDCAA effect investigation. The Chapter 4 starts with a technique which has been used before for geomagnetic analyses, the survey on the methodologies that could be used for this kind of research. Chapter 5 presents the results and discussion of the thesis. Finally, Chapter 6 gives a concise conclusion of the results presented in the thesis.

2 PHENOMENOLOGY ON GEOMAGNETIC DISTURBANCES

This chapter presents the geomagnetic activities and their connections with the solar activities during its maximum and minimum. Different interplanetary structures produced by the Sun are described. They are solar coronal mass ejections, interplanetary coronal mass ejections, Magnetic clouds, interplanetary shocks, corotating interaction regions, heliospheric current sheet, and Alfvén waves. As consequence of the interaction of the Sun with the Earth, magnetic disturbances occur, which are designated as geomagnetic storms, substorms, and HILDCAA events. During this interaction, complex magnetospheric current systems are established, composed mainly by magnetopause current, tail current, ring current, and field aligned current. There is also deposition of energy in polar regions, evaluated by a polar cap potential parameter, and into all magnetosphere partially evaluated by the Akasofu parameter.

2.1 Effects of geomagnetic activity

The solar wind is a stream of energized charged particles released from the upper atmosphere of the Sun. It consists mostly of electrons and protons with energies usually between 1.5 and 10 keV. It is continuously released by the Sun. However, the Sun carries out very active regions responsible for phenomena such as solar flares, coronal mass ejections and their interplanetary counterparts, and coronal holes, regions of open field lines where solar wind particles flow at high speed (BURLAGA, 1995; HARVEY et al., 2000). The magnetized collisionless solar wind plasma confines the magnetic field of the earth to a region around the planet called magnetosphere (KIVELSON; RUSSEL, 1995). The shape of the magnetosphere is determined by the flow of the solar wind and the electric currents that run inside of the magnetosphere (PARKS, 2004). For this reason, the solar wind is highly influenced by solar activity which is known to be controlled by a cycle of 11 years (KIVELSON; RUSSEL, 1995). Every eleven years, there is a reversal in polarity of the solar magnetic field. During the maximum of the solar cycle, coronal holes, which are regions of open field lines to the interplanetary medium, are located at high solar latitudes. The solar low latitudes and equator are populated during this phase by sunspots, characterized as a kind of active region. As the solar cycle progresses to its minimum, coronal holes begin to stretch or move toward the solar equator. At the same time, the number of sunspots decreases significantly. After this phase, the number of sunspots increases again and a reversal of polarities of the magnetic field occurs (EDDY, 1976). Through these activities, a larger number of different phenomena may release huge amounts

of energy and particles into space affecting velocity, density, temperature, energy and composition of the particles of the interplanetary medium.

Particles and magnetic fields, the latter known as interplanetary magnetic fields (IMF), present in the solar wind can influence strongly the Earth's magnetospheric dynamics. As a consequence, geomagnetic activities, permeated by magnetic storms, substorms, and high-intensity long-duration continuous AE activity (HILDCAAs) deposit large amounts of energy into the magnetosphere. The geomagnetic activity related to solar maximum and solar minimum is discussed in sections 2.2 and 2.3 respectively. Figure 2.1 shows an artist's depiction of solar wind particles interacting with the Earth's magnetosphere.

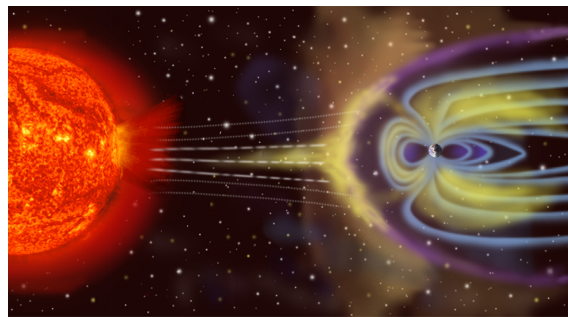


Figure 2.1 - Artist's depiction of solar wind particles interacting with Earth's magnetosphere.

[Source:http://en.wikipedia.org/wiki/Geomagnetic_storm].

2.2 Solar maximum

The solar cycle maximum is the period of the greatest solar activity during the 11-year solar cycle of the Sun. During this period, a large number of sunspots appear and the Sun's irradiance output grows by about 0.07% (CAMP; TUNG, 2007). At Solar maximum, the Sun's magnetic field lines are highly distorted due to the rotation of low latitude regions being faster than one of the polar regions. During this phase, the major interplanetary structures emanating from the sun are erupting filaments and their associated Coronal Mass Ejections (CMEs) (KLEIN; BURLAGA, 1982). If the ICMEs coming from the sun into interplanetary space are fast enough (> 500 km/sec), i.e the relative velocity of solar wind is higher than the magneto sonic speed (50-70 km/sec), a forward shock is formed (KENNEL, 1985). Another strong shocked field structure known as sheath region can be found in between the shocks and ICMEs (TSURUTANI et al., 1988). The structure of slowly varying and strong

magnetic fields (10-25 nT) called as magnetic cloud can be found if the ICME has a well organized magnetic field structure (BURLAGA et al., 1981; KLEIN; BURLAGA, 1982). These interplanetary structures contain relatively high densities if compared to normal solar wind. Then, the interaction between these structures with the front of the magnetosphere causes compression of the magnetosphere. It leads to intensifications of the magnetopause current, appearing as a positive sudden impulse in the Dst index (NISHIDA, 1978). Such a sudden impulse in the Dst index is characterized as the storm sudden commencements (SSC) caused by the abrupt increase in the solar wind ram pressure at interplanetary shock (ARAKI, 1977) and also followed by the initial phase of geomagnetic storm which may be of any length, from zero to more than 25 hours. However, not all geomagnetic storms have an initial phase and not all sudden impulses in geomagnetic field (SI) are followed by a geomagnetic storm (TSURUTANI et al., 2001). In the main phase of the storm the horizontal components of the Earth's low-latitude magnetic fields are significantly depressed by 100 (or more) nT and can be as short as a few hours or as long as a day. It is related to a plasma process caused when the southward directed IMF and the northward pointed Earth magnetic field lines merge (DUNGEY, 1961; GONZALEZ et al., 1994) at the dayside magnetopause. This idea of reconnection was first proposed by Dungey (1961). In this process, the increase in the solar wind pressure initially compresses the magnetosphere and the southward directed IMF interacts with northward pointed Earth's magnetic field and transfers an increased energy into the magnetosphere (DUNGEY, 1961; GONZALEZ et al., 1994) Both interactions cause an increase in the movement of plasma through the magnetosphere (driven by increased electric fields inside the magnetosphere) and an increase in electric currents in the magnetosphere and ionosphere (GONZALEZ et al., 1994). If the southward directed IMF (B_z) is sustained for a long time with high amplitude, a large number of energetic particles will inject into the magnetosphere. These injected particles will produce a ring current inside the magnetosphere which is the reason for decrease in Dst index (DAGLIS et al., 1999; GONZALEZ et al., 1994). The recovery phase is the period where the field gradually recovers to the ambient value. During this phase, injected particles start to dissipate, through several mechanisms (such as wave-particle interactions, Coulomb scattering and Joule heating), and the Dst index slowly returns to its ambient value (DAGLIS et al., 1999). Figure 2.2 shows major interplanetary structures responsible for geomagnetic disturbances during solar maximum.

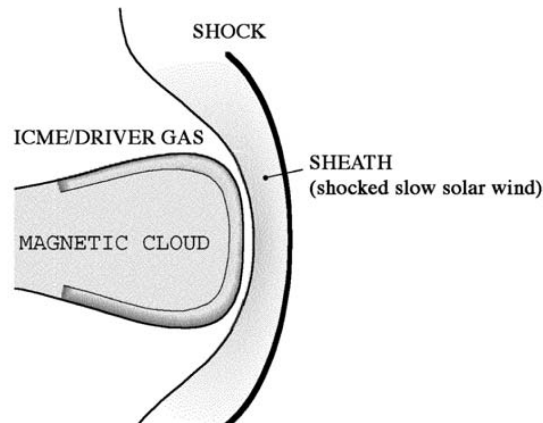


Figure 2.2 - Schematic of a Coronal Mass Ejection (ICME). [Source Gonzalez et al. (1999)].

2.3 Solar minimum

The Solar minimum designates the minimum in solar activity about in eleven-year cycle. During this period, sunspot and solar flare activity diminishes. On the other hand, Solar maximum is the period when activities reach higher intensities. During solar minimum, CMEs become more rare, and coronal holes are more frequent. As these holes migrate or extend toward lower solar latitudes, the geoeffectiveness latter increases significantly. These coronal holes are characterized by regions of open field lines in which particles flow at high speed. This flow is called a beam or fast or high speed stream (KRIEGER et al., 1973; GONZALEZ et al., 1994; HARVEY et al., 2000; TSURUTANI et al., 2006). During the descending phase of the solar cycle, these structures are not capable of producing severe storms and their geoeffectiveness is generally moderate (GONZALEZ et al., 1994). These holes are characterized by coronal regions of open magnetic field in the solar corona, because they have lower temperatures than their surroundings. These coronal regions appear dark in satellite images. The solar wind flowing from these regions of open field contains fluctuations in magnetic field and speed. These fluctuations are known as Alfvén waves and play an important role in the geomagnetic disturbances (GARRET et al., 1974), because they are long-lived and common for coronal holes. The high speed streams have velocities of 750 to 800 km/s, which are much higher than the typical velocities of solar wind. Due to this velocity difference, the fast streams intercept the slow streams and an interface region is formed. At large heliocentric distances, this stream interface region is bound by fast forward and fast reverse shocks (SMITH; WOLF, 1976a; PIZZO, 1985; BALOGH et al., 1999). They may persist for more than one solar rotation so that the high speed streams from the same region re-appear at one solar

rotation leading to typical recurrent high-speed, slow-speed solar wind conditions, designated as corotating interaction regions (CIR) (SCHWENN, 2006). Figure 2.3 is an X-ray image for large polar coronal hole during solar minimum.

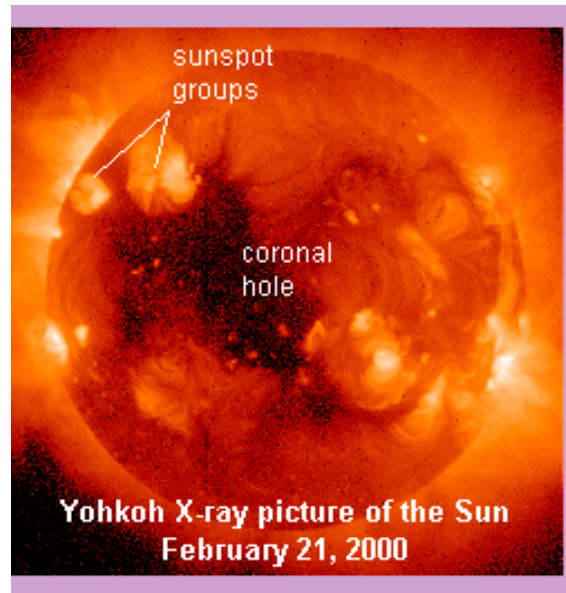


Figure 2.3 - X-ray image of the Sun, captured on Feb 21, 2000, by the Japanese Yohkoh X-ray Observatory.

[Source:http://www.nasa.gov/vision/universe/solarsystem/killer_electrons.html]

2.4 Different Interplanetary structures

2.4.1 Solar Coronal Mass Ejections

Solar coronal mass ejections (CME) have been intensively studied for several decades and recognized as a major ICME structure for space weather effects (WEBB et al., 2000a). About forty years ago, before the first space-borne white-light coronagraph observations started, our knowledge of the solar corona was limited to observations made by very few ground-based coronagraphs or during total solar eclipses (HUNDHAUSEN et al., 1984; GOSLING; PIZZO, 1999). In the early 1970s, CMEs were discovered with the help of OSO-7 (Orbiting solar observatory). Figure 2.4 is an example of a drawing of the eclipse of 18 July 1860. It was probably the most thoroughly observed eclipse up to that time. From all the drawings found about these events, it is possible to observe a peculiar feature in the corona regarding a CME. At the time of the first observations, the Solar corona was considered very quiet, almost static, with a very slow evolution in its appearance over the 11-years solar activity cycle.

Later, with the advent of the new technologies and the improvement on the observation techniques, the corona was recognized by its very dynamic behavior, with activity occurring over a wide range of temporal and spatial scales (HUNDHAUSEN et al., 1984; CYR et al., 2000; CREMADES; BOTHMER, 2004; VOURLIDAS et al., 2010). The current space-based coronagraph observations to receive images are LASCO (large angle and spectrometric coronagraph) (BRUECKNER et al., 1995), on board SOHO (Solar and Helispheric Observatory) and SECCHI (Sun-Earth Connection Coronal and Helispheric Investigation) instrument package (HOWARD et al., 2008) on STEREO twin spacecraft (Solar Terrestrial Relation Observatory). These observational results show that CMEs are very large and dynamic, contain more than 10^{15} grams of solar materials and have a radial size of 0.25 AU when they pass by the Earth which is 1 AU from the Sun. The occurrence rate of CMEs depends on the phase of solar cycle and is more frequent and more intense around solar maximum (GOPALSWAMY et al., 2007).

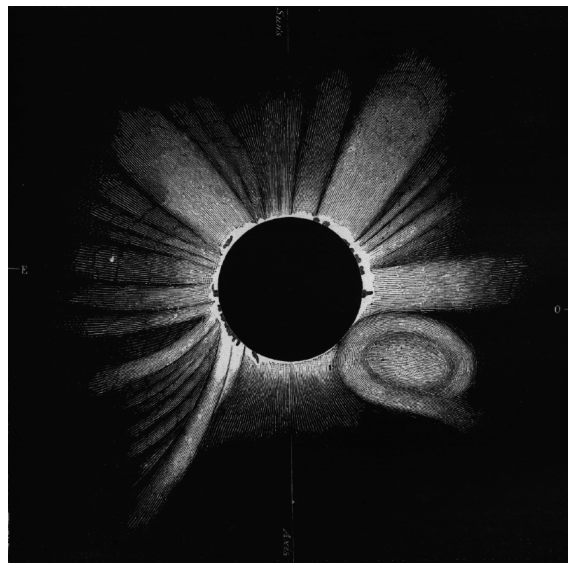


Figure 2.4 - Drawing of the corona as it appeared to Tempel at Torreblanca, Spain during the total solar eclipse of 18 July 1860 that may be the first register of a CME [Source:Eddy (1974)]

2.4.2 ICMEs

Interplanetary coronal mass ejections (ICMEs) are seen at several distances and characterized by regions of lower than usual solar wind proton temperature, strong magnetic fields, low plasma beta and smooth field rotation, designated as magnetic

clouds (MC) (GOSLING, 1997). ICMEs are supposed to release huge amount of energy in the solar atmosphere which can lead to significant explosion of mass from the Sun. Sometimes, ICMEs are associated with shock waves and large southward interplanetary magnetic fields (IMFs) and can cause large geomagnetic disturbances. Therefore, ICME investigation and forecasting are of great importance. There are two possible ICME structures discussed in the literature. The first possibility is that ICMEs are like flux rope structures which remain magnetically connected to the Sun while they are carried outward by the solar wind (BURLAGA, 1988; CHEN, 1996; KUMAR; RUST, 1996; BOTHMER; SCHWENN, 1998). The other possibility is that ICMEs may be disconnected from the Sun and form plasmoids (VANDAS et al., 1993). ICMEs, originated from the closed field region on the Sun, cause the most energetic phenomena in the heliosphere and are referred by various names such as driver gas, ejecta and plasma cloud (TSURUTANI et al., 1988).

2.4.3 Magnetic Clouds

Magnetic clouds are the regions of strong magnetic fields, within which the solar wind ion temperature is usually low and the field direction rotates slowly (BURLAGA et al., 1981). They are also known as subset of ICMEs (BURLAGA et al., 1981; KLEIN; BURLAGA, 1982; GOSLING, 1990). They occur mainly in the region of low plasma beta, where angular changes in the orientation of magnetic field occur slowly and magnetic fields are relatively free of discontinuities (TSURUTANI et al., 1988; ECHER et al., 2005). MCs often contain long interval of strong IMF B_z and therefore can be a source of intense geomagnetic storms (BURLAGA et al., 1990; LINDSAY et al., 1995).

2.4.4 Interplanetary Shocks(IS)

Shocks are arbitrary transition layers where plasma properties change abruptly (FELDMAN et al., 1987; ECHER et al., 2008; ZONG et al., 2009). These layers are formed whenever a wave moves faster than the speed of sound in a liquid, gas or plasma. When the shocks form in the space, the properties of the solar wind plasma change almost instantaneously. There are three modes of shocks: fast, intermediate and slow. These modes of shocks depend on the angle between the direction of flow and magnetic field. When upstream plasma flow to downstream plasma the velocity decreases and density increases. This causes compression at the shock and a fast mode shock is formed. The intermediate shocks are associated with the steepening of Alfvén waves. These modes of shock have greater speed than the Alfvén wave. The slow mode shocks are associated with the steepening of sound wave which propagate faster than sonic wave. As ICMEs, MCs and CIRs, shock waves play a

significant role for amplifying the southward magnetic field in the interplanetary medium (GOSLING et al., 1991). Interplanetary shocks have a larger size in area than the other interplanetary structures and usually spacecraft near 1 AU observed only the shock (DRYER, 1975; ECHER et al., 2004). They can produce a sudden high impulse (SI), which increases the horizontal component of low-latitude magnetic field due to the intensification of Chapman-Ferraro current (NISHIDA, 1978; ECHER et al., 2003). They can also have an important role in amplifying the southward magnetic field in the interplanetary medium (GOSLING et al., 1991; GONZALEZ et al., 1999; ECHER et al., 2004). An example of geomagnetic activity caused by fast mode shocks is to energize trapped particles, which causes dayside aurora and night side magnetospheric substorms (GOSLING et al., 1991; TSURUTANI et al., 2009).

2.4.5 Corotating Interaction Regions(CIRs)

During the descending phase and solar minimum, ICMEs and solar flares become less frequent and coronal holes become the dominant interplanetary structure leading to geomagnetic disturbances. Coronal holes, which are observed as dark regions in X-ray images of the sun, are confined to the solar poles during solar maximum. But during solar cycle minimum, they expand in size and migrate toward the solar equator (HUNDHAUSEN, 1972). Isolated and new holes may also be observed near low solar latitudes. The coronal holes are open magnetic structures in the solar corona from which high speed solar wind streams are emitted (HARVEY et al., 2000). High speed streams have velocity of 750 to 800 km/s, which are much higher than the typical velocity (<500 km/s) of solar wind. Due to this velocity difference, the fast streams intercept the slow streams and an interface region is formed – an interaction region. At large heliocentric distances, this stream interface region is bounded by fast forward and fast reverse shocks (SMITH; WOLF, 1976b). The coronal holes may persist for more than one solar rotation so that the high speed streams from the same region re-appear at one solar rotation leading to recurrent streams. The structure formed by these streams are like spirals which are distorted due to the solar rotation and an interaction region with slower streams is formed which is known as corotating interaction region (CIR)(SMITH; WOLF, 1976b; GOSLING; PIZZO, 1999). The characteristic appearance of CIRs is shown in Figure . The study of CIRs is very important for research because of many reasons. Some of which are listed herein. The first reason is that CIRs are capable of generating shocks which are able to accelerate energetic charged particles (LARIO; ROELOF, 2007). The second reason is that they are associated with recurrent geomagnetic activity and may enhance the strength of non-recurrent geomagnetic storms (GOSLING, 1990). Another reason is

that for many years, people have been developing a good basic understanding of them. They believe that CIR phenomena may be accessible to physics-based prediction within the foreseeable future (RILEY et al., 2001). More details about the geoeffectiveness of CIRs can be found in Alves et al. (2006). Figure 2.5 shows a schematic of a Co-rotating Interaction Regions (CIRs).

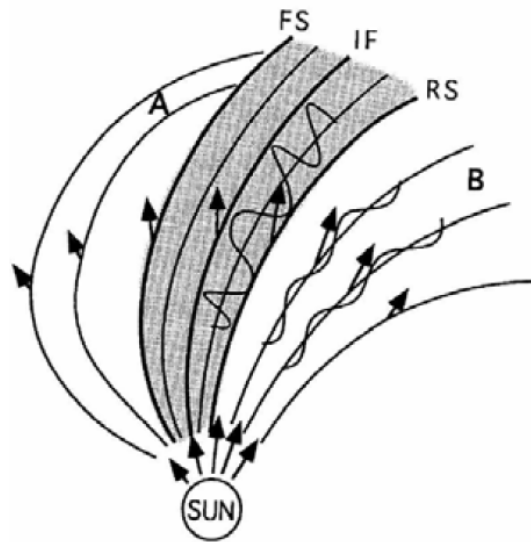


Figure 2.5 - A schematic of a Corotating Interaction Region (CIR), where A represents the slow solar wind, and B is marking the high-speed stream. The shocks are marked as FS (forward shock) and RS (reverse shock), and IF marks the interface region. [Source: Tsurutani et al. (1995)]

2.4.6 Heliospheric Current Sheet (HCS)

When solar wind flows away from the Sun, the interplanetary magnetic field (IMF) is carried with it in a spiral shape, known as Parker spiral (PARKER, 1958). During minimum solar activity, IMF takes on a rather simple topology pointing away from or toward the sun. The surface within the solar system where the polarity of the Sun's magnetic field changes from one polarity to the other is known as the heliospheric current sheet (HCS). This field extends throughout the Sun's equatorial plane through the entire solar system and is the largest structure in the heliosphere (SZABO et al., 1999). Many observations have suggested that at large heliocentric distances, the heliospheric current sheet is formed when the plasma from a coronal hole

or other magnetically open regions meets the plasma from another coronal hole with opposite magnetic polarity at the tip of a helmet streamer (SCHULZ, 1973; ALFVEN, 1977; NEUGEBAUE, 2008). Similarly, the observation seen in eclipses have suggested that streamers may have open field lines coming from more than one source and thereby contain several field reversals (EDDY, 1973).

2.5 Alfvén Waves

The idea of Alfvén waves was introduced by Alfvén (1942). It is a type of magnetohydrodynamics wave in which the periods of oscillation are of the order of several minutes where ions propagate along the field lines with magnetic tension as the restoring force (IWAI et al., 2003). According to Hollweg (1978), the Alfvén waves in the interplanetary solar wind are the remnants of heating processes in the solar corona. They were originally identified through the measurements of the solar wind for several decades. However, the properties of this wave are still not fully understood (MEDVEDEV et al., 1997; GOLDESTINE et al., 1999; HOLLWEG, 1999; VASQUEZ; HOLLWEG, 1999; VASQUEZ; HOLLWEG, 2001; BUTI et al., 2001). Near the Sun, the phase velocity of Alfvén waves is extremely high around 1200 km/s but at a distance of 1AU, the phase velocity decreases to 50 to 70 Km/s. The existence of Alfvén waves in the interplanetary medium was discovered first by Coleman (1968), Belcher and Davis (1971). Later, many researchers have studied the existence of Alfvén waves and their properties in the interplanetary medium and shown that this wave was incompressible and dispersion-less (MEDVEDEV; DIAMOND, 1995; MEDVEDEV et al., 1997; BUTI et al., 2001; VASQUEZ; HOLLWEG, 2001). This wave has strong contribution from a variety of physical processes in space plasmas, for example: solar and stellar wind acceleration, wave-particle interaction, turbulence, generation of auroral activity, etc. The Alfvén wave in a plasma has a low frequency when compared to the ion cyclotron frequency. This kind of wave propagates in the direction of the magnetic field. During the solar minimum, the solar wind flowing from coronal holes contains fluctuations in magnetic field and speed and these fluctuations contain Alfvén waves of large amplitudes of the order of $\Delta B/|B| = 1$ or 2 and play an important role in the geomagnetic disturbances (GARRET et al., 1974). So, as those waves commonly in connection to coronal holes are long-lived, they can reach the Earth's position. The fluctuation on the south component of IMF is the reason for injection of particles inside the magnetosphere, which produce geomagnetic disturbance in the Earth's environment (SORAAS et al., 2004).

The propagation of Alfvén wave in the interplanetary medium (PARKS, 1991) is

expressed as

$$V_A = \pm \frac{B}{(\mu_o \rho)^{1/2}}, \quad (2.1)$$

where V_A is the speed of Alfvén wave in the medium, B is the magnetic field strength, μ_o is the permeability of the vacuum and ρ is the total mass density of the charged plasma particles. Sign in the expression is related to the orientation of propagation on IMF.

2.6 Geomagnetic Disturbances

2.6.1 Geomagnetic Storms

Geomagnetic storms are episodes of extraordinary fluctuations in the Earth's magnetic field caused by injection of energetic particle in the Earth's magnetosphere (GONZALEZ et al., 1994). The major interplanetary causes for geomagnetic storms are high speed streams (co-rotating interaction region or CIR), magnetic clouds and ICMEs (TSURUTANI et al., 1988; ECHER et al., 2008). During a geomagnetic storm main phase, charged particles in the near Earth plasma sheet are energized and injected deeper in to the magnetosphere. Thus, these energized particles cause large scale distribution in the magnetosphere (AKASOFU, 1964; GONZALEZ et al., 1994) and a large amount of energy is stored in the magnetotail and magnetosphere producing the storm time ring current. The ring current in the magnetosphere produces diamagnetic effect. Magnetic storms are caused by the mechanisms of viscous interaction (AXFORD; HINES, 1961), predominantly by magnetic reconnection (DUNGEY, 1961) and resonant wave-particle interaction (TSURUTANI; THORNE, 1982). Among them, magnetic reconnection is the main and the most important mechanism. The storm time magnetic field variation produced by the ring current is measured in Dst (disturb storm time) index (SUGIURA; KAMEI, 1991). This index represents the longest commonly used measure of the state of the ring current, and therefore it is essential in such forecasting (BAKER, 1998). For the estimation of Dst index, the observatories are placed near low latitudes magnetic equator but they are not too close. As revealed in the variation of Dst, the geomagnetic storm has three phases: an initial phase where the magnetic field increases anywhere from +10 to +50 nT, a main phase where the field magnitude decreases by 100 (or more) nT, and a recovery phase where the field gradually recovers to the ambient value (TSURUTANI et al., 2001). The initial phase, usually preceded by a sudden commencement (SSC), starts suddenly and lasts an indeterminate amount of time. It is caused by the abrupt increase in the solar wind ram pressure at interplanetary shock (ARAKI, 1977). However, not all geomagnetic storms have an initial phase and not all storm sudden commencement

(SSC) are followed by a geomagnetic storm (AKASOFU; CHAPMAN, 1963; GONZALEZ et al., 1994; TSURUTANI et al., 2001). The main phase can be as short as an hour or as long as a day. The recovery phase typically lasts as short as 8 hours or as long as 7 days (CHAPMAN; BARTELS, 1940; TSURUTANI et al., 1995). Geomagnetic storms are of two types: recurrent and non-recurrent. Recurrent storms occur every 27 days and most frequently in the declining phase of solar cycle. They are caused by the interaction of low and high speed solar wind streams co-rotating with the Sun. Non-recurrent geomagnetic storms occur most frequently near solar maximum, and are caused by fast interplanetary coronal mass ejections (ICMEs) (GONZALEZ et al., 1994; TSURUTANI et al., 2001).

2.6.2 Substorms

A magnetic substorm is a disturbance in the Earth's magnetosphere that occurs when the interplanetary magnetic field turns southward (MCPHERRON, 1991; TSURUTANI et al., 2004; LAKHINA et al., 2006). The southward directed IMF and the northward pointed Earth magnetic field lines merges (DUNGEY, 1961; GONZALEZ et al., 1994) at the dayside magnetopause in which a significant amount of energy derived from the solar wind is deposited in the magnetosphere and ionosphere. The main process for energy dissipation during substorms is directly driven and loading-unloading (ROSTOKER, 1987; BAKER et al., 1997a). The driven process dissipates energy globally and continuously. The energy dissipation for loading-unloading processes depends on the phase of substorm. An isolated substorm has three phases: growth phase, expansion phase, and recovery phase (LEWIS et al., 1997). During the growth phase, energy is stored in the Earth's magnetotail. In this phase, the auroral oval expands equatorward and there is an increase in the strength of the DP2 auroral electrojets. During the expansion phase, the energy stored in the tail is released into the magnetosphere and ionosphere (BAKER et al., 1997b). Then, the released energy significantly changes the currents and strength of the high latitude surface magnetic field in the polar ionosphere. The most visible magnetic disturbance observed from the Earth is an increase in the intensity and size of polar auroras. During the recovery phase, the activity may diminish in the midnight sector and the magnetosphere returns to its normal state.

2.6.3 HILDCAAs

During the descending and solar minimum phases, the CIRs formed by the high speed stream contain large fluctuations in $\text{Alfv}\ddot{u}n\frac{1}{2}n$ waves. When these fluctuations in Alfvén waves go through shocks, their geoeffectiveness increases. A new type

of geomagnetic activity is discovered which is different from classical geomagnetic activities. This is known as High-intensity, long-duration, continuous AE activity (HILDCAA) (TSURUTANI; GONZALEZ, 1987; TSURUTANI et al., 2004). Time intervals with AE index of large and long term intensity are caused by intermittent magnetic reconnection between southward components of interplanetary Alfvén wave fluctuations and magnetopause magnetic fields. The identification of these events occurred during the recovery phase of geomagnetic storms. The long recovery phase is due to the continuous injections of ions in the ring current. These injections occur even without a continuous southward oriented magnetic field and interrupt all major physical processes for ring current decay (charge exchange, Coulomb collisions, convection, and wave-particle interactions). These injection phenomena were well correlated with fluctuations in Alfvén waves present in the magnetic field (SORAAS et al., 2004) and the occurrence of HILDCAAs were well correlated with the presence of $\text{Alfvén} \frac{1}{2}n$ fluctuations in the solar wind. Electrons having energies above 40-400 KeV are injected during these events and can be responsible for damaging satellites. For an event to be considered a HILDCAA, it must satisfy the following criteria (TSURUTANI; GONZALEZ, 1987):

- a) AE index is expected to reach over 1000 nT at least once during the event.
- b) It should last at least two days.
- c) It should not occur AE values below 200 nT for periods longer than two hours at a time.
- d) It must occur outside the main phase of geomagnetic storms.

Gonzalez et al. (1994) studied the difference between magnetic storms, substorms and HILDCAAs, in terms of AE and Dst indices and IMF z-component. They found that a modest southward IMF lasting about one hour is a sufficient condition for a substorm. They also pointed out that the IMF Bz with intensities higher than -10 nT and sustained for at least 3 hours is sufficient to cause an intense geomagnetic storm ($\text{Dst} < -100$ nT) (GONZALEZ; TSURUTANI, 1987). The known mechanisms for the decay of injected particles in the radiation belt, wave-particle interactions, Coulomb scattering and Joule heating, have time scales of hours to fraction of days (DAGLIS et al., 1999). But these mechanisms cannot explain the recovery phases of magnetic storms that last as long as days or weeks. Then, Tsurutani and Gonzalez (1987) observed that the source of high intense auroral activity is an intermittent magnetic reconnection between the southward component of interplanetary Alfvén $\frac{1}{2}n$ wave

fluctuations with magnetopause magnetic fields (TSURUTANI et al., 2004). Tsurutani et al. (1990) found that Alfvén wave intervals were present over 60 percent of the time and the southward component of the Alfvén waves was well correlated with AE with a time lag of 43 minutes. Similarly, Alves et al. (2006) show that one third of the CIR events observed near the Earth are geoeffective followed by moderate magnetic activity ($Dst < -50nT$).

Soraas et al. (2004) studied the evidence for particle injection as the cause of Dst reduction during HILDCAA events. They showed that injection of protons in the ring current occurs in the regions between $L = 4$ and $L = 5.6$ and into smaller distances (such as between $L = 2$ and $L = 4$) only during the main phase of storms. These events can occur after ICME storms as well as CIR storms or with out occurrence of any storms (GUARNIERI et al., 2006; HAJRA et al., 2013). Hajra et al. (2013) studied one hundred thirty-three AE events satisfying the HILDCAA criteria suggested by Tsurutani and Gonzalez (1987) and found that 94 % were associated with interplanetary CIRs/HSSs. The remaining 6 % occurred after the passage of ICMEs. More research has been done on the topic of HILDCAAs and can be found in Gonzalez et al. (2006), Sobral et al. (2006), Koga et al. (2011), Hajra et al. (2014a), Hajra et al. (2014b).

2.6.4 Solar quiet variation of geomagnetic field

The time variations of the geomagnetic field can be classified into two main categories. The variations on time scales shorter than 1 year are of external origin. The longer time scale variations are of internal origin, commonly referred to as secular variation. The Sun, in fact, is a decisive factor for the external origin. External variations are of two types: regular variations (daily variations) and irregular phenomena of magnetic variations. A Regular variation is a day- to- day variation which depends on the phase of the sunspot cycle, seasons, movement of the solar quiet foci, atmospheric tide and longitude. It is also called as Sq(H) (solar quiet variation) (CHAPMAN; BARTELS, 1940; RASTOGI; IYER, 1976). It shows seasonal behavior with a maximum and minimum in local summer and local winter respectively at high and mid-low latitudes (GREENER; SCHLAPP, 1979; RASTOGI, 2007). It shows maximum at the equinox in the inter-tropical area for H and Z components (SCHLAPP, 1968; OWOLABI et al., 2014). The day- to- day variability of Sq(H) show a greater coherent length in the east-west direction compare to north-south direction (GREENER; SCHLAPP, 1979; RASTOGI, 2007). It is generated by two large vortices of electric currents in the day-side ionosphere . The dynamo currents flowing in the ionosphere

due to atmospheric tidal motion across the geomagnetic field are responsible for it. These vortices are centered at 40 degree latitude near to the Sun meridian. At the level of the equator, there is a concentration of the current (west-east) called equatorial electrojet. It leads to a daily variation value up to 200 nT.

The contribution of irregular variation of the geomagnetic field can be defined as: one contribution characterizes the actual magnetic storm and the other represents the variations depending on local time (magnetic substorms). Mid latitude observatories also show other important irregular variations known as convection bays. These convection bays occur in the evening and night hours and have a duration of 1-2 hours. The ionospheric currents flowing at latitudes between 65-70 degree along magnetic field lines are the main sources for these bays. The seasonal variations of Sq(H) are explained on the basis of solar cycle, annual and semi annual variability. There are seasonal variations of the Sq current in the low to mid latitudes (CAMPBELL; SCHIFFMACHER, 1988; CHANDRASEKHAR et al., 2003; MANSILLA, 2014). On the other hand, the high latitude observatories show annual variations due to large ionospheric conductivity differences between winter and summer seasons. The solar zenith angle is minimum in equinoxes and maximum in both solstices at mid-low latitudes. This is the main cause for large ionospheric conductivities at equinoxes. However, the seasonal variations of the Sq amplitude at low-mid latitudes are not enough to be observed due to the presence of equatorial electrojet (RASTOGI, 1974; ONWUMECHILI, 1997) This is because the equatorial electrojet also exhibits a semi-annual variation (CHAPMAN; RAJARAO, 1965; STENING, 1995).

2.7 Magnetospheric Current Systems

Interaction of the IMF of the solar wind plasma with charged particles in the boundary of the magnetosphere, with the Earth's magnetic field and as consequence the convection electric fields within the magnetosphere cause the generation of several current systems in the various magnetospheric regions. The major currents in the magnetosphere are: the magnetopause currents, the ring current, the cross-tail current and the field-aligned currents. Figure 2.6 shows a schematic of various current systems and their rough geographical locations inside the magnetosphere.

2.7.1 Magnetopause current

At about $14 R_E$ (Earth radius) along the Earth-Sun line, the first signature of its existence is the bow shock, a shock wave standing in the supersonic solar wind flow in front of the magnetosphere. Solar wind parameters like flow velocity, plasma

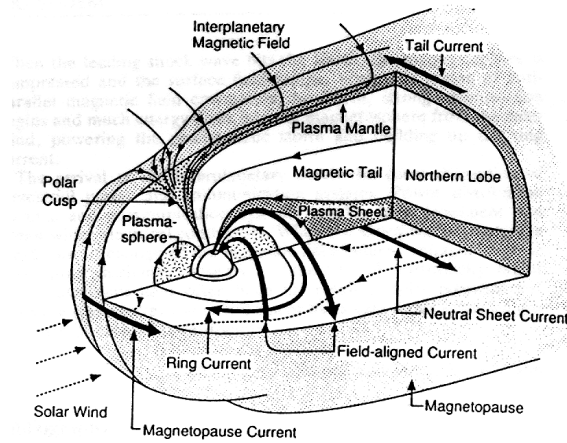


Figure 2.6 - Current systems in the cross section of Earth's magnetosphere. [Source Russell and Luhmann (1997)]

density and magnetic field change significantly across the bow shock. When the proton and electron penetrate the magnetopause, they bend from their paths by the Lorentz force. As a result, protons and electrons gyrate oppositely about the magnetic field lines. The different gyro-radii of proton and electron generate a current, which is called magnetopause current or Chapman-Ferraro current (GOMBOSI, 1998; BAUMJOHANN *et al.*, 2010). This current system generates a magnetic field that prevents the terrestrial dipole field from penetrating into the solar wind and the field induced by this current decreases the magnetic field just outside the magnetopause and increases it inside (GOMBOSI, 1998). This current is largely perpendicular to the Earth's dipole field if the magnetic field outside the magnetosphere is small. When a sudden increase in solar-wind dynamic pressure or an interplanetary shock, reaches the Earth, the magnetosphere is compressed; the magnetopause moves nearer the Earth, and at the same time the magnetopause current intensifies. The intensification of this current is observed as a sudden increase in H-component of geomagnetic field intensity of a few tens of nanotesla. If such a sudden increase in H-component of geomagnetic field is followed by geomagnetic storm, this feature is known as a sudden impulse (SI) or a sudden storm commencement (SSC).

2.7.2 Tail current

The narrow and elongated region of the Earth's magnetosphere that stretches away from the Sun behind the Earth by the solar wind is called the geomagnetic tail. It is the largest reservoir of plasma and energy in the magnetosphere. The energy and the plasma are released into the inner magnetosphere periodically during the

episodes of geomagnetic disturbances. The magnetotail consists of two lobes of oppositely directed magnetic field, referred to as the northern and southern tail lobes (BAUMJOHANN et al., 2010). The northern tail lobe is directed earthwards in the northern half of the tail and the southern tail lobe away from Earth in the southern half, separated by plasma-sheet. The diamagnetic current produced in the current sheet is called the cross-tail current. This current system separates the magnetotail into two adjacent hemispheres with opposite magnetic field polarities and also consists of dawn-dusk directed neutral sheet currents (ALEXEEV et al., 1975).

2.7.3 Ring current

The ring current is a westward flowing electric current around the Earth located at a distance between 4 to 9 R_E (DAGLIS et al., 1999). Enhancements in this current are responsible for shielding the lower latitudes of the Earth from magnetospheric electric field. Therefore, it has a large effect on the global decrease in the Earth's surface magnetic field, which has been used to define geomagnetic storms. This current is formed partially from ions with direct convective access to low L ($L = R_E$) values and partially from higher energy ions on closed drift paths diffusing in under the influence of fluctuating electric and magnetic fields (KOZYRA; LIEMOHN, 2003). During the quiet condition of the magnetosphere, the effect of this current is negligible. However, during geomagnetic disturbances, it produces the magnetic field in opposition to the Earth magnetic field and an earthly notice would observe a decrease in the magnetic field in this area. It has been accepted that the solar wind and ionosphere are the two sources for ring current. However, the relative contribution of each source remains unresolved (ELLIOTT et al., 2001). The ions are generated from both the solar wind and the ionosphere, but the low initial energy of the ionospheric ions ($\leq 10\text{ev}$) compared to the solar wind protons ($\geq 1\text{kev}$) led scientists to believe initially that the ionosphere was not a relevant contributor to the population of energetic H^+ observed in the magnetosphere. However, the Earth ionosphere could no longer be considered a negligible contributor for ring current after the discovery of energetic O^+ ions in the magnetosphere (SHELLEY et al., 1972; MOORE; DELCOURT, 1995). Evidence shows that during intense geomagnetic storms, the primary source of the ring current is terrestrial in origin (KRIMIGIS et al., 1985; HAMILTON et al., 1988; SHELDON; HAMILTON, 1993) and the O^+ ion is the dominant contributor (LENNARTSSON; SHARP, 1982; MOORE et al., 1999; LOTKO, 2007) which shows that magnetospheric processes are capable for energizing low-energy ionospheric ions and transporting them from the ionosphere to the magnetotail and back into the inner magnetosphere (CHAPPELL et al., 1987). Thus, during active

periods, the ionosphere is a significant source for the development of ring current (CHAPPELL *et al.*, 1987). The measurements of the ring current strength can be done by observing the depression of the magnetic field on the surface of the Earth. The growth and recovery of the ring current are monitored by changes in the Dst index, which serves as the standard measure of ring current activity (SUGIURA, 1964; ROSTOKER, 1972).

2.7.4 Field aligned currents

The existence of the Earth's magnetic field was established a long time ago with the alignment of compass needle. The Earth's magnetic field behaves like a dipole near the Earth's surface and its source is believed to be due to motion of electrically charged materials inside the core (KIVELSON; RUSSEL, 1995). In the regions further away from the surface of the Earth, the dipole magnetic field of the Earth is surrounded by a region called magnetosphere (CHUN; RUSSEL, 1997). In the boundary of magnetosphere, geomagnetic field lines interact with the magnetized plasma of solar wind that was ejected from the upper atmosphere of the Sun (PARKER, 1963). The solar wind has its own magnetic field known as interplanetary magnetic field (IMF), which interacts with the Earth's dipole to facilitate the transfer of an increased amount of energy into the magnetosphere (DUNGEY, 1961; GONZALEZ; MOZER, 1974). This interaction causes an increase in the movement of plasma through the magnetosphere and an increase in electric currents in the magnetosphere and ionosphere. The major electric currents are: the magnetopause current, tail current, ring current, partial ring current, field aligned currents and auroral electrojet. Figure 2.6 shows a schematic of various current systems and their rough geographical locations inside the magnetosphere. Among these current systems, the field-aligned current provides a strong link between the magnetosphere and the ionosphere. This current was first proposed by K. Birkeland (BIRKELAND, 1908) and is also known as Birkeland current. It is a set of currents which flow along the magnetic field lines connecting the magnetosphere to the ionosphere. It plays an important role for the coupling between the magnetosphere and the ionosphere. This coupling is directly influenced by solar wind and interplanetary magnetic field (IMF). Research related to field aligned currents has involved many important physical processes such as magnetic reconnection, field aligned current acceleration, auroral activities and plasma convection. FACs have very low electric current density ($<1 \mu A m^{-2}$) so it is very difficult for direct measurement (ZMUDA *et al.*, 1966; IJIMA; POTEIRA, 1976). Due to this reason, the intensity and distribution of these currents are estimated from ground based, rocket and satellite measurements. The initial satellite observation

for the distribution of FACs over high latitudes was carried out in the 1960s. Iijima and Potemra determined the global characteristics of the Field Aligned Currents by using magnetometer observations from TRIAD satellite (IJJIMA; POTE MRA, 1976). They also studied the flow direction of FACs and found similar results obtained by Zmuda and Armstrong (ZMUDA; ARMSTRONG, 1974), Imp 4 and Imp 5 (FAIRFIELD, 1973) and Ogo 5 (SUGIURA, 1975). They observed two principal regions of large scale FACs encircling the polar caps. These two currents were designated as Region 1 and Region 2. The Region 1 currents are located near the poleward boundary typically at magnetic latitudes 70-75 degrees, and flow into the ionosphere in the pre-midnight to morning sector (2300-1100 MLT) and away from the ionosphere in the afternoon to pre-midnight sector (1300-2300 MLT), where MLT stands for Magnetic Local Time. Whereas the Region 2 currents are observed near the equatorward boundary and flow into the ionosphere in the afternoon to pre-midnight sector, and away from the ionosphere during the pre-midnight to forenoon sector. The field aligned current was derived as suggested by Iijima and Potemera (IJJIMA; POTE MERA, 1982), in which its intensity is given by:

$$FAC = 0.0328[N_p^{\frac{1}{2}}V_{sw}B_T\sin(\theta/2)]^{\frac{1}{2}} + 1.4, \quad (2.2)$$

where FAC is in μAm^{-2} , solar wind density (Np) is in cm^{-3} , solar wind velocity (V_{sw}) is in kms^{-1} and $B_T = (B_y^2 + B_z^2)^{\frac{1}{2}}$ is in nT. The angle θ is measured between the positive Z-axis and the IMF vector in the Y-Z plane. It is given as $\theta = atan(\frac{B_y}{B_z})$ for $Bz \geq 0$ and $\theta = 180 - atan(\frac{|B_y|}{|B_z|})$ for $Bz < 0$.

2.8 Polar Cap Potential

The polar cap potential has long been considered an indicator for the development of magnetospheric convection. The relationship between the solar wind parameters and the polar cap potential is important to understand the coupling process between the solar wind and the magnetosphere and also the magnetosphere and the ionosphere (WEIMER, 1995; BOYLE et al., 1997; KIM et al., 2011). The connection between the solar wind drivers and convection patterns in the Earth's polar ionosphere has been studied extensively for the past two decades. Among these solar wind drivers, the role of southward IMF conditions has been understood very well (HEELIS, 1984; HEPPNER; MAYNARD, 1987; RICHMOND; KAMIDE, 1998; RICH; HAIRSTON, 1994; WEIMER, 1995; BOYLE et al., 1997; RUOHONIEMI; BAKER, 1998; HAIRSTON et al., 2005). As the solar wind is embedded with the interplanetary magnetic field that flows toward the Earth, a cross-magnetospheric electric field is generated along the magnetopause.

When the IMF is oriented southward, it reconnects directly with the Earth's magnetic field and a part of this electric field transfers to the polar ionosphere. This creates a potential difference in the ionosphere known as cross polar cap potential, which can be directly measured from low Earth orbiting satellites (PAPITASHVILI et al., 1999; HAIRSTON et al., 1999), from radars (RUOHONIEMI; GREENWALD, 1995; GREENWALD et al., 1999; SHEPHERD et al., 1999) and from ground magnetometers (KAMIDE et al., 1981). Much research has been done in order to understand the relationship between IMF-Bz and cross polar cap potential (CPCP) (REIFF; LUHMANN, 1986; WEIMER, 1995). They found that as the magnitude of IMF-Bz increases, the cross-magnetospheric electric field also increases, which in turn increases the ionosphere cross polar cap potential. They also observed that the polar cap potential is a linear function of the solar wind speed and the magnitude of IMF Bz. The ionospheric and magnetospheric convection state can be obtained through the difference between the maximum and the minimum of the potential (CPCP) in one hemisphere. The saturation of polar cap potential during intense geomagnetic storms has been studied by many researchers. In the language of geophysics, saturation simply means a physical quantity which is less than an expected value for a given strength of solar wind parameters. There are two main reasons for the saturation of polar cap potential. The first one is the decrease in the efficiency of dayside magnetic reconnection at the magnetopause (SONNERUP, 1974; HILL, 1975). The other one is the decrease in the polar cap potential induced in the ionosphere (HILL, 1976; FEDDER; LYON, 1987; WEIMER et al., 1990). The former may be caused by imbalance between the magnetic field intensities whereas the latter may be related to coupling between the magnetosphere and the ionosphere. The energy coupling function plays an important role to understand the relationships between ionosphere-magnetosphere and solar wind energy input. Initially, it was derived by Perreault and Akasofu (PERREAULT; AKASOFU, 1978) and showed that interplanetary energy flux is estimated on the basis of Poynting flux. Based on magnetic reconnection geometry, Kan and Lee introduced the concept of merging electric field (E_m) and the polar cap potential (ϕ_m) and expressed as below (KAN; LEE, 1979):

$$E_m = V_p B_T \sin^2 \left(\frac{\theta}{2} \right) \quad (2.3)$$

and

$$\phi_m = V_p B_T \sin^2 \left(\frac{\theta}{2} \right) L_o \quad (2.4)$$

Where Vp is the solar wind velocity, $B_T = \sqrt{B_y^2 + B_z^2}$ is the transverse magnitude of IMF, $\theta = \arccos\left(\frac{B_z}{B}\right)$, L_o ($7R_E$) is the effective length and R_E is the Earth radius. Later, it was developed by Kan and Lee (1979) based on the magnetic reconnection geometry. Nagatsuma (2004) studied the saturation of PCV and found that the degree of saturation does not depend on components of IMF but depends on the value of merging electric field. Similarly, Borovsky et al. (2009) found that the saturation of the PCV occurred statistically during storm-times, solar maximum, and low-Mach number solar wind. Troshichev et al. (1996) studied the statistical dependence of the PCV with PCI (Polar Cap Index) and showed a linear relationship. A more detailed description of saturation of polar cap potential during large geomagnetic storms can be found in Raeder and Lu (2005), Nikolaeva et al. (2013).

2.9 Akasofu's parameter and solar wind energy

The principal cause of geomagnetic disturbance is the magnetic reconnection, which establishes an electrodynamic coupling between the solar plasma and the magnetosphere. The mechanism for such modifications is associated with intensifications in the current systems that increased auroral ionospheric currents at high and mid-latitudes and by enhancements in the ring current at lower latitudes (TSURUTANI; GONZALEZ, 1997). One of the major phenomena observed during geomagnetic disturbance is the enhancement in the ring current.

The enhancement of the equatorial ring current causes a decrease in the H-component of the low latitude magnetic field. The principal cause for this decrease in the H-component is the enhanced energy transfer from solar wind to the magnetosphere. This enhancement occurs, if the southward oriented B_z component of the interplanetary magnetic field (IMF) interconnects with the Earth's magnetic field and is sustained for enough time (DUNGEY, 1961; GONZALEZ et al., 1994; GONZALEZ et al., 1999). The presence of high values of the southward oriented IMF- B_z and solar wind velocity (u) result in an increased interplanetary electric field (dusk-ward), which is given as $E_y = uB_z$ and is responsible for magnetospheric energization. In order to understand this phenomena several energy functions have been studied by Gonzalez et al. (1989), Gonzalez (1990). Among them, the $\epsilon(W)$, first defined by Perreault and Akasofu (1978) is used in this work. As defined by Perreault and Akasofu (1978), both coupling function and total energy input are expressed as:

$$\epsilon = 10^7 u B^2 l_0^2 \sin^4\left(\frac{\theta}{2}\right) [W] \quad (2.5)$$

and

$$W_\epsilon = \int_{t_0}^{t_m} \epsilon dt [J], \quad (2.6)$$

where B is IMF strength, θ is IMF clock angle ($\theta = \text{atan}(By/Bz)$) and $l_0 = 7R_E$ is empirically determined factor (all are in SI system). In Equation 2.6, the energy input to the magnetosphere is obtained by integration over the HILDCAA interval. After the interaction of the Solar wind magnetic field with the Earth magnetic field through the process of magnetic reconnection, the solar wind energy is dissipated into different regions of the magnetosphere and ionosphere (AKASOFU, 1981; de Lucas et al., 2007). For example, in the high-latitude ionosphere as the form of Joule heating (U_j), in the auroral region as the form of auroral precipitation (U_c), in the inner magnetosphere as the form of ring current energization (U_{DR}) and in the magnetotail as the form of plasma sheet particle heating (U_T) and plasmoid ejection U_{PL} . Then the total energy budget can be estimated through the sum of these contributions (AKASOFU, 1981). The Akasofu parameter given in Equation 2.5 is supposed to be an approximation for the total power input into the magnetosphere (GONZALEZ, 1973; GONZALEZ; MOZER, 1974; GONZALEZ; CLUA-GONZALEZ, 1981). This approximation is obtained by taking the ratio between the geomagnetic field at the magnetopause (BG) and the magnetosheath field at the magnetopause (BM). If BG is sufficiently large than BM, in this case the reconnection line does not tilt enough. Due to this reason, the reconnection electric field, E_y , does not differ much from the total field (GONZALEZ; CLUA-GONZALEZ, 1984). Another problem is related to the radius of the effective area of the dayside magnetopause. MonrealMacMahon and Gonzalez (1997) considered the magnetopause position as a function of solar wind ram pressure by substituting the value of l_0 in Equation 2.5. Then, they derived the corrected form of Akasofu parameter (ϵ^*) by replacing the old effective magnetospheric cross-section by R_{CF}^2 . Where $R_{CF}^2 = (B_0^2/4\pi\rho v^2)^{1/6}R_E$ is in SI system. Then the corrected form of Akasofu parameter (ϵ^*) is expressed as,

$$\epsilon^* = \left(\frac{R_{CF}}{l_0} \right)^2 \epsilon \quad (2.7)$$

In this expression the radius of effective areas is obtained by considering the balance between the kinetic plasma and the magnetic pressure. In this work, we also try to express another correction on Akasofu parameters as proposed by Vasyliunas (VASYLIUNAS et al., 1982) and expressed as

$$\epsilon^{**} = \left(\frac{P_{SW}}{P_0} \right)^{1/n} \epsilon^*, \quad (2.8)$$

where P_{SW} is the solar wind pressure, \bar{P}_0 is the average solar wind ram pressure for solar cycle 22 (which is 2.5 nPa) and $1/n$ is substituted by $1/2$ as suggested by Gonzalez (GONZALEZ, 1990). A more detailed description of Akasofu parameter (ϵ) and corrections can be found in de Lucas et al. (2007).

3 DATASETS

3.1 Ground based observations

3.1.1 Geomagnetic field

Continuous observations and measurements taken at proper locations contribute comprehensive knowledge about various complex processes occurring in the Sun and near and far space regions of the Earth. The external and internal variations in the geomagnetic field are recorded with the help of magnetic instruments. At any location, the Earth's magnetic field can be represented by a three-dimensional vector and can be represented in at least two ways. The first representation is called the XYZ representation where X represents the northward component, Y represents the eastward component and Z represents the vertical component. Another set of representation is called HDZ representation where H represents the horizontal component, Z represents the vertical component and D represents the declination (CHAPMAN; BARTELS, 1962; CAMPBELL, 1997). Figure 3.1 shows the relation between XYZ-HDZ components of the magnetic field vector in three coordinate systems: Cartesian, polar, and spherical. The graphical representation of HDZ and XYZ variation is called magnetogram. It is used to measure the temporal variation of the local strength and direction of the geomagnetic field produced either in the laboratory or existing in the nature. In this thesis work, the digital magnetic data of 1 minute resolution from high, mid, low and equatorial ground based magnetic observatories are used.

Figure 3.2 shows the locations of currently operating geomagnetic observatories.

The geomagnetic observatories selected to provide measurements on surface are presented both in Table 3.1, organized by latitudes, and Table 3.2, by longitude. The tables show the names and the coordinates of geomagnetic observatories with their IAGA (International Association of Geomagnetism and Aeronomy) codes. Those observatories allow analyses that take into account both the longitude and latitude features. In this list, GUAM is an equatorial station where the influence of equator current systems can be monitored. Similarly, THL is a high latitude station where the influence of the high latitude current systems can be monitored. Except for these two, the others are low and mid-latitudes observatories that are useful in order to monitor the contribution of the ring current during geomagnetic disturbances. There are more than 150 geomagnetic observatories to monitor the change in the Earth's magnetic field. Considering the latitude and longitude, the global distribution of observatories are very uneven. These observato-

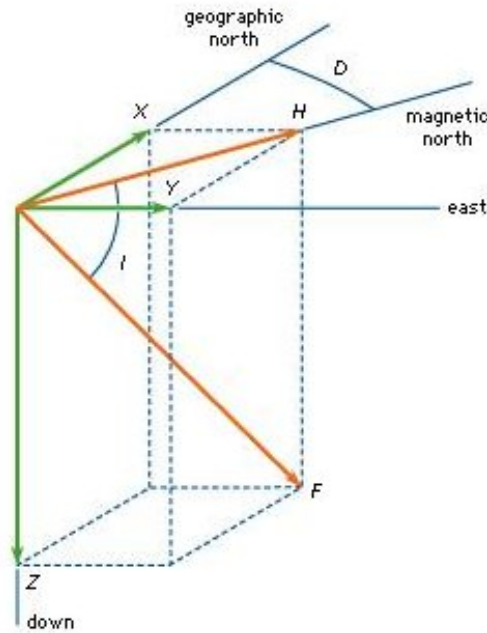


Figure 3.1 - The relation between XYZ-HDZ components of the magnetic field vector in three coordinate systems: Cartesian, polar, and spherical. [Source Kivelson and Russel (1995)]

ries give data of different temporal resolution which are distributed through several World Data Centers. For the calculation of external field variation, traditionally, annual mean values have been used but the availability of hourly mean values or one minute value in digital form makes it easy for better characterization. [<http://www.springerreference.com/docs/html/chapterdbid/205053.html>]

The main aim of magnetic observatories is to monitor the Earth's magnetic field with an absolute accuracy in the geodetic reference frame (JANKOWSK; SUCKSDORFF, 1996). Achieving accuracy, However is very difficult due to the unknown contribution of magnetic field near crustal sources. In order to monitor the changes in the Earth's magnetic field, some relevant sources of datasets have been derived from ground based geomagnetic measurements through the program known as INTERMAGNET. This program supported by IAGA, has encouraged the magnetic observatories to collect the datasets of one minute data in near real time. The ground geomagnetic observatories are characterized by the production of continuous long term and stable data of suitable quality for the studies of secular variation. In this thesis, datasets are used from different observatories and downloaded from a web page : <http://ottawa.intermagnet.org/apps/download/index-eng.php>.

Table 3.1 - Geomagnetic observatories (organized by latitude)

Observatory	Geomagnetic latitude	Geomagnetic Longitude
Thule (THL)	88.46	14.10
Istanbul Kandilly (ISK)	38.31	108.87
Guimar-Tenerife (GUI)	33.96	61.0
Kakioka (KAK)	26.62	207.77
Tammanrasset (TAM)	24.94	81.23
Honolulu (HON)	21.46	268.57
Alibag (ABG)	9.64	145.39
Guam (GUA)	4.57	214.76
Vassouras (VSS)	-12.53	25.70
Charters Towers (CTA)	-28.01	220.97
Trelew (TRW)	-32.28	4.81
Gnangara (GNA)	-42.71	187.94

Table 3.2 - Geomagnetic observatories (organized by longitude)

Observatory	Geomagnetic latitude	Geomagnetic Longitude
Honolulu (HON)	21.46	(-88.57) 268.57
Charters Towers (CTA)	-28.01	(-40.97) 220.97
Guam (GUA)	4.57	(-34.76) 214.76
Kakioka (KAK)	26.62	(-27.77) 207.77
Gnangara (GNA)	-42.71	(-7.94) 187.94
Trelew (TRW)	-32.28	4.81
Thule (THL)	88.46	14.10
Vassouras (VSS)	-12.53	25.70
Guimar-Tenerife (GUI)	33.96	61.0
Tammanrasset (TAM)	24.94	81.23
Istanbul Kandilly (ISK)	38.31	108.87
Alibag (ABG)	9.64	145.39

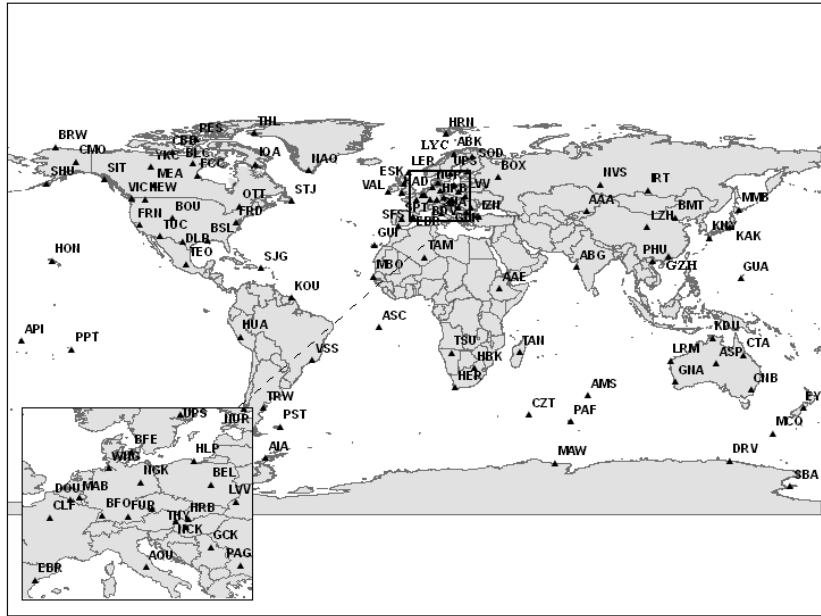


Figure 3.2 - Locations of currently operating geomagnetic observatories.
 [Source:<http://www.intermagnet.org/imos/imomap-eng.php>]

The variation in H and D components are obtained by removing average quiet days from each disturbed day and depicted as ΔH and ΔD . Several geomagnetic indices have been proposed to compute the degree of disturbance on the geomagnetic field due to the injection of charged particles from the sun into the magnetosphere at different latitudes. They are computed by using the records from several distributed geomagnetic observatories following some criteria. Some of them, the major geomagnetic indices useful for this thesis are discussed in the next session. For illustrative purposes, Figure 3.3 shows the variations of H-component obtained from GUAM, ABG, VSS, KAK and THL and also SYM-H (nT), ASY-H (nT) and AE (nT) indices during the HILDCAA event on 20-23 April, 2003.

3.2 Geomagnetic indices

The geomagnetic disturbances occurring over short periods of time are measured by geomagnetic indices (ROSTOKER, 1972; MAYAUD, 1980). It was found that the magnetic field measured near Earth surface varies in wide ranges (VERBANAC et al., 2011). The main cause for geomagnetic field variations are the solar wind coupling with the Earth's magnetosphere (GONZALEZ et al., 1999) and magnetosphere coupling with ionosphere. The main indices used to measure variations in the Earth's

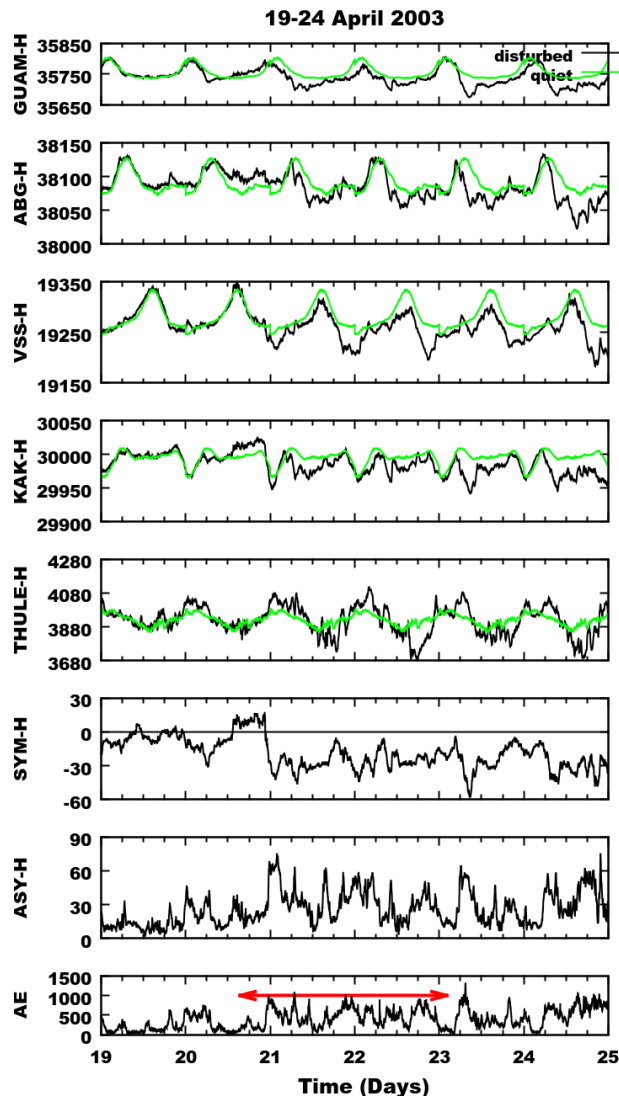


Figure 3.3 - From top to bottom, the panels show variations of H-component (nT) at the observatories GUAM, ABG, VSS, KAK, THL along with the geomagnetic indices SYM-H (nT), ASY-H (nT) and AE (nT) respectively during the HILDCAA event on 20-23 April, 2003. The green line represents the average quietest day variation, the black line represents the disturbed day variation and the red horizontal arrow in the AE panel indicates the HILDCAA interval.

magnetic field strength are given as follows.

3.2.1 The K and Kp Index

The geomagnetic index K is a 3-h quasi-logarithmic index developed by Bartels (1938). It measures the range of irregular and short-term geomagnetic activity. The K index reflects the maximum range of any component of the field over the 3-h interval at each station (ROSTOKER, 1972; SABA et al., 1997). Its value varies from

observatory to observatory but the historical occurrence rates are about the same for all observatories. The K index data are recorded for a 3-hour interval of time from each observatory. Then these data are converted to a quasi logarithmic K integer according to a scale that is specific to each geomagnetic station (ROSTOKER, 1972; LOVE et al., 2007). The total maximum fluctuations in the magnetic field during the 3 -hour period are obtained by adding maximum positive and negative deviations. These types of deviations may occur at any time during the 3-hour interval. The scale values of K range from 0 (low activity) to 9 (strong activity). The values of $K_p < 4$, $K_p = 4$ and $K_p > 4$ represent quiet, unsettled and indication of the geomagnetic storm respectively. The other equivalent linear scale planetary indices are ap, Ap and aa (MAYAUD, 1980). The geomagnetic index Ap is a daily index obtained simply by averaging the eight values of ap for each day. The three-hour index ap is directly related to the Kp index. It is derived from the 3-hourly Kp values. The aa index is similar to the Ap index. It is estimated by taking the datasets from two approximately antipodal observatories. The main purpose of this index is to monitor the global geomagnetic behavior.

3.2.2 The AE Index

The AE index was developed by Davis T. N. and Sugiura (1966). The main purpose of this index is to measure the global auroral zone magnetic activity produced by enhanced ionospheric currents. It is constructed by taking one minute datasets of H-component from auroral-zone observatories located around the world (ROSTOKER, 1972; KIVELSON; RUSSEL, 1995). Thus, the constructed values are plotted as a function of universal time (UT). The amplitude of upper and lower envelopes are defined as AU and AL respectively. The amplitude of AU represents the maximum perturbation generated by eastward electrojet current in the afternoon sector and AL represents the maximum perturbation generated by westward electrojet current in the morning and midnight sectors. The difference between AU-AL gives the AE index and $(AU + AL)/2$ gives the AO index. In general, the term "AE" is used to indicate AU, AL, AE and AO. Thus AU and AL give individual strength of eastward and westward electrojets. On the other hand, AE gives overall horizontal current strength and AO provides equivalent zonal current. Nowadays, this index is widely used in the field of geomagnetism, aeronomy and solar-terrestrial physics. To illustrate, Figure 3.4 shows an interval of continuous high AE values occurring on 12 January, 1997. Figure 3.5 shows the distribution of the main observatories used for the calculation of AE index in the auroral region of the northern hemisphere.

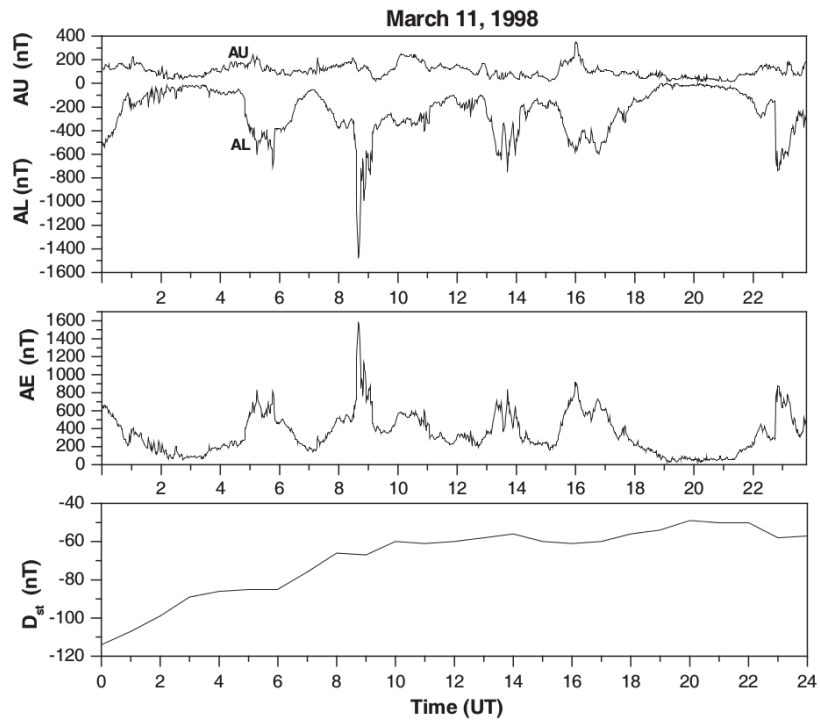


Figure 3.4 - A HILDCAA interval detected on March 11, 1998. From top to bottom are the 1 min average AU and AL indices, the AE index and D ST.

[Source:(TSURUTANI et al., 2004)]

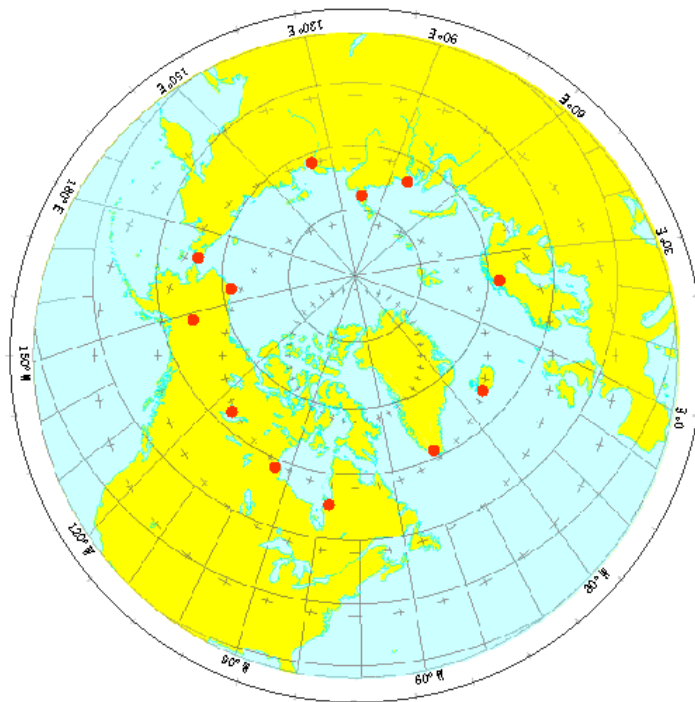


Figure 3.5 - Distribution of AE(12) observatories.

[Source:<http://wdc.kugi.kyoto-u.ac.jp/aedir/ae2/AE0bs.html>]

3.2.3 The Dst Index

The storm time disturbance index (Dst) (SUGIURA, 1964; ROSTOKER, 1972) is a geomagnetic index which monitors the world wide geomagnetic storm strength. It is constructed by averaging the axially symmetric disturbance in the horizontal component of the geomagnetic field recorded on the observatories at near dipole equator on the Earth's surface. The major effect of geomagnetic disturbances are recorded as a negative value in Dst. This is due to the the storm time ring current which flows around the Earth from east to west in the equatorial plane. This ring current is formed by the differential gradient and curvature drifts of electrons and protons in the near Earth region (around $2R_E$ - $7R_E$) (GONZALEZ et al., 1994; DAGLIS et al., 1999). The ring current injection inside the magnetosphere is significant when the southward interplanetary magnetic field (IMF) reconnects with the geomagnetic field (DAGLIS et al., 1999). This current is composed by linear and non-linear processes from the dawn-dusk electric field. The injection of particles and its magnetic effect may be approximated as a linear process. Although the trapping mechanism and consequently the resultant ring current intensity may not be approximated as a linear process, it depends on the history of the cross tail potential difference. This effect will limit the efficiency of the linear prediction filter of the ring current from the solar wind parameters (TAKAHASHI et al., 1990). The understanding of ring current state is a necessity to forecast the magnetic field in the magnetosphere. The magnetic field variation produced by the ring current decreases the magnetic field at the Earth's surface. Then, this variation is measured by the Dst index (SUGIURA, 1964; SUGIURA; KAMEI, 1991) which represents the longest commonly used measure of the state of the ring current and therefore it is essential in such forecasting (BAKER, 1998). Hence by knowing the solar wind conditions and intensity of ring current, an estimation of the Dst index can be made. The ranges of Dst depends on activity of sun. The approximate ranges of Dst are +100 nT to -600 nT (GONZALEZ et al., 1994). The positive value of Dst is caused by compression of magnetosphere due to the increase of solar wind ram-pressure (FRANK, 1967; FOK et al., 1996; VERBANAC et al., 2011). Figure 3.6 represents the network of the Dst Observatories indicated by black spots inside the red circles.

3.2.4 The Polar Cap Index

The Polar Cap Index (PCI) is a newly introduced index which has been designed to monitor the polar cap magnetic activity (TROSHICHEV et al., 1988). The main objective of this index is to monitor the polar cap magnetic activity generated by

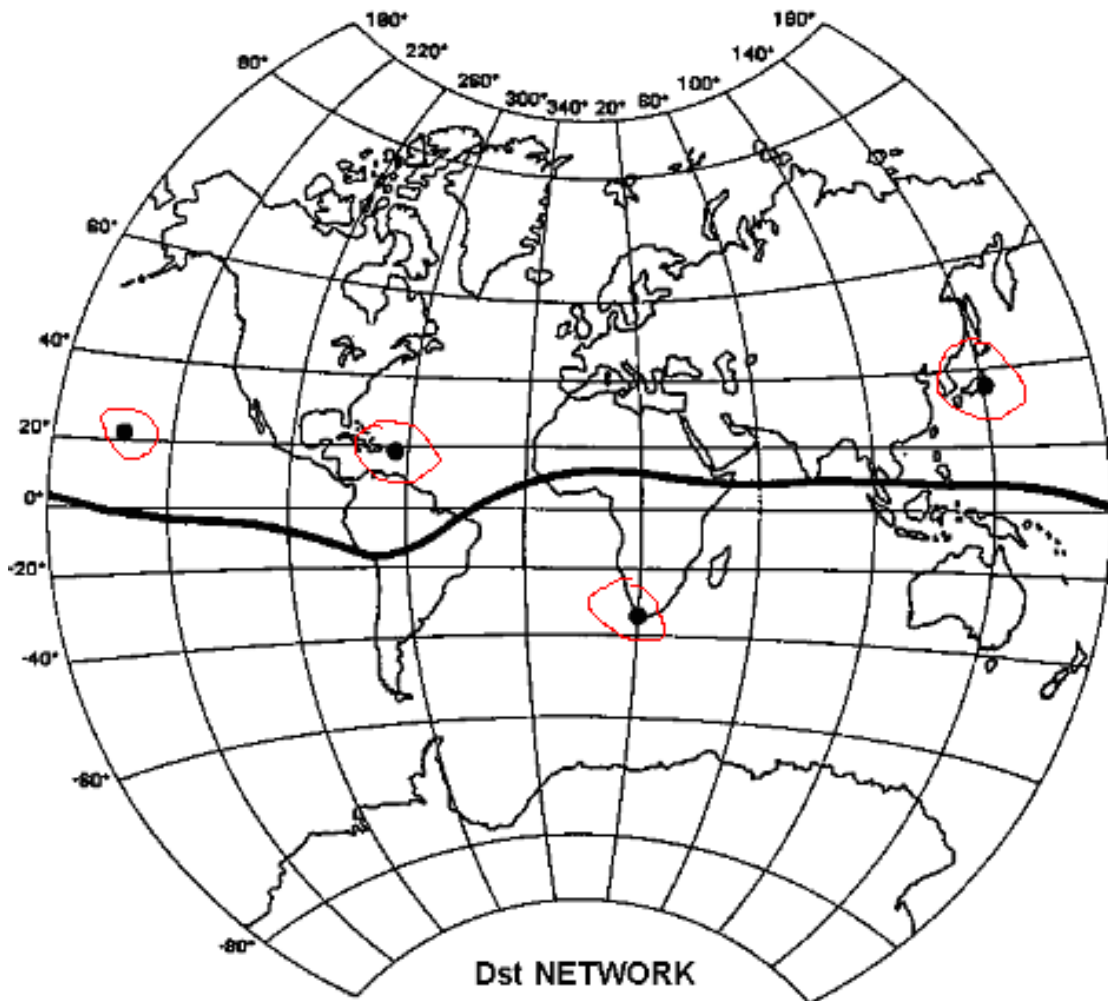


Figure 3.6 - Distribution of the Dst Observatories.
 [Source:<http://wdc.kugi.kyoto-u.ac.jp/aedir/ae2/AE0bs.html>]

solar wind parameters. These indices are available for both the north (Thule) and south (Vostok) poles. The geomagnetic latitudes for Thule and Vostok are 86.44 and 83.3 degrees respectively. It was derived based on the idea given by Troshichev et al. (1979) and has remained unchanged up to now. This index can be used to derive polar cap potential and to monitor auroral and midlatitude magnetic activities characterized by the AE and Kp indices. The AL index is derived from geomagnetic variation measure from twelve longitudinally spaced stations located at northern auroral latitudes and provides the information about the intensity of westward electrojet in the auroral ionosphere (DAVIS T. N. ANDSUGIURA, 1966; BAL-LATORE; MACLENNAN, 1999; MOON, 2012). Conversely, the PC index is used for the measurement of current in the polar cap. It is derived from magnetic data at a single ground-based station near-pole (TROSHICHEV et al., 1988). For illustrative purposes, Figure 3.7 shows the variation of interplanetary electric field (E_y , in mV/m), merging electric field (E_m , in mV/m), polar cap potential (PCV, in kv), polar cap index (PCI, in mV/m) and AL (nT) for the HILDCAA event on 20-23 April 2003. The horizontal red line with double arrows on AL index at the the last panel shows the HILDCAA interval.

3.3 Space based observations

The interplanetary datasets are essential for the identification of geomagnetic disturbances in the Earth environment. The interplanetary datasets are usually differentiated magnetic field and plasma data because they come from different instruments. Those magnetic field data have higher temporal resolution and constitute magnetic field vector components. They also include measurements of plasma velocity (in vector components), ion density, temperature and pressure. Generally, they have lower temporal resolutions due to technical limitations. The most widely used coordinate reference systems are the Geocentric Solar-Magnetosphere (GSM) and the Geocentric Solar-Ecliptic system (GSE). The GSM system located at the center of the Earth, where the vector X points toward the Earth-Sun line, vector Z orientes in the plan containing earth dipole and the vector Y completes the coordinate system (RUSSELL, 1971). Similarly, the GSE coordinate system is centered on the Sun where the X-axis points toward the Sun-Earth line, the Y-axis points toward the ecliptic plane and the z axis completes the coordinate system (RUSSELL, 1971; KIVELSON; RUSSEL, 1995). Figure 3.8 represents the relationship between the ecliptic reference systems (GSE) and the magnetosphere reference systems (GSM) (MENDES, 1992). About X_{GSE} axis, the orientation is from The Earth toward the Sun, and direction Z_{GSE} is perpendicular to the Ecliptic, i.e. the plane defined by translation movi-

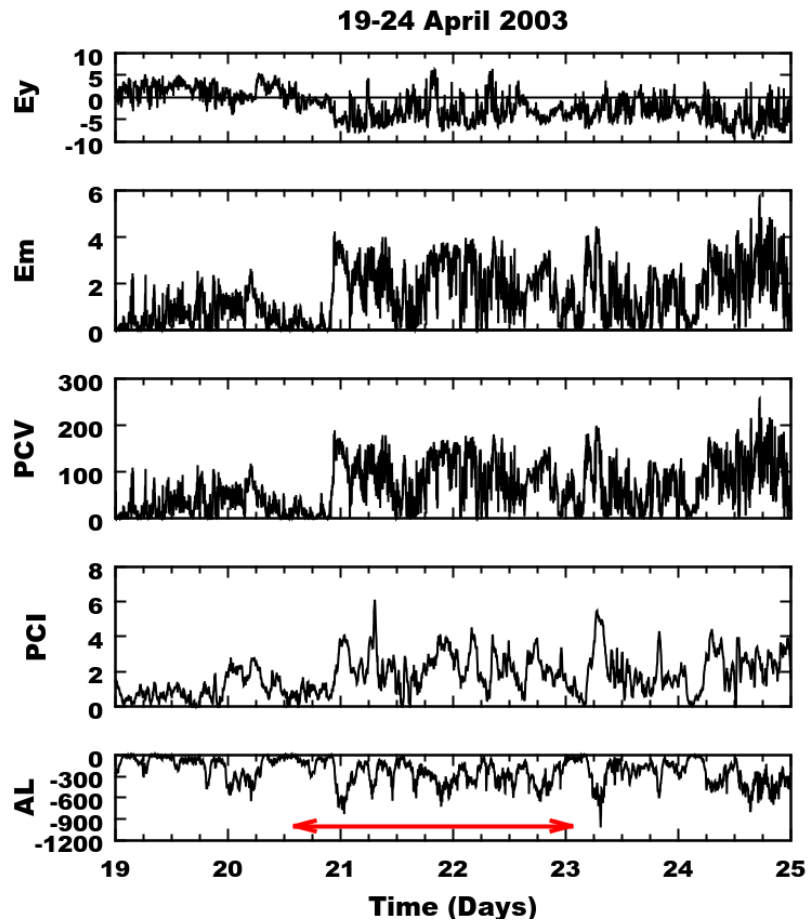


Figure 3.7 - From top to bottom, the panels represent the variations of interplanetary electric field (E_y in mV/m), merging electric field (E_m in mV/m), polar cap potential (PCV in kv), and geomagnetic index PC (mV/m) and AL (nT) for the non-storm HILDCAA event. The HILDCAA interval is marked by red horizontal arrow in AL panel. It occurs during 20-23 April, 2003.

ment of the Earth. The symbol D is the representation of the magnetic dipole of the Earth, that establishes a direction.

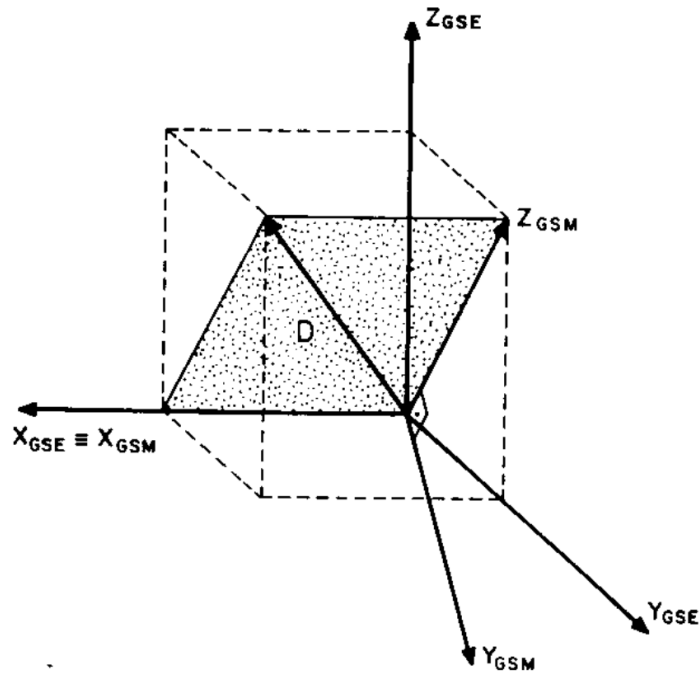


Figure 3.8 - The relationship between the ecliptic reference systems (GSE) and the magnetosphere reference systems (GSM). D represents the direction of the Earth's magnetic dipole.

[Source:Mendes (1992)]

There are several satellites used for interplanetary data. Some of them are ACE , Wind, Geotail, and IMP-8. In this thesis, interplanetary datasets were downloaded from the web page :http://omniweb.gsfc.nasa.gov/form/omni_min.html in the Solar magnetospheric (GSM) coordinate system. This site gives the high resolution OMNI data set consisting of 1-min averaged. For illustrative purposes, Figure 3.9 shows an example of HILDCAA event which occurred on April 20-23, 2003. The panels are from top to bottom, the solar wind temperature (T_{sw} in 10^4 K), speed (V_{sw} in km/s), plasma density (N_{sw} in cm^{-3}), IMF magnitude (B_0 in nT), B_y (nT), B_z (nT), SYM-H (nT) and AE (nT). The HILDCAA interval is marked by a red horizontal arrow in AE panel

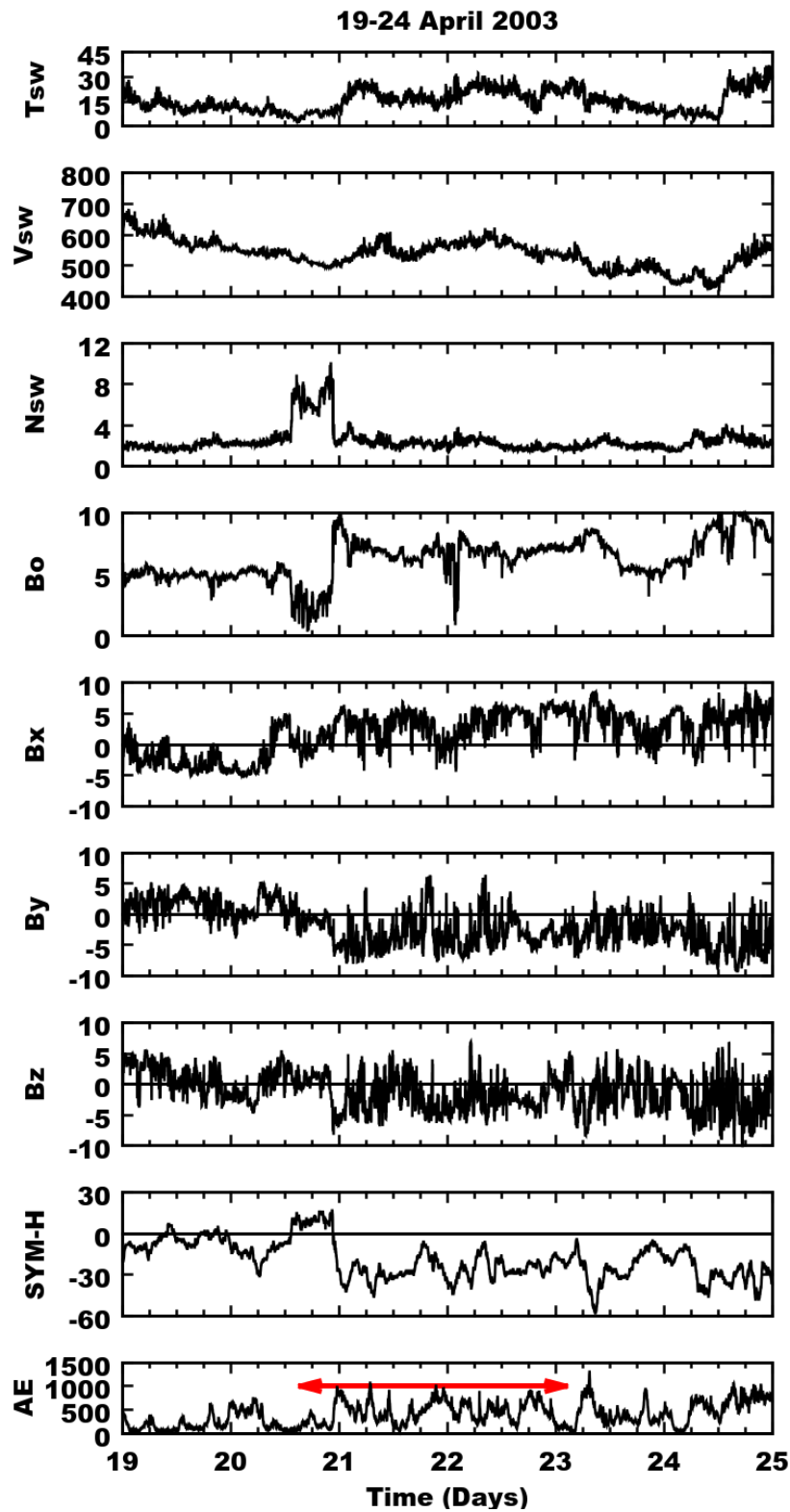


Figure 3.9 - From top to bottom, variations of solar wind temperature (T_{sw} in 10^4 K), speed (V_{sw} in km/s), plasma density (N_{sw} in cm^{-3}), IMF magnitude (B_o in nT), B_y (nT), B_z (nT), SYM-H(nT) and AE(nT). The HILDCAA interval is marked by red horizontal arrow in AE panel. It occurs during April 20-23, 2003.

3.4 Events to be analyzed

In this work, we will investigate the multiscale aspects related to HILDCAAs recorded by geomagnetic observatories in low and middle latitudes, in complementary manner the geomagnetic indices (AE, AL, PC), field aligned current density, merging electric field, polar cap potential, interplanetary parameters, magnitude of IMF and its components. We will also analyse all these parameters during quiet periods. The HILDCAA events were selected using the criteria suggested by [Tsurutani and Gonzalez \(1987\)](#) from the list of HILDCAA events discussed by [Hajra et al. \(2013\)](#). The list of events are shown in Table 3.3. Of the three events, two were associated with interplanetary HSSs and the remaining one occurred after the passage of ICMEs. The events associated with HSSs were typically associated with large-amplitude IMF-Bz fluctuations whereas the ICME-related event was characterized by small steady southward Bz intervals or low-frequency variations. Case labels indicate the interplanetary conditions for each period under analysis.

Table 3.3 - Selection of HILDCAA events

Year	Month	Day	Interplanetary Condition:	Case:
2003	04	20-23	HILDCAA not preceded by geomagnetic storm	NON-storm
2004	02	12-15	HILDCAA preceded by CIR	CIR
2005	05	15-18	HILDCAA preceded by ICME	ICME
2006	07	18-21	geomagnetically quiet period	QUIET

4 METHODOLOGIES FOR SIGNAL ANALYSIS

This chapter focuses on the wavelet transforms and their properties and methods used in this study to identify multiscale aspects during HILDCAA events recorded in middle and low latitude magnetometers, geomagnetic indices (AE, AL, PC), field aligned current density, merging electric field, polar cap potential, interplanetary parameters, magnitude and the components of IMF. These techniques are being used in this work to understand the multiscale aspect of these signal during this events.

4.1 From Fourier to Wavelet Analysis

The Fourier transform is a tool that breaks the frequency components of the signal into a representation characterized by sine and cosine functions. For any real or complex-valued function $f(t)$, the Fourier transform can be denoted $F(\xi)$, where the product of t and ξ is dimensionless. Generally, t is a measure of time (i.e., the time-domain signal) and ξ corresponds to inverse period, or frequency (i.e., the frequency-domain signal). It is defined by

$$F(\xi) = \int f(t) \exp^{-2\pi i \xi t} dt \quad (4.1)$$

It is a reversible and linear transform with many well known properties, as described for instance in [Bracewell \(2000\)](#).

Usually, for data analysis one considers the Discrete Fourier Transform (DFT). It requires a discrete input whose non-zero values have a limited (finite) duration. Similarly, the Fast Fourier Transform (FFT) is a computationally efficient form of the DFT, as described in [Cooley et al. \(1969\)](#) and [Cooley and Tukey \(1965\)](#).

Two main tools related to this transform are used here. The first one is the power spectrum that is very useful to analyse the energy content of signals. It is estimated by taking the square modulus of the DFT. It is defined by

$$S(\xi) = \left| F(\xi) \right|^2 = \left| \int f(t) \exp^{-2\pi i \xi x} dt \right|^2 \quad (4.2)$$

For a given signal $f(t)$, this tool gives a portion of a signal power (energy per unit time) falling within given frequency bins.

The basic concept of power spectrum is related to Parseval theorem. The Parseval's

theorem refers to an isometry between the Fourier space and physical space. It means that the integral of the square of a function is equal to the integral of the square of its transform (energy conservation), *i.e.*,

$$\int |f(t)|^2 dt = \int |F(\xi)|^2 d\xi \quad (4.3)$$

A convolution is an integral that expresses the amount of overlap of one function g as it is shifted over another function f producing a third function that is typically viewed as a modified version of one of the original functions. More specifically speaking, for continuous functions, f and g , a convolution is defined as:

$$(f \star g)(t) = \int \overline{f(\tau)} g(t + \tau) d\tau, \quad (4.4)$$

where \star denotes the convolution operator, and the over-line symbol the complex conjugate. Similarly, for discrete functions, a convolution is defined as:

$$(f \star g)[k] = \sum_m \overline{f[m]} g[k + m], \quad (4.5)$$

where m is the time lag.

The method of correlation defines the degree of relationship between variables. Several methods of correlation have been derived depending on requirement. The best known is the Pearson's Correlation Coefficient (r), which is obtained by dividing the covariance of the two variables by the product of their standard deviations. The coefficient of correlation r has value ranging between -1 to +1, which indicate a perfect fit to a positive or negative linear model. A value close to +1 or -1 means a good linear fit and a value near 0 depicts poor fit to linear model.

The other method is a tool to compute cross-correlation. Cross-correlation is a measure of statistical relationships involving two variables as a function of a time-lag applied to one of them (FINCH; M., 2007; MANNUCCI et al., 2008; VICHARE et al., 2009). It is also referred to a sliding dot product or sliding inner-product. It is generally used to measure information between two different time series. The range of the data is -1 to 1 . The closer cross-correlation value is 1 . The cross-correlation of two functions is similar to their convolution. The difference arises in the reversal of the time variable. It is a standard method of estimating the degree to which two

series are correlated. The cross-correlation of functions $f(t)$ and $g(t)$ is defined as

$$\int \overline{f(\tau)} g(t + \tau) d\tau = \int \overline{f(t)} e^{-i\xi t} dt \int g(t) e^{-i\xi t} dt \quad (4.6)$$

If $f = g$, we have the Wiener-Khinchin theorem (BRACEWELL, 2000). This theorem states that the autocorrelation function of a wide-sense-stationary random process has a spectral decomposition given by the power spectrum of that process (CHATFIELD, 1989).

Nevertheless, the Fourier transform cannot tell at what time interval a particular frequency arises (details in (DAUBECHIES, 1992; HUBBARD, 1998; CASTILHO et al., 2012), and references therein). To overcome this, new transforms must be used, as described in the following.

Window Fourier transform

(WFT)

The WFT is an another form of Fourier transform. It replaces the Fourier transform sinusoidal wave by the product of a sinusoid and a window which is localized in time. It takes two arguments: time and frequency. It has a constant time frequency resolution in which the resolution can be changed by rescaling the size of window. It is a complete and stable representation of the signal. This transform uses a sliding window to find information about time and frequency that uses a tool to represent it, the so called spectrogram. However, this technique is unable to give precise information about time and frequency representation due to the fix length of window. In order to get more precise information for a scale representation, the wavelet transforms have been developed (HUBBARD, 1997).

Wavelet: the beginning

The first concept of a function wavelet was constructed by Haar (1910). However, the wavelet theory as we know today, did not exist at that time. This theory remained in obscurity for several years. Since the mid 40's, material related to it was developed in various independent working groups. The concepts that today form the wavelet theory were initiated by the geophysicist Jean Morlet and the physicist Alex Grossman in the early 1980's. They define the necessary conditions for a function to be called a wavelet function, as follows:

- a) The integral of the wavelet function (ψ) must be zero and assumed to

satisfy the admissibility condition.

$$\int \psi(t) dt = 0, \quad (4.7)$$

where ψ is the so called analysing wavelet function. This equation shows that ψ has a wave-like localized oscillation. This determined the word wavelet, originally emerged from the French language *ondelette*, which means small wave in contrast with the sine waves that are defined in all real axis.

- b) The wavelet functions are usually normalized and they must have unitary energy

$$\int |\psi(t)|^2 dt = 1. \quad (4.8)$$

This equation shows that the wavelet function has compact support or has a fast amplitude decay. A more detailed description about the wavelet analysis can be found in Farge (1992), Daubechies (1992), Hubbard (1998), Domingues et al. (2005), Antoine et al. (2008).

Morlet and Grossman also started the theory of continuous wavelet transform (CWT) that will be discussed in the next section. Basically, wavelet transforms are the mathematical tools that can be used to transform data representation into its multilevel components (DAUBECHIES, 1992).

At that time, many researchers thought that there was no orthogonal wavelet besides the Haar wavelet. Then, the mathematician Yves Meyer constructed the second orthogonal wavelet, which is known today as the Meyer wavelet (DAUBECHIES, 1992; CHUN; LIN, 2010). This research started the ideas of the multiresolution analysis, formalized by him and, at that time, his student Stephane Mallat.

Mallat showed in 1988 that with a multiresolution analysis we can construct orthogonal bases of wavelets with desired regularity and polynomial reproduction locally. Mallat also associated the MR analysis to the filter bank theory and designed fast algorithms to the discrete wavelet transform (MALLAT, 1989). In the same year, Ingrid Daubechies built a set of orthonormal wavelets of smooth bases with compact support. See details in (DAUBECHIES, 1992). This transform shows linear complexity as long as the wavelet is compactly defined. After that, the wavelet transform had numerous applications in the signal processing. The history of the wavelet can be found in the book of (HUBBARD, 1998). In the next section, the former wavelet

transform is described, than the discrete wavelet transform (DWT). Both are used in this work, the first help us to identify main aspects of the disturbances due to its redundancy and the the second are used in the identification of short duration phenomena.

4.1.1 Continuous Wavelet Transform (CWT)

A CWT provides redundant and continuous detailed description of a signal in terms of both time (t) and scale (a). It possesses the ability to construct a time-frequency representation of a signal. The coefficients of CWT are assumed to have zero mean and finite energy defined as

$$W_f^\psi(a, b) = \frac{1}{\sqrt{a}} \int f(t) \overline{\psi\left(\frac{t-b}{a}\right)} dt, \quad (4.9)$$

where $f(t)$ represents the signal, $W_f^\psi(a, b)$ the wavelet coefficients, over-line symbol the complex conjugate. The continuous parameters a and b are the scale and translation in time.

With the normalization factor $\frac{1}{\sqrt{a}}$ the squared wavelet coefficients represent the signal energy in the concept of square integrable function $L^2(R)$, and the Parseval Theorem is valid in this case. The variation of scale parameter gives dilation effect when $a > 0$ and contraction effect when $a < 0$ of the analysing wavelet function. Therefore, it is possible to analyse the low and the high frequency by changing this parameter.

We can have wavelet functions, even in the same family, with different properties. Their selection depends both on the datasets and the objectives of the analyses, see [Domingues et al. \(2005\)](#) and references therein to a discussion on this subject.

There are different forms to express Morlet wavelet. For these analysis, we are considering the Morlet wavelet function expressed as

$$\psi(t) = \exp\left(\frac{-t^2}{2\sigma^2}\right) \exp(i5t),$$

The adjustment of σ provides the information for better time and frequency resolution. For example, the small values of σ give good time resolution whereas the large values of it provide good frequency resolution. On the other hand, the problem of the admissibility condition breaks down when σ is below 1. Specifically, we use the standard Morlet wavelet function for time-scale representation of a signal because we

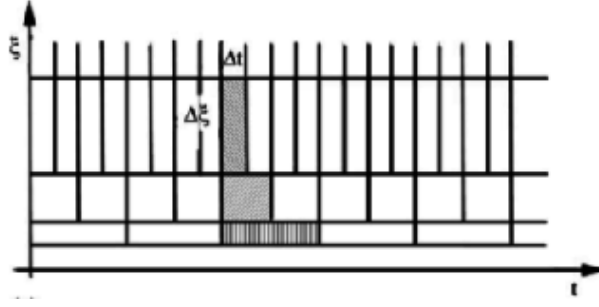


Figure 4.1 - Time-frequency plane representation $t \times \xi$ in the wavelet context. [Source: Mendes et al. (2005)].

are looking for an energy balance between the time and scale representation, where the frequency is inversely proportional to scale, therefore we choose $\sigma = 1$ (FRICK et al., 1997). For instance, it is possible to represent a signal in a time-scale plane, where the time-frequency localization is represented as a Heisenberg box located in the time-frequency plan. This is a rectangular box with a time width and frequency height, see Figure 4.1. The best possible area balance is given by this choice of the standard Morlet wavelet function, which happens because this relationship depends also on the pseudo-frequency or central frequency of the analyzing wavelet function, as expressed by

$$\xi_a = \frac{\xi_\psi}{a\Delta t}, \quad (4.10)$$

where Δt is the sampling time and ξ_ψ is the central frequency. For our choice of Morlet wavelet $\xi_\psi \approx 1$ and in this work we use $\Delta t = 1$ minute. Therefore, in this case

$$\xi_a \approx \frac{1}{a}, \quad (4.11)$$

So that the center period or pseudo period is approximately a .

In general, this transform is very expensive computationally due to the redundancy caused by the *practically continuously computation* of the scale and translation parameters on the integral. However, it is a wonderful tool to perform an exploratory study as the one done in this work.

Scalogram

In order to obtain a wavelet power spectrum, a tool for this analysis is the called scalogram, which is obtained by taking the square modulus of the wavelet coefficients (ANTOINE et al., 2008; FARGE, 1992). This increases the dimension of the data representation. For instance, for one dimensional signal, the scalogram is a two-

dimensional representation of analysis executed. Usually, we can visualize it using a color-map or isolines to visualize the energy topography.

The signal energy distributions are visible on scalograms with some specific characteristics. The first characteristic is to compare amplitude amplification by shocks or discontinuities, in mathematical sense, that exist in data records or function, and the another is to see abrupt changes. These characteristics appear on the scalograms through the scattering of frequencies. To illustrate, Figure 4.2 represents the scalograms for ΔD component from Vassouras observatory during HILDCAA event on 20-23 April, 2003. In figure, the horizontal axis represents the time in days and the vertical axis represents the scale in minutes. For an easy visualization, a highlight in the two-dimensional representation was obtained applying \log_2 function in the signal of energy distribution. So, the scale of color on the right side has unit in nT the same unit of real data, as we use a \log_2 function to highlight details in the scalogram values. This figure gives an important piece of information. Along the work, we obtained the results by using the mean-varnished value. As we are interested in variations of the records, we represent the graphics in a more comfortable scales. However, with this methodology, the same results are obtained by using the original data sets, which mostly have different absolute values.

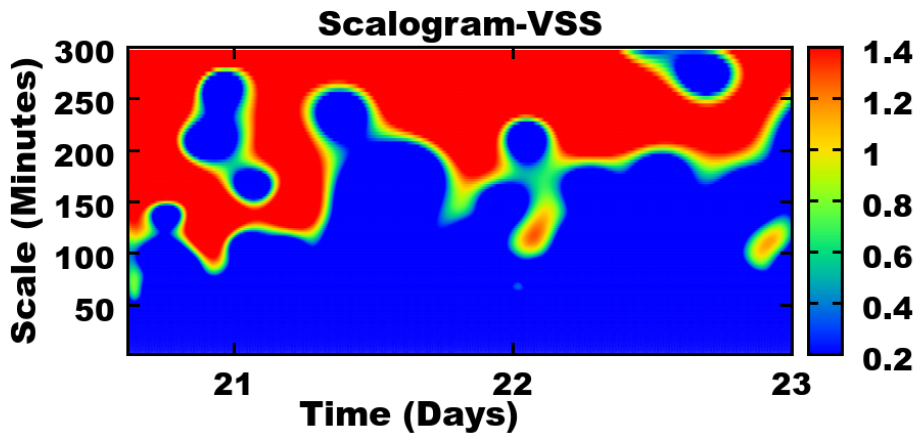


Figure 4.2 - Scalogram for ΔH -component from VSS observatory during HILDCAA event on April 20-23, 2003.

Global wavelet spectrum

To understand the scale view of the analysing processes, the global wavelet spectrum is obtained by the time integration of the scalogram (ANTOINE et al., 2008). It is expressed as:

$$S_\psi(a) = \int W_f^\psi(a, t) dt \quad (4.12)$$

Correlation by scale

The approach of correlation by scale $r_\psi(a)$ is used to study the correlation, that depends on scale (a), between the wavelet coefficients of two datasets. For that we compute

$$r_\psi(a) = \frac{\int W_{f_1}^\psi(a, t) W_{f_2}^{\psi*}(a, t) dt}{\left[\int [W_{f_1}^\psi(a, t)^2 dt] \left[\int W_{f_2}^\psi(a, t) dt \right]^2 \right]^{\frac{1}{2}}}, \quad (4.13)$$

where

$$W_i(a, t) = \left| W_i(a, t) - \overline{W_i} \right|, \quad (4.14)$$

where W_i are the wavelet coefficients, $\overline{W_i}$ is the arithmetic mean in time and $i = 1$ or 2 is related to what datasets are being used. More information about this approach can be found in NesmeRibes et al. (1995), Frick et al. (2001).

In particular, we use this technique to study the correlations by scale of the magnetograms and parameters of the solar plasmas, for instance, with the components of interplanetary magnetic field B_y and B_z . For illustrative purposes, Figure 4.3 shows the results of wavelet modulus correlation of ΔH -component from GUAM, ABG, VSS, KAK and THL with interplanetary magnetic field (B_z) for the HILDCAA event on 20-23 April, 2003. The horizontal axis represents the scale in minutes and the vertical axis represents the modulus correlation. In this figure, the scale of 1, 10, 100 and 1000 are labelled in horizontal axis.

Fixing small gaps on the dataset

In this work some datasets have gaps on the records. In those cases we used the gapped wavelet transform. This technique is a variant of the CWT introduced by (FRICK et al., 1997), in order to overcome problems with the estimation of energy and scale of the wavelet coefficients. Recently, this technique is used successfully in similar datasets with gaps (KLAUSNER et al., 2013).

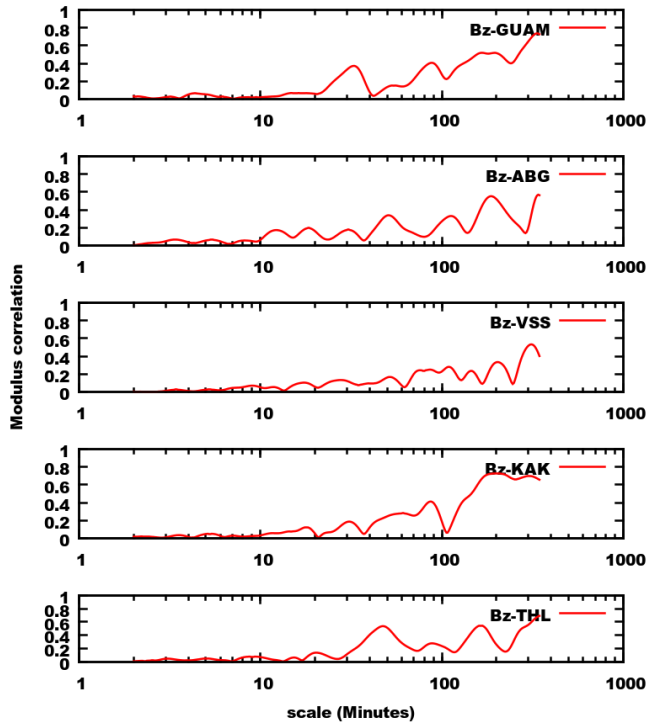


Figure 4.3 - From top to bottom, the panels represent the correlation of IMF-Bz with ΔH -component from geomagnetic stations GUAM, ABG, VSS, KAK and THULE during the HILDCAA event on 20-23 April, 2003.

In this technique, the continuous wavelet transform convolutes the signal, a gap transfer function, and the wavelet function. This can be thought as we move the unknown signal function, where the gap is, to a known new wavelet function, which is created from the original wavelet function and the gap transfer function. The main idea of this technique is to restore the admissibility condition by repairing it in some way through the wavelet function itself. The admissibility condition is broken when the wavelet function overlaps data gaps.

More precisely, let us consider a function $f(t)$ which is known for some interval of time t , and then, we can think of it as $g(t) = f(t)G(t)$, where $G(t)$ is the transfer function for data gaps. In this construction, the function $G(t)$ is considered one (i.e. 1) if the signal is correctly registered and it is zero (i.e. 0) otherwise. After that, we can construct the new analysing wavelet function

$$\psi'(t; a, b) = \frac{1}{\sqrt{a}} \psi\left(\frac{t-b}{a}\right) G(t), \quad (4.15)$$

Near the data gap, the function ψ' is used instead of ψ . As it is the function ψ'

will no longer satisfy admissibility condition. This problem was fixed in [Frick et al. \(1997\)](#) for the standard Morlet analyzing wavelet defining a adaptive wavelet,

$$\tilde{\psi}(t; a, b) = [\exp(i\xi_0(t - b)) - K(a, b)] \exp\left(\frac{-(t - b)^2}{2\sigma^2}\right) G(t), \quad (4.16)$$

where ξ_0 is the central frequency for Morlet wavelet. The main aim of the oscillatory part of this wavelet function is to fit this condition with a new oscillatory part $K(a, b)$ which depends on the gap itself and the oscillatory and envelop part of the wavelet function. More precisely,

$$K(a, b) = \left[\int \exp\left(\frac{-(t - b)^2}{2\sigma^2}\right) G(t) dt \right]^{-1} \times \left[\int \exp(i\xi_0(t - b)) \exp\left(\frac{-(t - b)^2}{2\sigma^2}\right) G(t) dt \right] \quad (4.17)$$

and therefore must be built continuously with the parameters a and b . It is important to note that it also helps to deal with boundaries of the datasets, and that the gaps should not cover all adaptive function on the lower level choosen.

4.1.2 Discrete Wavelet Transform (DWT)

The Discrete Wavelet Transform (DWT) is a linear multilevel efficient transform which operates usually on a data vector whose length is an integer power of two. This transform is very popular in data compression methodologies ([MALLAT, 1989](#); [DAUBECHIES, 1992](#); [HUBBARD, 1997](#)) due to its fast algorithms and good local representation in multilevel. It contains discrete values of scale ($a = 2^j$) and translation ($b = 2^j k$). The DWT may or may not have redundant representation which depends on the discrete scheme used, see details for instance in ([DAUBECHIES, 1992](#); [DOMINGUES et al., 2005](#)). The use of an orthogonal DWT is a solution to avoid redundant representation. This transform is defined as

$$d_k^j = 2^{-j} \int_{-\infty}^{\infty} f(t) \psi(2^{-j}t - k) dt, \quad (4.18)$$

where the discrete wavelet coefficients d_k^j are known as details (details are higher frequency structure or local approximation errors). They represent the different signals on two approximate consecutive levels. A tool known as multiresolution (MR) analysis helps on the construction of the wavelet functions that are used in the DWT. Inspired by the description presented in ([DOMINGUES, 2001](#)), lets us define the MR analysis and its basic proprieties.

More formally, a multiresolution analysis of the space $L^2(\mathbb{R})$ is a sequence of closed subspaces $\{V^j\}_{j \in \mathbb{Z}}$ from $L^2(\mathbb{R})$ and is associated with a function ϕ such that $\phi \in V^0$ (MALLAT, 1989). A MR analysis must satisfy the following conditions.

a)
$$\dots \supset V^{-2} \supset V^{-1} \supset V^0 \supset V^1 \supset V^2 \dots \quad (4.19)$$

b)
$$\bigcap_{j \in \mathbb{Z}} V^j = \{0\} \quad (4.20)$$

c)
$$L^2(\mathbb{R}) = \overline{\bigcup_{j \in \mathbb{Z}} V^j} \quad (4.21)$$

d)
$$f(x) \in V^j \Leftrightarrow f(2x) \in V^{j+1} \quad (4.22)$$

e)
$$f(x) \in V^0 \Leftrightarrow f(x - k) \in V^0, \forall k \in \mathbb{Z} \quad (4.23)$$

f)
$$\phi(x - k)_{k \in \mathbb{Z}}, \text{ is an Riesz basis for } V^0. \quad (4.24)$$

Based on these conditions, a MR analysis has the following properties. There is a sequence $h \in l^2$ such that

$$\phi(x) = 2 \sum_{k \in \mathbb{Z}} h(k) \phi(2x - k), \quad (4.25)$$

where $\phi(x)$ is scaling function and $h(k)$ are coefficients of scaling filter. For each level j ,

$$\phi_k^j(x) = 2^{\frac{j}{2}} \phi(2^j x - k), k \in \mathbb{Z} \quad (4.26)$$

where $\phi_k^j(x)$ form a Riesz basis of V^j . Then, the scaling function in the frequency domain is $\hat{\phi}(\xi) = H(\frac{\xi}{2})\hat{\phi}(\frac{\xi}{2})$ such that

$$H(\xi) = \sum_{k \in \mathbb{Z}} h(k) \exp^{-ik\xi} \quad (4.27)$$

where H represents a low pass filter, i.e $H(0) = 1$ and $H(\pi) = 0$. The contribution of wavelet theory for the space W_j is characterized by the addition of two embedded spaces $V_j \subset V_{j+1}$ and given as $V_{j+1} = V_j + W_j$. The function W^j contains the

difference of information between the levels j and $j + 1$. Then the wavelet function is expressed as

$$\psi(x) = 2 \sum_{k \in \mathbb{Z}} g(k) \phi(2x - k) \quad (4.28)$$

where $\psi_k^j(x)$ form a Riesz basis of W^j .

In Equations 4.25 and 4.28, $h(k)$ and $g(k)$ are the basic ingredients to compute this transform. Where h and g are related to low and high frequencies filters for the scale function and wavelet function respectively. These filters are used to compute the scale and the wavelet coefficients as:

$$c_k^j = \sqrt{2} \sum h(m - 2k) c_m^{j+1}, \quad (4.29)$$

and

$$d_k^j = \sqrt{2} \sum g(m - 2k) c_m^{j+1} \quad (4.30)$$

The multilevel transform is done by repeating this procedure recursively. In which the scale coefficients are convoluted with the filters and performing the down-sampling procedure, i.e., removing one data point between two. Therefore in each scale decomposition level the number of data is reduced by two. A more detailed description about the multiresolution approximations can be found in [Mallat \(1991\)](#), [Domingues \(2001\)](#) [Castilho et al. \(2012\)](#) and [Domingues and Kaibara \(2013\)](#).

The Daubechies wavelet functions are the most popular used set of multiscale approximation to functions in the wavelet context. There are families of orthogonal wavelets defining a discrete wavelet transform. As they form an orthogonal system, no redundant information is stored within the wavelet coefficient. These functions have no analytical expressions and are not symmetrical. One property that is used here is that, in the wavelet domain of smooth data with few localized structures, many wavelet coefficients with small amplitudes can be neglected, and one still has a good representation of the data. Therefore in these cases we can have a compact representation of the data, and moreover we can identify the disturbed regions on the data just by looking at the amplitudes of the wavelet coefficients.

In this work, the Daubechies wavelet function of order two was chosen because it can detect first order local disturbances in the signal and its derivatives. The non zero values of the low and high pass filters for Daubechies scale and wavelet functions

are:

$$[h_0, h_1, h_2, h_3] = [0.4829629131445, 0.8365163037378, 0.2241438680420, -0.1294095225512]$$

and

$$[g_0, g_1, g_2, g_3] = [h_0, -h_1, h_2, -h_3].$$

For the chosen analysing wavelet, the wavelet function frequency is $\xi_\psi = 0.66667$. Therefore, considering one minute data sampling, the pseudo-periods of the first seven levels ($j = 1, \dots, 7$) are 3, 6, 12, 24, 48, 96, and 192 minutes. Herein, the wavelet coefficients of seven levels are denoted by $d^{1, \dots, 7}$. More details on that can be found in [Abry \(1997\)](#). For illustrative purposes, [Figure 4.4](#) represents the DWT for ΔH -component from VSS observatory during HILDCAA event occurred on 20-23, April 2003. We used Daubechies order 2 orthogonal wavelet transform of seven levels ($j = 1, \dots, 7$) denoted by $d^{1, \dots, 7}$. For the chosen wavelet with frequency 0.66667 and sampling rate of one minute, the pseudo periods for the seven levels are 3, 6, 12, 24, 48, 96, and 192 minutes, respectively. The panels from top to bottom, the ΔH -component and the 7th levels of the square wavelet coefficients are shown. The red color identify where the HILDCAA events is happening.

The main objective of the use of this technique is to identify the variations that occur in observed parameters at the time of HILDCAAs. As discussed in ([MENDES et al., 2005](#); [DOMINGUES et al., 2005](#); [da COSTA et al., 2011](#); [SIMOES, 2011](#); [KLAUSNER et al., 2014a](#); [OJEDA et al., 2014](#)) small and large amplitudes of square wavelet coefficients indicate calm and disturbed conditions of magnetosphere respectively. The amplitude of the square wavelet coefficients present at that time can indicate disturbances associated with HILDCAAs. The major steps to process parameters observed during period of HILDCAAs are:

- a) To calculate the discrete wavelet transform.
- b) To analyze the wavelet coefficients of the seven decomposition levels (enough for the purpose of this study in analyzing periods equal or less than 200 min).
- c) To choose the wavelet coefficient thresholds that allow the singularity detection in the magnetic disturbance during HILDCAAs.

The importance of this technique is to highlight the singularities associated with

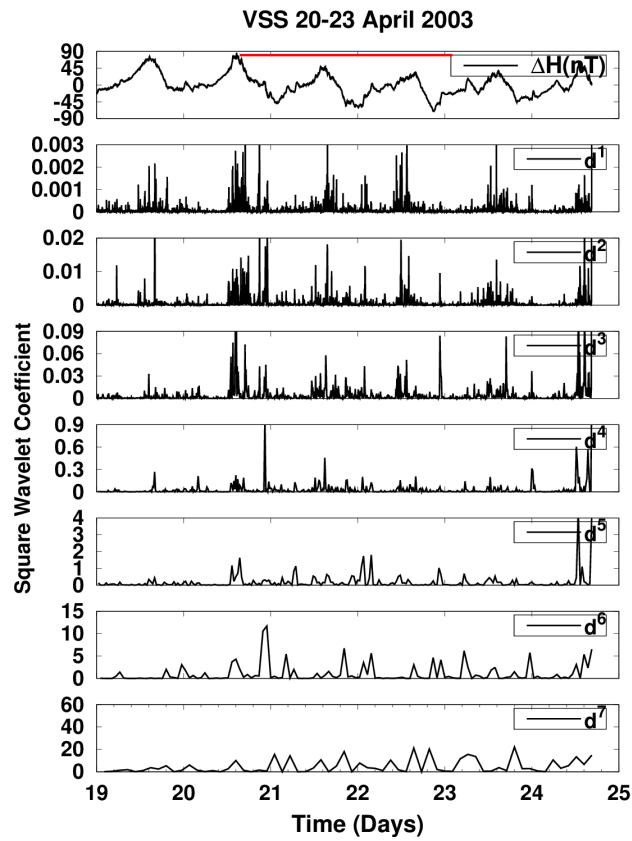


Figure 4.4 - Daubechies Wavelet coefficients d^j (for $j= 1,2,3,\dots,7$) for ΔH -component from VSS observatory during HILDCAA event occurred on 20-23, April 2003. The red color identify where the HILDCAA events occurs.

discontinuities present in ΔH -component of the Earth's magnetic field, geomagnetic indices (AE, AL, PC), Field aligned current, interplanetary parameters and magnetic fields during HILDCAAs.

5 RESULTS AND DISCUSSIONS

Although HILDCAAs are not very intense geomagnetic disturbance phenomena in terms of intensity, studies on this kind of events are important to identify the processes connecting the solar wind to the magnetosphere. The analyses considering the effects upon high latitude regions must be completed for the simultaneous manifestation on the rest of the globe. In order to study the geomagnetic effects recorded in observatories of middle-to-low latitudes during HILDCAA events, some HILDCAA phenomena were selected based on different conditions of the interplanetary environment. First of all, the characterizations of HILDCCA phenomena are presented. Multiscale analysis tools are used to extend the traditional information. As follows, analyses are developed to consider effects as function of longitudes and latitudes. The contribution of field aligned currents are considered in the HILDCAA period. Also the influence of interplanetary-electric-field coupling function is investigated.

5.1 Characterization of HILDCAAs

The understanding on the ground magnetic manifestation during HILDCAAs demands an adequate characterization of basic phenomena. With this purpose in this part, one geomagnetic quiet period and three different HILDCAA events of different interplanetary causes will be studied. The quiet period acts as a control because it identifies the background behavior. The other phenomena are related to HILDCAAs preceded by a disturbance produced by a interplanetary coronal mass ejection - designated as ICME HILDCAA, preceded by high speed stream (co-rotating interaction region or CIR) of the solar wind originating from a region of open magnetic field on the Sun's surface - designated as CIR HILDCAA, and an occurrence of a HILDCAA not preceded by geomagnetic storm - designated as NONSTORM HILDCAA. Each of those events represents all situations involving HILDCAAs.

For the analysis, the south-north component, B_z , of the interplanetary magnetic field in GSM coordinate reference system is used. This parameter is related to the cause of geoeffectiveness by the magnetic reconnection or the viscous interaction. The geomagnetic index AE is used as variable connected to the geomagnetic effects on the ground, basis for the HILDCAA identification. To enable a quantitative analysis, the Akasofu parameter estimates the ratio of amount energy injected through the magnetopause. This parameter interconnects the relevant variables of the interplanetary medium (density, velocity and magnetic field) related to HILDCAA effects. In a complementary way, the magnitude of interplanetary electric field applied to the magnetosphere during reconnection (E_y), the currents aligned with the geomagnetic

field which produce magnetic variations (FAC) and the pressure of the plasma which modulates magnetosphere itself are also calculated.

These events are selected using the four criteria suggested by Tsurutani and Gonzalez (1987) from the list of HILDCAA events discussed by Hajra et al. (2013).

- a) The AE index is expected to reach over 1000 nT at least once.
- b) It never occurs below 200 nT for periods longer than two hours at a time.
- c) These conditions should last at least two days.
- d) It should occur outside the main phase of geomagnetic storms.

Figure 5.1 presents the cases under study.

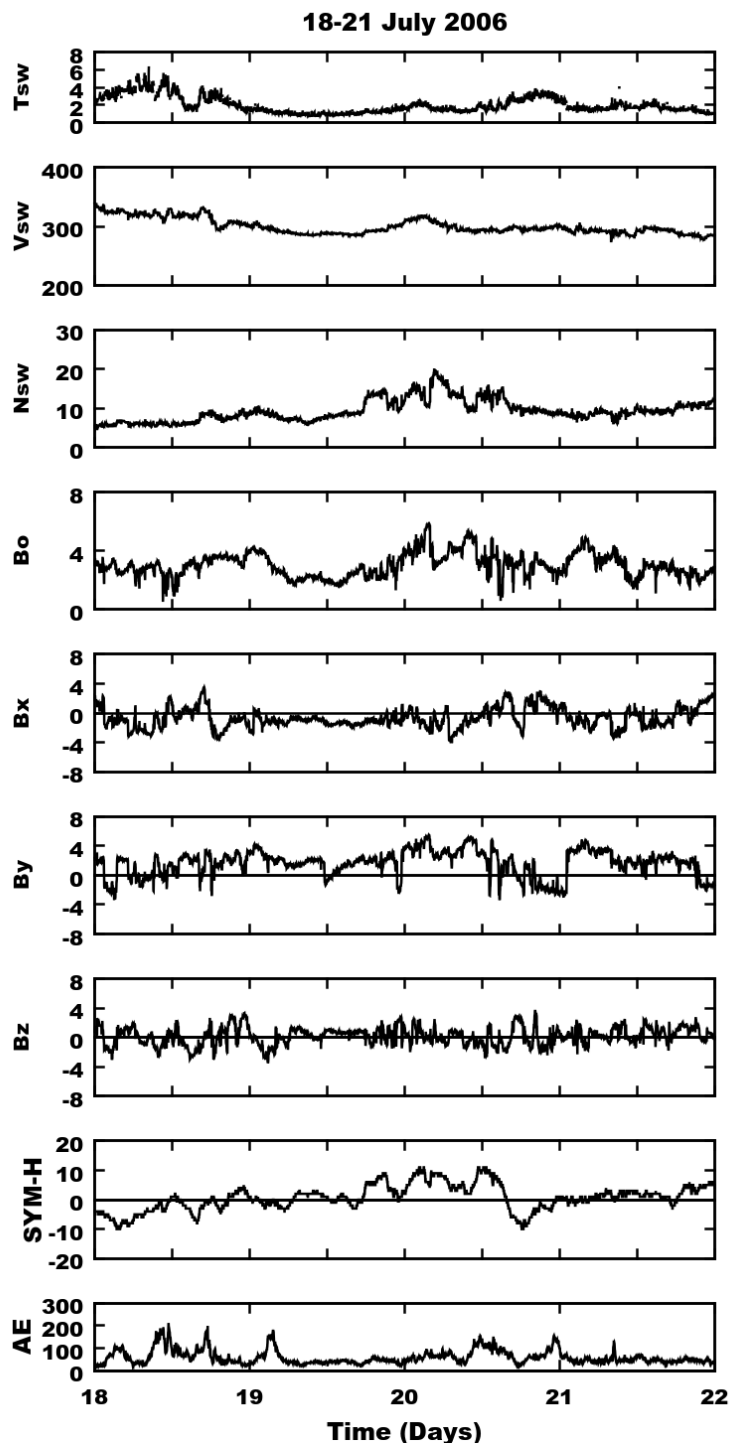
Figure 5.1(a) represents the omni datasets during quiet periods from 18 to 21 July, 2006. According to Mendes (1992) and Gonzalez et al. (1994), geomagnetic storms can be classified as: weak ($-50 < Dst \leq -30nT$), moderate ($-100 < Dst \leq -50nT$), intense ($-250 < Dst \leq -100nT$), and very intense ($Dst \leq -250nT$). On the other hand, a geomagnetically quiet period is understood at middle-low latitude regions. In this figure, the geomagnetic indices present low values. The AE is below 250 nT. The range of $SYM - H$ is about zero, with maximum amplitude varying between -20 to 20 nT. The solar wind parameters, interplanetary magnetic field and components show very weak values, characterizing a quiescent condition. During, a geomagnetic disturbance, there is an energy input inside the magnetosphere and ionosphere which changes ionospheric parameters, such as composition, temperature and circulation. But during quiet periods, measurements on the ground do not present significant disturbances. Sometimes little variations as enhancements or depletions are observed in the ionospheric parameters. These mechanisms are related to some drivers other than the Dst , such as traveling ionospheric disturbances (TID's) or the incidence of particles established by solar flares (DAVID, 2013). At current time, this scenario characterizes the background behavior of the magnetograms on the ground.

Figure 5.1(b) shows an example of non-storm HILDCAA occurred on 20-23 April 2003. The HILDCAA event starts at the mid day of April 20, 2003 to the beginning of April 23, 2003. During this time, the components of magnetic field (B_x , B_y and B_z) show fluctuations due to the presence of Alfvén waves (GUARNIERI et al., 2006). Those magnetic fluctuations are corroborated by fluctuations in density and speed

of the solar wind plasm. The decrease in SYM-H index is very weak between -20 nT to -30 nT. The AE index shows intense activity from mid day of 20 to the beginning of 23.

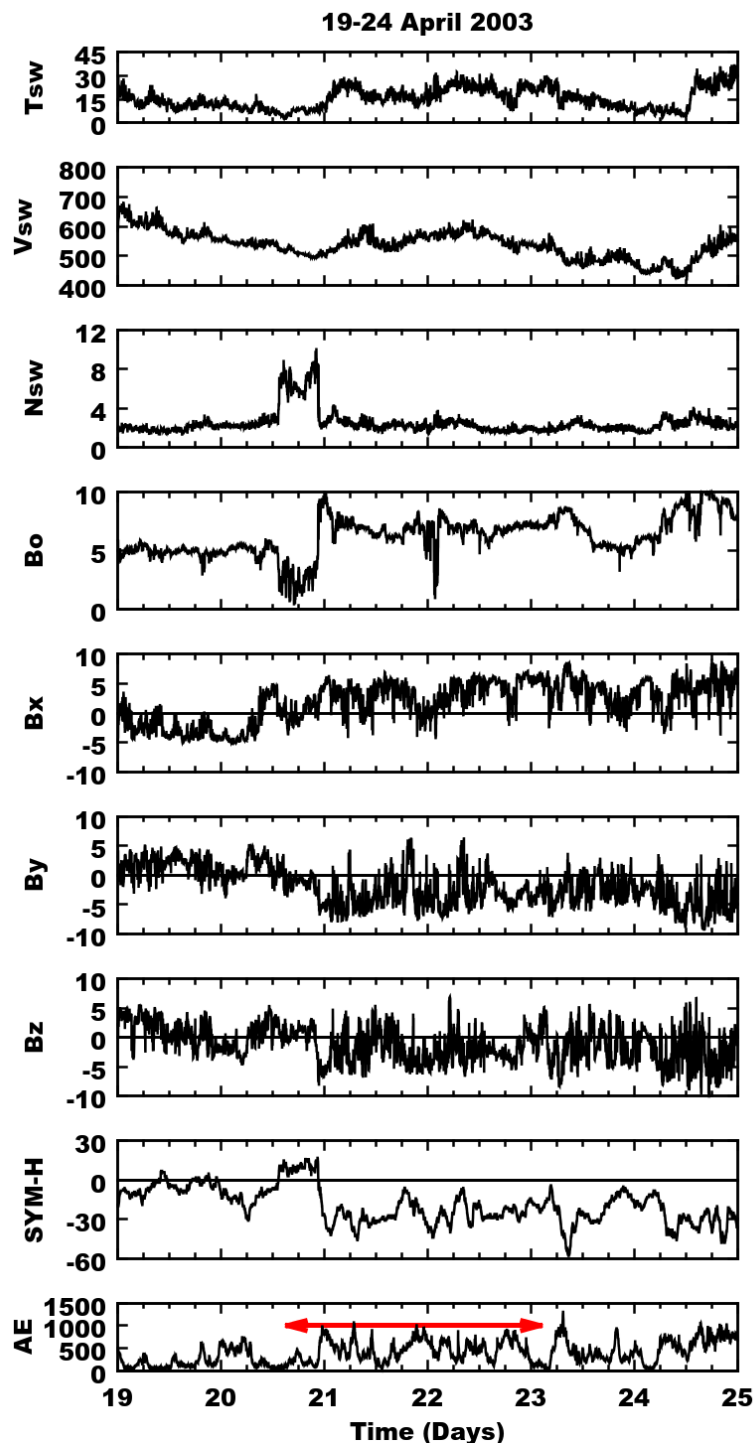
Figure 5.1(c) represents the OMNI datasets for the HILDCAA preceded by a Co-rotating interaction region-storm (CIR-storm) which occurred on 12-15 February 2004. In this figure, the solar wind parameters and the magnitude of IMF (B_0) clearly show the nature of CIR storm. The initial phase of this storm starts at the late day of 11 February 2004. The main phase starts around midnight and the long recovery phase (the HILDCAA event) lasts from the beginning of 12 February 2004 to mid-day of 15 February 2004. During the main phase, the solar wind temperature (T_{sw}), plasma density (N_{sw}), speed (V_{sw}) and magnitude of IMF (B_0) show the values of 2×10^5 (K), 40 (cm^{-3}), 400 (km/s) and 20 (nT), respectively. At the time of HILDCAA, solar wind temperature (T_{sw}) shows fluctuations between 2×10^5 K to 4×10^5 (K), speed increases from 400 to 600 km/s, plasma density (N_{sw}) and magnitude of IMF (B_0) remain almost constant and the IMF components, B_x , B_y , B_z show high level of fluctuation due to presence of Alfvén waves (GUARNIERI et al., 2006). The SYM-H index shows strong depression at the main phase and shows almost constant negative value for more than three days during the recovery phase. The AE index at the last panel of this figure shows intense activity and its values are always higher for the entire event.

Figure 5.1(d) presents the last case, where an ICME precedes HILDCAA that occurred on 15-18 May 2005. The interplanetary cause for this storm was the shock driven by an ICME which contained a magnetic cloud structure (HAJRA et al., 2013; OJEDA et al., 2013; OJEDA et al., 2014) characterized by large southward IMF- B_z with a peak of -50 nT. The magnetic cloud has large time extension including sheath region at the beginning of 15 May, 2005 (BURLAGA et al., 1981; BURLAGA, 1988; KLEIN; BURLAGA, 1982; DEMOULIN; DASSO, 2009; OJEDA et al., 2013; OJEDA et al., 2014). During the main phase, the SYM-H and the AE indices show peak values of about -300 nT and 2000 nT, respectively. The recovery phase lasts from mid day of 15 May to mid day of 18 May, i.e it lasts about 3 days. The variations on the AE index during this long lasting phase indicates the presence of HILDCAA.



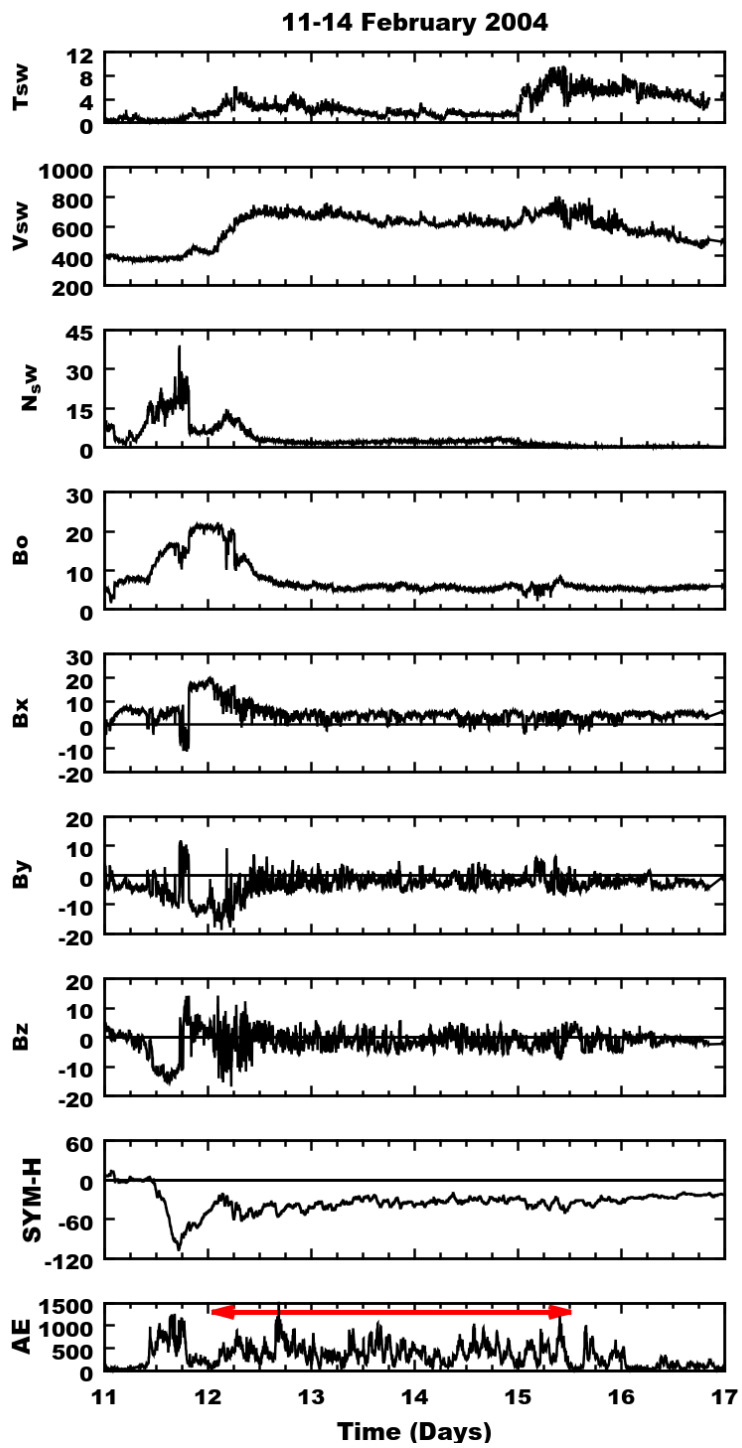
(a)

Continue...



(b)

continue...



(c)

continue...

... continuation.

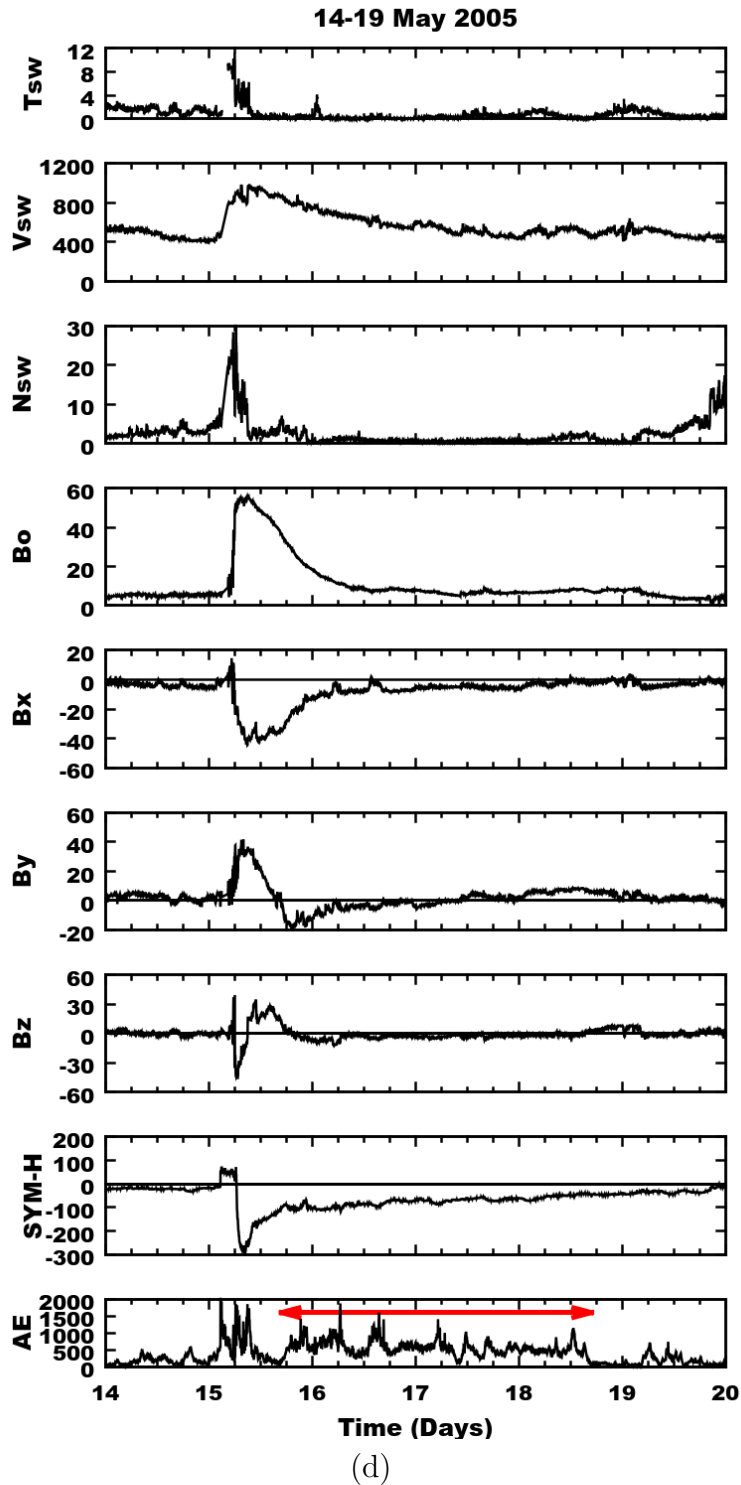


Figure 5.1 - From (a) to (d), variations of solar wind temperature (T_{sw} in 10^4 K), speed (V_{sw} in km/s), plasma density (N_{sw} in cm^{-3}), IMF magnitude (B_o in nT), B_y (nT), B_z (nT), SYM-H(nT) and AE(nT) during (a) quiet period (QUIET) from 18-21 July 2006 and HILDCAA events on (b) 20-23 April 20-23 2003 (NON), (c) 12-15 February 2004 (CIR), and (d) 15-18 May 2005 (ICME). The HILDCAA intervals are marked by red horizontal arrow in AE panel.

CWT analysis

Figure 5.2 represents the scalograms for IMF-Bz during (a) a quiet period from 18-21 July 2006 and HILDCAA events on (b) 20-23 April 2003 (c) 12-15 February 2004 and (d) 15-18 May 2005. The same data sets that we presented above are used here, but only for HILDCAA interval. The signal energy in the wavelet space represented in the scalograms are visualized using a \log_2 function that also highlights small perturbations. In these figures, the horizontal axis represents the time in days and the vertical axis represents the periodicity in minutes. The amplitudes represented in the plot, whose colors are indicated on the right side, have units in $(nT)^2$, that means, the squared value of actual data. When Analyzing the scalograms, the characteristic of Bz signal shows highly variable in time without presence of continuous periodicities. The power areas of higher intensity are seen at different time scales on different events. For example, during the quiet days, the power areas of the highest intensity are at time scale between 150-200 minutes. Similarly, during non-storm HILDCAA, the power areas of the highest intensities are seen at time scales between 50-300 minutes. During CIR-preceding HILDCAA, the power areas of similar intensities are seen at time scales between 25-300 minutes. But during ICME-preceding HILDCAA, the power areas of the highest intensities are seen at time scales between approximately 80-300 minutes. For all events, despite the presence of signals, they are not occurring in a continuous way at different times scales. However, the higher spectral intensities calculated by the CWT technique are seen at scale axis between 50–300 minutes. In case of non-storm and ICME-preceding HILDCAAs, some continuous periodicity of the higher intensities are seen at scales between 100-300 minutes. These results show that longer periodicities are most continuous on the series. As compared to HILDCAA events, quiet days show relatively very weak spectral variabilities.

Figure 5.3 represents the scalograms for AE index during (a) a quiet period from 18-21 July 2006 and HILDCAA events on (b) 20-23 April 2003, (c) 12-15 February 2004, and (d) 15-18 May 2005. The scalograms of AE follow the same numerical treatment executed. Interpretation is done in a similar way. The same scale range and time interval are used for each case, respectively. Like Bz, the characteristics of AE signals also show high variability in the signals. In time, the variables are seen without presence of completely continuous periodicities. During the geomagnetically quiet interval, the AE index does not show periodicity for the similar scale range. A range of periods between 100-300 minutes is the one with the highest spectral variability during HILDCAAs. In these regions the background of intensity around $9.5 (nT)^2$

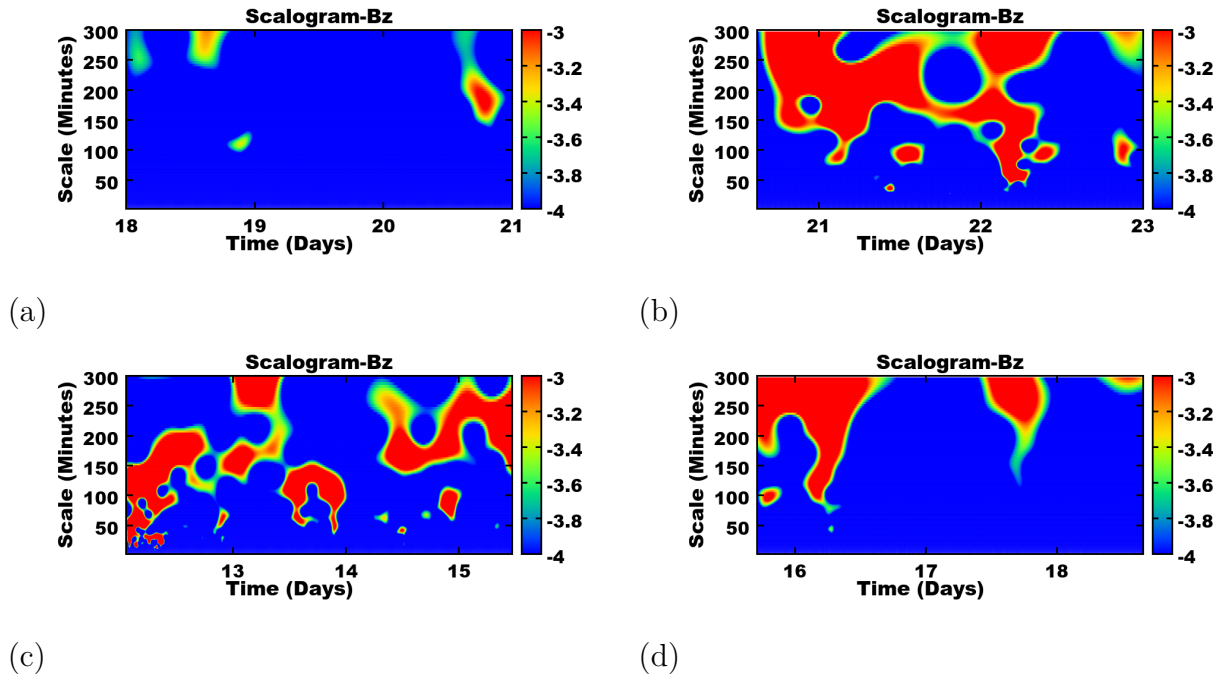


Figure 5.2 - Scalograms for IMF-Bz during (a) quiet period (QUIET) from 18-21 July 2006 and HILDCAA events on (b) 20-23 April 2003 (NON), (c) 12-15 February 2004 (CIR), and (d) 15-18 May 2005 (ICME). For a better highlight, the representation of energy in this scalogram is showed after an application of a \log_2 function.

are registered and increases up to about 10 (nT)^2 . Mainly longer scales between 200-300 minutes show more continuous cwt power answer throughout the time interval. To complete the pattern identification, Figure 5.4 presents details of the scalograms for AE index during quiet period from 18-21 July 2006 (calm interval). The range for intensity in the plot is modified to highlight any existence of very weak variations. Although they exist, compared to intensities during HILDCAAs, the intensities of its fluctuations are negligible for our purposes of studies.

When observing the results, we can notice that some characteristics of the solar wind are visible on scalograms. The first analysis is to compare amplitude amplification caused by interplanetary parameters and the other one is to check abrupt changes in the magnetic field. These variations appear on the scalograms through the scattering of frequencies, ie, even short and medium periods have their high amplitudes. Another very important analysis is to observe the distribution of amplitudes in longer scales. Abrupt changes in the magnetic field are characterized. These characteristics appear on the scalograms presenting a scattering of frequencies. It indicates that higher amplitudes are present even for short and medium time scales. In the

AE index, the values higher than 50 nT over longer periods were almost constant. However, B_z can have positive or negative values. The presence of fluctuations in B_z in longer periods creates remanent effects of the south-oriented component of IMF. These longer term trends have significant effects on the shape and intensity of HILDCAAs. That means coupling processes linked to the magnetic reconnection with transference of particles and energy into the Earth's magnetosphere. Scalograms identify the scales of interaction and their duration.

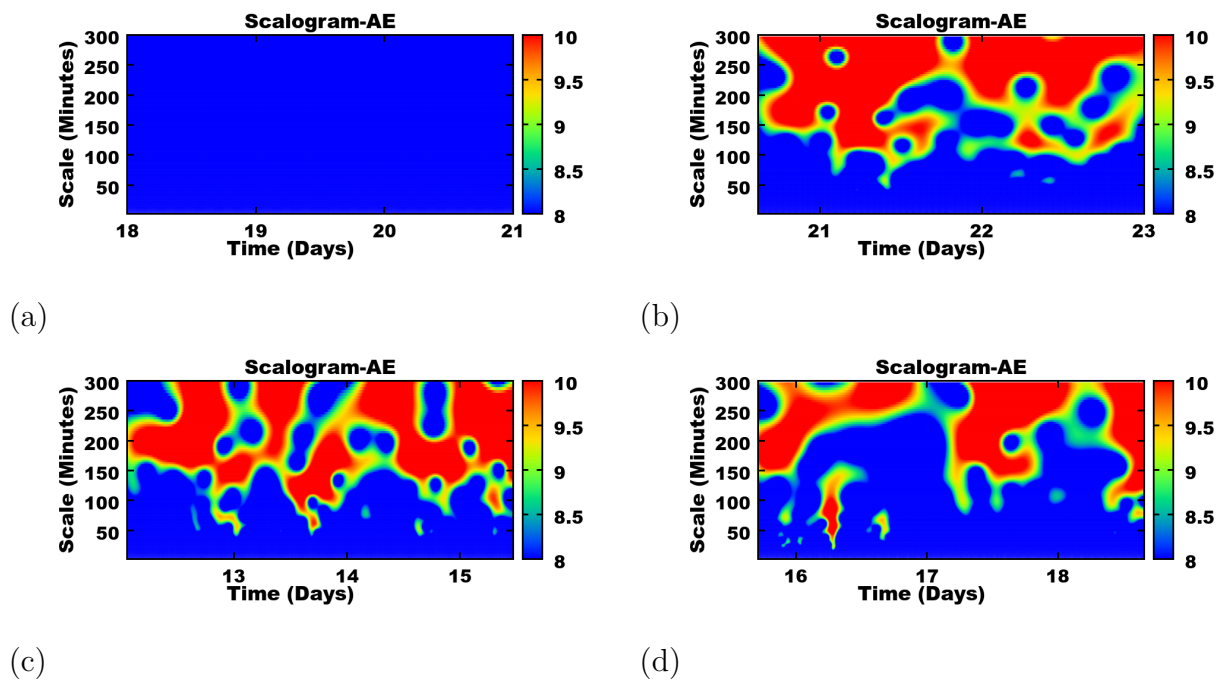


Figure 5.3 - Scalograms for AE index during (a) quiet period (QUIET) from 18-21 July 2006 and HILDCAA events on (b) 20-23 April 2003 (NON), (c) 12-15 February 2004 (CIR), and (d) 15-18 May 2005 (ICME).

Figure 5.5 represents the global wavelet spectrum for (a) IMF- B_z and (b) AE index during quiet and HILDCAAs periods. The red line represents the quiet time, the yellow line represents non-storm HILDCAA, the green line represents HILDCAA preceded by CIR-storm and the blue line represents HILDCAA preceded by ICME-storm periods. The global wavelet spectrum is the variance averaged at each scale over the whole time series. It is obtained by the time integration in the scalogram. It helps to compare the spectral power at different time scales. In both panels, higher energies are located in long periods. But from the comparison of the top panel and bottom panel, someone can notice the filtering action of the magnetosphere-

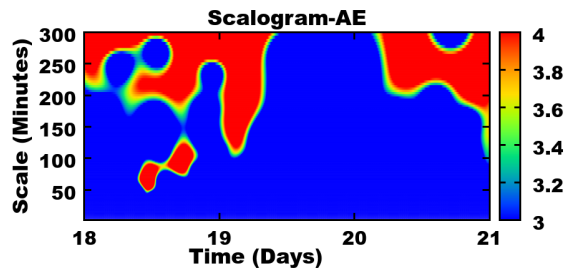
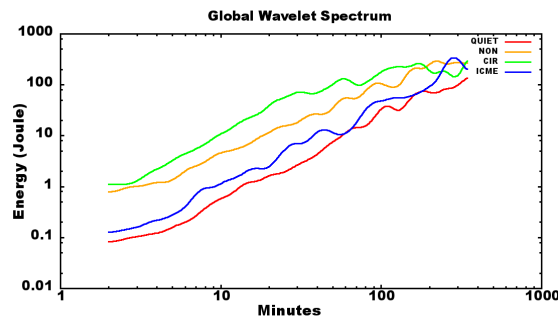
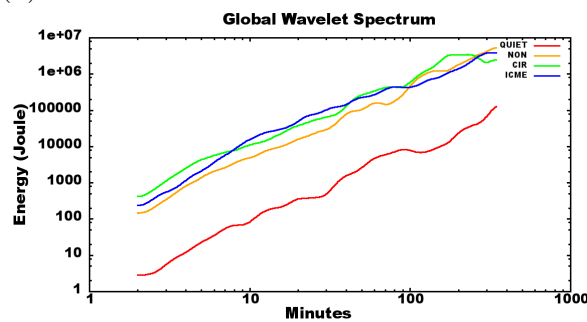


Figure 5.4 - Details of the scalograms for AE index during quiet (QUIET) period from 18-21 July 2006. The range is modified to highlight very weak variations.

ionosphere system during quiet conditions. In this figure, both panels show less energy during quiet days compared to the answers of the other events.



(a)



(b)

Figure 5.5 - Global wavelet spectrum for (a) IMF-Bz and (b) AE index during quiet and HILDCAAs periods. Where the red line represents quiet, the orange line represents non-storm HILDCAA, the green line represents HILDCAA preceded by CIR-storm and the blue line represents HILDCAA preceded by ICME-storm.

DWT analysis

Figure 5.6 shows the results of a discrete wavelet transform applied to IMF-Bz in order to be discussed. In this figure, the red color represents the HILDCAA preceding time. The higher amplitudes of the square wavelet coefficients indicate the singularities or discontinuities in records associated with geomagnetic storm or HILDCAA. Smaller and larger amplitude of square wavelet coefficients indicated calm and disturbed conditions of magnetosphere respectively. The main objective of this technique is to identify the sudden variations that occur on IMF-Bz at the time of HILDCAA. Figure 5.6(a) represents the results of discrete wavelet transform for IMF-Bz during quiet periods from 18 to 21 July 2006. During these quiet days, IMF-Bz shows small scale of fluctuations between -3 to 3 nT. When it changed direction, at that time, the square wavelet coefficients observe relatively higher than its background smooth levels. Figure 5.6(b) is similar to (a) but refers to non-storm HILDCAA occurred on 20-23 April 2003. During this event, the time series of IMF-Bz also shows fluctuations between -5 to 5 nT which is due to the presence of Alfvén waves (GUARNIERI et al., 2006). Due to this reason, it shows both singularities and larger amplitude of square wavelet coefficients. Figure 5.6(b) is similar to (a) but refers to the HILDCAA preceded by a CIR-storm which occurred on 12-15 February 2004. Also in this case, the singularities pattern and significant amplitude of square wavelet coefficients can be observed. Finally, Figure 5.6(b) is similar to (a) but refers to the HILDCAA preceded by ICME-storm which occurred on 15-18 May 2005. This event shows relatively small amplitude of square wavelet coefficients as compared to other two events. The interplanetary cause for this storm was the shock driven by an ICME which contained a magnetic cloud structure (HAJRA et al., 2013; OJEDA et al., 2013; OJEDA et al., 2014). The recovery phase begins about 3 days without variations in IMF-Bz. During this event, it was continuously negative but steady. Due to this reason, this event shows relatively smaller amplitude of square wavelet coefficients. However, the amount of energy injection was continuous and higher when compared to other events. The amount of energy injection during quiet and HILDCAAs periods can be seen in next section. A more detailed description about the Daubechies order 2 orthogonal wavelet transform can be found in Mendes et al. (2005), Ojeda et al. (2014), Klausner et al. (2014b).

Figure 5.7(a) represents the results of discrete wavelet transform for geomagnetic index AE during quiet periods from 18 to 21 July 2006. For these days, it shows larger coefficients for larger values on the time series. Figure 5.7(b), (c) and (d) represents the results of discrete wavelet transform for AE during HILDCAAs which occurred

on 20-23 April 2003, 12-15 February 2004 and 15-18 May 2005 respectively. Out of three events, Figure 5.7(b) and (c) were associated with interplanetary HSSs and the remaining one (d) occurred after the passage of ICMEs. The events associated with HSSs were typically associated with large-amplitude IMF-Bz fluctuations whereas the ICME-related event was characterized by small steady southward Bz intervals or low-frequency variations.

Similarly, Figure 5.8 represents wavelet modulus cross correlation of IMF-Bz with AE index during (a) quiet period from 18-21 July 2006 and HILDCAA events on (b) 20-23 April 2003 (c) 12-15 February 2004 and (d) 15-18 May 2005. In the figure, the horizontal axis represents the scale in minutes and the vertical axis represents the modulus correlation. The scale of 1, 10, 100 and 1000 are labeled in the horizontal axis. During the quiet period (a), they show peak modulus correlation about 0.4 at the scale of approximately 200 minutes. Similarly, during the HILDCAA events for the corresponding indication (b), (c) and (d), they show modulus correlation 0.8 about 200 minutes. When observing these results, we can state that during HILDCAAs, IMF-Bz is highly correlated with AE index. These results also show scale dependent characteristics.

Akasofu Parameters

In this section, we observe the variation in the Akasofu parameter and its corrections during quiet and HILDCAAs periods. The calculation of the Akasofu parameter was made as suggested by Perreault and Akasofu (1978) and can be seen in Equation 2.5. The Akasofu parameters given in Equation 2.5 are supposed to be an approximation for the total power input into the magnetosphere. So it was corrected many times. In this work, we will observe the corrected Akasofu parameter as suggested by MonrealMacMahon and Gonzalez (1997) and Vasyliunas et al. (1982) and can be seen in Equation 2.7 and Equation 2.8.

Figure 5.10(a) represents the variations in solar wind pressure (P_{sw} in nPa), IEF (Ey in mV/m), the Akasofu parameter (ϵ in 10^{11} watts), the first correction (ϵ^* in 10^{11} watts) and second correction (ϵ^{**} in 10^{11} watts) during quiet periods from 18 to 21 July 2006. The calculation of ϵ , ϵ^* , and ϵ^{**} only for HILDCAA interval are shown in Equations 2.5, 2.7 and 2.8 respectively. The quiet time averages for these quantities are given in the first row of Table 5.1. Figure 5.10 (b) similar to (a) but refers to non-storm HILDCAA which occurred on 20-23 April 2003. The HILDCAA time average values of ϵ , ϵ^* and ϵ^{**} are given in the second row of Table 5.1. When observing these results, one can notice that the average values for ϵ^* and ϵ^{**} are

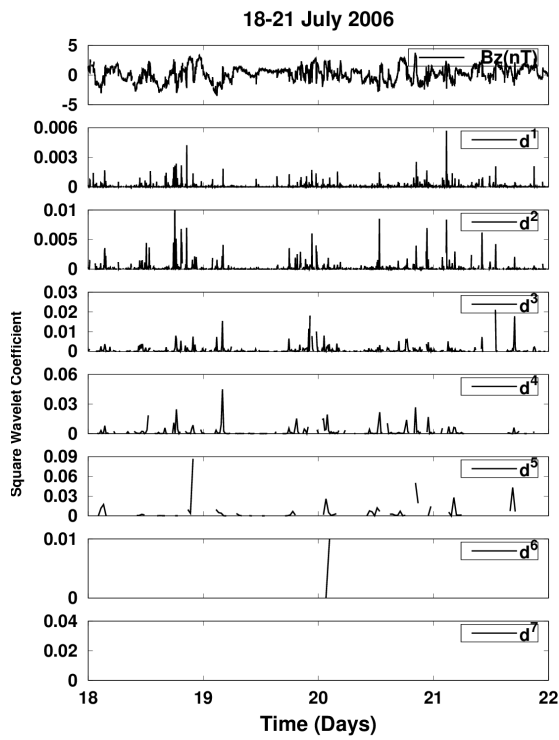
greater than ϵ . However ϵ^{**} is slightly lower than ϵ^* . This shows that the effective area is higher than that which was first considered by Perreault and Akasofu (1978). A more detailed description about the variation in the Akasofu parameter and its correction can be found in (de Lucas et al., 2007). Figure 5.10 (c) is similar to (a) but refers to the HILDCAA preceded by CIR-storm which occurred on 12-15 February 2004. The third row of Table 5.1 shows the average values of ϵ , ϵ^* and ϵ^{**} only for the HILDCAA interval. As compared to previous events, the calculated average values of ϵ , ϵ^* and ϵ^{**} are slightly higher for this event. This event also shows that the effective area is higher than that was first considered by Perreault and Akasofu (1978). Figure 5.10(d) is similar to (a) but refers to the HILDCAA preceded by ICME-storm which occurred on 15-18 May 2005. During the main phase, P_{sw} shows the peak value about 60 nPa. But at the time of HILDCAA, it highly fluctuated between 0 to 8 nPa. Similarly, E_y shows the peak value about 45 mV/m but at the time of HILDCAA, it highly fluctuated between -7 to 7 mV/m. The HILDCAA time average values of ϵ , ϵ^* and ϵ^{**} are given in fourth row of Table 5.1. As compared to other two events, the calculated average values of ϵ , ϵ^* and ϵ^{**} are higher for this event. However, as in the other two events, it also shows higher average value for ϵ^* .

Table 5.1 - Average values of ϵ , ϵ^* and ϵ^{**} during HILDCAAs and quiet periods

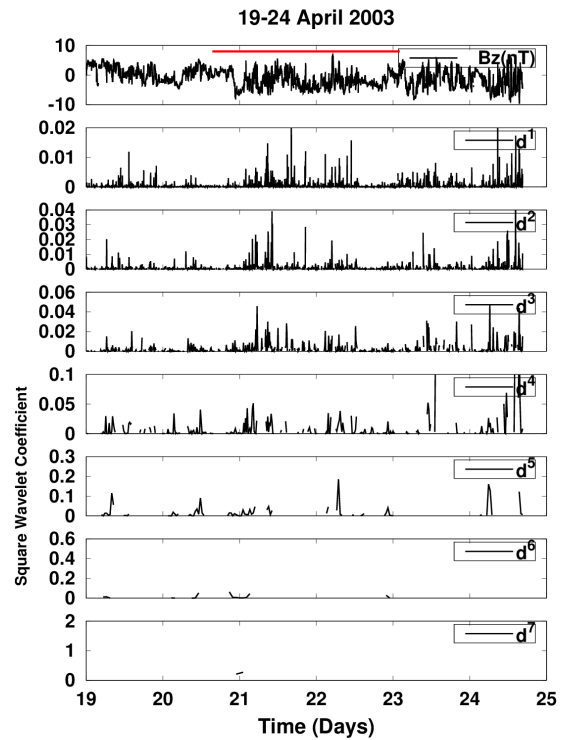
Events	$\epsilon(10^{11})W$	$\epsilon^*(10^{11})W$	$\epsilon^{**}(10^{11})W$
2006-07-18:21h-UT (QUIET)	0.16	0.57	0.42
2003-04-20:23h-UT (NON)	2.61	8.36	7.07
2004-02-12:15h-UT (CIR)	3.24	9.94	9.13
2005-05-15:18h-UT (ICME)	7.89	36.21	18.47

Figure 5.11(a) gives the cross-correlation results of ϵ , ϵ^* and ϵ^{**} with SYM-H index during the quiet period from 18-21 July 2006. In these quiet days, ϵ^* and ϵ^{**} show positive correlation with SYM-H with time lag of many hours. It indicates that there is energy injection inside the low latitudes. In this case, the ionosphere may be the source for energy transfer inside the magnetosphere (VORONKOV; KUZNETSOV, 1989; GONCHAROVA, 2004). The possible ionospheric sources may be the solar illumination and atmospheric heating effects at ionosphere (LYATSKY; MALTSEV, 1975; VORONKOV; KUZNETSOV, 1989; GONCHAROVA, 2004; KLAUSNER et al., 2013). Figure 5.11(b) is similar to (a) but refers to non-storm HILDCAA which occurred on 20-23 April 2003. This figure shows very good negative correlations of ϵ , ϵ^* and

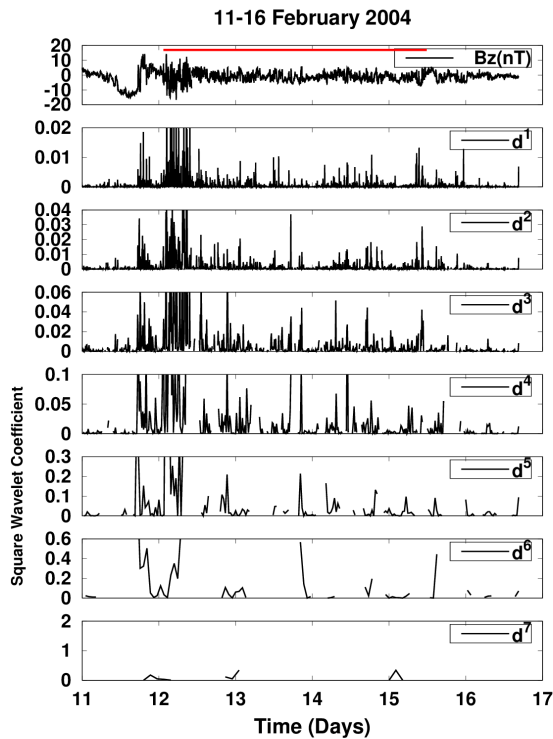
ϵ^{**} with SYM-H index. Similarly, Figure 5.11(c) is similar to (a) but refers to the HILDCAA preceded by CIR-storm which occurred on 12-15 February 2004. In this figure, the SYM-H index shows peak values of -0.6, -0.7 and -0.5 with ϵ , ϵ^* and ϵ^{**} respectively. Finally, Figure 5.11(d) is similar to (a) but refers to the HILDCAA preceded by ICME-storm which occurred on 15-18 May 2005. In this figure, the SYM-H index shows peak values of -0.7, -0.75 and -0.6 with ϵ , ϵ^* and ϵ^{**} respectively. Like other two events, it also shows negative correlation of ϵ , ϵ^* and ϵ^{**} with the SYM-H index. When observing these, results it is noticed that ϵ , ϵ^* and ϵ^{**} are negatively correlated with SYM-H index during the events. These results also suggest that the effects of HILDCAAs, displayed on the value of the SYM-H index, depends on the amount of the energy injected into the ring current.



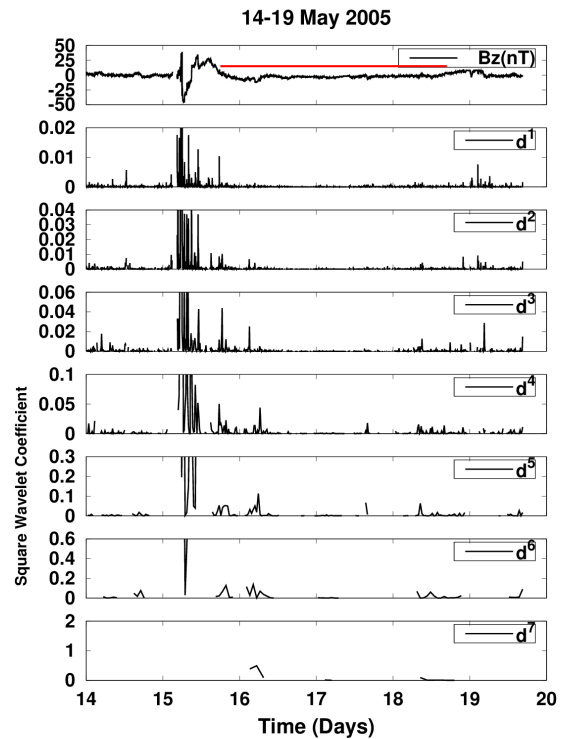
(a)



(b)

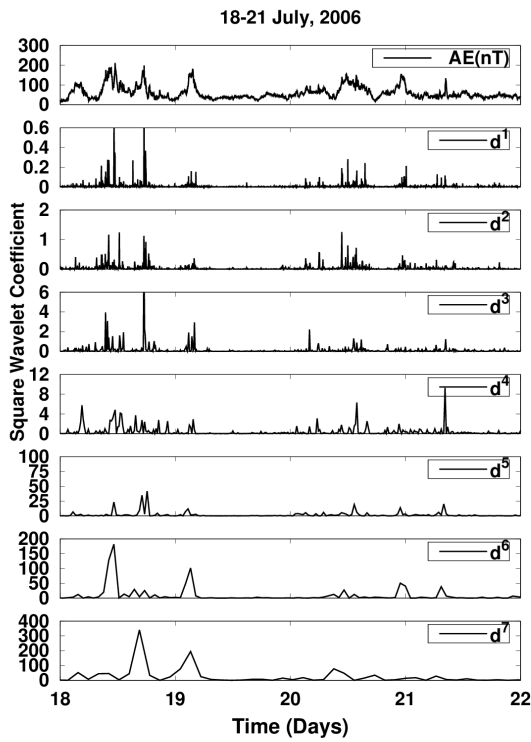


(c)

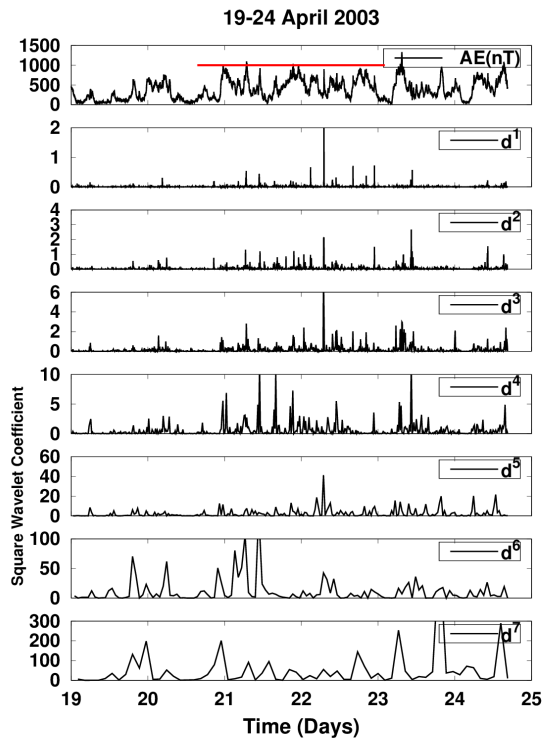


(d)

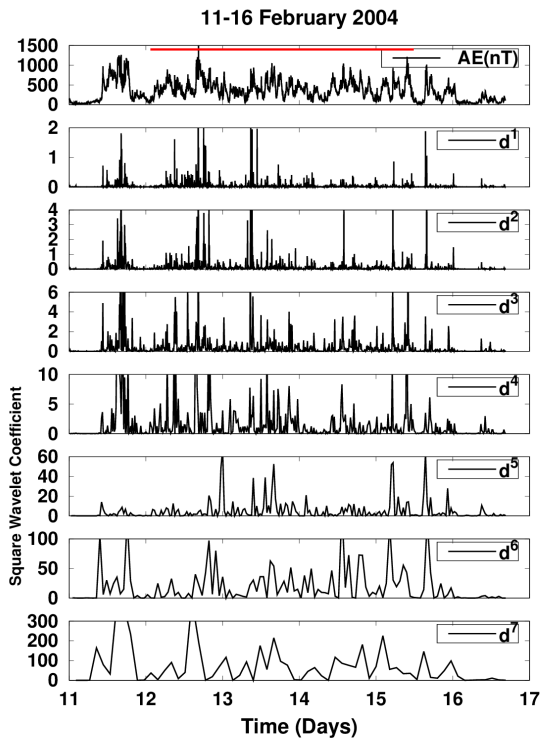
Figure 5.6 - The squared Daubechies Wavelet coefficients $(d^j)^2$ (for $j= 1,2,3,\dots,7$) for IMF-Bz during during (a) quiet period (QUIET) from 18-21 July 2006 and HILDCAA events on (b) 20-23 April 2003 (NON), (c) 12-15 February 2004 (CIR), and (d) 15-18 May 2005 (ICME). The red color identifies where the HILDCAA event is happening.



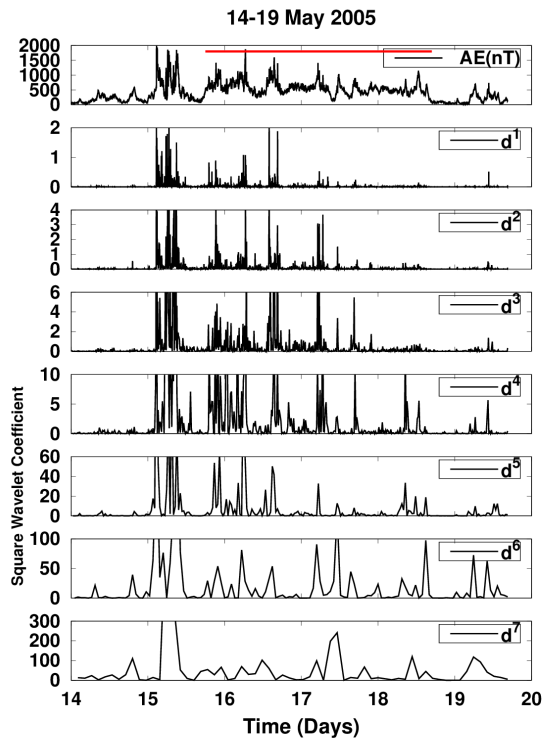
(a)



(b)



(c)



(d)

Figure 5.7 - Daubechies Wavelet coefficients d^j (for $j= 1,2,3,\dots,7$) for geomagnetic index AE during during (a) quiet period (QUIET) from 18-21 July 2006 and HILDCAA events on (b) 20-23 April 2003 (NON), (c) 12-15 February 2004 (CIR), and (d) 15-18 May 2005 (ICME). The red color identifies where the HILDCAA event is happening.

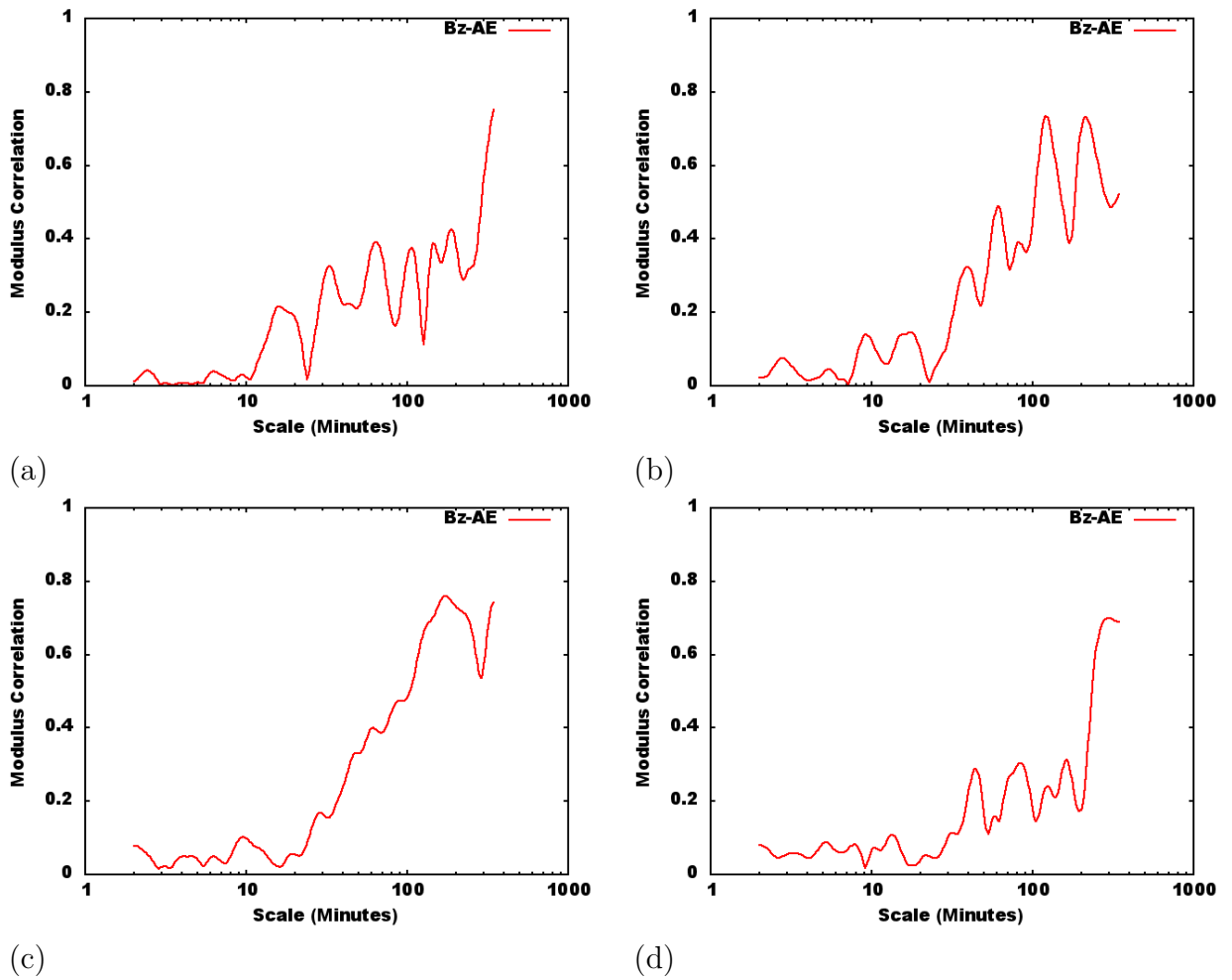


Figure 5.8 - Wavelet modulus cross correlation of IMF-Bz with AE index during (a) quiet period (QUIET) from 18-21 July 2006 and HILDCAA events on (b) 20-23 April 2003 (NON), (c) 12-15 February 2004 (CIR), and (d) 15-18 May 2005 (ICME).

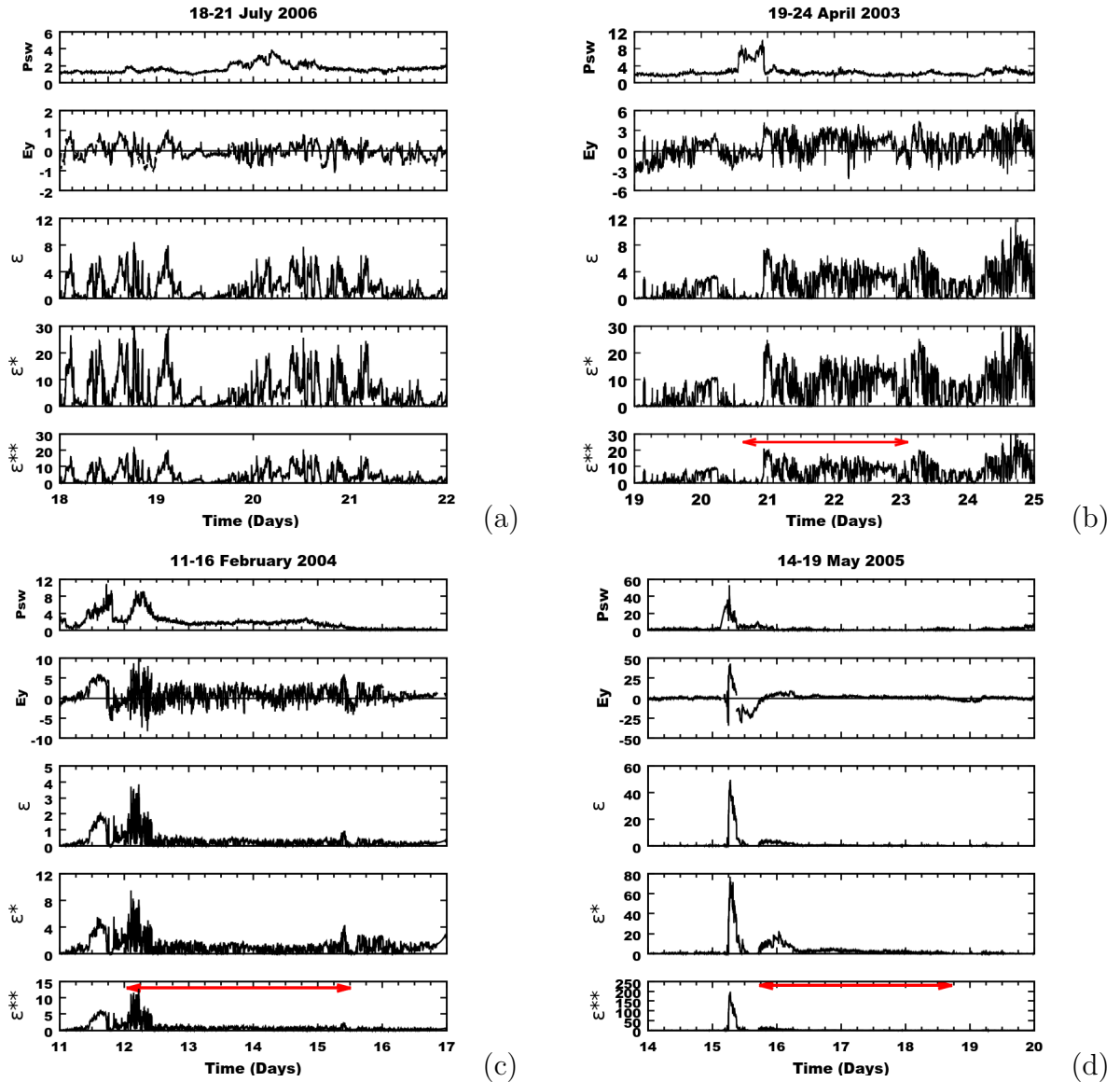


Figure 5.9 - From top to bottom, the panels represent variations in solar wind pressure (P_{sw} in nPa), IEF (E_y in mV/m), Akasofu parameter (ϵ in 10^{11} watts), first correction (ϵ^* in 10^{11} watts) and the second correction (ϵ^{**} in 10^{11} watts) during (a) quiet period (QUIET) from 18-21 July 2006 and HILDCAA events on (b) 20-23 April 2003 (NON), (c) 12-15 February 2004 (CIR), and (d) 15-18 May 2005 (ICME). The HILDCAA interval is marked by red horizontal arrow in ϵ^{**} panel.

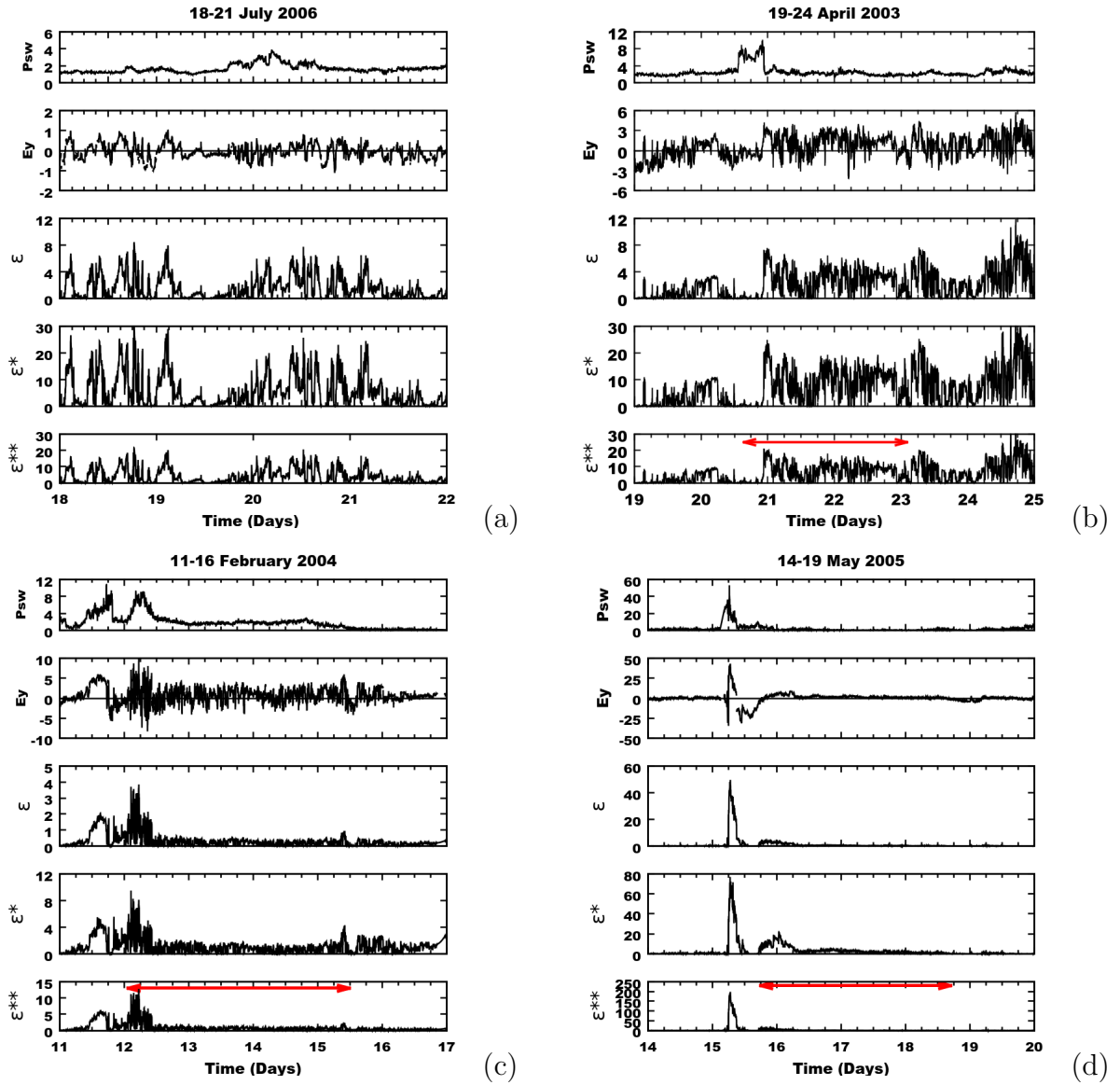


Figure 5.10 - From top to bottom, the panels represent variations in solar wind pressure (P_{sw} in nPa), IEF(E_y in mV/m), Akasofu parameter (ϵ in 10^{11} watts), first correction (ϵ^* in 10^{11} watts) and second correction (ϵ^{**} in 10^{11} watts) during (a) quiet period (QUIET) from 18-21 July 2006 and HILDCAA events on (b) 20-23 April 2003 (NON), (c) 12-15 February 2004 (CIR), and (d) 15-18 May 2005 (ICME). The HILDCAA interval is marked by red horizontal arrow in ϵ^{**} panel.

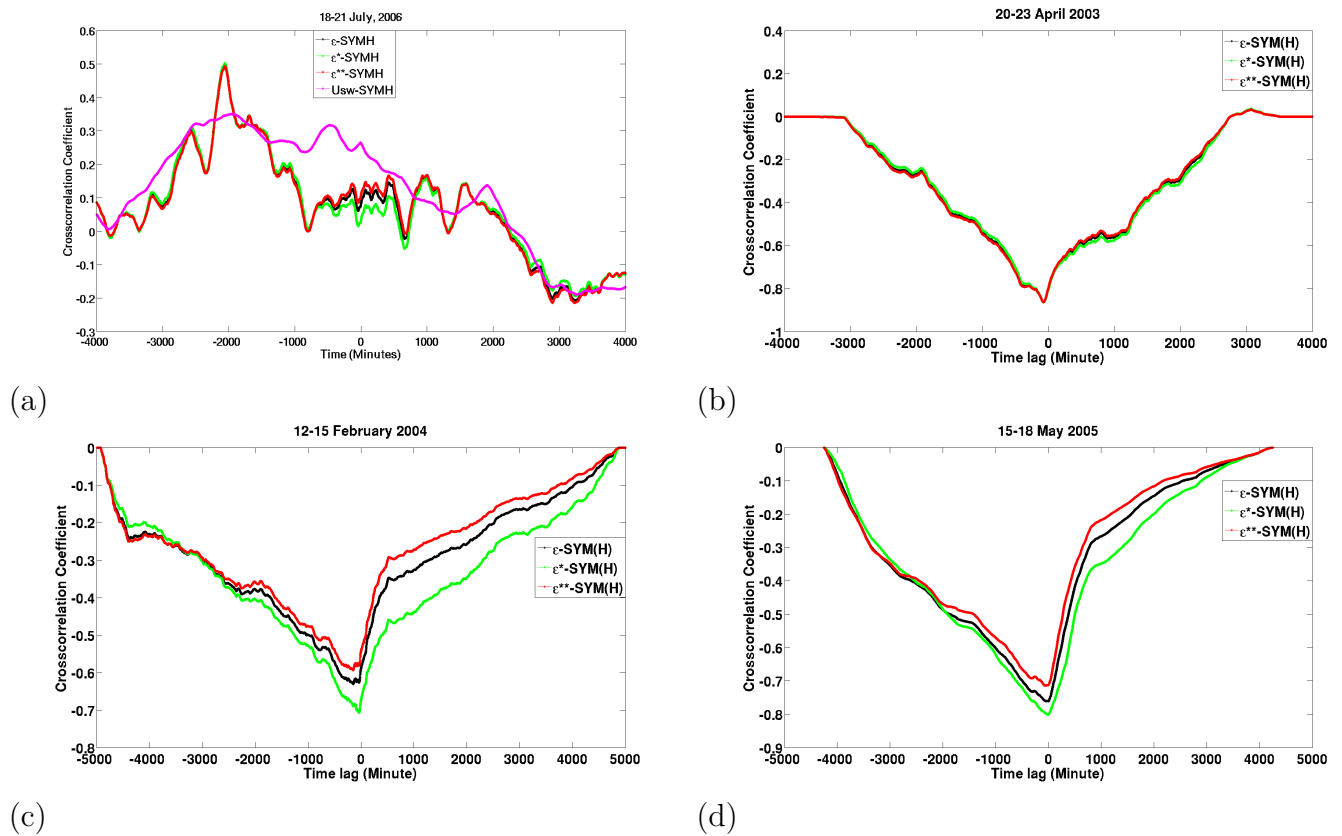


Figure 5.11 - Cross-correlation of Akasofu parameter (ϵ), first correction (ϵ^*) and second correction (ϵ^{**}) with SYM-H index during (a) quiet period from 18-21 July 2006 and HILDCAA events on (b) 20-23 April 2003 (c) 12-15 February 2004 and (d) 15-18 May 2005.

Partial conclusions

In this section, we have presented the characteristics of HILDCAAs using geomagnetic and solar wind/interplanetary datasets. Out of three events, two were associated with interplanetary HSSs. The remaining one occurred after the passage of an ICME. The HILDCAA events related to HSSs were typically associated with large-amplitude IMF-Bz variances. On the other hand, the ICME-related HILDCAA was characterized by small, steady southward Bz interval or low-frequency fluctuations. From these three case studies, we are able to identify a possible different interplanetary mechanism for the geomagnetic activity/HILDCAAs.

The HILDCAA signatures are clearly present in the AE index for the selected events. Except for one case, whose situation is for background control.

As a result from the CWT analysis of Bz-components, the presence of signal structures were identified along the time interval, varying from 50 to 300 min. By the same procedure, the control case does not present significant answer from the analysis. Some peculiarities appear among the events due to the different conditions of the interplanetary environment.

From the CWT analysis of AE index for each event, a correspondence was identified among the behavior of the interplanetary parameter, as connected to causes, and a geomagnetic answer on ground. The signal structure extends between 50 to 300 min along the time interval. Except for the result (no signal) of the geomagnetically quiet interval, that is in agreement with the consistency of physical analysis.

In this analysis, the higher amplitudes of square wavelet coefficients of the seven decomposition levels were able to identify the common singularities presence on Bz and AE datasets during HILDCAAs. On the other hand, the larger amplitudes indicate that there are impulsive energy injections superposed to the smooth background process. While smaller amplitudes observed in the wavelet coefficients mean that the energy transfer process was smooth. The north or south turning of IMF-Bz plays a significant role for the intensity of HILDCAAs. We also use the results of wavelet modulus cross correlation and obtain very good correlation of IMF-Bz with AE index during the events.

We also observed the solar wind ram pressure, interplanetary electric field, the ϵ parameter and its corrections (ϵ^* and ϵ^{**}) during the events. The results show that the HILDCAA time averages of ϵ , ϵ^* and ϵ^{**} are higher for ICME preceding HILD-

CAA than other two. In the results, the HILDCAAs time average values of ϵ^* shows slightly higher than ϵ and ϵ^{**} . This indicates that the effective area is higher than that which was first considered by [Perreault and Akasofu \(1978\)](#). We also perform cross correlation of ϵ , ϵ^* and ϵ^{**} with SYM-H index. In this analysis, all the parameters show very good negative correlation with SYM-H index. This shows that the effects of HILDCAAs, which are displayed on the value of the SYM-H index, depend on the amount of the energy injection into the ring current.

5.2 Magnetic effects during HILDCAAs recorded from low latitudes geomagnetic observatories

In this section, we show a case study of perturbation on the geomagnetic field recorded at low latitude observatories during three different HILDCAA events and a quiet period. Among them, two events were caused by CIRs and one was caused by ICMEs associated with magnetic clouds. The coordinates, names and IAGA codes of the observatories are shown in Table 3.1. The case studies are discussed separately for all events as follows:

Case 1: Non-storm HILDCAA which occurred on 20-23 April 2003

The geomagnetic signatures and indices are reproduced in Figure 5.12 for the HILDCAA event that occurred on 20-23 April 2003. In the figure, the green line represents the average quietest day signatures, the black line represents the disturbed days signatures and the red horizontal arrow in the AE panel represents the HILDCAA interval. Starting from the top, the first panel stands for TAM, the second panel for CTA, the third panel for HON, the fourth panel for VSS and the other three remaining panels represent the geomagnetic indices SYM-H, ASY-H and AE respectively. All these observatories belong to low latitudes in which CTA and VSS located in the southern hemisphere and TAM and HON located in the northern hemisphere. They have been included to check the HILDCAA time behavior at low latitudes. In this figure, both the quietest and the disturbed days values are plotted against universal time. When observing the conversion between UT to LT, the quietest day variations show maximum at mid day and minimum at dusk time for all observatories (GONCHAROVA, 2004; RASTOGI, 2005; BOLAJI et al., 2013). The first observation to identify the characteristics of geomagnetic storm at low latitude was done by Moos (1910) (RASTOGI, 1999). In this observation, he noticed that there was an additional disturbance daily variation (SD) imposed on the normal daily variation (Sq) during disturbed days. Later, Egedal (1947) noticed that the range of disturbance daily variation of the horizontal geomagnetic field H, showed a maximum within $\pm 3^\circ$ latitudes around the magnetic equator. Chapman (1951) also studied the contribution of disturbance daily variation (SD) on the normal daily variation and found that the effect was due to an eastward-flowing current in E region of the ionosphere, which he named as Equatorial Electrojet. In this work, we are not making any equatorial observations, so our main objective is to observe the HILDCAA time signatures recorded at low latitudes.

During geomagnetic disturbances, a large number of charged particles and energy

are injected into the magnetosphere and ionosphere (KAMIDE et al., 1998) and the current systems existing inside the magnetosphere and ionosphere will be widened and intensified (JANKOVICOVA et al., 2002). As a result, middle and low latitudes will be dominated by ring current and this effect is well-represented by the equatorial Dst index as suggested by (SUGIURA, 1964). The HILDCAA event occurred from mid day of 20 April, 2003 to the beginning of 23 April, 2003. Before the event, both the quietest day and the disturbed day graphs show identical signatures for all observatories. But at the time of HILDCAA, all the observatories show significant separation from their quietest days curves. The nature of fluctuations for each observatory is different. As compared to the northern hemisphere observatories (TAM and HON), southern hemisphere observatories (CTA and VSS) show more depressed fluctuations on H-component. This shows that in the southern hemisphere the geomagnetic field variations are larger when compared to the northern hemisphere (DEVI et al., 2008). More detail about the geomagnetic storm effects at low latitudes can be found in Rastogi (1999). The physical mechanism for these phenomena may be related to intermittent magnetic reconnection between IMF-Bz with the earth magnetic field (GONZALEZ et al., 1994). The SYM-H index at the fifth panel of this figure shows a very weak depression between -20 nT to -30 nT. Other two indices ASY-H and AE show intense activity from mid day of 20 to the beginning of 23.

Figure 5.13 gives the ΔH signatures for the corresponding observatories during the same event. The first four panels of this figure show the ΔH signatures for TAM, CTA, HON and VSS. Other three panels are similar, as Figure 5.12. In this figure, the horizontal straight line shows the base line. Before HILDCAA, the ΔH signatures were approximately zero for all observatories except VSS but during HILDCAA, TAM shows fluctuations between -30 nT to 0 , both CTA and VSS show fluctuations approximately between -75 nT to 0 and HON shows fluctuations between -50 nT to 0 . Although occurring in all observatories, the simultaneous disturbances present fluctuations with specific features and intensities for each magnetometers. Those aspects are related to several reasons, for example: global position, type of magnetometers, ionospheric conditions, ground conductivity and local time. The wavelet techniques (CWT, DWT and wavelet modulus correlation) used below will help to reveal some common features of these signatures.

Figure 5.14 represents the data series of the ΔH -component and the results of the wavelet analysis (scalograms) for TAM, CTA, HON and VSS. In this figure, the horizontal axis represents the time in days and the vertical axis represents the scale in minutes. The scale of color indicates the amplitude of each scale (or frequency).

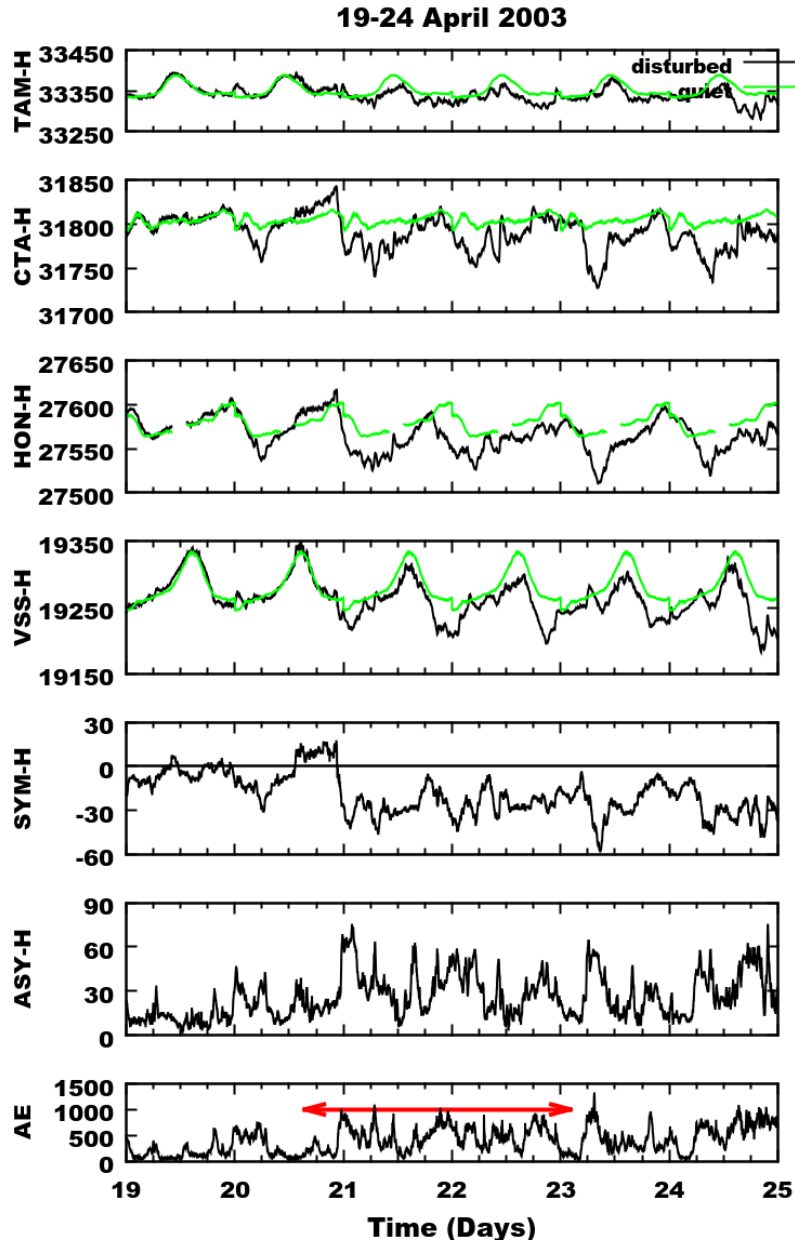


Figure 5.12 - From top to bottom, the panels show variations of H-component (nT) at the observatories TAM, CTA, HON, VSS along with the geomagnetic indices SYM-H (nT), ASY-H (nT) and AE (nT) respectively during the HILDCAA event on 20-23 April 2003. The green line represents the average quietest day variation, the black line represents the disturbed day variation and the red horizontal arrow in AE panel indicates the HILDCAA interval.

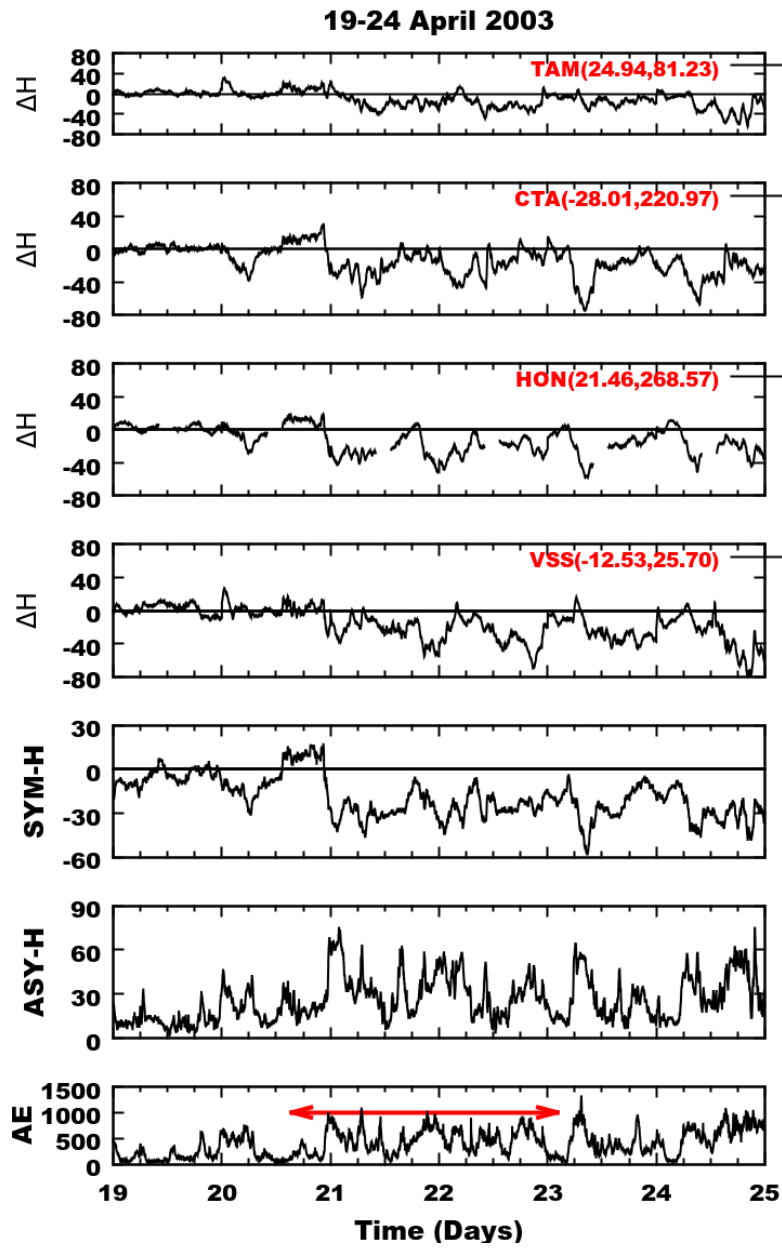


Figure 5.13 - From top to bottom, the panels represent the variation of ΔH signatures from TAM, CTA, HON, VSS and geomagnetic indices SYM-H (nT), ASY-H (nT) and AE (nT) during HILDCAA event during 20-23 April 2003. The red horizontal arrow in AE panel represents the HILDCAA interval.

The amplitude whose color is indicated on the right color bar has unit in nT^2 , i.e the square of same unit of real data.

Figure 5.14(a) represents the scalogram for TAM. In this observatory, stronger wavelet power areas of intensities between 1.2-1.4 nT are seen more continuous at time scales between 100-300 minutes. Other wavelet power areas of intensities between 0.6-0.8 nT are seen at different times and scales. Figure 5.14(b) represents the scalogram for CTA. As like TAM, the wavelet powers areas of intensities between 1.2-1.4 nT are seen at time scales between 100-300 minutes. The less intense power areas are seen at different times and scales. Figure 5.14(c) and (d) represent the scalograms for HON and VSS for the same event respectively. These two observatories also show similar phenomena as the other two observatories. All these results suggest that the power areas of higher intensities are seen at medium to higher time scales. This analysis is restricted to the period range 0 to 300 minutes. It is noticed that for all observatories except HON, the wavelet powers corresponding to the period between 100-300 minutes are highly evolving during the event. The main periodicities present are approximately near 150-300 minutes. Compared to TAM and HON, other two observatories (CTA and VSS) show wavelet power of higher intensity more continuous at time scale between 150-300 minutes. This shows that during HILDCAA, the effects were more in the southern hemisphere when compared to the northern hemisphere (DEVI et al., 2008). However, some similar characteristics effects of HILDCAA are visible on the results of the wavelet analysis of ΔH -component from TAM, CTA, HON and VSS. The first characteristic is the presence of wavelet power areas of higher amplitude at higher time scale which may be related to discontinuities present in datasets. The other characteristic is the distribution of lower and higher frequencies on both medium and higher time scales. Both characteristics observed on the results of the wavelet analysis may be related to the shape of highly fluctuated datasets.

In this section, we explain the results obtained from discrete wavelet transform. Here, we used Daubechies order 2 orthogonal wavelet transform of levels 7 ($j=1, 2, 3, 4, 5, 6, 7$). For the chosen wavelet of frequency 0.66667 and sampling rate of one minute, the pseudo periods of the seven levels were 3, 6, 12, 24, 48, 96, 192 minutes. Figures 5.15 and 5.16 show the behavior of the squared wavelet coefficients for the HILDCAA event that occurred on 20-23 April 2003 at levels $j= 1, 2, 3, 4, 5, 6, 7$ denoted by $d^1, d^2, d^3, d^4, d^5, d^6$ and d^7 . In each panel, from top to bottom, the ΔH -component of geomagnetic field and the first seven levels of the wavelet coefficients of the discrete wavelet transform are shown. The left side of Figure 5.15 stands for

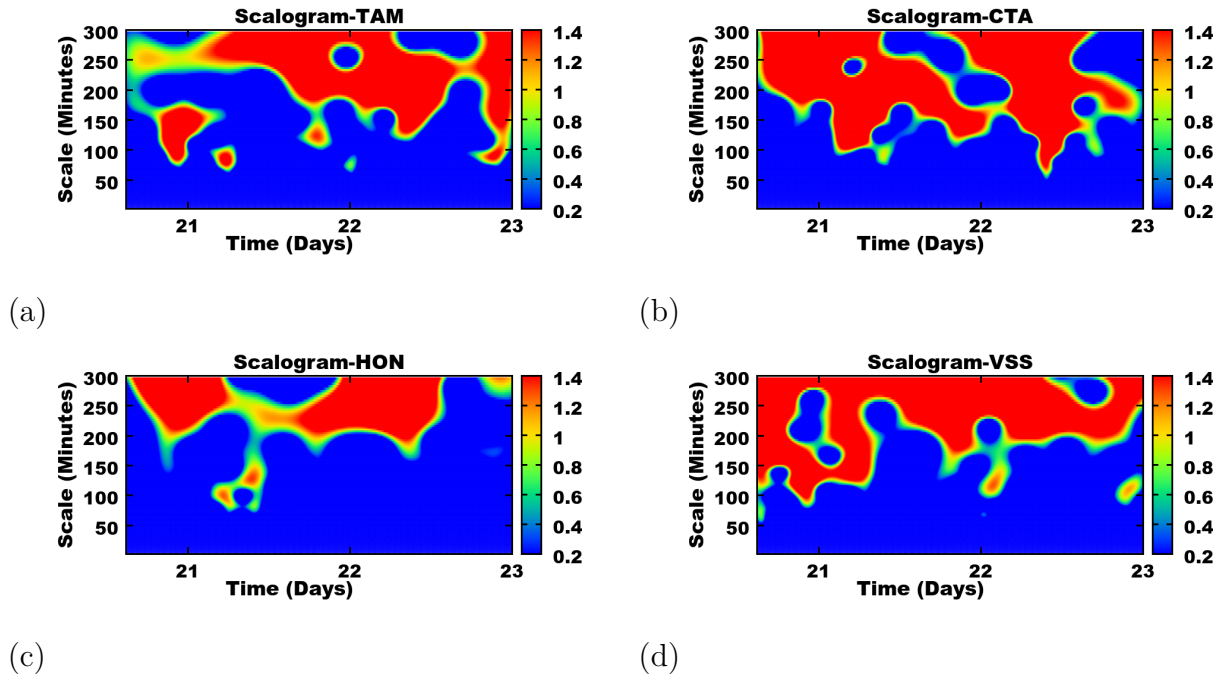


Figure 5.14 - Scalograms for ΔH -component from (a) TAM (b) CTA (c) HON and (d) VSS during HILDCAA event on April 20-23, 2003.

the observatory TAM and the right side of this figure stands for the observatory CTA. Similarly, the left side of Figure 5.16 stands for the observatory HON and the right side of this figure stands for the observatory VSS. In each figure, the highest amplitude of the squared wavelet coefficients indicates singularities associated with HILDCAA. On the other-hand, the smaller amplitude of the squared wavelet coefficients observed during the HILDCAA interval indicates the processes of smooth energy transfer while the larger amplitudes indicate the impulsive energy injections inside the magnetosphere. The red marked color in each first panel of each figure represents the HILDCAA preceding time. In the figures, the smooth squared wavelet coefficients represent the quiet conditions (magnetically quiescent periods) and the significant squared wavelet coefficients indicate the disturbed conditions (magnetically disturbed periods) of the magnetosphere. The main objective of this analysis is to understand geomagnetic activity related to HILDCAAs and distinguish quiescent from non-quiescent periods. In this analysis, the local regularity changes can be highlighted by means of amplitude of squared wavelet coefficients.

By visual inspection of the signal, the analysis is not so easy in order to see discontinuities that exist in high order derivatives during disturbances. For example, the discontinuities higher than the first derivatives can be detected and measured,

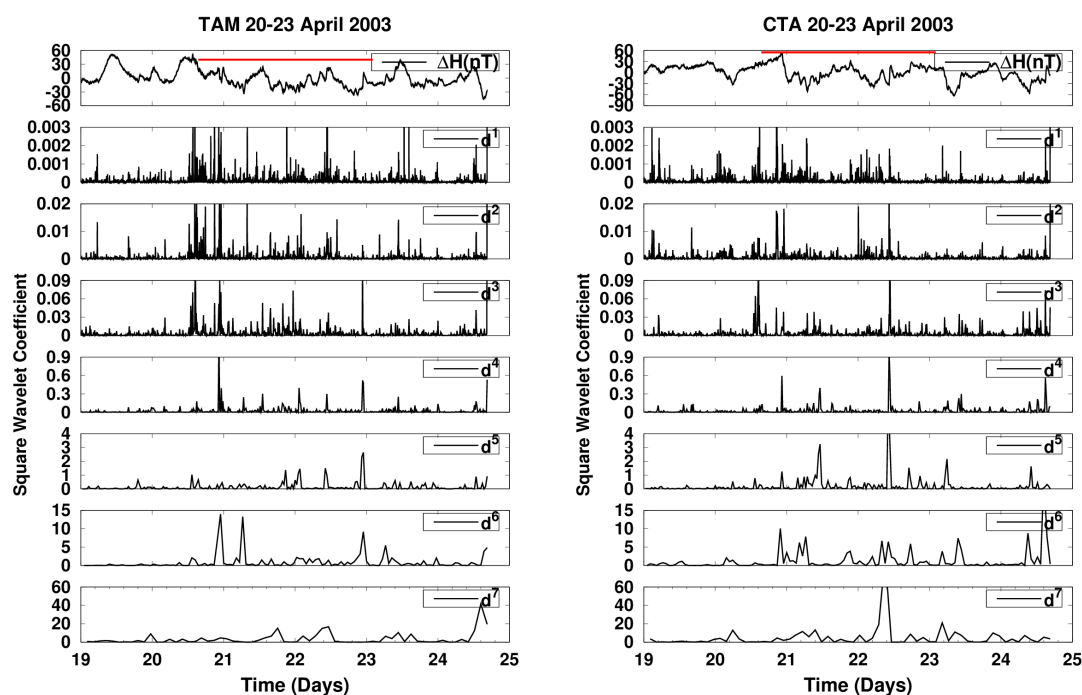


Figure 5.15 - Daubechies Wavelet coefficients d^j (for $j= 1,2,3,\dots,7$) for ΔH -component from TAM (left) and CTA (right) during HILDCAA event occurred on 20-23 April 2003. The red color identifies where the HILDCAA events is happening.

respectively. On the basis of squared wavelet coefficients, we may be able to analyze time localization of higher frequencies and lower frequencies associated with HILDCAAs. All these results can be used as a marker of HILDCAA, an indicator that a process of continuous energy transfer is going on. In these figures, all the observatories show significant amplitude of squared wavelet coefficient during the event. However, the nature of the coefficients is different. Such a different behavior may be related to different reasons, for examples: magnetic coordinates, type of magnetometer used, local time, ground conductivity and Sq current effects. A more detailed description about the Daubechies order 2 orthogonal wavelet transform can be found in (MENDES et al., 2005; OJEDA et al., 2014; KLAUSNER et al., 2014b).

Figure 5.17 shows the results of wavelet modulus correlation of ΔH -component from TAM, CTA, HON and VSS with interplanetary magnetic field (Bz) for the HILDCAA event on 20-23 April 2003. The horizontal axis represents the scale in minutes and the vertical axis represents the modulus correlation. In this figure, the scales of 1, 10, 100 and 1000 are labeled in the horizontal axis. The first panel of this figure represents the modulus correlation of IMF-Bz with TAM. It shows the peak about 0.4 at time scale 150 minutes. Similarly, the second panel represents the

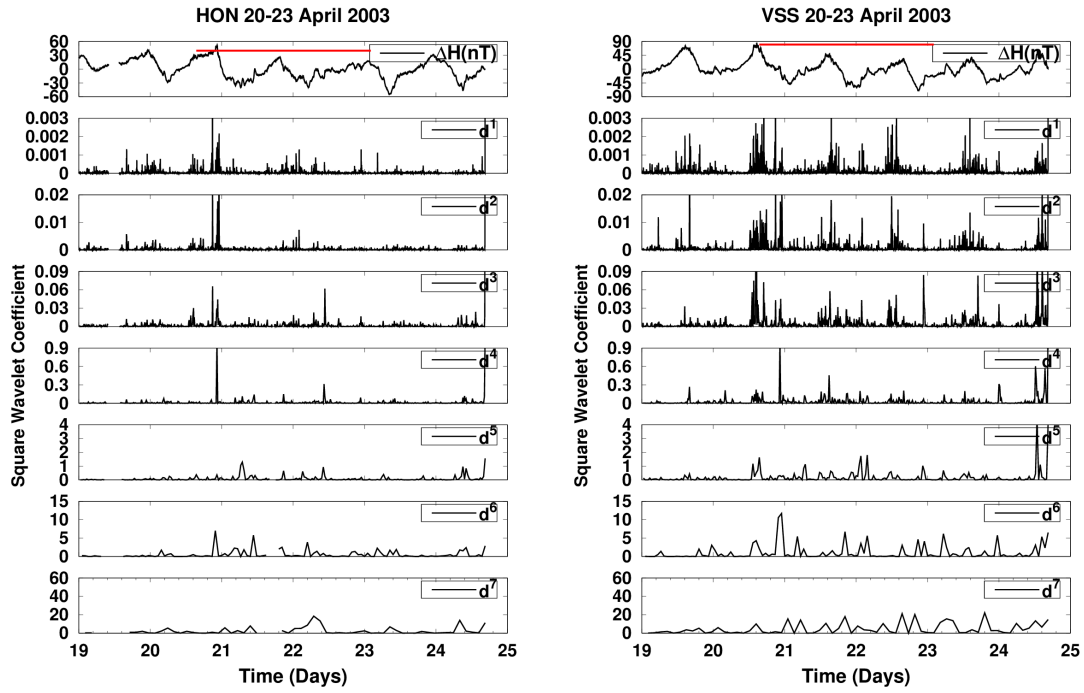


Figure 5.16 - Daubechies Wavelet coefficients d^j (for $j= 1,2,3,\dots,7$) for ΔH -component from HON (left) and VSS (right) during HILDCAA event occurred on 20-23 April 2003. The red color identifies where the HILDCAA events is happening.

modulus correlation of IMF-Bz with CTA. It shows the peak about 0.85 at time scale approximately 300 minutes. Other two panels show the modulus correlation of IMF-Bz with HON and VSS. They show peaks correlation about 0.9 and 0.45 at time scale approximately 350 minutes respectively. When observing these results, we can make the following remarks. The HILDCAA time ΔH signatures recorded at low latitude observatories are correlated with IMF-Bz. These results also show scale dependent characteristic. When compared to TAM and VSS, CTA and HON show very good correlation with IMF-Bz.

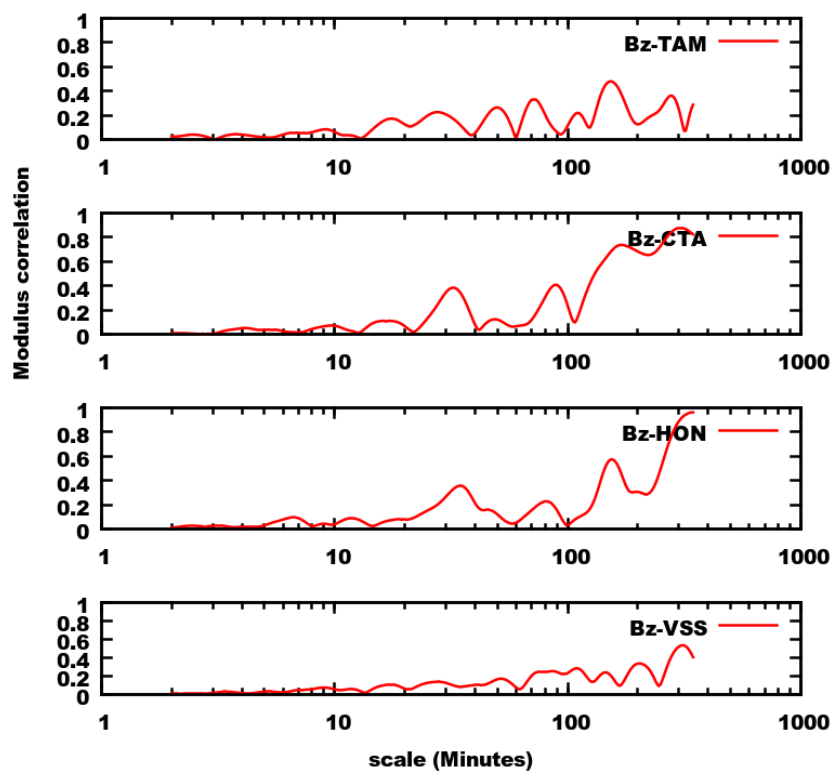


Figure 5.17 - From top to bottom, the panels represent the correlation of IMF-Bz with H component from geomagnetic observatories TAM, CTA, HON and VSS during the HILDCAA event on 20-23 April 2003.

Case 2: HILDCAA preceded by CIR-storm which occurred on 12-15 February 2004

Figure 5.18 shows the geomagnetic signatures of H component obtained from TAM, CTA, HON and VSS for HILDCAA preceded by CIR-storm which occurred on 12-15 February 2004. The panels representation and labeling are similar to like Figure 5.12. The quietest day signatures for this event is also similar to the previous event. However, the disturbed days signatures are different. During the main phase of the storm, all the observatories show strong depression on H-component. The SYM-H index shows depression around -115 nT, ASY-H index shows the peak vale about 160 nT and AE index shows the peak about 1600 nT. At the time of HILDCAA, all the observatories show fluctuations below quietest day curves. The SYM-H index shows approximately constant negative value. Both ASY-H and AE indices show intense activity. It is a event preceded by CIR-storm in which IMF-Bz shows higher level of Alfvénic fluctuation in IMF-Bz (GUARNIERI et al., 2006). Generally, geomagnetic storms caused by CIRs have moderate intensity because of highly fluctuation in IMF-Bz (GONZALEZ et al., 1994). When the fluctuations in IMF-Bz diminish, the storm starts its long recovery phase. This long magnetic storm recovery phase seen simultaneously with intense and continuous auroral activity (TSURUTANI; GONZALEZ, 1987; TSURUTANI et al., 2004; GUARNIERI et al., 2006; HAJRA et al., 2013; HAJRA et al., 2014a; HAJRA et al., 2014b). At that time, the Dst and AE indices are in good correspondence with ring current particle injections (SORAAS et al., 2004). Such an injection of ring current particles can be found in the outer portion of the ring current (the regions between $L=4 RE$ and $L=5.6 RE$), where RE is the Earth radius (SORAAS et al., 2004).

Figure 5.19 gives the ΔH signatures for the corresponding observatories during the same event. The panels representation and labeling are similar to Figure 5.13. During the main phase, all the observatories show strong depression on ΔH -component. The level of depressions for TAM, CTA, HON and VSS were approximately -180 nT, -80 nT, -50 nT and -150 nT respectively. At the time of HILDCAA, all the observatories show fluctuations below zero. However, the ΔH signatures recorded by each magnetic observatory are quiet dissimilar. As previous events, here we also used the same wavelet techniques in order to get some common features between these signatures.

Figure 5.20 depicts the scalograms for ΔH -component from (a) TAM (b) CTA (c) HON and (d) VSS during the HILDCAA event on 12-15 February 2004. In the

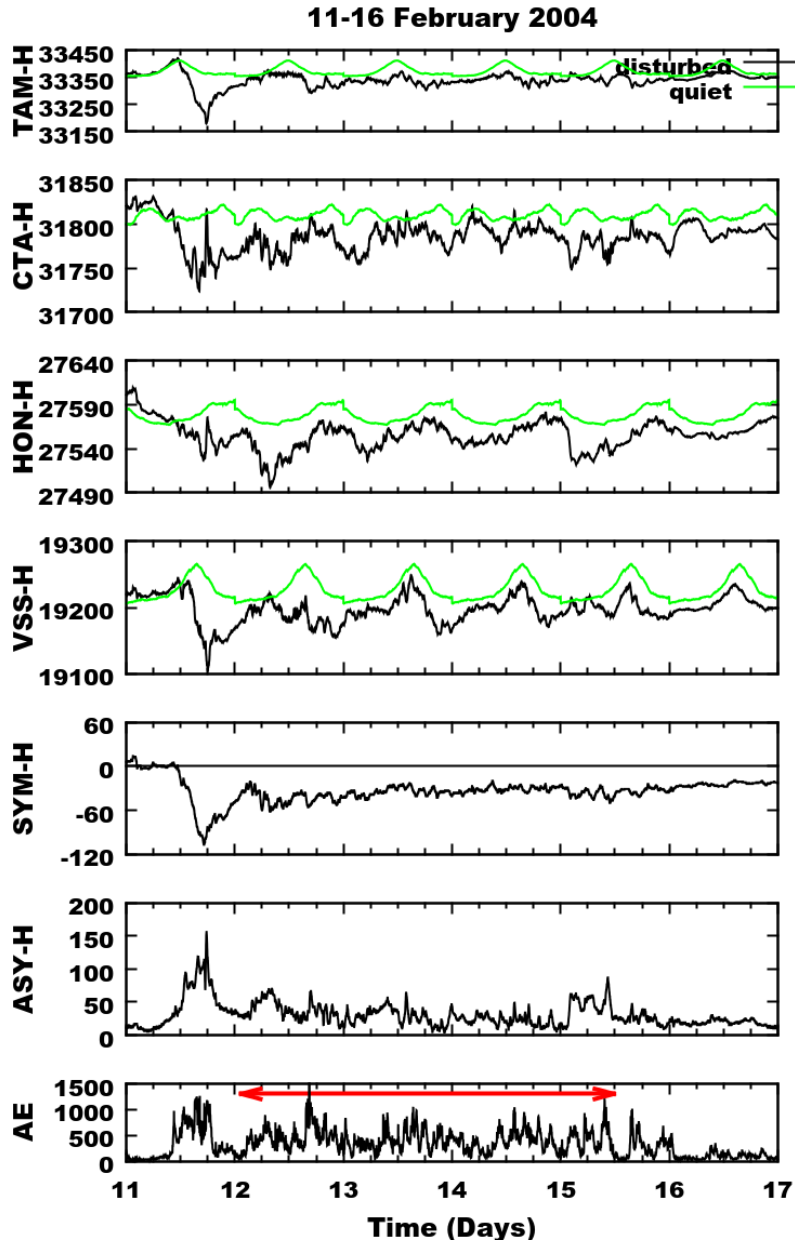


Figure 5.18 - From top to bottom, the panels show variations of H-component (nT) at the observatories TAM, CTA, HON, VSS along with the geomagnetic indices SYM-H (nT), ASY-H (nT) and AE (nT) respectively during the HILDCAA event on 12-15 February 2004. The green line represents the average quietest day variation, the black line represents the disturbed day variation and the red horizontal arrow in AE panel indicates the HILDCAA interval.

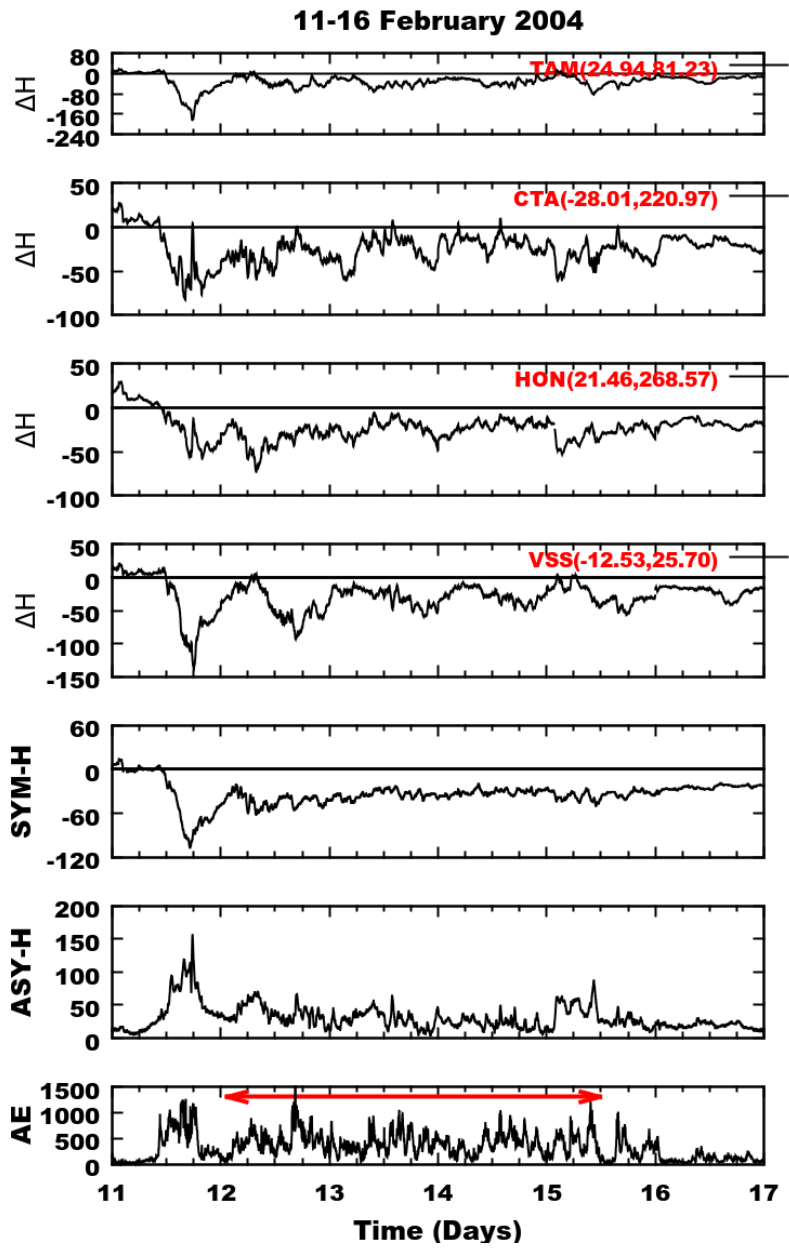


Figure 5.19 - From top to bottom, the panels represent the variation of ΔH signatures from TAM, CTA, HON, VSS and geomagnetic indices SYM-H (nT), ASY-H (nT) and AE (nT) during HILDCAA event during 12-15 February 2004. The red horizontal arrow in AE panel represents the HILDCAA interval.

figure, TAM shows the power areas of the highest intensity more continuously at time scales approximately between 100-300 minutes. Similarly, CTA HON and VSS show the wavelet power areas of higher intensities between 1.2-1.4 nT at time scales approximately between 100-300 minutes. Other less intense power areas are seen at medium to higher time scales. As compared to all, TAM and CTA show more continuously wavelet powers at medium to higher time scales.

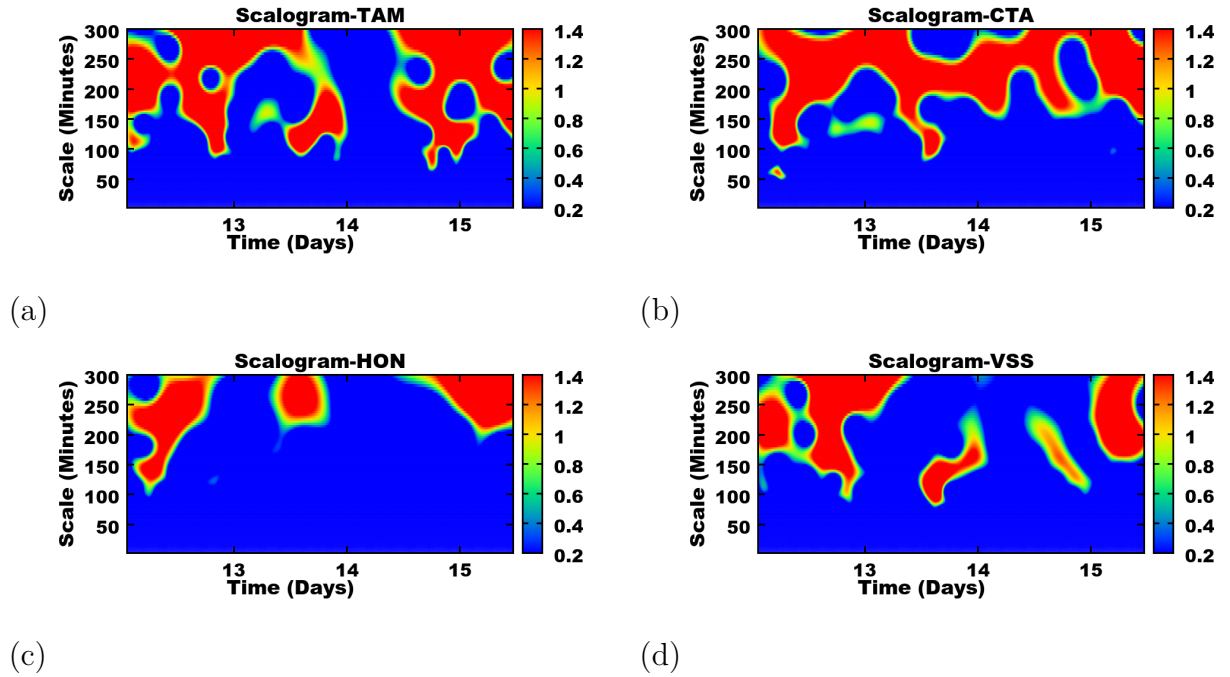


Figure 5.20 - Scalograms for ΔH -component from (a) TAM (b) CTA (c) HON and (d) VSS during the HILDCAA event on 12-15 February 2004.

Figures 5.21 and 5.22 are similar to Figures 5.15 and 5.16 but refer to HILDCAA preceded by CIR-storm occurred on 12-15 February 2004. Also in this case, larger and smaller amplitudes of squared wavelet coefficients can be observed for all the observatories considered.

Figure 5.23 is similar to Figure 5.17 but refers to HILDCAA preceded by CIR-storm occurred on 12-15 February 2004. In this figure, Bz-TAM, Bz-CTA, Bz-HON and Bz-VSS show the peaks modulus correlation about 0.65, 0.6, 0.6 and 0.6 at time scales 200, 250, 100 and 200 minutes respectively. As the previous event, this event also shows correlation of IMF-Bz with ΔH -component and also shows scale dependent characteristic.

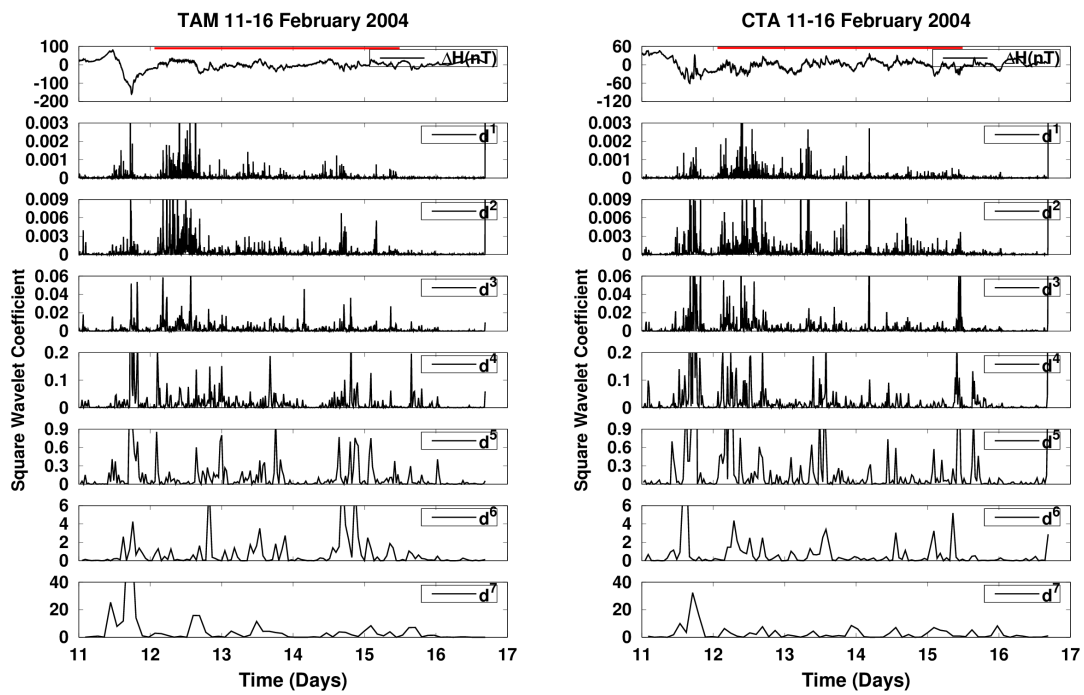


Figure 5.21 - Daubechies Wavelet coefficients d^j (for $j= 1,2,3,\dots,7$) for ΔH -component from TAM (left) and CTA (right) during HILDCAA event occurred on 12-15 February 2004. The red color identifies where the HILDCAA events is happening.

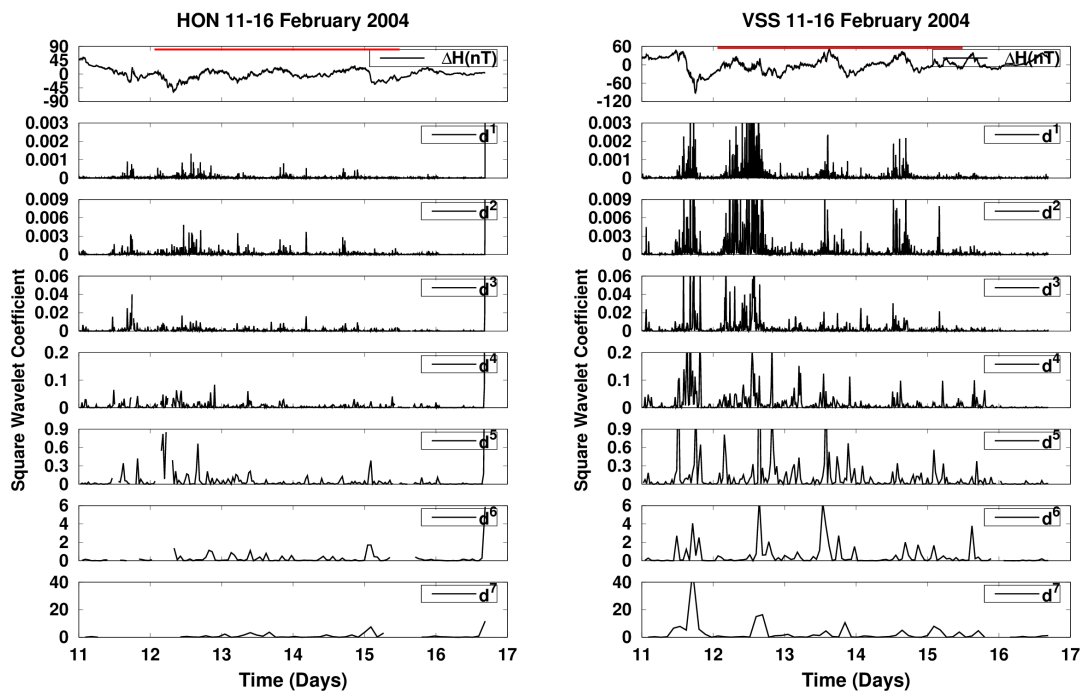


Figure 5.22 - Daubechies Wavelet coefficients d^j (for $j= 1,2,3,\dots,7$) for ΔH -component from HON (left) and VSS (right) during HILDCAA event occurred on 12-15 February 2004. The red color identifies where the HILDCAA events is happening.

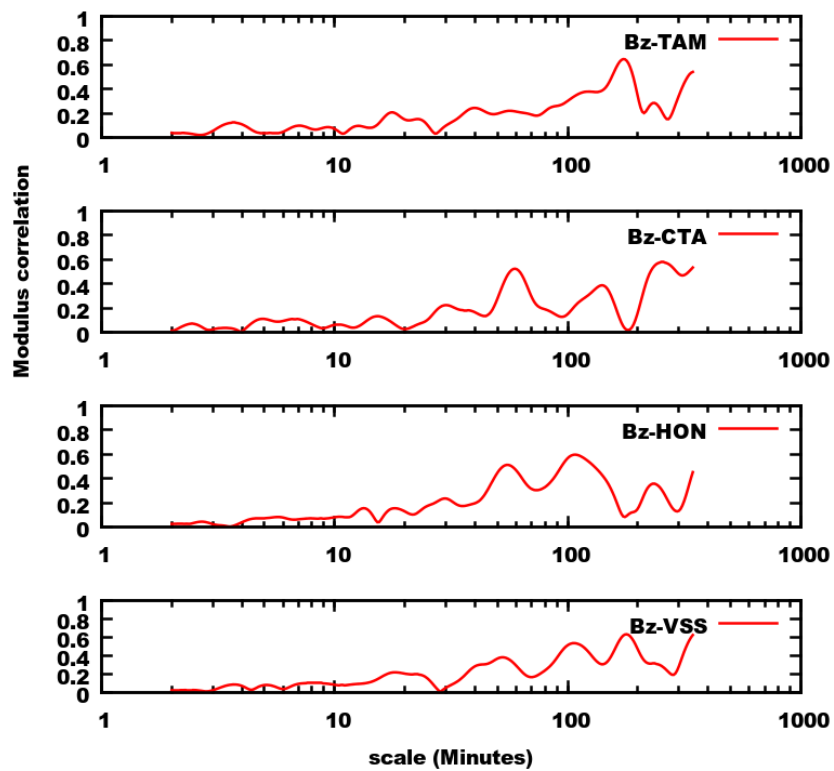


Figure 5.23 - From top to bottom, the panels represent the correlation of IMF-Bz with ΔH -component from geomagnetic observatories TAM, CTA, HON and VSS during the HILDCAA event on 12-15 February 2004.

Case 3: HILDCAA preceded by ICME which occurred on 15-18 May 2005

Figure 5.24 represents the geomagnetic signatures and geomagnetic indices for an ICME preceding HILDCAA occurred on 15-18 May 2005. The panels representation are similar to Figures 5.12 and 5.18. The interplanetary cause for this storm was the shock driven by an ICME contained a magnetic cloud structure (HAJRA et al., 2013; OJEDA et al., 2013; OJEDA et al., 2014) characterized by large southward IMF-Bz with a peak of -50 nT. In the figure, the second last panel represents the SYM-H index. When observing the variation in this index, the three different phases of the storm can be easily identified (TSURUTANI et al., 2001). The initial phase of this storm is caused by the abrupt increase in the solar wind ram pressure at interplanetary shock (ARAKI, 1977). This phase typically starts suddenly and lasts for an indeterminate amount of time. This phase is also known as a storm sudden commencement (SSC). However, not all geomagnetic storms have an initial phase and not all storms sudden commencement (SSC) are followed by a geomagnetic storm (AKASOFU; CHAPMAN, 1963; GONZALEZ et al., 1994; TSURUTANI et al., 2001). During the main phase, the H-component of geomagnetic field shows strong depressions. At that time, the SYM-H, ASY-H and the AE indices show peak values of about -300 nT, 275 nT and 2000 nT respectively. The recovery phase of this storm lasts from the mid day of 15 May to the mid day of 18 May, about 3 days. (CHAPMAN; BARTELS, 1940). During this phase, all the observatories show very strong negative fluctuations. The SYM-H index shows fluctuation between -100 to -30 nT. The ASY-H index shows fluctuation between 100 - 30 nT and the AE index shows intense activity.

Figure 5.25 depicts the ΔH signatures and geomagnetic indices for the same event. The panels representation are similar to Figures 5.13 and 5.19. This storm shows very strong initial phase for all observatories with positive values on ΔH component. That is caused by the abrupt increase in the solar wind ram pressure at interplanetary shock (ARAKI, 1977). During the main phase, TAM, CTA, HON and VSS show strong depression on ΔH component about -200 nT, -350 nT, -350 nT and -200 nT respectively. At the time of HILDCAA, all the observatories show very strong negative fluctuations. As compared to previous events, the HILDCAA time fluctuations for this event were very strong. However, each observatory shows quiet dissimilar signatures.

Figure 5.26 is similar to Figure 5.14 or Figure 5.20 but it refers to HILDCAA preceded by ICME-storm which occurred on 15-18 May 2005. In the figures, all the observatories show the wavelet power areas of higher and lower intensities on both

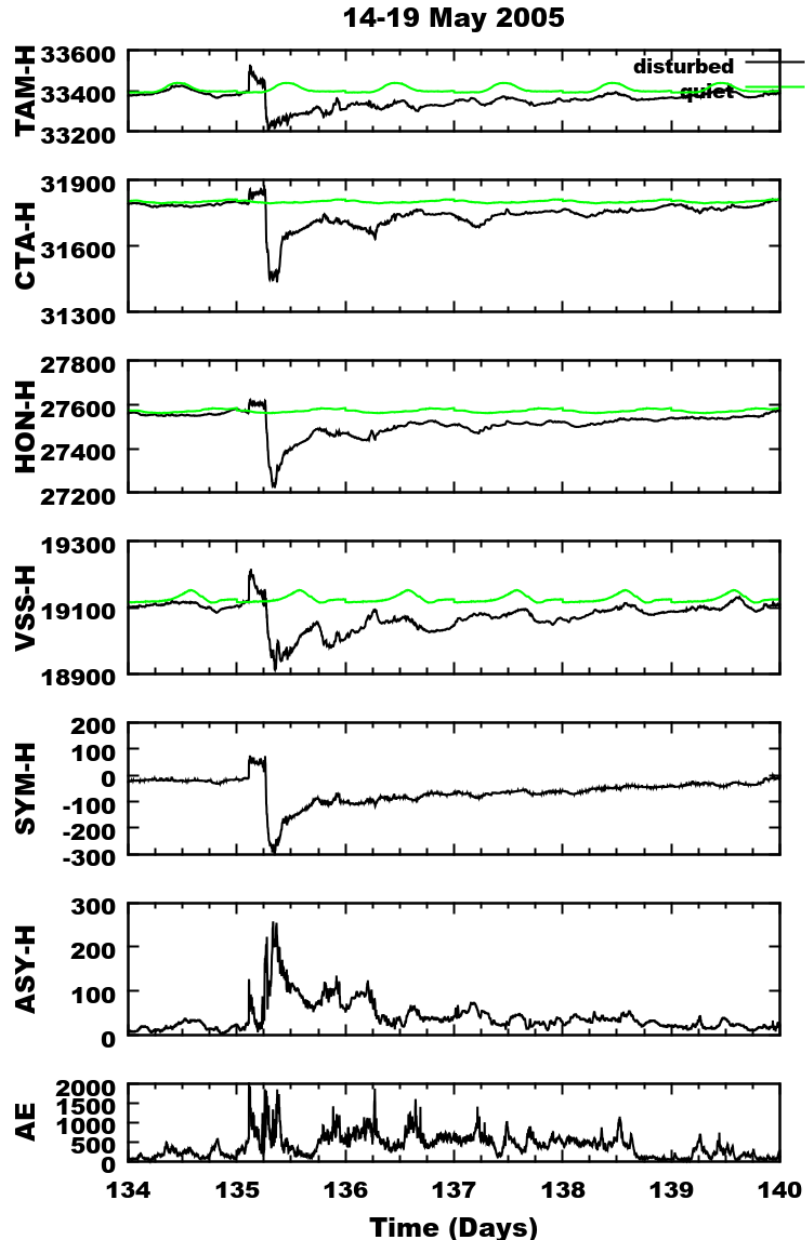


Figure 5.24 - From top to bottom, the panels show variations of H-component (nT) at the observatories TAM, CTA, HON, VSS along with the geomagnetic indices SYM-H (nT), ASY-H (nT) and AE (nT) respectively during the HILDCAA event on 15-18 May 2005. The green line represents the average quietest day variation, the black line represents the disturbed day variation and the red horizontal arrow in AE panel indicates the HILDCAA interval.

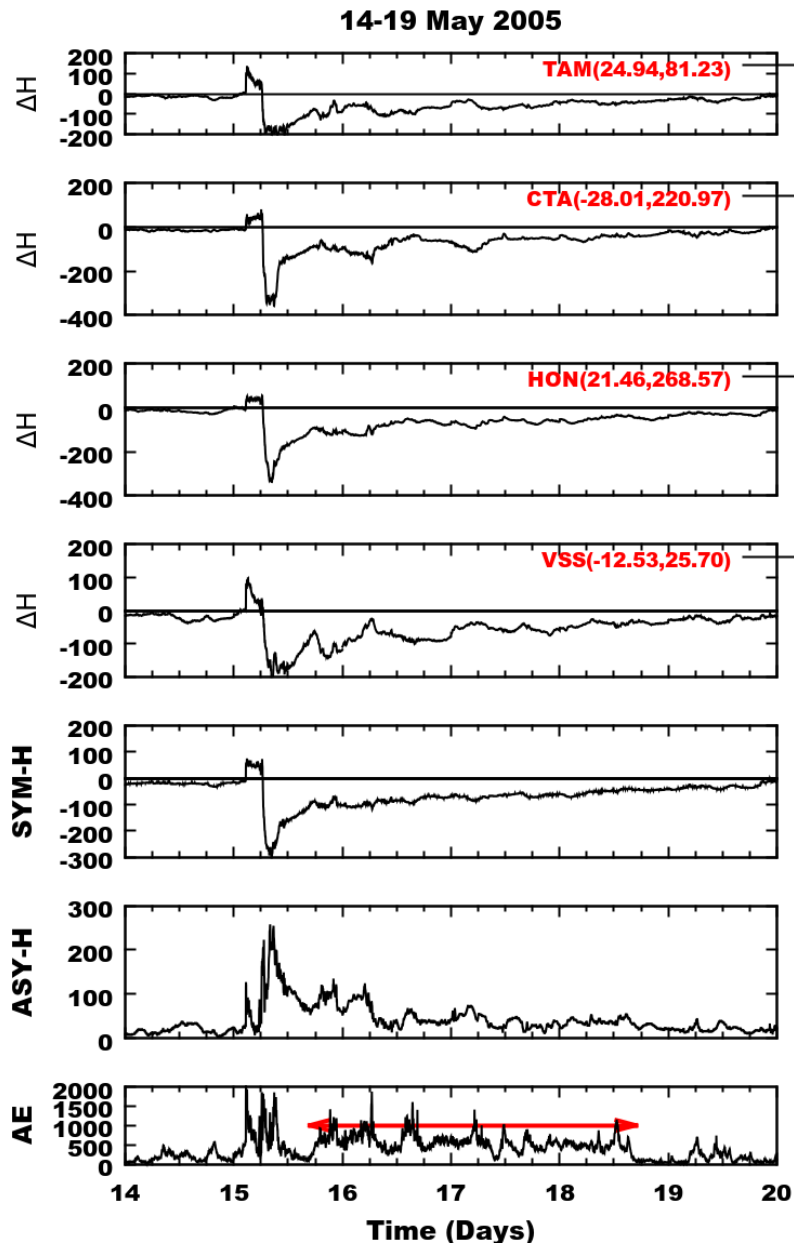


Figure 5.25 - From top to bottom, the panels represent the variation of ΔH signatures from TAM, CTA, HON, VSS and geomagnetic indices SYM-H (nT), ASY-H (nT) and AE (nT) during HILDCAA event during 15-18 May 2005. The red horizontal arrow in AE panel represents the HILDCAA interval.

medium and higher time scales. As compared to HON, TAM, CTA and VSS show continuous periodicity at time scales between 100-300 minutes during the beginning of HILDCAA.

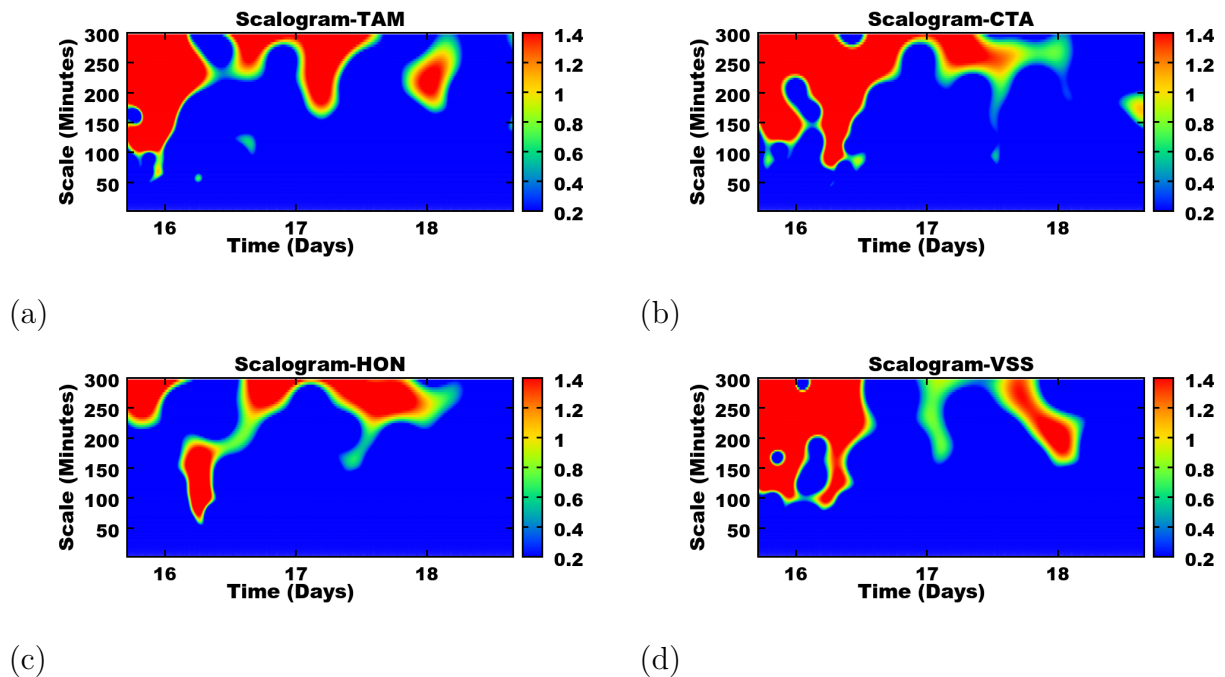


Figure 5.26 - Scalograms for ΔH -component from (a) TAM (b) CTA (c) HON and (d) VSS during HILDCAA event on 15-18 May 2005.

Figure 5.27 and Figure 5.28 are similar to Figure 5.15 and Figure 5.16 or Figure 5.21 and similar to Figure 5.22 but refers to HILDCAA preceded by ICME-storm which occurred on 15-18 May 2005. As the other two events, the singularities pattern, larger and smaller amplitude of squared wavelet coefficients are present for all observatories. However, this event shows relatively higher amplitude of squared wavelet coefficients during the event. Other two events were caused by CIRs where the fluctuation of Alfvén waves were present. These waves are the main causes for freshly injection of charged particles inside the magnetosphere. But the interplanetary cause for this storm was the shock driven by an ICME contained a magnetic cloud structure. During the main phase, the magnitude of southward IMF- B_z was very strong. At that time, the energy injection was huge and the observatories show strong depression on the ΔH -component of geomagnetic field. But during the HILDCAA interval, a small magnitude of IMF- B_z was continuously southward. Due to this reason, this event shows relatively higher energy injection as compared to other two

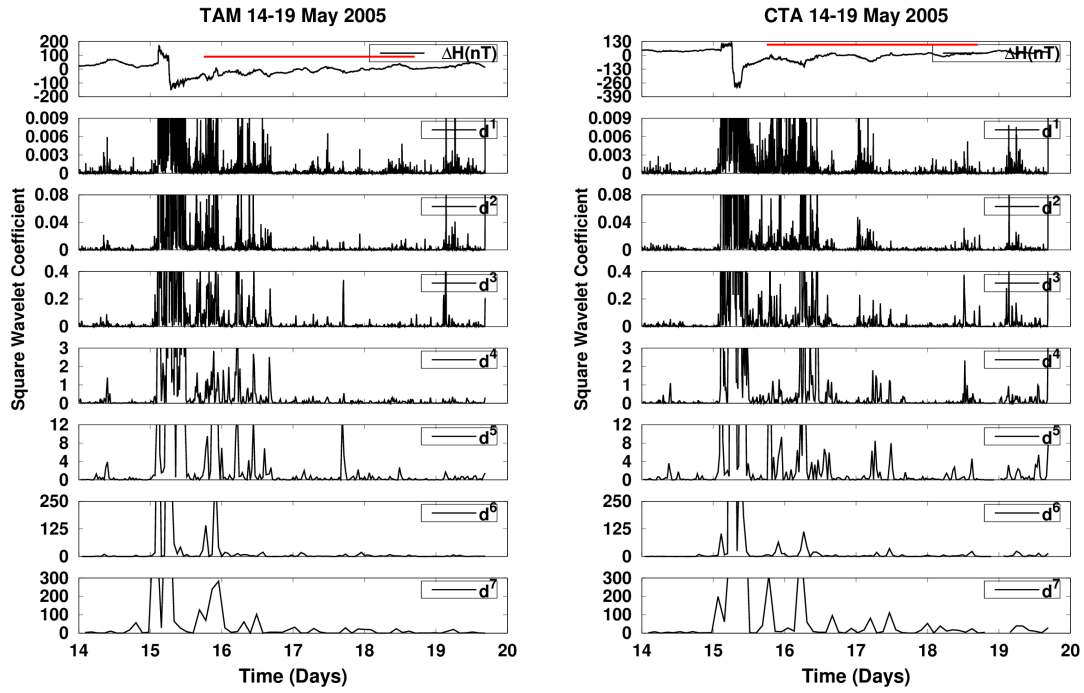


Figure 5.27 - Daubechies Wavelet coefficients d^j (for $j= 1,2,3,\dots,7$) for ΔH -component from TAM (left) and CTA (right) during HILDCAA event occurred on 15-18 May 2005. The red color identifies where the HILDCAA events is happening.

events.

Figure 5.29 is similar to Figure 5.17 or Figure 5.23 but refers to HILDCAA preceded by ICME-storm which occurred on 15-18 May 2005. In this figure, Bz-TAM, Bz-CTA, Bz-HON and Bz-VSS show the peaks modulus correlation about 0.6, 0.5, 0.5 and 0.4 at time scales 300, 250, 300 and 250 minutes respectively. Like the other two events, this event also shows correlation of IMF-Bz with ΔH -component and also shows scale dependent characteristic.

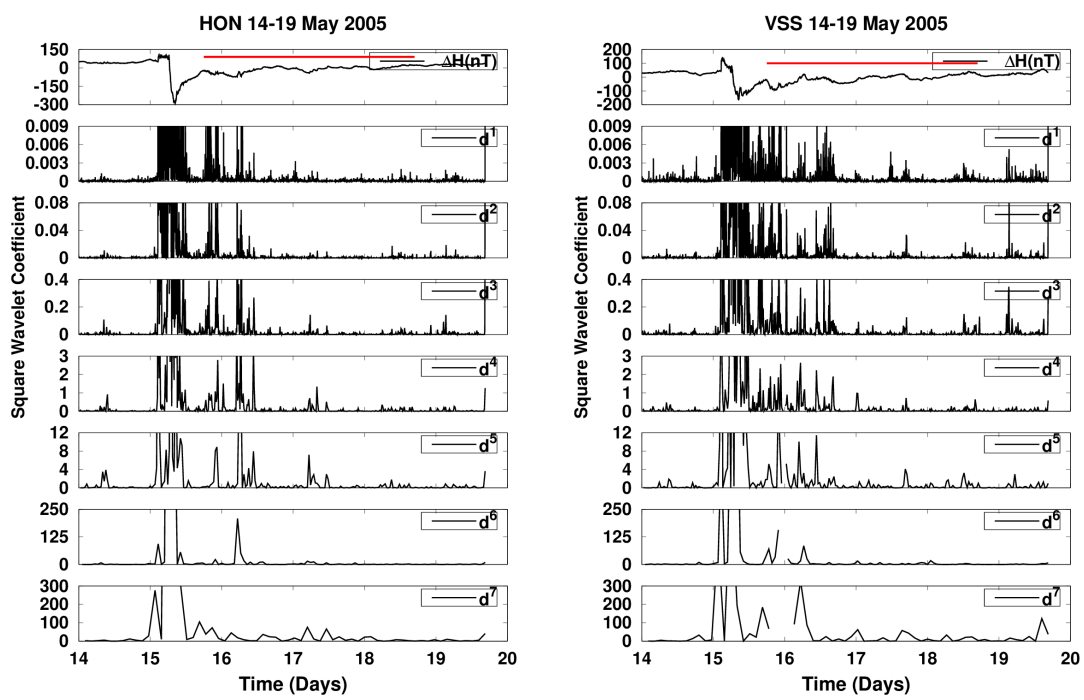


Figure 5.28 - Daubechies Wavelet coefficients d^j (for $j= 1,2,3,\dots,7$) for ΔH -component from HON (left) and VSS (right) during HILDCAA event occurred on 15-18 May 2005. The red color identifies where the HILDCAA events is happening.

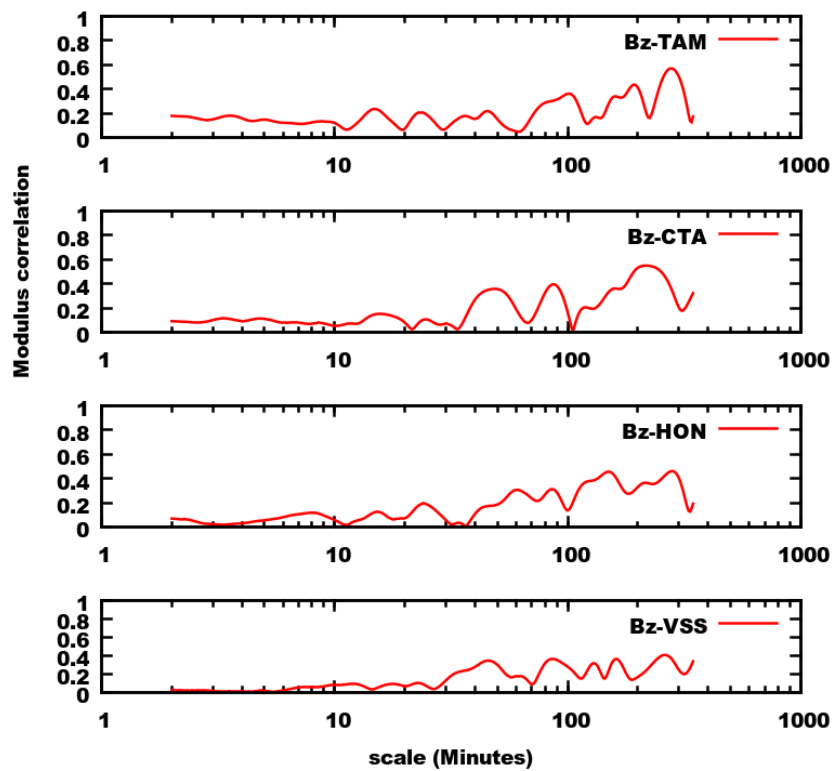


Figure 5.29 - From top to bottom, the panels represent the correlation of IMF-Bz with ΔH -component from geomagnetic observatories TAM, CTA, HON and VSS during the HILDCAA event on 15-18 May 2005.

Case 4: quiet period 18-21 July 2006

Figure 5.30 represents the geomagnetic signatures and geomagnetic indices for quiet periods from 18 to 21 July, 2006. The panels representation are similar to Figure 5.12, Figure 5.18 and Figure 5.12. In this figure, the quiet days values are plotted against universal time. The local time and universal time differences for TAM, CTA, HON and VSS are +1, +11, -10 and -3 hours respectively. When observing these differences, the quiet day variations show maximum at midday and minimum at dusk for all observatories (GONCHAROVA, 2004; RASTOGI, 2005; BOLAJI et al., 2013). Such a quiet days variations in geomagnetic field at low latitudes may be attributed to the variability of the ionospheric processes and physical structures such as conductivity and winds structures (JAMES et al., 1996; ABBAS; SALIHU, 2014). During very quiet state of magnetosphere, ionospheric currents at auroral latitudes calm down.

At that time, it is possible to observe the response of the auroral ionosphere due to internal effects. These effects are supposed to be produced basically by the dynamo action of the thermospheric winds (CHAPMAN; BARTELS, 1940; CAMPBELL, 1997). Then, the quiet-time geomagnetic variations at low-latitudes are generally described by the Sq (solar quiet) current system (CHAPMAN; BARTELS, 1940). The quiet time variations of geomagnetic field depends on latitudinal positions of the observatories. The enhanced quiet time field variations at equatorial observatory is due to the equatorial electrojet current (RASTOGI, 1999). It exhibited a dusk to dawn phenomenon with a non zero variation observed in the night and the variability of the nighttime is from sources other than the ionosphere (RASTOGI, 2005; BOLAJI et al., 2013).

Figure 5.31 is similar to Figure 5.14 or Figure 5.20 or Figure 5.26 but refers to quiet periods from 18 to 21 July, 2006. In these figures, all the observatories show wavelet power areas of lesser amplitudes as compared to above three HILDCAA events. All these low latitude geomagnetic observatories are located in the northern and southern hemispheres and have been included as guidelines to quiet periods time behavior at low latitudes. As we know, during quiet periods the signatures of geomagnetic field at low latitude observatories show maximum at midday and minimum at dusk time (GONCHAROVA, 2004; RASTOGI, 2005; BOLAJI et al., 2013). The quietest time variation is a day to day variation which depends on the phase of the sunspot cycle, seasons, movement of the solar quiet foci, atmospheric tide and longitude. It is generated by two large vortices of electric currents in the day-side ionosphere. The dynamo currents flowing in the ionosphere due to atmospheric

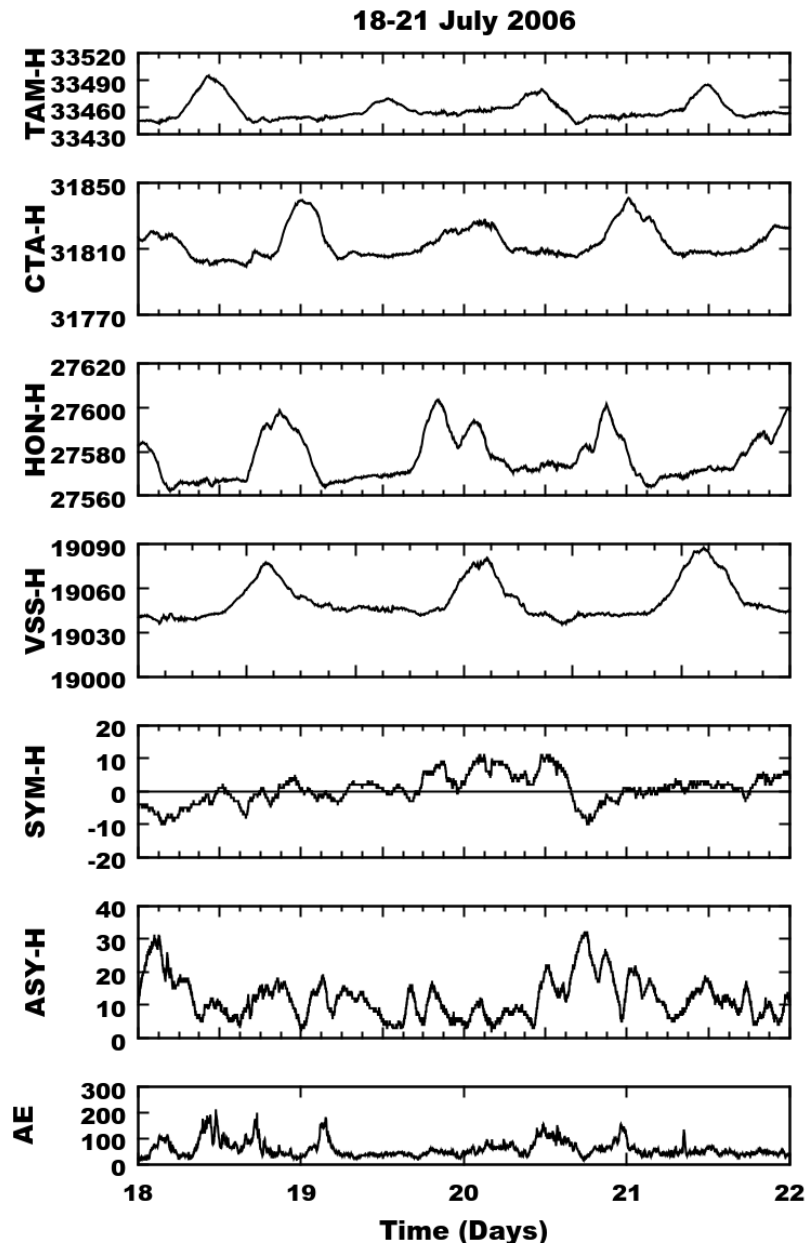


Figure 5.30 - From top to bottom, the panels show variations of H-component (nT) at the observatories TAM, CTA, HON, VSS along with the geomagnetic indices SYM-H (nT), ASY-H (nT) and AE (nT) respectively during quiet periods from 18 to 21 July, 2006.

tidal motion across the geomagnetic field are responsible for it. In this figure, each observatory shows wavelet power of different intensities at different time scales, which may be related to different reasons such as magnetic coordinates, type of magnetometer used, local time or ground conductivity.

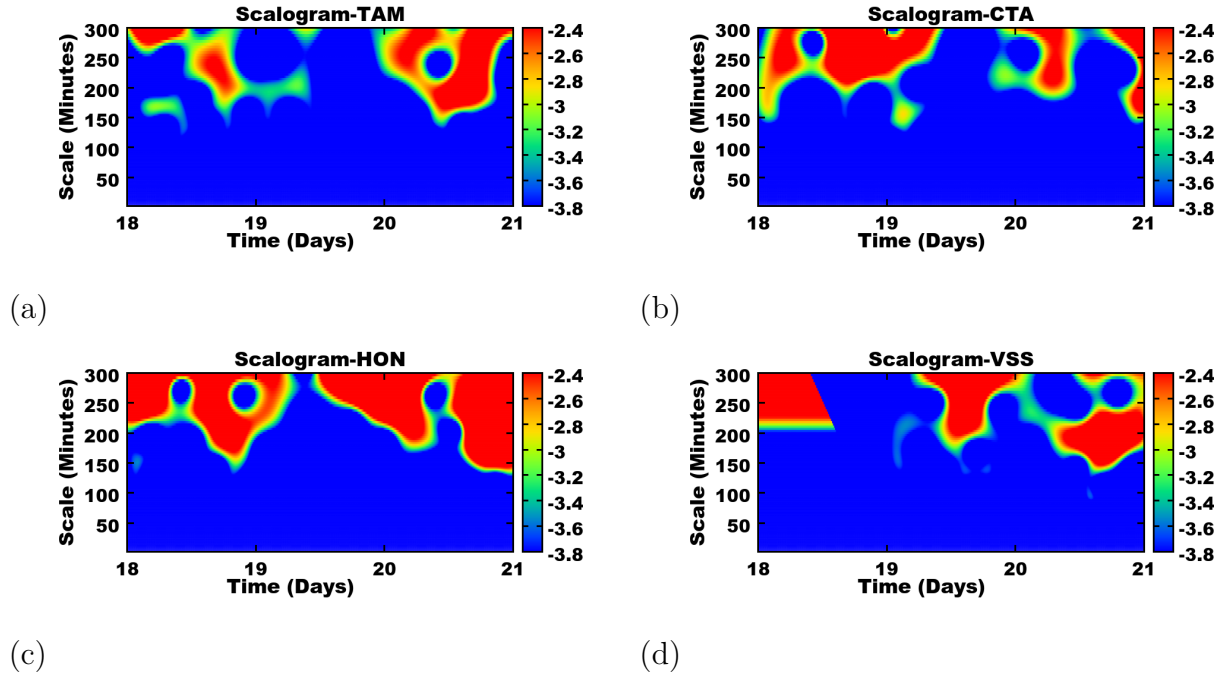


Figure 5.31 - Scalograms for ΔH -component from (a) TAM (b) CTA (c) HON and (d) VSS during quiet periods from 18 to 21 July, 2006.

Figure 5.32 and Figure 5.33 are similar to Figure 5.15 and Figure 5.16 or Figure 5.21 and Figure 5.22 or Figure 5.27 or Figure 5.28 but refer to quiet periods from 18 to 21 July, 2006. In these figures, all observatories show both smaller and larger squared wavelet coefficients. These coefficients may be related to the variability of the ionospheric processes and physical structures such as conductivity and winds structures (JAMES et al., 1996; ABBAS; SALIHU, 2014). However, the amplitude of squared wavelet coefficients are smaller if compared to HILDCAAs events.

Figure 5.34 is similar to Figure 5.17 or Figure 5.23 or Figure 5.29 but refers to quiet periods from 18 to 21 July, 2006. In this figure, all the observatories show peak modulus correlation about 0.6 at time scales approximately 150 minutes with IMF-Bz.

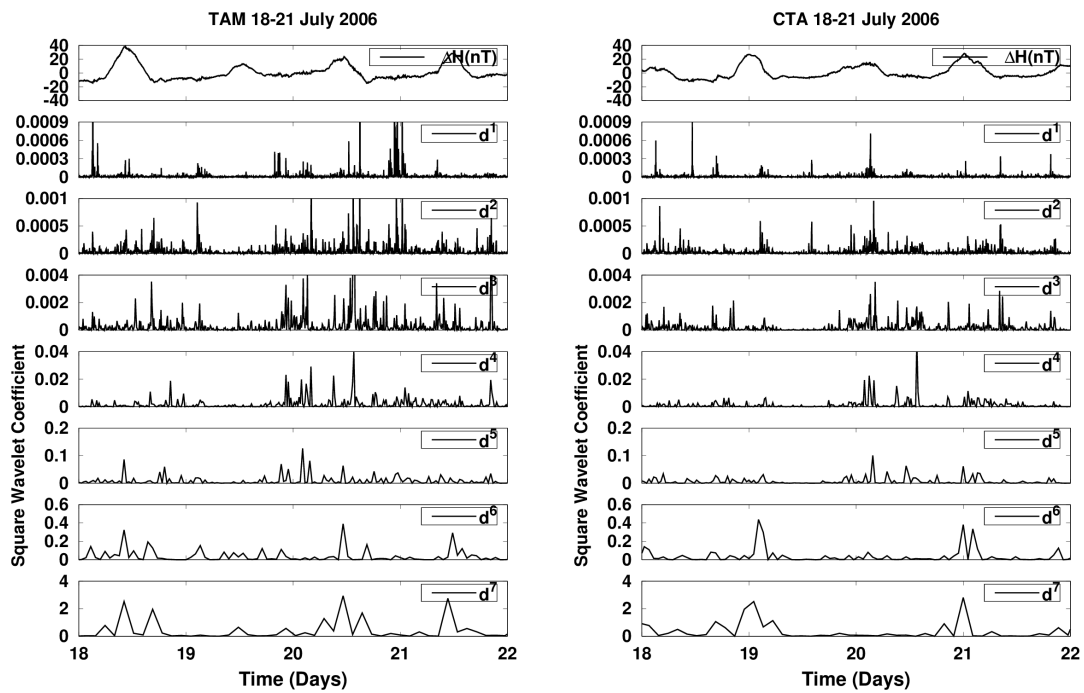


Figure 5.32 - Daubechies Wavelet coefficients d^j (for $j= 1,2,3,\dots,7$) for ΔH -component from TAM (left) and CTA (right) during quiet periods from 18 to 21 July, 2006.

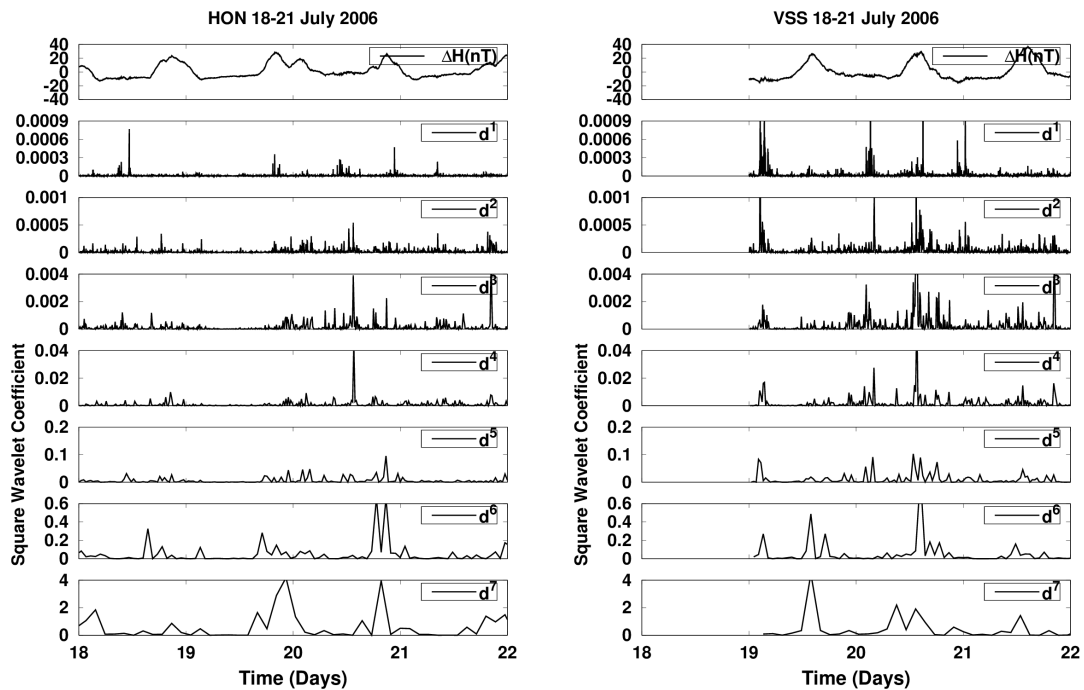


Figure 5.33 - Daubechies Wavelet coefficients d^j (for $j= 1,2,3,\dots,7$) for ΔH -component from HON (left) and VSS (right) during quiet periods from 18 to 21 July, 2006.

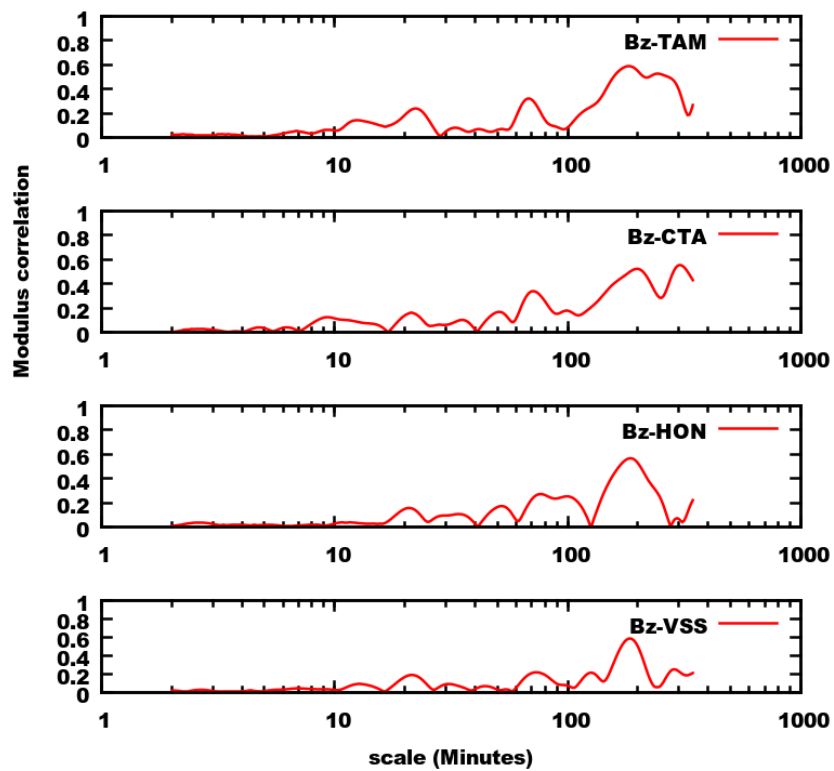


Figure 5.34 - From top to bottom, the panels represent the correlation of IMF-Bz with H component from geomagnetic observatories TAM, CTA, HON and VSS during quiet periods from 18 to 21 July, 2006.

Partial conclusions

The study of HILDCAA is an important issue for the study of space weather because it helps to clarify mechanisms related to the coupling of solar wind and magnetosphere-ionosphere system. Among other geomagnetic indices, AE is a very important index because it indicates the presence of HILDCAAs according to [Tsurutani and Gonzalez \(1987\)](#)'s criteria. Using a modified approach, this study was done to observe the geomagnetic effects recorded at low latitudes ground databases during HILDCAAs.

As a basic comprehension, the quietest time variation is a day to day variation which depends on the phase of the sunspot cycle, seasons, movement of the solar quiet foci, atmospheric tide and longitude. It is generated by two large vortices of electric currents in the day-side ionosphere. The dynamo currents flowing in the ionosphere due to atmospheric tidal motion across the geomagnetic field are responsible for it. At the equator, there is a concentration of an ionospheric electrical current (west-east) called equatorial electrojet. It leads to a daily variation value up to 200 nT. On the other hand, at the time of HILDCAAs, a large number of charged particles and energies are injected into the magnetosphere and ionosphere ([KAMIDE et al., 1998](#)) and the current systems existing inside the magnetospheric and ionospheric will be widened and intensified ([JANKOVICOVA et al., 2002](#)). As a result, middle and low latitudes will be dominated by ring current and this effect is well-represented by the equatorial Dst index as suggested by ([SUGIURA, 1964](#)). During HILDCAA, the nature of fluctuations for each observatory is different. As compared to northern hemisphere observatories (TAM and HON), southern hemisphere observatories (CTA and VSS) show more depressed fluctuations in H-component. This shows that in the southern hemisphere the geomagnetic field variations are larger when compared to the northern hemisphere ([DEVI et al., 2008](#)). Although the physical mechanism is related to the intermittent magnetic reconnection between IMF-Bz with earth magnetic field ([GONZALEZ et al., 1994](#)), specific characteristics with the morphology of the magnetosphere-ionosphere system must be considered.

Wavelet techniques (CWT, DWT and wavelet modulus correlation) employed in the present work help to decompose the time series of geomagnetic field in to different scales. There may be different dominant scales at different times in different parameters that depend on the regularity of their variation. During the events, it is seen that the wavelet power of higher time scales is highly enhanced due to the presence of discontinuities in the datasets. That may be related to the transfer of energy and

momentum, the geomagnetic field also gets affected and leads to HILDCAAs. Some similar characteristic effects of HILDCAAs are visible on the results of the wavelet analysis on ΔH -component for all observatories. The first characteristic is the presence of wavelet power areas of higher amplitudes at higher time scale which may be related to the amplitude amplification by shocks or discontinuities (in mathematical sense). Another characteristic is the distribution of lower frequencies on both medium and higher time scales. Both characteristics observed in the results of the wavelet analysis may be related to the shape of highly fluctuated datasets. However, the results of CWT vary from one event to another.

Similarly, we use DWT for the ΔH -component of geomagnetic field for same observatories. In each figure, the highest amplitude of the squared wavelet coefficients indicate the singularities associated with HILDCAAs. On the other-hand, smaller amplitude of the squared wavelet coefficients observed during the HILDCAAs interval indicates the processes of smooth energy transfer while the large amplitudes indicate the impulsive energy injections inside the magnetosphere. Similarly, the smooth squared wavelet coefficients represent the quiet conditions (magnetically quiescent periods) and the significant squared wavelet coefficients indicate the disturbed conditions (magnetically disturbed periods) of the magnetosphere. In the results, all the observatories show significant amplitude of squared wavelet coefficients during the events. However, the nature of the coefficients show totally different features for each observatory during the events. Such different features may be related to different reasons, for examples: magnetic coordinates, type of magnetometer used, local time, ground conductivity and Sq current effects.

We also use the wavelet modulus correlation of IMF-Bz with ΔH -component from the same observatories. The results of modulus correlation show that the ΔH behavior during HILDCAA time recorded at low latitude observatories is correlated with IMF-Bz. These results also show scale dependent characteristic. Like CWT and DWT, it also shows different results for each observatory during the events.

Thus, based on these used techniques, we are able to justify characteristic behavior on the geomagnetic records at low latitudes during HILDCAAs.

5.3 Geomagnetic signatures recorded at different longitudinal observatories during HILDCAAs.

In this section, we show case studies of fluctuations on H-component of geomagnetic field recorded at different longitudinal observatories during three different HILDCAA events (20-23 April 2003, 12-15 February 2004 and 15-18 May 2005) from its respective quietest day value. For this study, we take five different longitudinal observatories whose coordinates and IAGA codes are shown in Table 3.1. We also present the interpretations made by different methodologies (CWT, DWT and wavelet modulus correlation) for each event.

Case 1: Non-storm HILDCAA which occurred on 20-23 April 2003

Figure 5.35 shows the magnetometer results obtained from GUAM, ABG, VSS, KAK and THL and the geomagnetic indices SYM-H, ASY-H and AE for a HILDCAA event occurred on 20-23 April 2003. Table 3.1 shows names and coordinates with IAGA (International Association of Geomagnetism and Aeronomy) codes. The green and the black lines indicate the average quietest day and disturbed days respectively. Starting from top to bottom, the first panel stands for GUAM, the second panel for ABG, the third panel for VSS, the fourth panel for KAK and the fifth panel for THL. Other three panels represent SYM-H, ASY-H and AE indices respectively. The horizontal red line with double arrow on AE index at the the last panel shows the HILDCAA interval. GUAM is an equatorial station located in northern hemisphere, and it has been used to check the HILDCAA time signatures at equator. ABG and VSS are low latitude geomagnetic observatories located in northern and southern hemisphere respectively. They have been included as guidelines to check HILDCAA time behavior at low latitudes. KAK and THL are mid and high latitudes observatories located in the northern hemisphere, have been included to check HILDCAA time behavior at mid and higher latitudes. As we know that during geomagnetic disturbances (storm or substorm), a large number of charged particles and energies are injected into the magnetosphere and ionosphere (KAMIDE *et al.*, 1998) and the current systems existing inside the magnetosphere and ionosphere will be widened and intensified (JANKOVICOVA *et al.*, 2002). As a result, middle and low latitudes will be dominated by ring current, higher latitudes will be dominated by a system of ionospheric electrojet currents flowing in the auroral oval and equatorial region will be dominated by a system of current flowing in the equator known as equatorial electrojet. In the figure, the quietest days signature for GUAM shows maximum around 2 UT but the difference between LT and UT for this station is +10 hours

so it has peak around 12 LT. Similarly, both low latitudes observatories ABG and VSS shows maximum around 12 LT. The quietest day signatures for KAK shows small peak around 6 UT, it means that it has peak around 15 LT. Finally, the quietest day signature for THL shows minimum around midday and maximum around dusk time. Observing the quietest day signatures, it is seen that except for THL and Kakioka, other three observatories show maximum at midday and minimum at dusk time (GONCHAROVA, 2004; RASTOGI, 2005; BOLAJI et al., 2013). Before HILDCAA, both the quietest day and the disturbed day graphs show identical signatures for all observatories. But at the time of HILDCAA, the nature of signatures are not identical. As compared to equatorial, low and mid latitudes observatories, the high latitude station (THL) shows a higher level of fluctuations. This may be due to the penetration of charged particles and energy injection associated with high frequency signal during the HILDCAA interval (MENDES et al., 2005). The SYM-H index at the fifth panel of this figure shows a very weak depression between -20 nT to -30 nT. Other two indices ASY-H and AE show intense activity from the midday of 20 to the beginning of 23. The activity observe in AE index gives support to verify the HILDCAA criteria as suggested by (TSURUTANI; GONZALEZ, 1987).

Figure 5.36 gives the ΔH signatures for the corresponding observatories during the same event. The first five panels of this figure show the ΔH signatures for GUAM, ABG, VSS, KAK and THL. Other three panels are similar to Figure 5.35. At the time of HILDCAA, all the observatories show ΔH signatures approximately lower than zero except THL. THL shows highly positive and negative fluctuations. The lower latitudes station ABG and VSS also do not show identical nature. This may be due to different reasons, for example: type of magnetometers used, ground conductivity and local time. However, KAK and ABG (same hemisphere) show somewhat identical signatures. The wavelet techniques (CWT, DWT and wavelet modulus correlation) used below will help to reveal some common features of these signatures.

In this section, we describe the results obtained from wavelet scalogram of ΔH -component recorded from different geomagnetic observatories. It provides an unfolding of the characteristics of a process in the time-scale plane. Figure 5.37 shows scalograms for ΔH -component from (a) GUA (b) ABG (c) VSS and (d) KAK. In the figure, the horizontal axis represents the time in days and the vertical axis represents the scale in minutes. The scale of color on the right side of the second panel has unit in nT same unit of real data. When observing the scalogram for GUAM (a), it is found that the power areas covered by red color of intensities between 1.2-1.4 nT are seen on both medium and higher time scales. Other two power areas covered

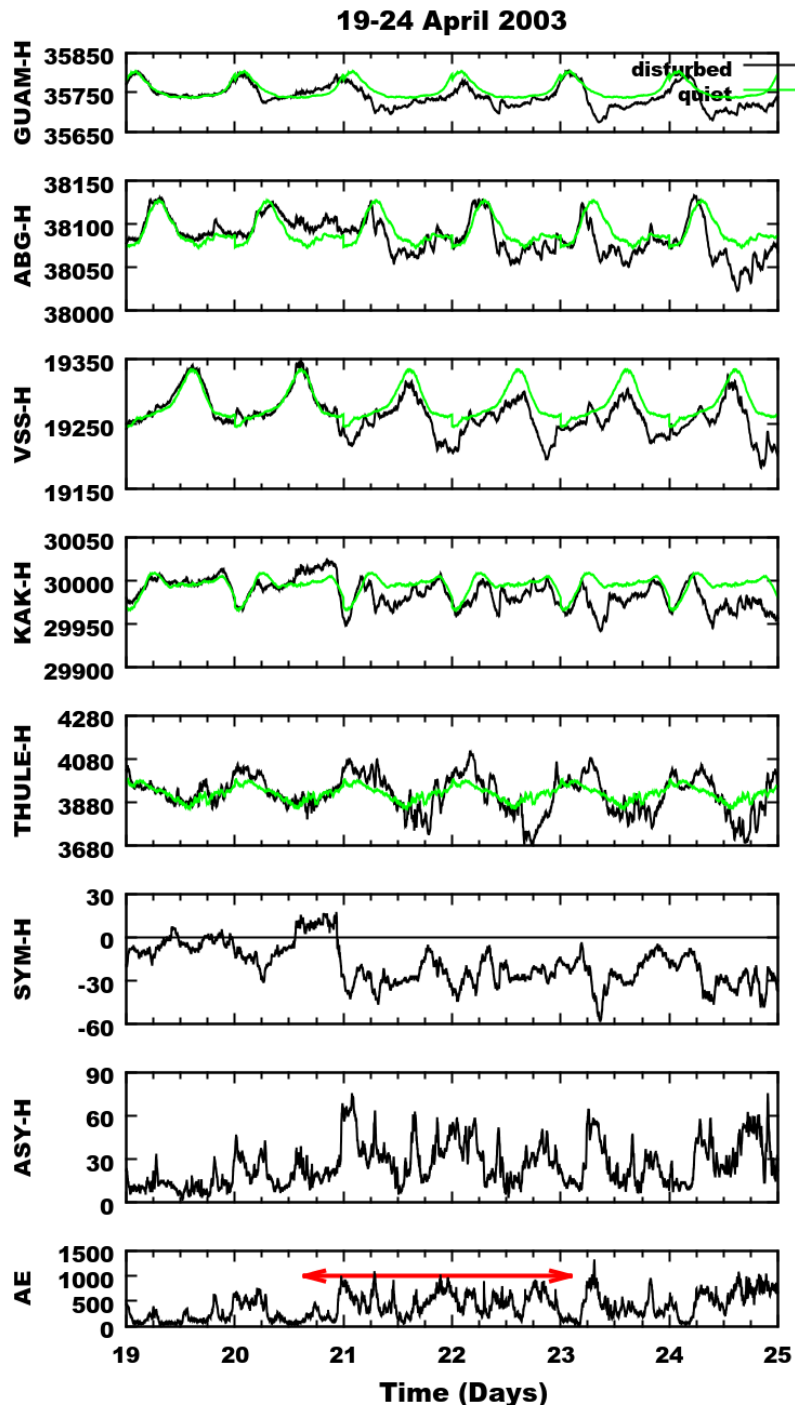


Figure 5.35 - From top to bottom, the panels show variations of H-component (nT) at the observatories GUAM, ABG, VSS, KAK, THL along with the geomagnetic indices SYM-H (nT), ASY-H (nT) and AE (nT) respectively during the HILDCAA event on 20-23 April 2003. The green line represents the average quietest day variation, the black line represents the disturbed day variation and the red horizontal arrow in AE panel indicates the HILDCAA interval.

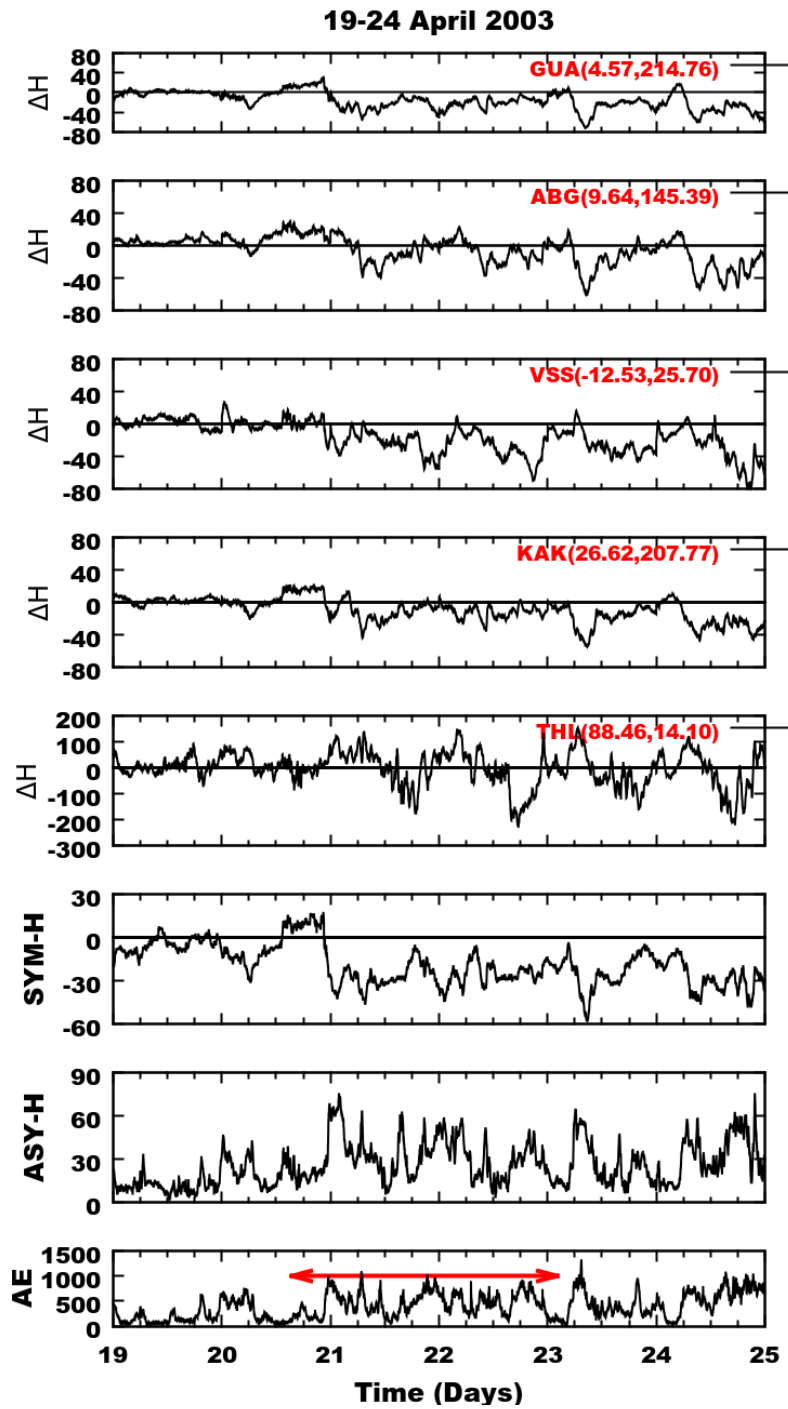


Figure 5.36 - From top to bottom, the panels represent the variation of ΔH signatures from GUAM, ABG, VSS, KAK, THL and geomagnetic indices SYM-H (nT), ASY-H (nT) and AE (nT) during HILDCAA event during 20-23 April 2003. The red horizontal arrow in AE panel represents the HILDCAA interval.

by yellow and green color of intensities between 0.7-0.8 and 0.4-0.6 nT are also seen on both medium and higher time scales. These results show that no periodicity is being expressed continuously throughout the event. Similarly, Figure 5.37(b) shows the scalogram for ABG. This station shows highly scattered wavelet powers. Like GUAM, both wavelet power areas of lesser and higher intensities are present at medium to higher time scales. In these scalograms, the presence of multiscale structures and their temporal locations are easily identified. Figure 5.37(c) and (d) show the scalograms for VSS and KAK. Both observatories show approximately similar results for scalograms. They also show scattered power areas on both medium and higher time scales.

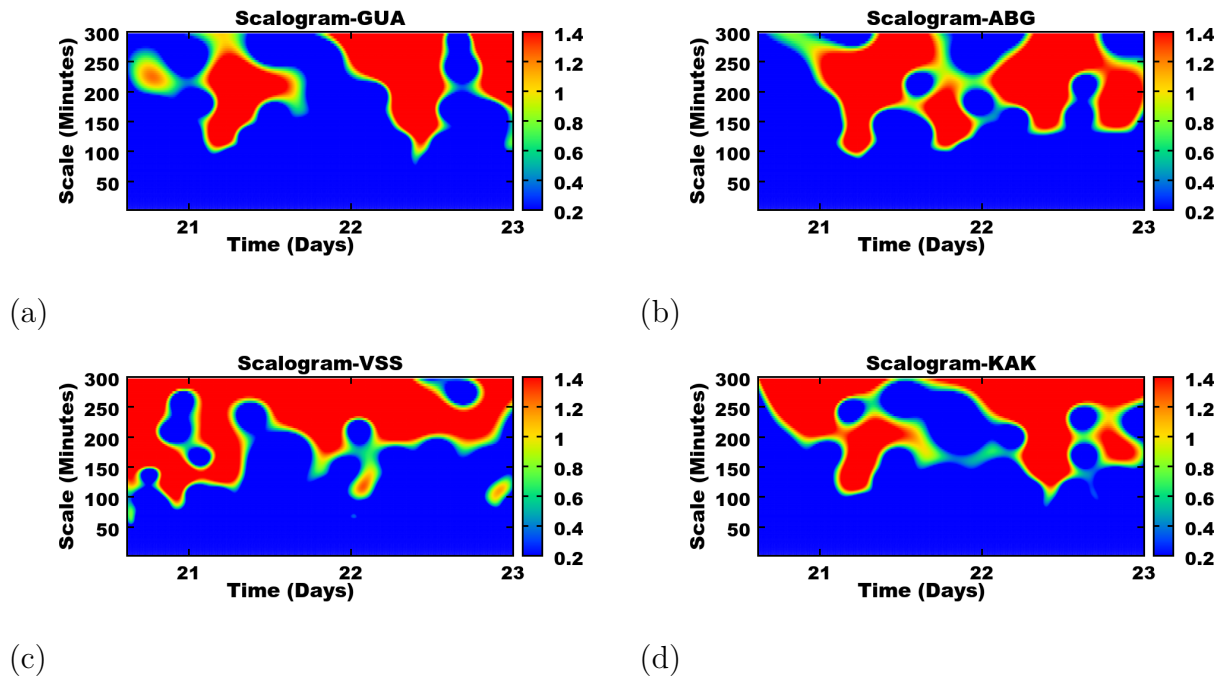


Figure 5.37 - Scalograms for ΔH -component from (a) GUA (b) ABG (c) VSS and (d) KAK during HILDCAA event on April 20-23, 2003.

Figure 5.38 is the scalogram for THL. This station shows very strong wavelet power areas at time scales between 100-300 minutes. Other less intense power areas are also seen at the same range of times scales. All these results show that the power areas of higher intensities are seen at medium to higher time scales. This analysis is restricted to the period range 0 to 300 minutes. It is noticed that for all observatories the wavelet powers corresponding to the period between 100-300 minutes are highly evolving during the event. For GUA, ABG, VSS and KAK, the main periodicities

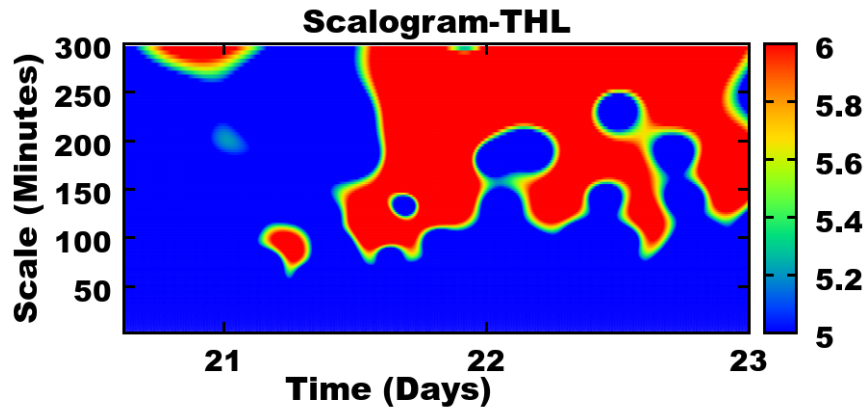


Figure 5.38 - Scalogram for ΔH -component from THL observatory during HILDCAA event on April 20-23, 2003.

present are approximately near 150-300 minutes. However, THL shows continuous periodicity at time scale between 150-300 minutes. Hence, when observing these results, we can explore following points: The high latitude station (THL) shows strong effect of HILDCAA, which may be related to direct penetration of charged particle and energy from solar wind at higher latitudes; The equatorial station (GUAM) shows significant effect of HILDCAA, which may be related to HILDCAA time effects on equatorial observatories (RASTOGI, 2005); Both low and mid latitudes observatories also show the effect of HILDCAA, indicating the presence of ring currents in these regions. More detail about the geomagnetic storm effects at low latitudes can be found in Rastogi (1999). Like the results obtained from H and ΔH signatures, wavelet scalograms also show different results for different longitudinal observatories.

The results obtained from discrete wavelet transform are mentioned below. Here, we used Daubechies order 2 orthogonal wavelet transform of seven levels ($j= 1, 2, 3, 4, 5, 6, 7$) denoted by $d^1, d^2, d^3, d^4, d^5, d^6$ and d^7 . For the chosen wavelet of frequency 0.66667 and sampling rate of one minute, the pseudo periods of the seven levels were 3, 6, 12, 24, 48, 96, 192 minutes. Figure 5.39, Figure 5.40 and Figure 5.41 show the results of the square wavelet coefficients for the non-storm HILDCAA occurred on 20-23 April 2003. The panels from top to bottom, the ΔH -component and the 7th levels of the square wavelet coefficients are shown. The left and the right sides of Figure 5.39 stand for the observatories GUAM and ABG respectively. Similarly, Figure 5.40 stands for the observatories VSS (left) and KAK (right). Finally, Figure 5.41 stands for the station THL. In each figure, the highest amplitude of the

square wavelet coefficients indicate singularities associated with HILDCAA. The smaller amplitude of the square wavelet coefficients observed during the HILDCAA interval indicates the processes of smooth energy transfer. On the other hand, the large amplitudes indicate the impulsive energy injection inside the magnetosphere. As a previously known fact, the wavelet coefficients have the property that their amplitudes are related to the local regularity of the analyzed data (MALLAT, 1989; DAUBECHIES, 1992). It means that the smaller wavelet coefficients are related to smooth datasets and the larger coefficients are related to disturbed dataset. This is the basic idea of data compression. Based on this idea, we are using the application of this analysis during HILDCAA. In this analysis, the amplitude of square wavelet coefficients is also related to the analyzing wavelet order and the scale level. The main objective of this technique applied to the dataset is to distinguish quiescent from non-quiescent periods. The square wavelet coefficients of the first decomposition level is locally associated with higher frequencies related to HILDCAA. It shows indeed a better time localization. In this case study, the first seven decomposition levels have proved to be sufficient to isolate the singularity patterns associated with HILDCAA. By careful inspection, it can be observed that the geomagnetic observatories do not show a pattern of wavelet coefficients in different decomposition levels. This may be related to several reasons, for example: type of magnetometer used, local time, ground conductivity and Sq current effects. From the present analysis, it is noticed that a station at higher latitude shows singularities and higher amplitudes of square wavelet coefficients more frequently if compared to lower latitudes. This fact may be related to the well known concept that at higher latitudes the penetration of charged particles and the the energy injection are characterized by phenomena that involve high frequency signals. While at lower and mid latitudes coupling processes do exist that attenuate high frequency signals (MORIOKA et al., 2003; MENDES et al., 2005). Similarly, the presence of singularities and higher amplitude of square wavelet coefficients at equatorial stations may be affected by equatorial phenomena known as equatorial electrojet. A more detailed description about the Daubechies order 2 orthogonal wavelet transform can be found in (MENDES et al., 2005; OJEDA et al., 2014; KLAUSNER et al., 2014b).

Figure 5.42 shows the results of wavelet modulus correlation of ΔH -component from GUAM, ABG, VSS, KAK and THL with interplanetary magnetic field (Bz) for the HILDCAA event on 20-23 April 2003. The horizontal axis represents the scale in minutes and the vertical axis represents the modulus correlation. In this figure, the scale of 1, 10, 100 and 1000 are labeled in horizontal axis. The first panel of this figure represents the modulus correlation of IMF-Bz with GUAM. It shows the peak

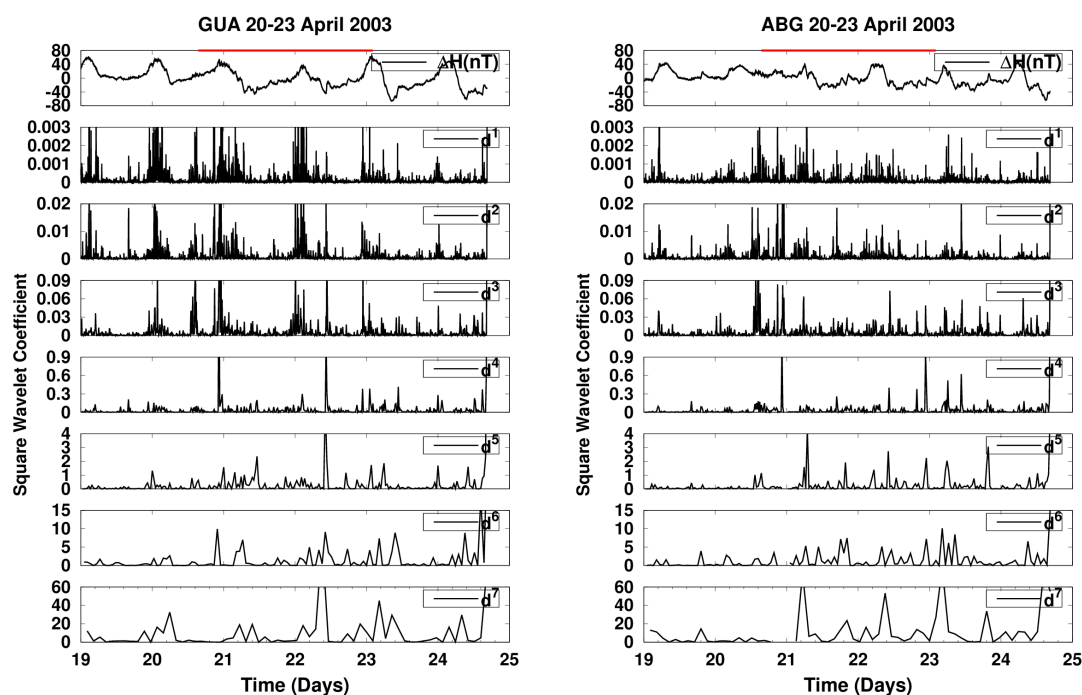


Figure 5.39 - Daubechies Wavelet coefficients d^j (for $j=1,2,3,\dots,7$) for ΔH -component from GUAM (left) and ABG (right) observatories during HILDCAA event occurred on 20-23, April 2003. The red color identifies where the HILDCAA events is happening.

about 0.8 at time scale 300 minutes. Similarly, the second panel represents the modulus correlation of IMF-Bz with ABG. It shows the peak about 0.6 at time scale approximately 200 minutes. Other three panels show the modulus correlation of IMF-Bz with VSS, KAK and THL. They show peak about 0.5, 0.7 and 0.7 at time scales 300, 200 and 325 minutes respectively. When observing these results, we can make the following remarks. The signatures recorded on ΔH -component from all observatories are correlated with IMF-Bz. These results show scale dependent characteristic. The ΔH -component of equatorial station (GUAM), mid latitude station (KAK) and high latitude station (THL) show higher peak modulus correlation as compared to low latitude observatories (ABG and VSS) with IMF-Bz during this event. A more detail description about the wavelet modulus correlation can be found in Klausner et al. (2013).

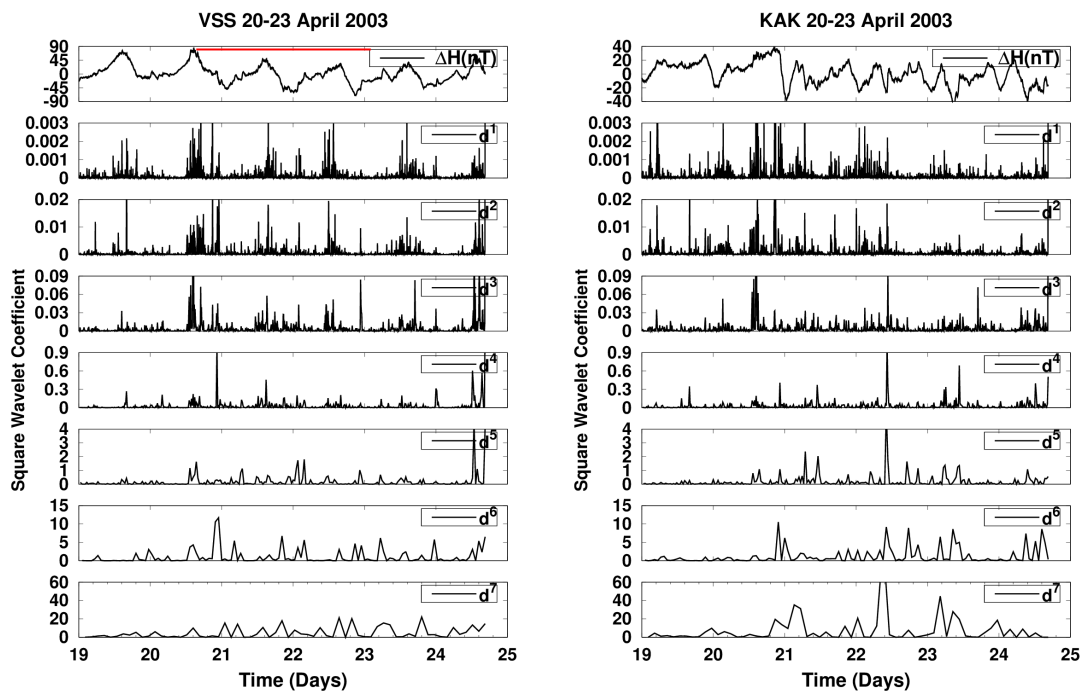


Figure 5.40 - Daubechies Wavelet coefficients d^j (for $j= 1,2,3,\dots,7$) for ΔH -component from VSS (left) and KAK (right) observatories during HILDCAA event occurred on 20-23, April 2003. The red color identifies where the HILDCAA events are happening.

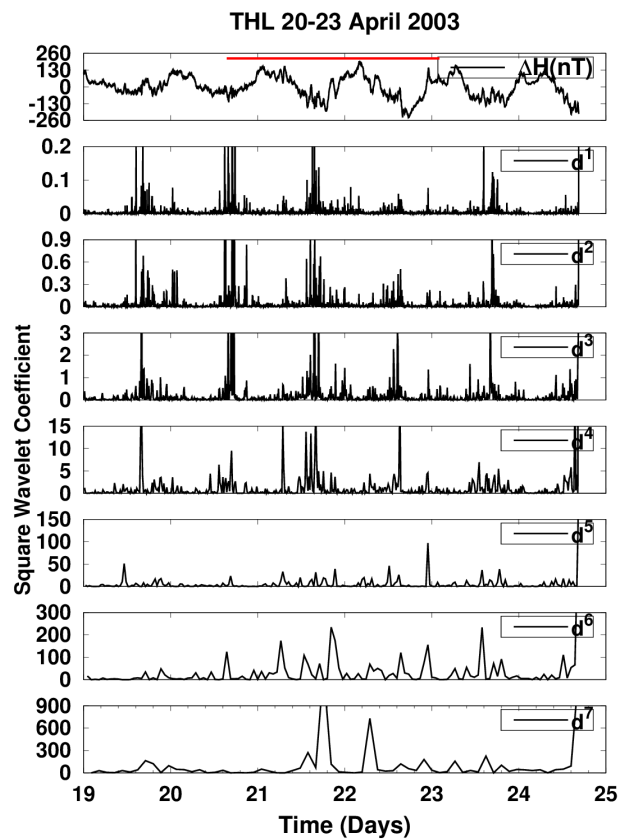


Figure 5.41 - Daubechies Wavelet coefficients d^j (for $j=1,2,3,\dots,7$) for ΔH -component from THL observatory during HILDCAA event occurred on 20-23, April 2003. The red color identifies where the HILDCAA events are happening.

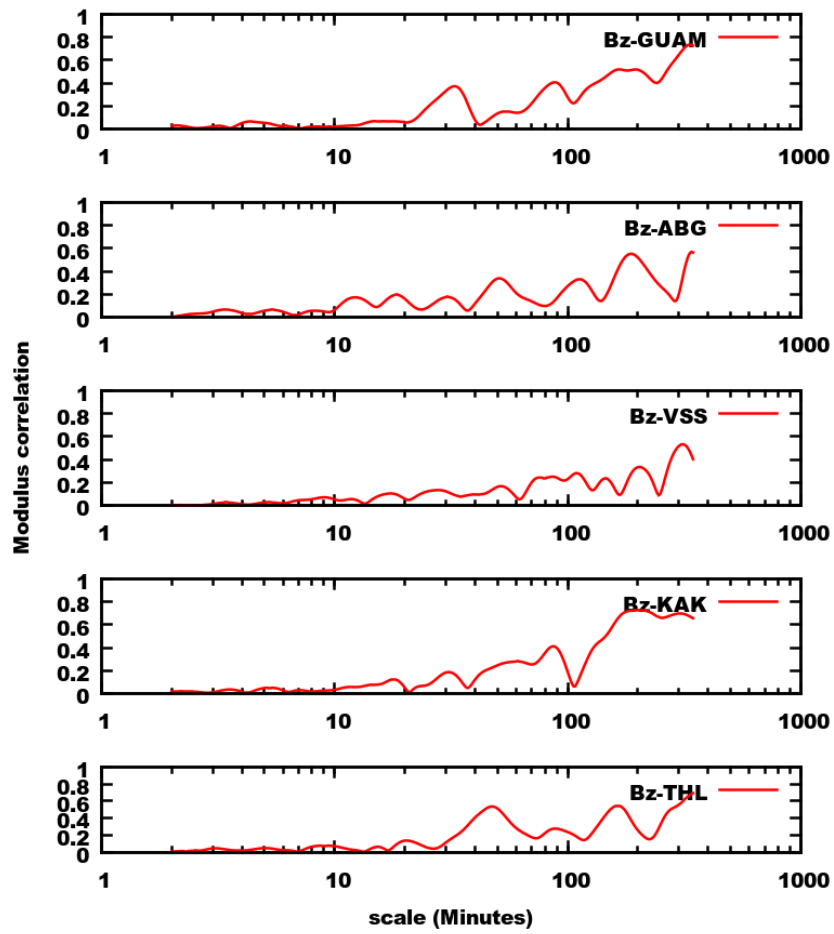


Figure 5.42 - From top to bottom, the panels represent the correlation of IMF-Bz with ΔH -component from geomagnetic observatories GUAM, ABG, VSS, KAK and THULE during the HILDCAA event on 20-23 April 2003.

Case 2: HILDCAA preceded by CIR-storm which occurred on 12-15 February 2004

Figure 5.43 shows the geomagnetic signatures of H-component obtained from GUAM, ABG, VSS, KAK and THL for the HILDCAA preceded by the CIR-storm which occurred on 12-15 February 2004. Where the green lines represent the quietest period and the black lines represent the disturbed period. The panels representation and labeling are similar to Figure 5.35. The quietest day signatures for this event are also similar to previous event for all observatories. However, the disturbed days signatures are different. It is an event preceded by CIR-storm in which the initial phase starts late on 11 February 2004, the main phase starts around midnight of 11 February 2004 and the long recovery phase (the HILDCAA event) lasts from the beginning of 12 February 2004 to midday of 15 February 2004. During the main phase of the storm, all the observatories show strong depression on H-component. The SYM-H index shows depression around -115 nT, ASY-H index shows the peak vale about 160 nT and AE index shows the peak about 1600 nT. At the time of HILDCAA, they show strong fluctuations on H-component. The levels of fluctuations for this event are totally different from that of a previous event. However, the nature of HILDCAA time fluctuations for GUAM, ABG and VSS show some similarity. Except for THL, other observatories show fluctuations below the quietest day graph. But, THL shows higher level of east-west perturbations. The SYM-H index shows approximately constant negative value and other two indices (ASY-H and AE) show intense activity.

Figure 5.44 shows the ΔH signatures and geomagnetic indices for the same event. The panels from top to bottom are similar to Figure 5.36. It is obtained by subtracting each disturbed day with the average quietest day of this month. In this figure, the horizontal straight line shows the base line. During the main phase, all the observatories show strong depression on ΔH -component. The levels of depression for GUAM, ABG, VSS, KAK and THL were approximately -100 nT, -180 nT, -150 nT, -100 nT and -200 nT respectively. At the time of HILDCAA, except THL, other observatories show fluctuations below zero. Whereas THL shows east-west fluctuations between 100 nT to -100 nT. Like previous event, here we also used same wavelet techniques in order to get some common features between these signatures.

Figure 5.45 represents the scalograms for ΔH -component from (a) GUA (b) ABG (c) VSS and (d) KAK during HILDCAA event on 12-15 February 2004. The scalogram for GUAM (a) shows the highest intensities at time scales between 200-300 minutes.

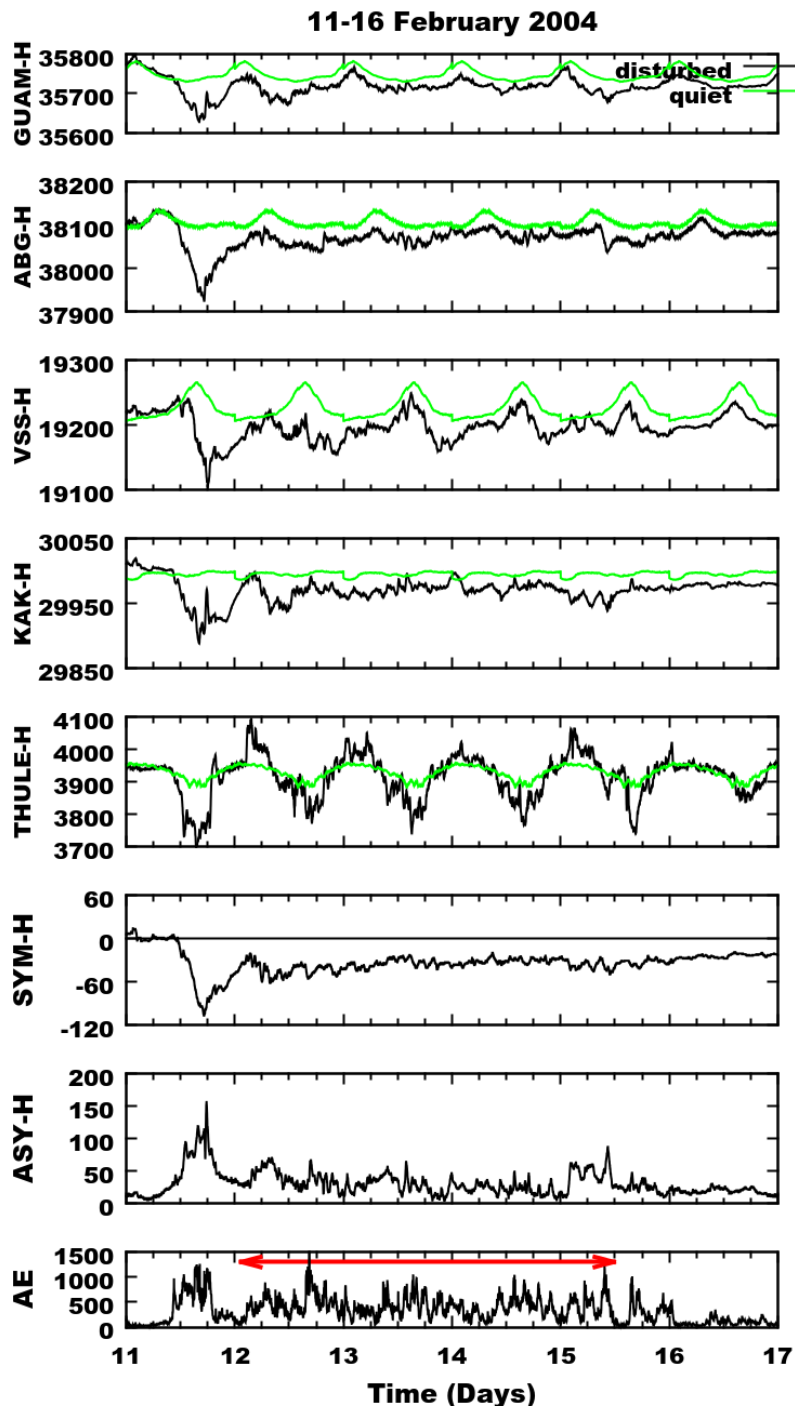


Figure 5.43 - From top to bottom, the panels show variations of H-component (nT) at the observatories GUAM, ABG, VSS, KAK, THL along with the geomagnetic indices SYM-H (nT), ASY-H (nT) and AE (nT) respectively during the HILDCAA event on 12-15 February 2004. The green line represents the average quietest day variation, the black line represents the disturbed day variation and the red horizontal arrow in AE panel indicates the HILDCAA interval.

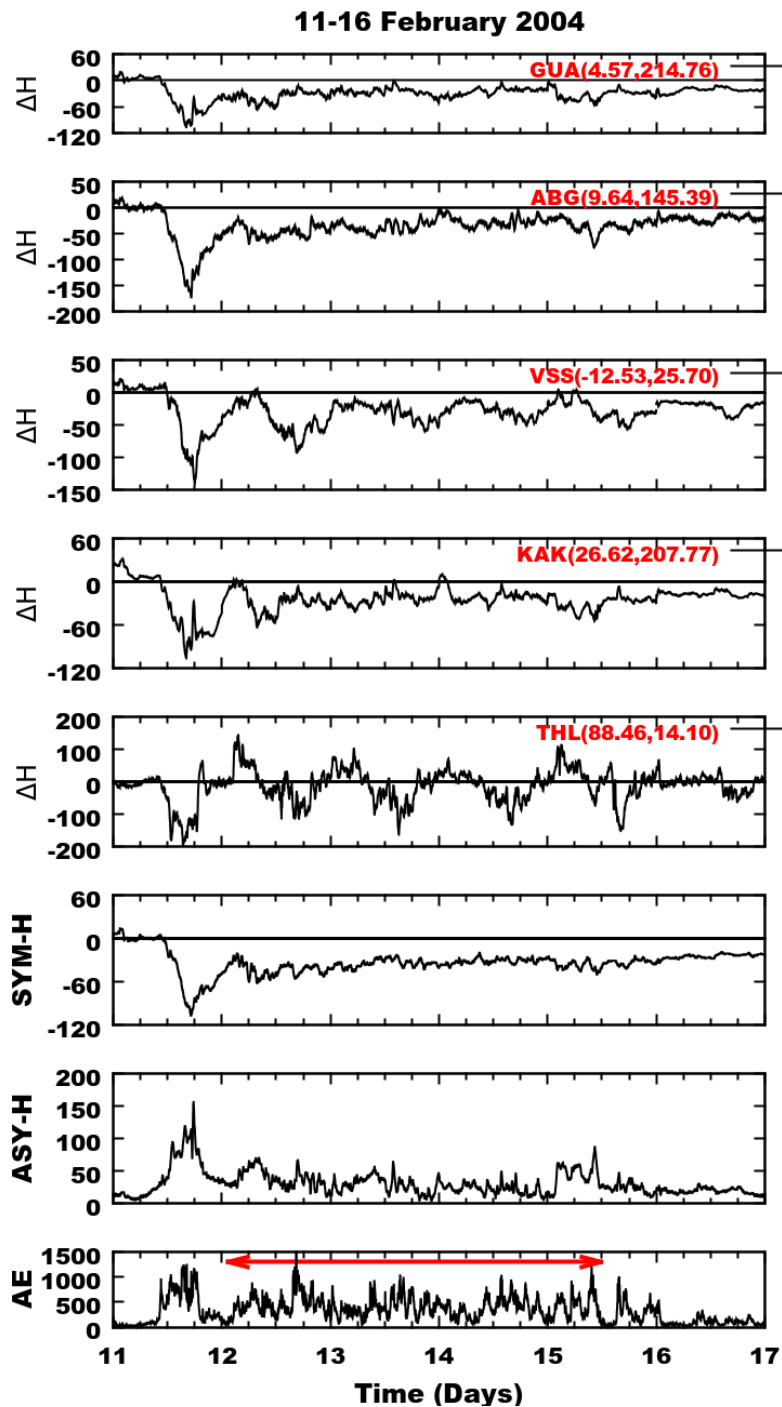


Figure 5.44 - From top to bottom, the panels represent the variation of ΔH signatures from GUAM, ABG, VSS, KAK, THL and geomagnetic indices SYM-H (nT), ASY-H (nT) and AE (nT) during HILDCAA event during 12-15 February 2004. The red horizontal arrow in AE panel represents the HILDCAA interval.

But the power areas of lesser intensities (yellow and green colors) are seen at time scales between 100-300 minutes. Similarly, Figure 5.45 (b) shows the scalogram for ABG. It also shows the highest intensities at time scales between 100-300 minutes. Other less intense wavelet powers are seen at time scales approximately between 80-300 minutes. Figure 5.45 (c) and (d) show the scalograms for VSS and KAK. In these two observatories, the power areas of the highest intensity (red color) are seen at time scale between 150-300 minutes. The power areas covered by yellow and green color of lesser intensities are seen at different time scales. All the observatories show highly scattered wavelet powers. Finally, Figure 5.3 represents the scalogram for THL. It shows wavelet power areas of strong intensity of 6 nT at time scale between 250-300 minutes. The other power areas represented by yellow and green colors are seen at time scale between 150-250 minutes. Like the previous event, this event also shows wavelet powers of different intensities on both medium and higher time scales.

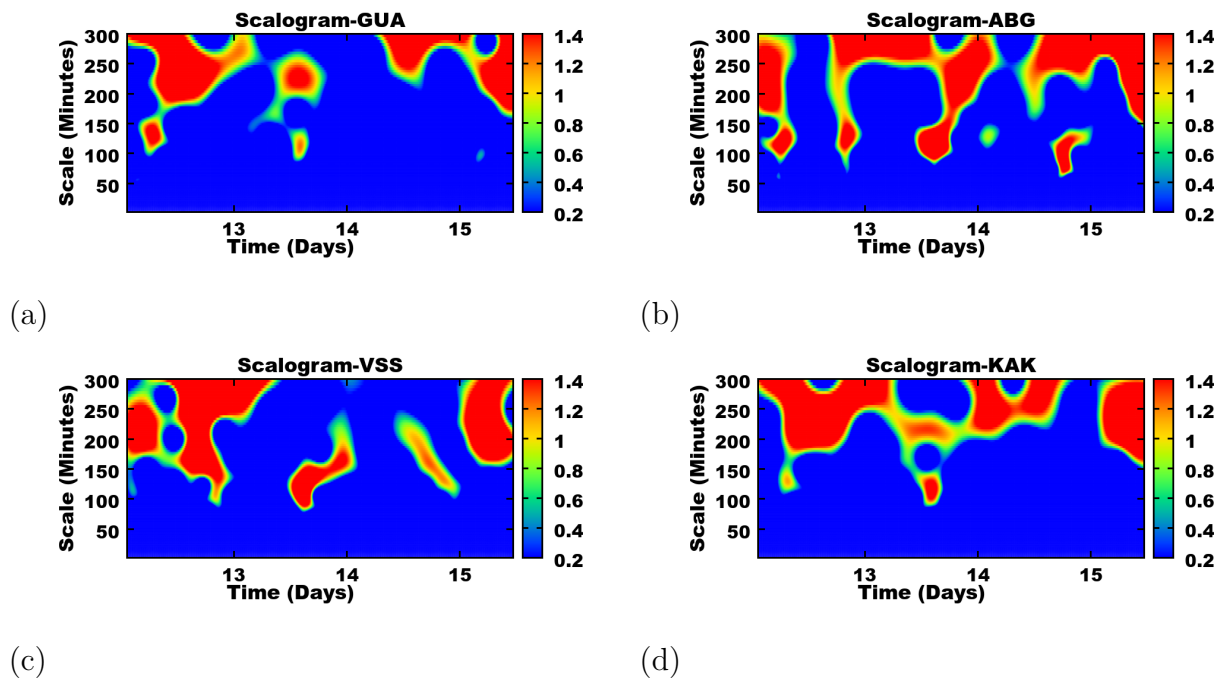


Figure 5.45 - Scalograms for ΔH -component from (a) GUA (b) ABG (c) VSS and (d) KAK during HILDCAA event on 12-15 February 2004.

Figure 5.47, Figure 5.48 and Figure 5.49 are similar to Figure 5.39, Figure 5.40 and Figure 5.41 respectively but refer to HILDCAA preceded by a CIR-storm which occurred on 12-15 February 2004. Like previous event, the singularities pattern,

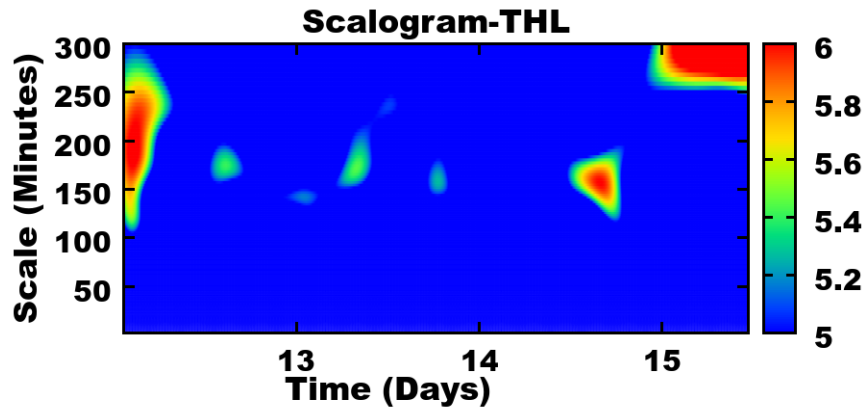


Figure 5.46 - Scalogram for ΔH -component from THL observatory during HILDCAA event on 12-15 February 2004.

larger and smaller amplitude of square wavelet coefficients can be observed for all observatories.

Figure 5.50 represents the wavelet modulus correlation of ΔH -component with IMF-Bz for the event on 12-15 February 2004. The first panel of this figure shows the peak modulus correlation about 0.6 at time scale 70 minutes for IMF-Bz with GUAM. Similarly, the second and the third panels show the peaks modulus correlation about 0.6 and 0.65 at time scales approximately 250 and 200 minutes for IMF-Bz with ABG and VSS respectively. Finally, the fourth and the fifth panels show the peaks correlation about 0.7 and 0.55 at time scales approximately 290 and 200 minutes for IMF-Bz with KAK and THL respectively. These results show that each station has different modulus correlation with IMF-Bz at the time of HILDCAA. Like previous event, this event also shows correlation of IMF-Bz with ΔH -component and also shows scale dependent characteristic.

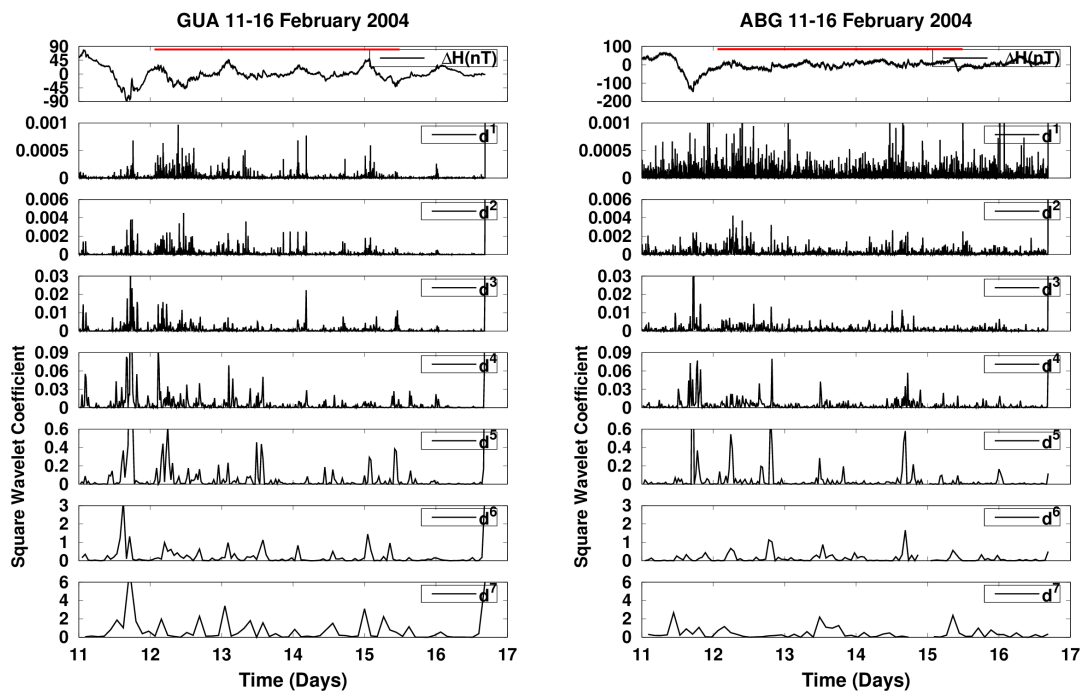


Figure 5.47 - Daubechies Wavelet coefficients d^j (for $j= 1,2,3,\dots,7$) for ΔH -component from GUAM (left) and ABG (right) observatories during HILDCAA event occurred on 12-15 February 2004. The red color identifies where the HILDCAA events is happening.

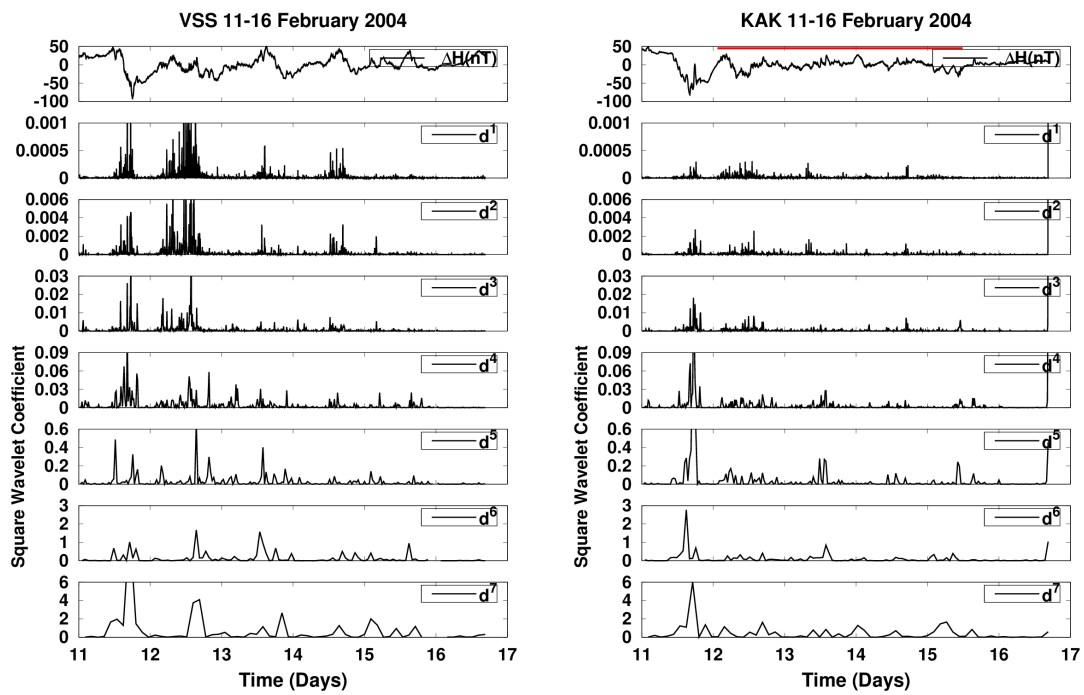


Figure 5.48 - Daubechies Wavelet coefficients d^j (for $j= 1,2,3,\dots,7$) for ΔH -component from VSS (left) and KAK (right) observatories during HILDCAA event occurred on 12-15 February 2004. The red color identifies where the HILDCAA events are happening.

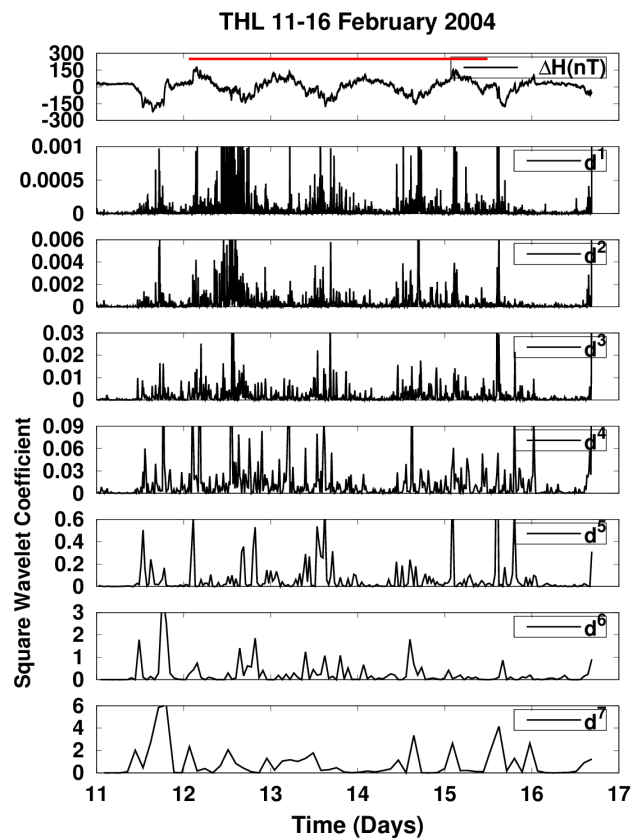


Figure 5.49 - Daubechies Wavelet coefficients d^j (for $j= 1,2,3,\dots,7$) for ΔH -component from THL observatory during HILDCAA event occurred on 12-15 February 2004. The red color identifies where the HILDCAA events are happening.

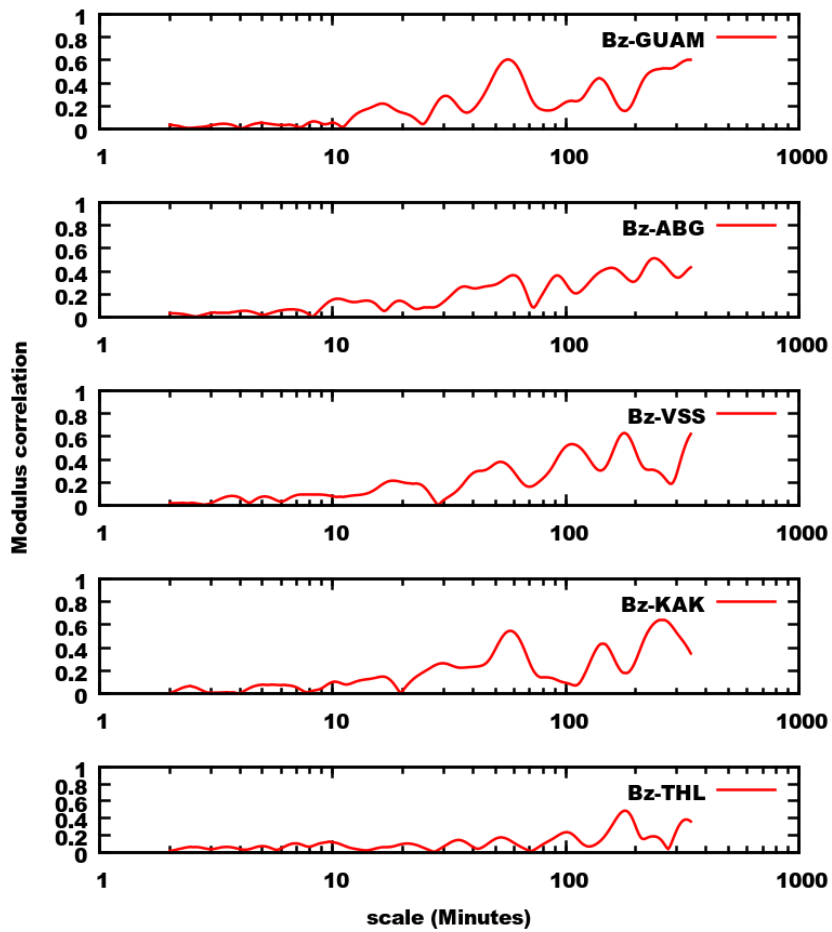


Figure 5.50 - From top to bottom, the panels represent the correlation of IMF-Bz with H component from geomagnetic observatories GUAM, ABG, VSS, KAK and THULE during the HILDCAA event on 12-15 February 2004.

Case 3: An ICME preceding HILDCAA which occurred on 15-18 May 2005

Figure 5.51 represents the geomagnetic signatures and geomagnetic indices for an ICME preceding HILDCAA which occurred on 15-18 May 2005. The panels representation are similar to Figure 5.35 and Figure 5.43. The interplanetary cause for this storm was the shock driven by an ICME contained a magnetic cloud structure (HAJRA et al., 2013; OJEDA et al., 2013; OJEDA et al., 2014) characterized by large southward IMF-Bz with a peak of $-50nT$. In the figure, the green lines indicate the quietest day graph for the month May 2005. It shows almost a similar behavior to two previous events for all observatories. The black lines indicate one day before and one day after the HILDCAA interval. In this line, three different phases (initial, main and recovery) of geomagnetic storm can be easily seen. The initial phase was marked by an abrupt increase in horizontal component of geomagnetic field (for all observatories) and a positive jump in SYM-H index of approximately 30 nT. It is caused by an increased solar wind dynamic pressure acting on the magnetosphere. The increased pressure compresses the dayside magnetosphere, forces the magnetopause current closer to the Earth, and at the same time increases it. The main phase was marked by strong depression in H-component for all observatories (except THL) and negative jump in SYM-H index approximately -300 nT. During this phase, ASY-H and AE indices show peak value of about 275 nT and 2000 nT respectively. The HILDCAA time (long recovery phase) lasts from midday of 15 May to midday of 18 May, about 3 days. During this phase, the differences between the quietest day and disturbed days curves show very big separation. These separations are different from one station to another.

In Figure 5.52, we depict the ΔH signatures and geomagnetic indices for the same event. The panels representation are similar to Figure 5.36 and Figure 5.44. The features of ΔH signatures are similar to H signatures. In this figure, during the main phase period, GUAM, ABG, VSS and KAK show strong depression about $-390 nT$, $-300 nT$, $-200 nT$, and $-300 nT$ respectively. But the signatures recorded on THL show totally different features if compared to other observatories. It shows very strong initial phases with positive jump about $600 nT$. During the main phase, it shows very weak depression. However, after 12 hours of main phase, it shows depression of about $-450 nT$. At the time of HILDCAA, except THL, all other observatories show fluctuations approximately between $-150 nT$ to $-30 nT$. On the other hand, THL shows periodically east-west perturbations approximately between $200 nT$ to $-200 nT$.

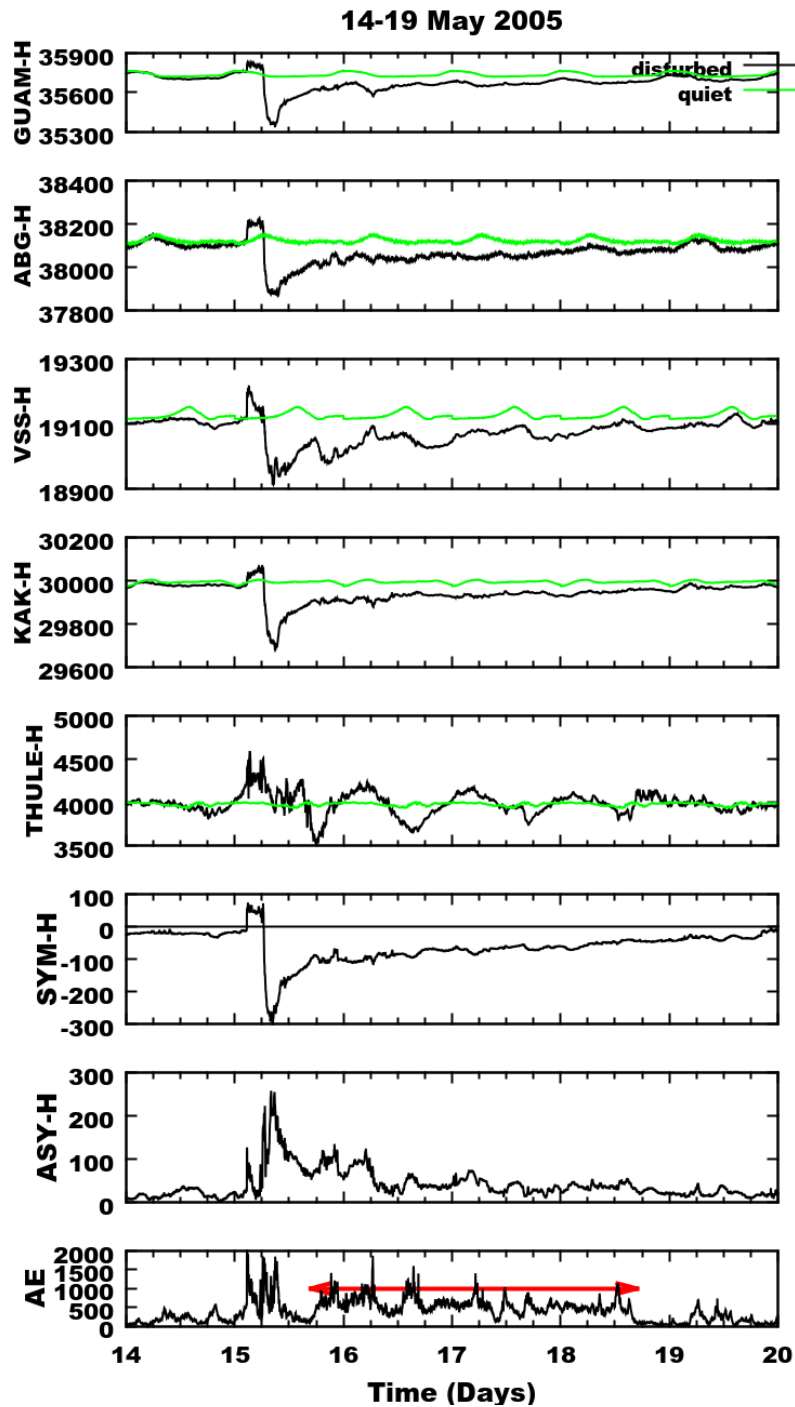


Figure 5.51 - From top to bottom, the panels show variations of H-component (nT) at the observatories GUAM, ABG, VSS, KAK, THL along with the geomagnetic indices SYM-H (nT), ASY-H (nT) and AE (nT) respectively during the HILDCAA event on 15-18 May 2005. The green line represents the average quietest day variation, the black line represents the disturbed day variation and the red horizontal arrow in AE panel indicates the HILDCAA interval.

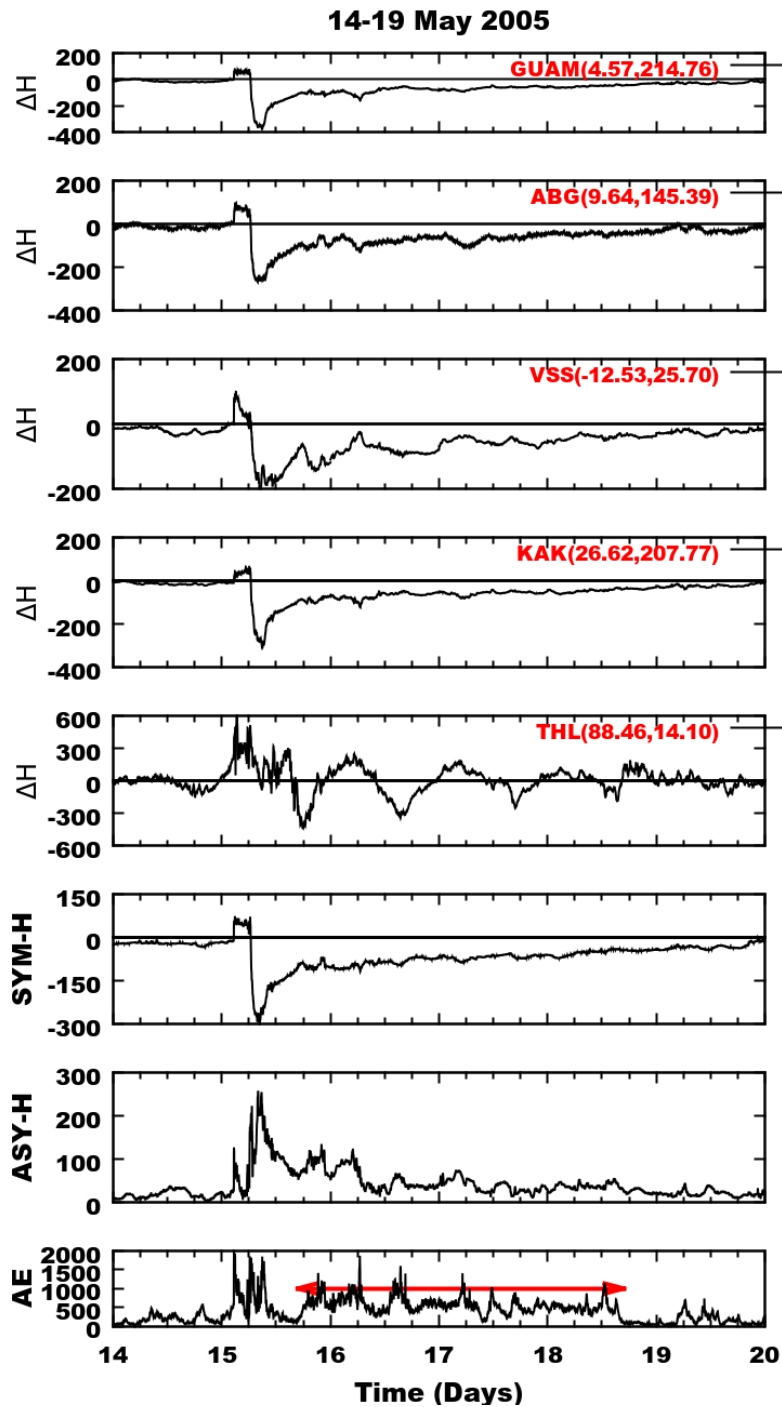


Figure 5.52 - From top to bottom, the panels represent the variation of ΔH signatures from GUAM, ABG, VSS, KAK, THL and geomagnetic indices SYM-H (nT), ASY-H (nT) and AE (nT) during HILDCAA event during 15-18 May 2005. The red horizontal arrow in AE panel represents the HILDCAA interval.

Figure 5.53 and Figure 5.54 depict the scalograms of ΔH -component from GUA, ABG, VSS, KAK and THL for the same event. In these figures, all the observatories show wavelet power areas of higher intensity at time scales approximately between 100-300 minutes. Like previous events, THL shows wavelet power of higher intensity which may be related to direct penetration of charged particle and energy from solar wind at higher latitudes.

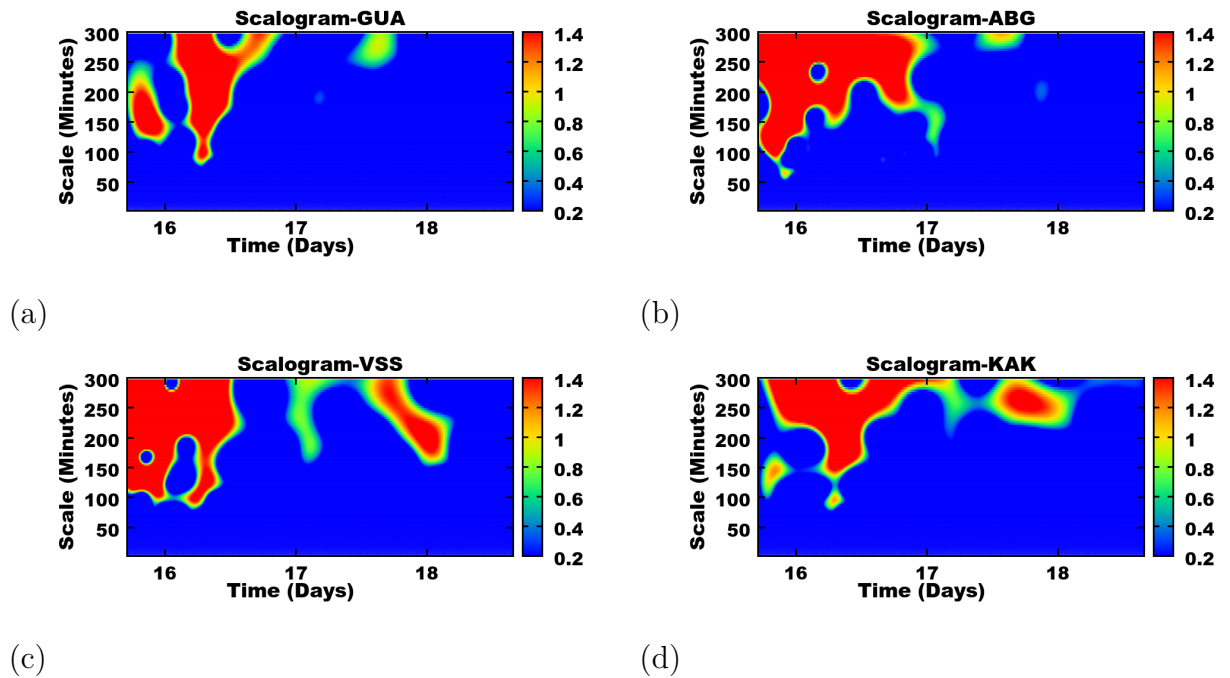


Figure 5.53 - Scalograms for ΔH -component from (a) GUA (b) ABG (c) VSS and (d) KAK during HILDCAA event on 15-18 May 2005.

Figure 5.55, Figure 5.56 and Figure 5.57 are similar to Figure 5.39, Figure 5.40 and Figure 5.41 or Figure 5.47, Figure 5.48 and Figure 5.49 but refer to HILDCAA preceded by ICME-storm which occurred on 15-18 May 2005. Like other two events, the singularities pattern and larger and smaller amplitude of square wavelet coefficients are seen for all observatories. In these figures, the singularities patterns indicate the discontinuities associated with shocks. Whereas the larger and smaller amplitude of square wavelet coefficients indicate the disturbed and quiet conditions of the magnetosphere.

Figure 5.58 gives the results obtained from wavelet modulus correlation of ΔH -component with IMF-Bz during the same event (only for HILDCAA interval).

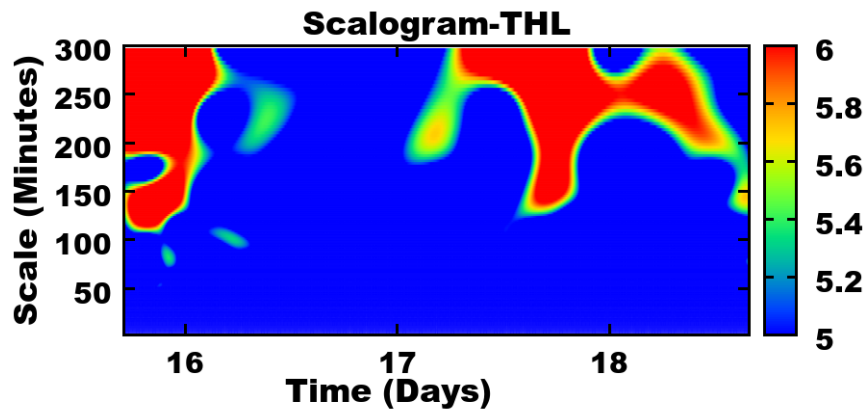


Figure 5.54 - Scalogram for ΔH -component from THL observatory during HILDCAA event on 15-18 May 2005.

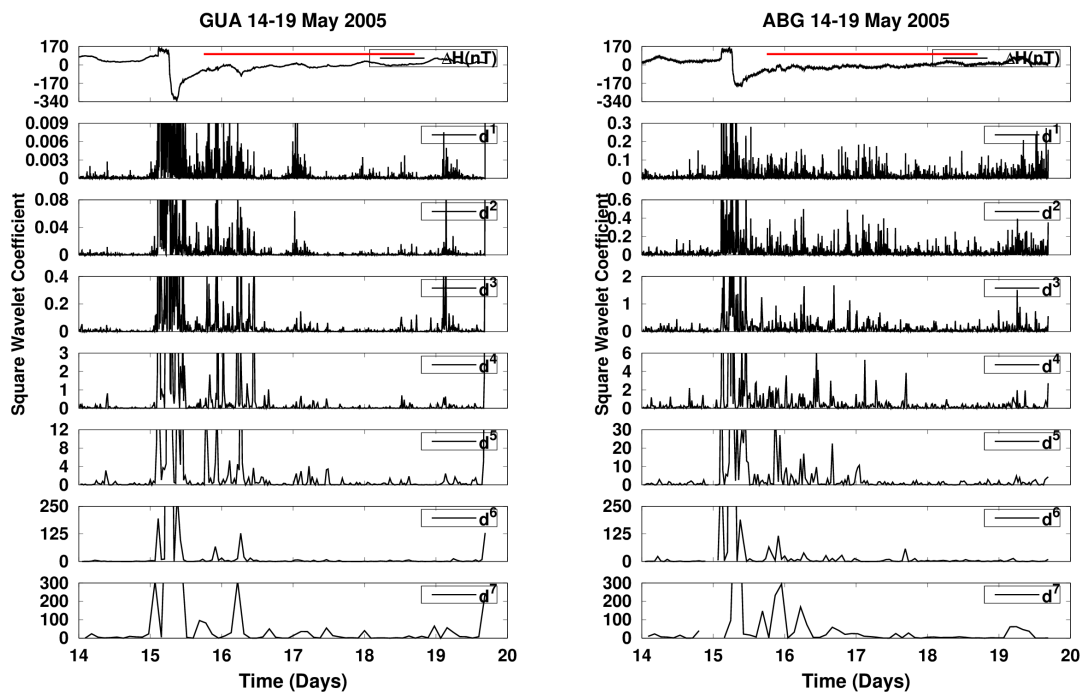


Figure 5.55 - Daubechies Wavelet coefficients d^j (for $j= 1,2,3,\dots,7$) for ΔH -component from GUAM (left) and ABG (right) observatories during HILDCAA event occurred on 15-18 May 2005. The red color identifies where the HILDCAA events is happening.

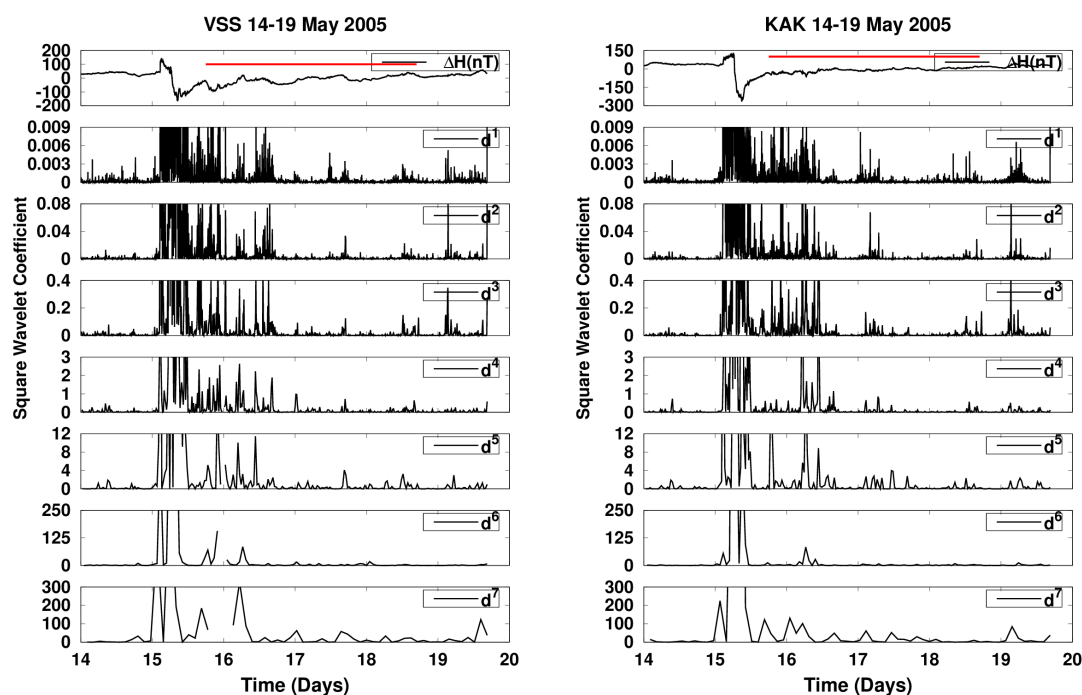


Figure 5.56 - Daubechies Wavelet coefficients d^j (for $j= 1,2,3,\dots,7$) for ΔH -component from VSS (left) and KAK (right) observatories during HILDCAA event occurred on 15-18 May 2005. The red color identifies where the HILDCAA events is happening.

Like the other two events, this event also shows correlation of IMF-Bz with ΔH -component of geomagnetic field from GUAM, ABG, VSS, KAK and THL during HILDCAA interval. However, each station shows a different peak correlation at different time scales. It means that this event also shows scale dependent characteristic.

Case 4: quiet periods 18-21 July, 2006

Figure 5.59 represents the geomagnetic signatures and geomagnetic indices for quiet periods from 18 to 21 July, 2006. The panels representation are similar to Figure 5.35, Figure 5.43 and Figure 5.51. In this figure, the quiet days values are plotted against universal time. The local time and universal time differences for GUAM, ABG, VSS, KAK and THL are +10, +5.30, -3, +9 and -4 hours respectively. When observing these differences, the quiet days variations for equatorial and low latitudes observatories (GUAM, ABG and VSS) show maximum at mid day and minimum at dusk time (GONCHAROVA, 2004; RASTOGI, 2005; BOLAJI et al., 2013). Other two observatories show small scale fluctuations on quiet days curves. The nature of quiet days

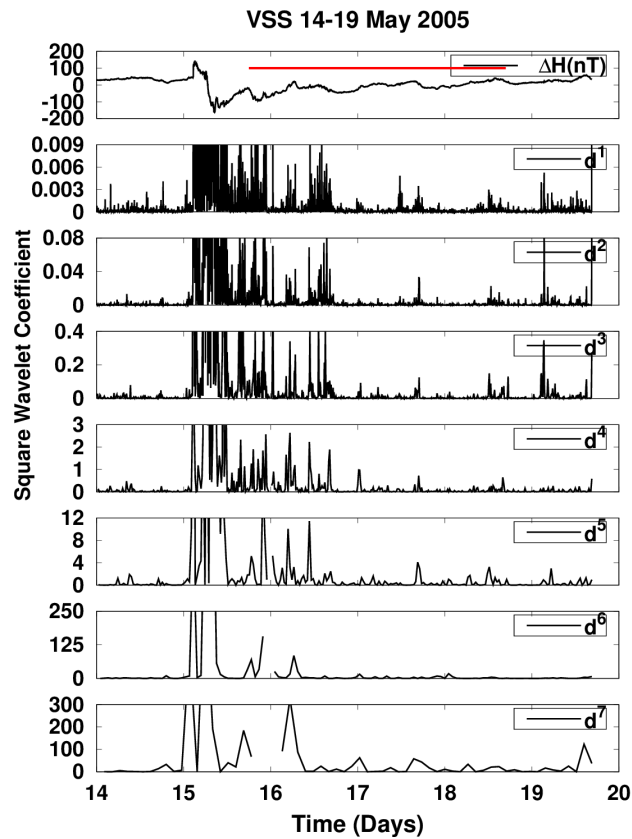


Figure 5.57 - Daubechies Wavelet coefficients d^j (for $j= 1,2,3,\dots,7$) for ΔH -component from THL observatory during HILDCAA event occurred on 15-18 May 2005. The red color identifies where the HILDCAA events is happening.

variations observe in Figure 5.59 will be summarized as:

- a) Latitudinal positions of the observatories affect the quiet days curves.
- b) The enhanced geomagnetic field variation at equatorial station (GUAM) may be related to the equatorial electrojet.
- c) At low latitudes, the quiet days variations exhibit maximum at midday and minimum at dusk time.
- d) The small scale fluctuations on quiet days curves at mid and high latitudes are from sources other than ionosphere, for example magnetosphere, polar cap etc.

Figure 5.60 and Figure 5.61 depict the the scalograms of ΔH -component from GUAM, ABG, VSS, KAK and THL during quiet periods from 18 to 21 July, 2006.

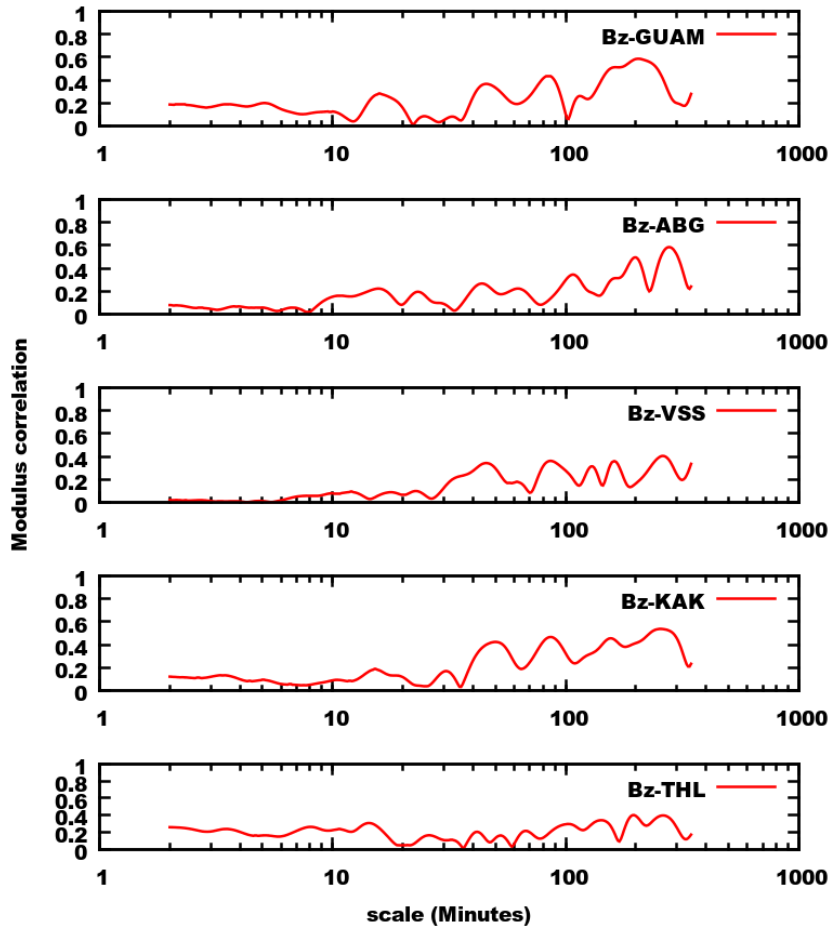


Figure 5.58 - From top to bottom, the panels represent the correlation of IMF-Bz with ΔH -component from geomagnetic observatories GUAM, ABG, VSS, KAK and THULE during the HILDCAA event on 15-18 May 2005.

In these figures, all the observatories show wavelet powers of different intensities at time scale between 150-300 minutes. These wavelet powers may be related to diurnal variation (KLAUSNER et al., 2013). As we know, the nature of average quietest day signatures for equatorial and low latitudes observatories show maximum at midday and minimum at dusk time. These quiet days signatures depend on the phase of the sunspot cycle, seasons, movement of the solar quiet foci, atmospheric tide and longitude. They are generated by two large vortices of electric currents in the day-side ionosphere. At high latitudes, the scatter wavelet powers of relatively higher intensities are seen at medium and higher time scales. These higher intensities at higher latitude may be related to the sources other than ionosphere, for example magnetosphere, polar cap etc. However, all observatories show wavelet power areas of lesser amplitudes as compared to above three HILDCAA events.

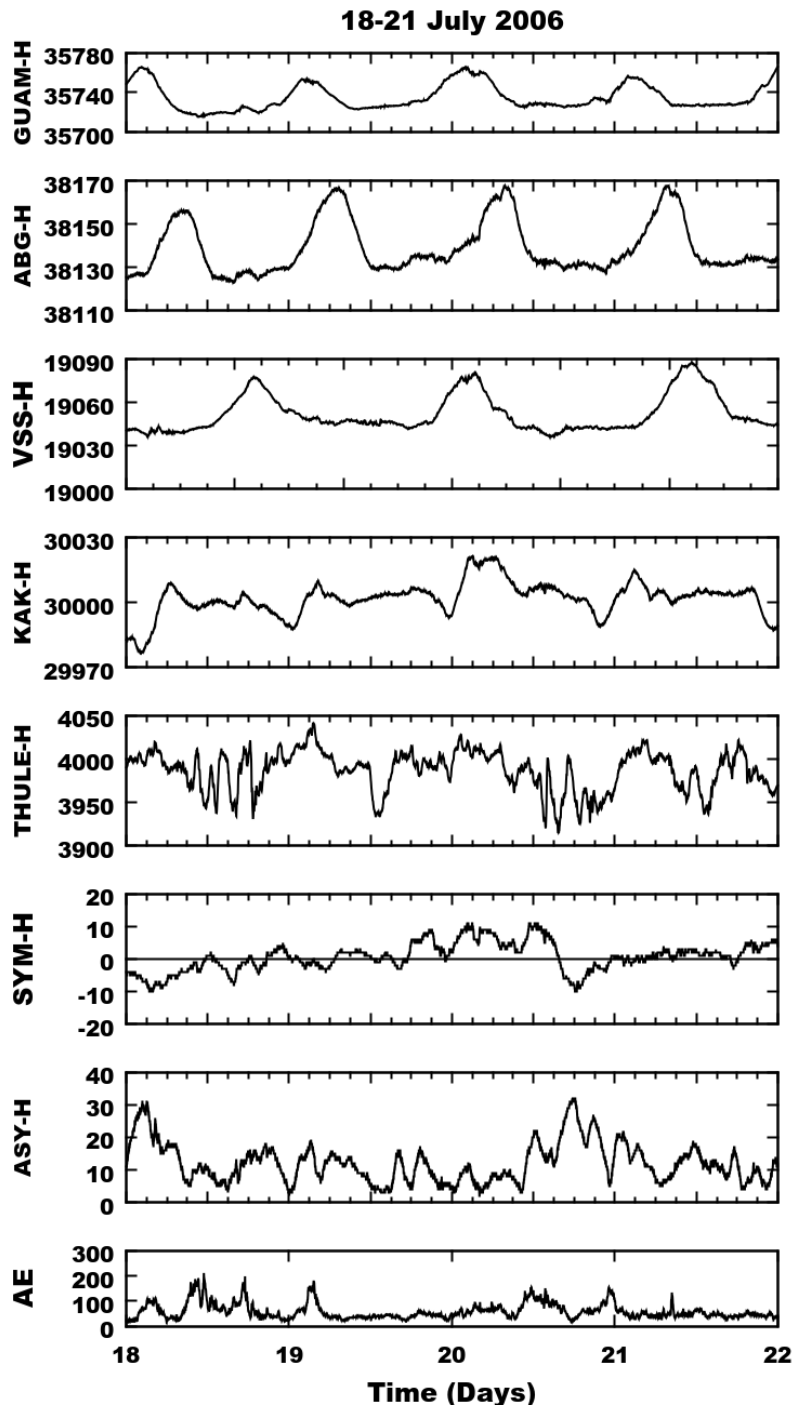


Figure 5.59 - From top to bottom, the panels show variations of H-component (nT) at the observatories GUAM, ABG, VSS, KAK, THL along with the geomagnetic indices SYM-H (nT), ASY-H (nT) and AE (nT) respectively during quiet periods from 18 to 21 July, 2006.

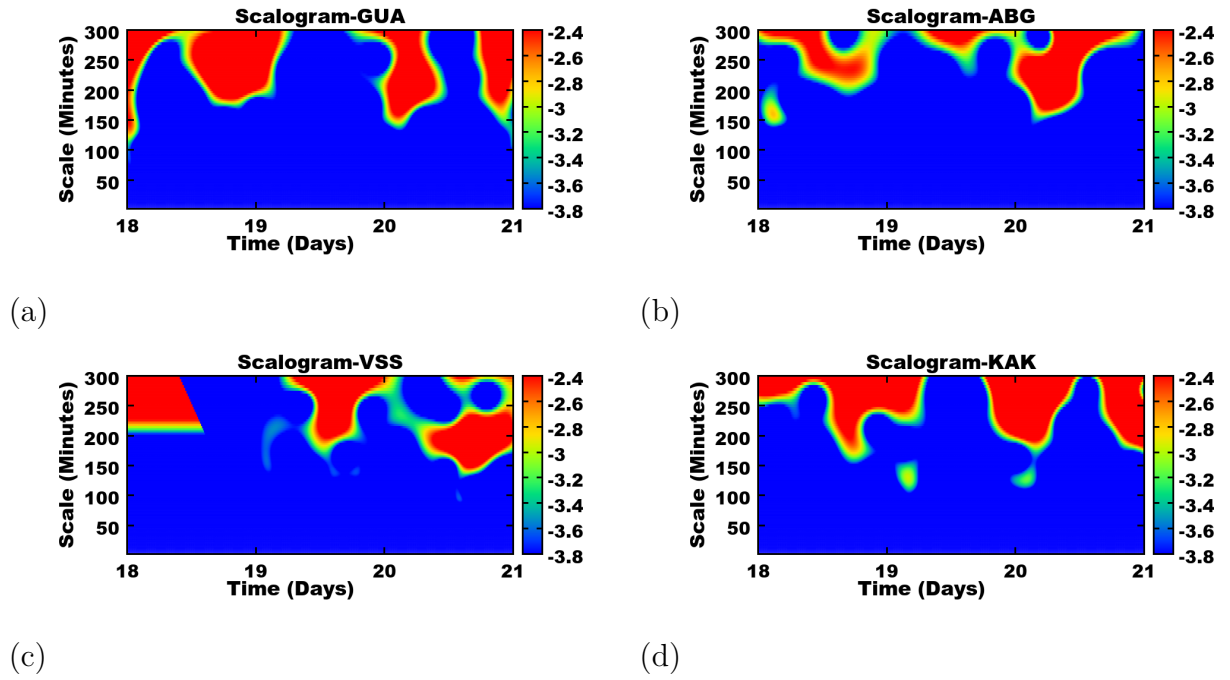


Figure 5.60 - Scalograms for ΔH -component from (a) GUA (b) ABG (c) VSS and (d) KAK during quiet periods from 18 to 21 July, 2006.

Figure 5.62, Figure 5.63 and Figure 5.64 represent the DWT results for ΔH -component from GUAM, ABG, VSS, KAK and THL during quiet periods from 18 to 21 July, 2006. In these figures, all observatories show both smaller and larger square wavelet coefficients. At equatorial and low latitudes stations, these coefficients may be related to ionospheric equatorial electrojet. On the other hand, at mid and high latitudes, these coefficients may be related to sources other than the ionosphere, for example the magnetosphere, polar cap etc. However, the amplitude of square wavelet coefficients are smaller when compared to HILDCAAs events.

Figure 5.65 gives the results obtained from wavelet modulus correlation of ΔH -component with IMF-Bz during quiet periods from 18 to 21 July, 2006. In the figure, all the observatories show correlation of IMF-Bz with ΔH -component of geomagnetic field. However, each station shows different peak correlations at different time scales.

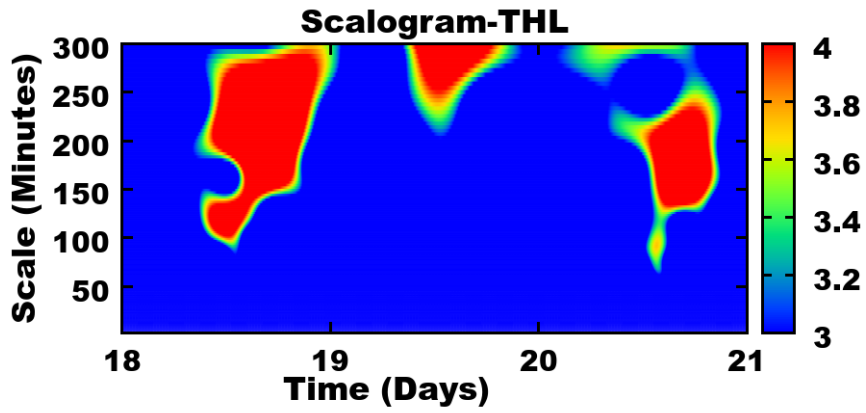


Figure 5.61 - Scalogram for ΔH -component from THL observatory during quiet periods from 18 to 21 July, 2006.

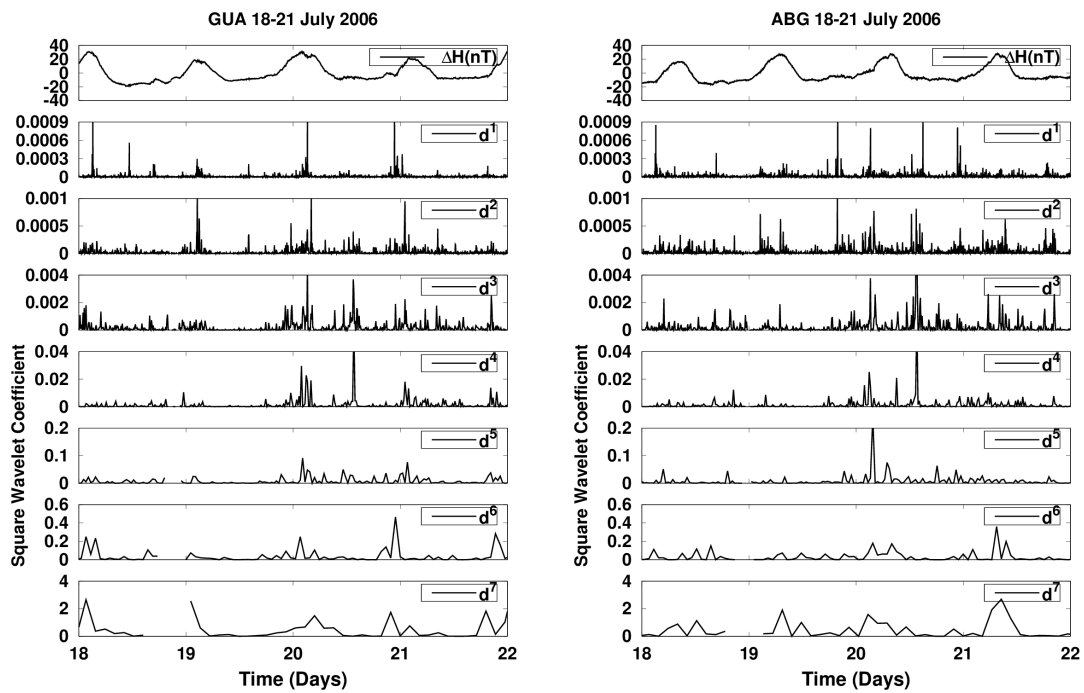


Figure 5.62 - Daubechies Wavelet coefficients d^j (for $j= 1,2,3,\dots,7$) for ΔH -component from GUAM (left) and ABG (right) observatories during quiet periods from 18 to 21 July, 2006.

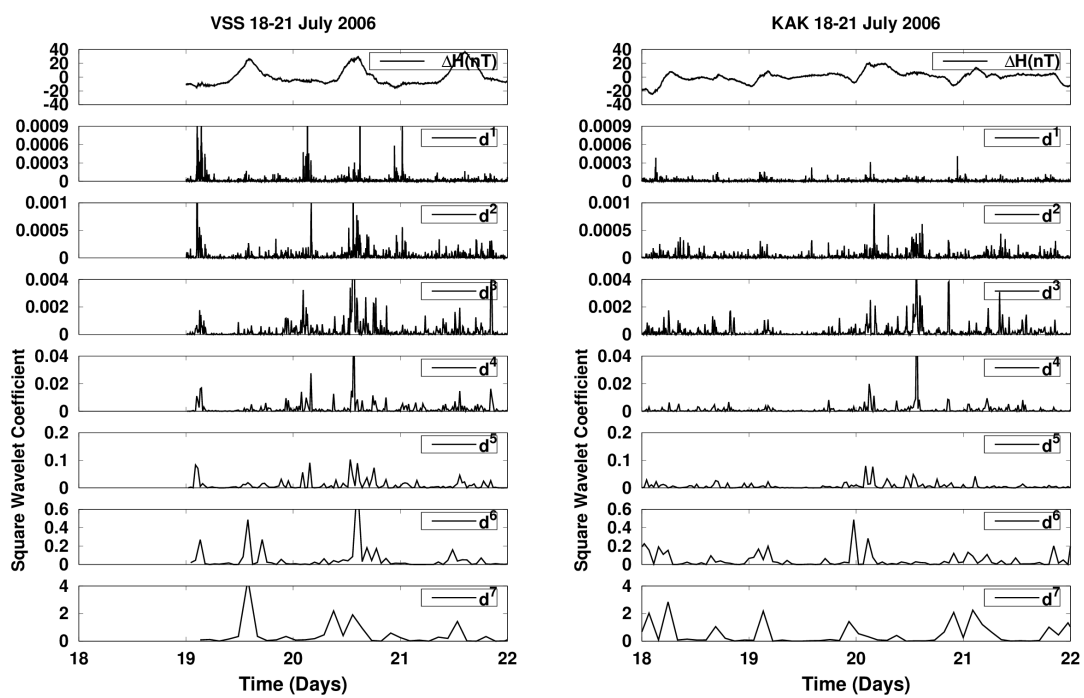


Figure 5.63 - Daubechies Wavelet coefficients d^j (for $j= 1,2,3,\dots,7$) for ΔH -component from VSS (left) and KAK (right) observatories during quiet periods from 18 to 21 July, 2006.

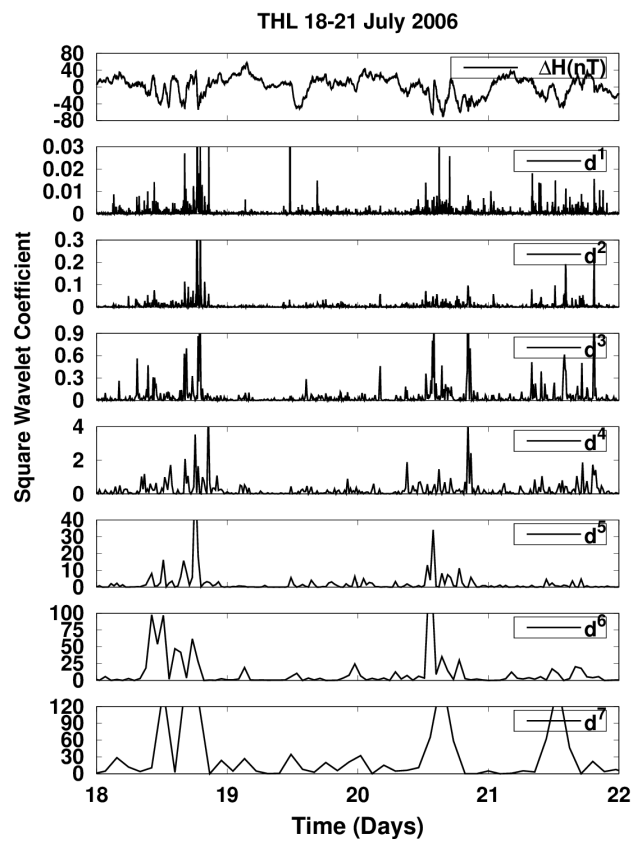


Figure 5.64 - Daubechies Wavelet coefficients d^j (for $j= 1,2,3,\dots,7$) for ΔH -component from THL observatory during quiet periods from 18 to 21 July, 2006.

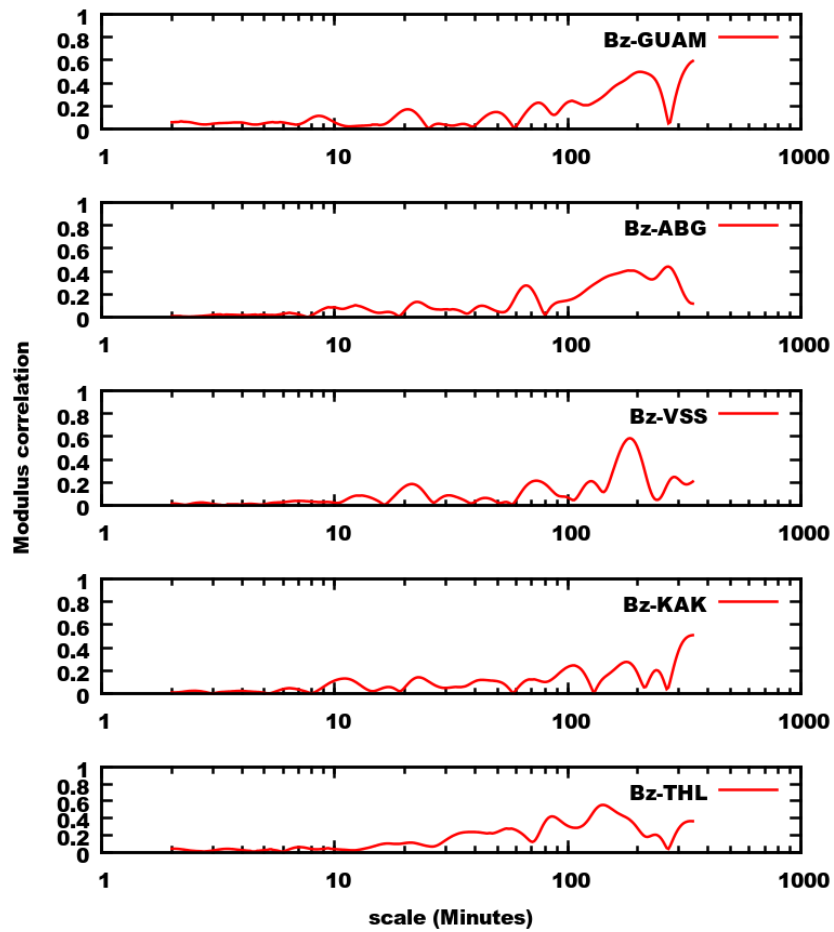


Figure 5.65 - From top to bottom, the panels represent the correlation of IMF-Bz with H component from geomagnetic observatories GUAM, ABG, VSS, KAK and THULE during quiet periods from 18 to 21 July, 2006.

Partial conclusions

Different interplanetary structures produced by the Sun have an important role for the generation of geomagnetic disturbances. HILDCAA events are among them. They are caused by magnetic reconnection with the southward component of the interplanetary Alfvén waves present in solar interplanetary structures. During the events, auroral expansion phases are present and the AE index shows an intense and continuous activity. During HILDCAAs, as we know, a large number of charged particles and energies are injected into the magnetosphere and ionosphere (KAMIDE et al., 1998). Also, the current systems existing inside magnetosphere and ionosphere will be widened and intensified (JANKOVICOVA et al., 2002). In this work, we have examined the geomagnetic signatures recorded on H and ΔH -component of geomagnetic field at different longitudinal observatories during three different HILDCAA events (20-23 April 2003, 12-15 February 2004 and 15-18 May 2005). Then, we examined signatures existing in interplanetary parameters and geomagnetic records with the help of signal analysis techniques in order to get some common features. The results obtained from analyses developed here can be shortly presented as follows:

The high latitude station, THL shows very strong wavelet power areas for both medium and higher time scales. This is expected due to its high latitude. The equatorial station (GUAM) also shows wavelet power areas at both medium and higher time scales. Both low and mid latitudes observatories (ABG, VSS and KAK) show scattered power areas for both medium and higher time scales. The results obtained from CWT show that the effects of HILDCAAs were more intense at higher latitude as compared to lower latitudes. It may be related to direct penetration of charged particle and energy from the solar wind. During the events, it is seen that the wavelet power of high time scales are highly enhanced due to the passage of interplanetary shock. It may be related to the transfer of energy and momentum, the geomagnetic field also gets affected and leads to HILDCAAs. Some similar characteristic effects of HILDCAAs are visible on the results of the wavelet analysis on ΔH -component for all observatories. The first characteristic is the presence of wavelet power areas of higher amplitudes at higher time scale which may be related to the amplitude amplification by shocks or discontinuities. Another characteristic is the distribution of lower frequencies on both medium and higher time scales. Both characteristics observed on the results of the wavelet analysis may be related to the shape of highly fluctuated datasets.

In the results of DWT, the geomagnetic observatories do not show the same singu-

larity pattern in different decomposition levels. This may be due to several reasons, for example: type of magnetometer used, local time, ground conductivity and Sq current effects. From the present analysis, it is noticed that station at higher latitude shows singularities and higher amplitudes of square wavelet coefficients more frequently as compared to lower latitudes. This fact may be related to the well known concept that at higher latitudes the penetration of charged particles and the the energy injection are characterized by phenomena that involve high frequency signals. While at lower and mid latitudes coupling processes do exist that attenuate high frequency signals (MORIOKA et al., 2003; MENDES et al., 2005). Similarly, the presence of singularities and higher amplitude of square wavelet coefficients at equatorial station may be affected by equatorial phenomena known as equatorial electrojet. Finally, the results obtained from wavelet modulus correlation show that the signatures recorded on ΔH -component from all observatories are correlated with IMF-Bz. These results also show scale dependent characteristic.

We have also analyzed HILDCAAs time fluctuations on H and ΔH and adopted the same techniques for other two events which occurred on 12-15 February 2004 and 15-18 May 2005. Like previous events, these two events also show HILDCAAs time variations on the geomagnetic field for all observatories. However, the effects were different for each observatory. The results of wavelet techniques (CWT, DWT and wavelet modulus correlation) show similar phenomena to previous events but different trends for each observatory. When observing these results, we can make the following summary. For each event:

- a) The effects during HILDCAAs, although under the same general tendency, present peculiarities.
- b) When compared to other observatories, the HILDCAAs time effects for THL were very strong, and this is likely related to the latitude of this station.
- c) When Observing these results, it can be suggested that during HILDCAAs, the predominantly high latitude station is dominated by a system of ionospheric electrojet currents flowing in the auroral oval, the middle-low latitudes observatories are dominated by ring current and the equatorial station is dominated by a system of current flowing in the equator known as equatorial electrojet.

Those features indicate an interconnection among different parts of the

magnetosphere-ionosphere system.

5.4 The effects of HILDCAAs recorded from mid latitudes geomagnetic observatories

In this section, we show a case study of perturbation on H and its mean vanished value, ΔH , recorded at mid latitude observatories for the four cases. We took four mid latitude observatories (ISK, GNA, TRW and GUI) whose coordinates and names are shown in Table 3.1.

Case 1: Non-storm HILDCAA which occurred on 20-23 April 2003

Figure 5.66 depicts the geomagnetic signatures and geomagnetic indices for the HILDCAA event that occurred on 20-23 April 2003. The top four panels of this figure represent the H-signatures for ISK, GNA, TRW and GUI observatories. The other three panels represent the geomagnetic indices SYM-H, ASY-H and AE. Where the green lines represent the average quietest day signatures, the black lines represent the disturbed days signatures and the red horizontal arrow in AE panel represents the HILDCAA interval. The typical quietest day signatures of H-components of the geomagnetic field variations for all observatories are obtained by averaging over all quiet days (5 days) of a respective month (VICHARE et al., 2012). The main objective of our work is to analyze HILDCAA time perturbations on H-component so we are not describing the nature of quiet day graphs for respective month. However, the nature of the quietest day curves for all observatories show different trends, which may be related to various reasons like local time, seasonal variation and location of the observatories from the focus of the Sq current system etc (STENING et al., 2007; VICHARE et al., 2012). In this figure, the deviation of H-component with its average quietest value shows different trends. As compared to all, GNA and TRW show more negative depression. However, they also do not show similar signatures. Such variations for approximated latitude observatories may be related to different reasons such as type of magnetometers used, the ground conductivity and local time. The SYM-H index at the fifth panel of this figure shows very weak depression between -20 nT to -30 nT. Other two indices ASY-H and AE show intense activity from the midday of 20 April 2003 to the beginning of 23 April 2003. The activity observed in AE index gives support to verify the HILDCAA criteria as suggested by (TSURUTANI; GONZALEZ, 1987).

Similarly, Figure 5.67 shows the ΔH signatures for the corresponding observatories during the same event. It is obtained by subtracting each disturbed day with its mean value. The first four panels of this figure shows the ΔH signatures for ISK, GNA, TRW and GUI observatories. Other three panels are similar to Figure 5.66.

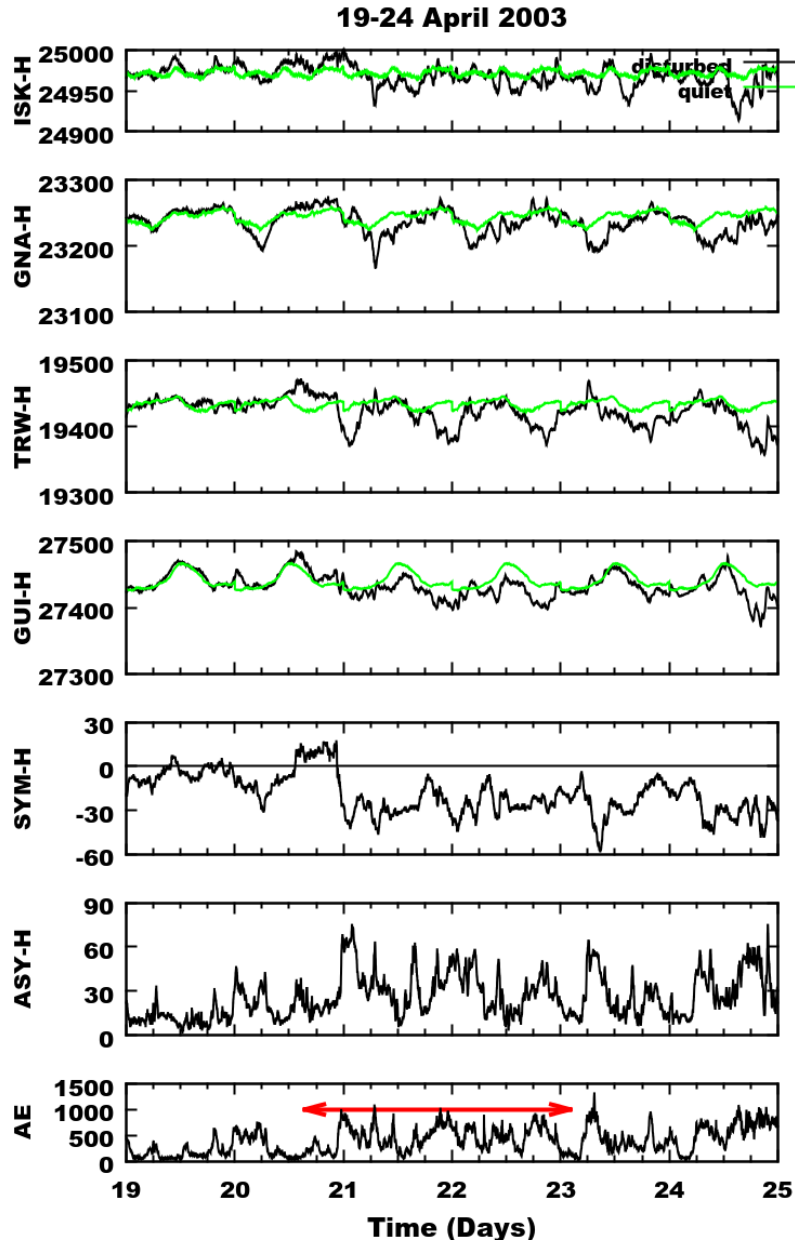


Figure 5.66 - From top to bottom, the panels show variations of H-component (nT) at the observatories ISK, GNA, TRW, GUI along with the geomagnetic indices SYM-H (nT), ASY-H (nT) and AE (nT) respectively during the HILDCAA event on 20-23 April, 2003. The green line represents the average quietest day variation, the black line represents the disturbed day variation and the red horizontal arrow in AE panel indicates the HILDCAA interval.

The time of variations on ΔH signatures for all observatories during HILDCAA were very similar to the time of variations on SYM-H index. In this figure, GNA and TRW show highly fluctuating variations between -60 nT to 30 nT. While the other two observatories (ISK and GUI) show fluctuation between -30 nT to 30 nT. However, the shape of ΔH signatures recorded by each magnetic observatory are quite dissimilar. The physical mechanism for the fluctuation on H (and ΔH) is related to intermittent magnetic reconnection between IMF-Bz with earth magnetic field (GONZALEZ et al., 1994). As a result, charged particles and energy are injected into the terrestrial magnetosphere (JANKOVICOVA et al., 2002) and the current systems inside the magnetospheric and the ionospheric were widened and intensified. Then, the mid latitudes may be dominated by ring current, low latitudes may be dominated by a system of ionospheric electrojet and high latitudes may be dominated by the currents flowing in the auroral oval. Hence, such an effect appearing on different mid latitudinal observatories are the source of energization of the ring current (RASTOGI, 2005). Another reason for the variations on magnetic field at mid latitudes may be related to variations on the solar wind ram pressure, which produces changes in the magnetopause current. This effect appears designated as storm sudden commencement (SSC) or storm gradual commencement (SGC) during initial phase of geomagnetic storm which causes an increase in the horizontal magnetic field observe at mid-to-low latitudes. In this moment, the solar wind ram pressure can be dynamical in nature and spatially dependent, which compress the magnetosphere and can affect the magnetometer locations with different strengths (VALDIVIA et al., 1999). The ionospheric current systems may also have contributed to the magnetospheric current systems observed in magnetograms (TSUNOMURA, 1998). In order to study such phenomena and to reveal some common features of these signatures recorded at mid latitude observatories, the wavelet techniques (CWT, DWT and wavelet modulus correlation) used below will be helpful tools.

Figure 5.68 represents the scalograms of ΔH -component from ISK, GNA, TRW and GUI for the HILDCAA event on 20-23 April 2003. In the figure, the horizontal axis represents the time in days and the vertical axis represents the scale in minutes. This analysis is restricted to the period range 0 to 300 minutes. This technique will be helpful to obtain a signal using time-frequency called wavelets that have good properties of localization in time and frequency domains (KUMAR; FOUFOULA, 1997). Through this analysis, the presence of multiscale structures and their temporal locations can be easily identified. We can also see embedding of some small-scale features within large-scale feature. Figure 5.68(a) and (b) shows the scalograms for ISK and GNA. Both observatories show the highest power areas of intensities be-

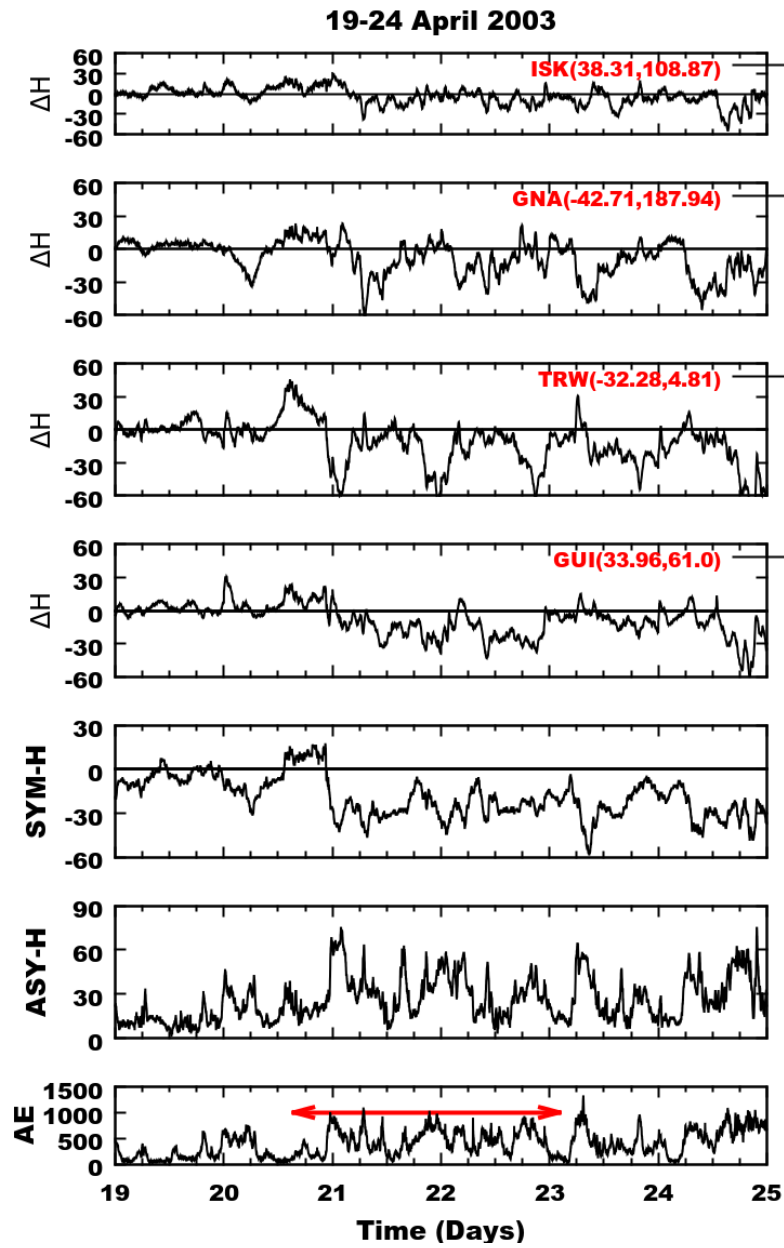


Figure 5.67 - From top to bottom, the panels represent the variation of ΔH signatures from ISK, GNA, TRW, GUI and geomagnetic indices SYM-H (nT), ASY-H (nT) and AE (nT) during HILDCAA event during 20-23 April, 2003. The red horizontal arrow in AE panel represents the HILDCAA interval.

tween 0.6 – 1.4 nT at time scale between 100-300 minutes. The other power areas of intensities between 0.8 – 1.2 nT are seen as continuous behavior. Similarly, Figure 5.68(c) and (d) shows the scalograms for TRW and GUI. These two observatories also show equivalent behavior. When observing the results of scalograms, it can be suggested that there are characteristic effects during HILDCAA visible on the scalograms. Those characteristics that we observe on scalograms may be related to the shape of highly fluctuating dataset.

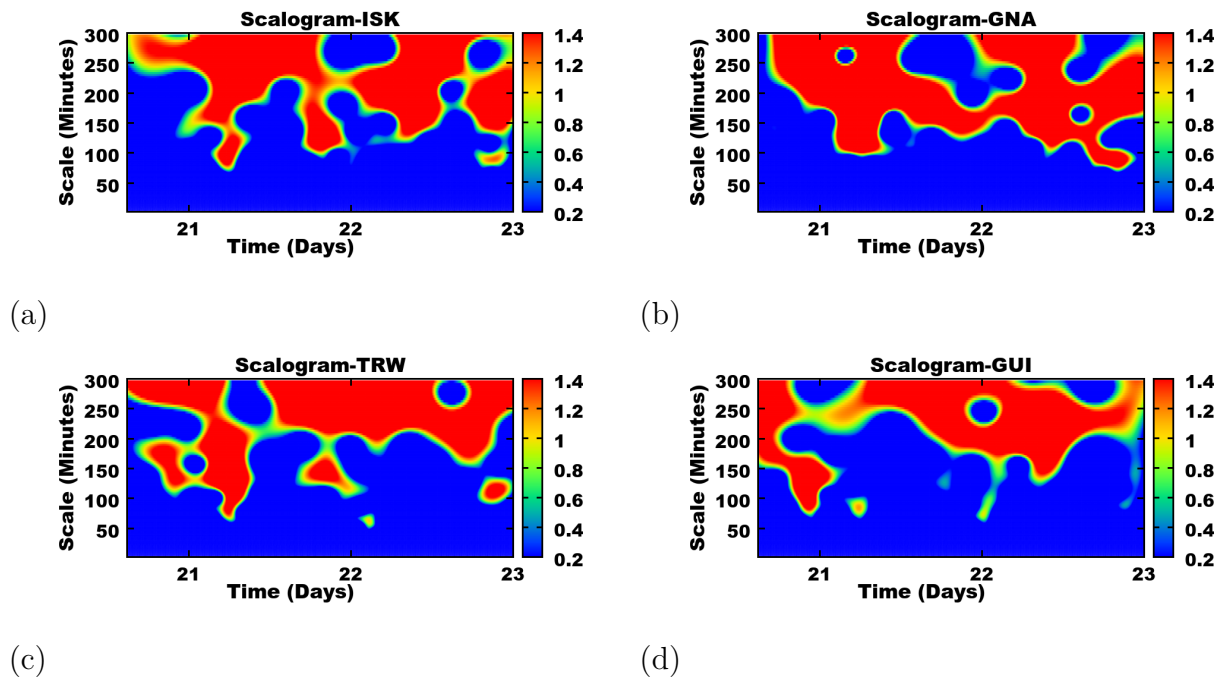


Figure 5.68 - Scalograms for ΔH -component from (a) ISK (b) GNA (c) TRW and (d) GUI during HILDCAA event on 20-23 April 2003.

In Figure 5.69 and Figure 5.70, an example of DWT applied to geomagnetic minutely signals from four mid latitude observatories using Daubechies orthogonal wavelet family 2 is presented. From top to bottom in this figure, the ΔH -component of the geomagnetic field and the first seven levels of the wavelet coefficients are presented for the HILDCAA event occurred on 20-23 April, 2003. In this analysis, the maximum amplitudes of square wavelet coefficients can be used to identify non-quietest from quietest periods. These results can be helpful for the interpretation of geomagnetic disturbances associated with HILDCAA. In these figures, the higher amplitudes values of the wavelet coefficients indicate singularity patterns associated with HILDCAA. On the other hand, the smaller amplitudes observed in the wavelet

coefficients mean that the energy transfer process is smooth. While the large amplitudes indicate that there are impulsive energy injections superposed to the smooth background process (MENDES et al., 2005). During the quiet periods, the horizontal components of the geomagnetic field recorded in the magnetometers can be represented by smooth functions, and accordingly the wavelet coefficients show very small amplitudes. But when a HILDCAA is under development the wavelet coefficients are significantly large. Thus, taking into account the amplitudes of the wavelet coefficients, we are able to identify the sudden variations that occur in the geomagnetic field components. The main purpose of this analysis applied to the dataset is to distinguish quiescent from non-quiescent periods. The wavelet coefficients on the first decomposition level gives us an idea about the time localization of higher frequencies during HILDCAA. Other six levels were used to validate the (numerical) shock candidate regions. In the figure, the larger amplitude of the wavelet coefficients can be used as a marker of the geomagnetic activity, an indicator that some process of impulsive energy transfer is going on. By careful inspection, one can observe that magnetic observatories do not show the similar pattern of wavelet coefficients in different decomposition levels. This may be due to several reasons, for example: type of magnetometer used, local time, ground conductivity and Sq current effects. However, the larger amplitudes of the wavelet coefficients presence in magnetic observatories indicate that the whole magnetosphere is globally affected. Hence, by the use of this analysis, the intrinsic processes of energy transfer during HILDCAA at mid latitudes are being surveyed. A more detailed description about of this analysis can be found in (MENDES et al., 2005; OJEDA et al., 2014; KLAUSNER et al., 2014b).

Figure 5.71 shows the results of wavelet modulus correlation of H-component from ISK, GUA, GUI and TRW with interplanetary magnetic field (Bz) for the same event. The horizontal axis represents the scale in minutes and the vertical axis represents the modulus correlation. In each figure, the scale of 1, 10, 100 and 1000 are labeled in horizontal axis. The first panel of this figure represents the modulus correlation of IMF-Bz with ISK. It shows the peak about 0.5 at time scale approximately 150 minutes. Similarly, the second panel represents the modulus correlation of IMF-Bz with GNA. It shows the peak about 0.8 at time scale approximately 200 minutes. Other two panels show the modulus correlation of IMF-Bz with GUI and TRW. Both observatories show the peak about 0.4 at time scale approximately 80 and 100 minutes respectively. When observing these results, it is noticed that the signatures recorded on ΔH -component are correlated with IMF-Bz. These results also show scale dependent characteristic. As compared to all, GNA shows very good correlation with IMF-Bz. More details about the wavelet modulus correlation can

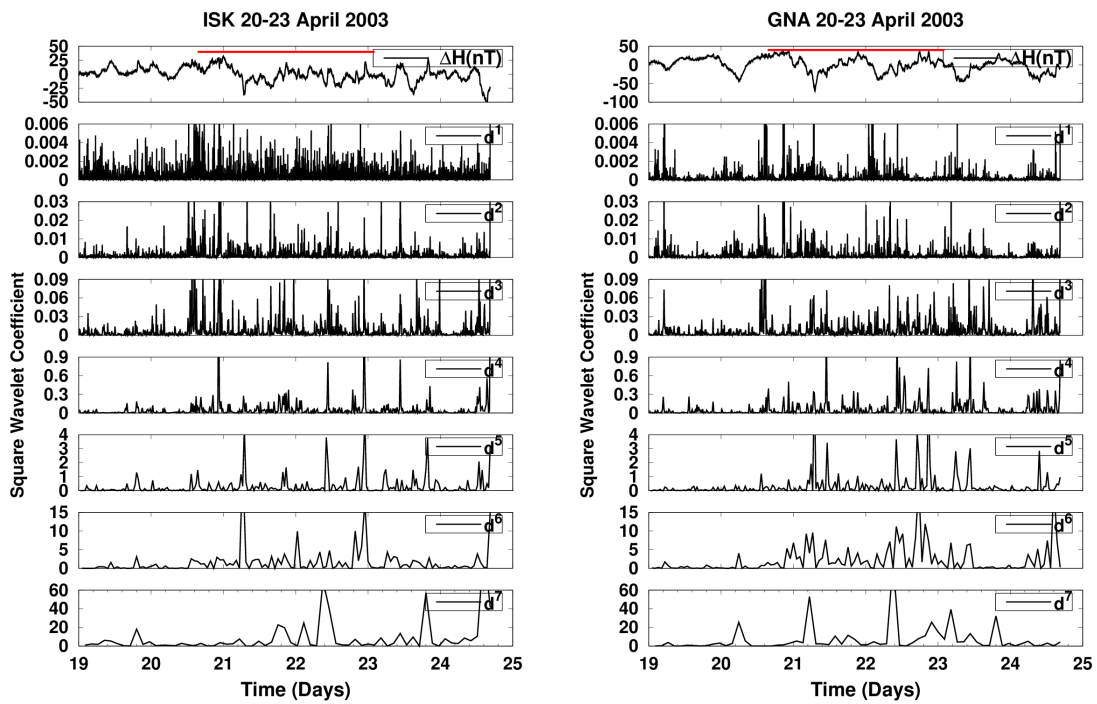


Figure 5.69 - Daubechies Wavelet coefficients d^j (for $j= 1,2,3,\dots,7$) for ΔH -component from ISK (left) and GNA (right) during HILDCAA event occurred on 20-23 April, 2003. The red color identifies where the HILDCAA events is happening.

be found in (KLAUSNER et al., 2013).

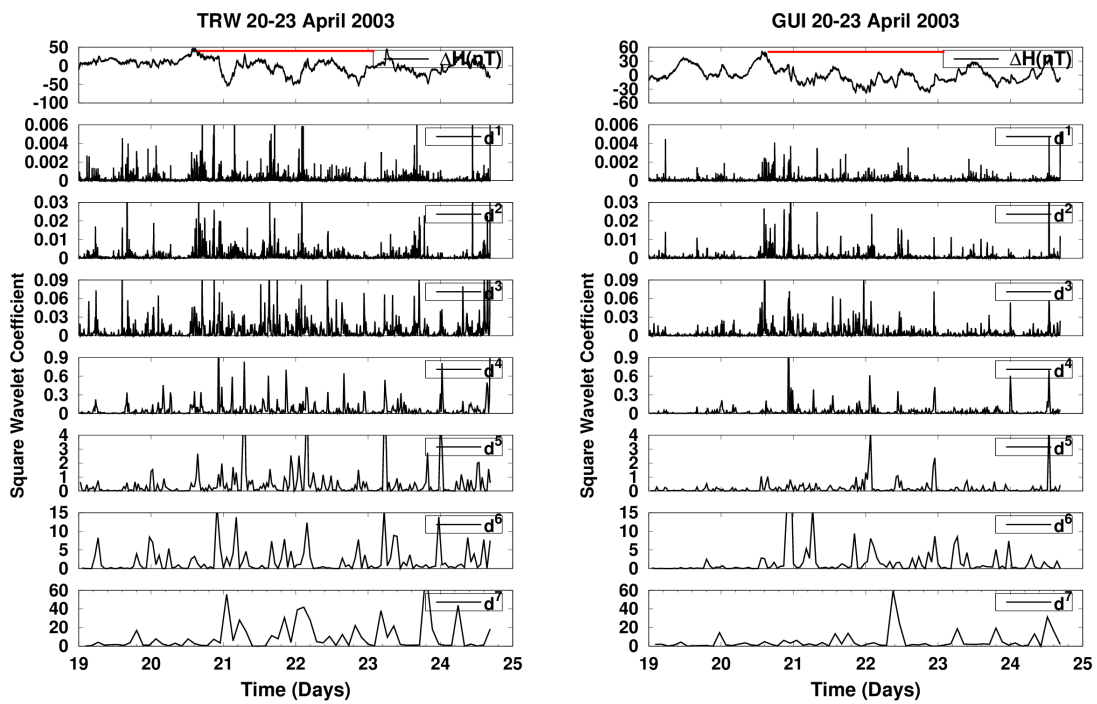


Figure 5.70 - Daubechies Wavelet coefficients d^j (for $j= 1,2,3,\dots,7$) for ΔH -component from TRW (left) and GUI (right) during HILDCAA event occurred on 20-23 April, 2003. The red color identifies where the HILDCAA events is happening.

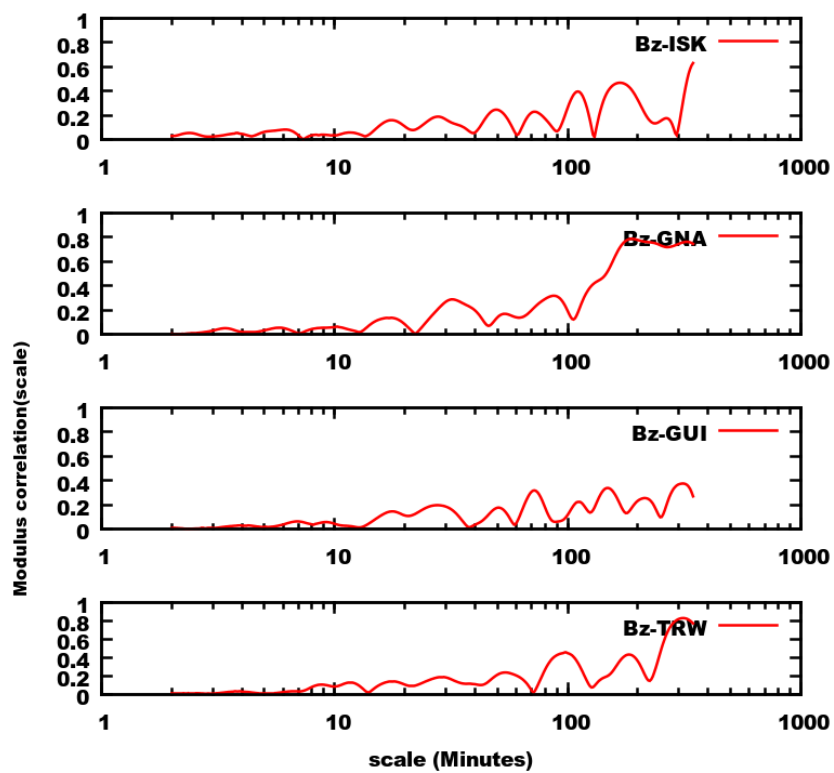


Figure 5.71 - From top to bottom, the panels represent the correlation of IMF-Bz with ΔH -component from geomagnetic observatories ISK, GNA TRW and GUI during the HILDCAA event on 20-23 April, 2003.

Case 2: HILDCAA preceded by CIR-storm when occurred on 12-15 February 2004

Figure 5.72 represents the geomagnetic signatures and geomagnetic indices for CIR preceding HILDCAA. The panels from top to bottom are similar to Figure 5.66. In this figure, we can clearly see the three different phases of CIR-storm. The initial phase starts late on 11 February 2004. The main phase of the storm starts around midnight of 11 February 2004. The long recovery phase (the HILDCAA event) lasts from the beginning of day 12 February 2004 to midday of 15 February 2004. The quietest day graphs for all observatories during this event also show similar nature to previous event. But the disturbed days signatures show totally different signatures. During the main phase, all observatories show strong depression on H-component. At the time of HILDCAA, all observatories show strong fluctuations. But the nature of fluctuations differ from each observatory. Such strong fluctuations in this event may be related to higher level of Alfvénic fluctuation in IMF-Bz (GUARNIERI et al., 2006). Other three panels of this figure represent the geomagnetic indices SYM-H, ASY-H and AE. During the main phase, SYM-H index shows strong depression about -115 nT, ASY-H index shows the peak about 160 nT and AE index shows the peak about 1600 nT. But at the time of HILDCAA, SYM-H index shows approximately constant negative value and both ASY-H and AE indices show intense activity.

Figure 5.73 shows the ΔH signatures and geomagnetic indices for the same event. The panels from top to bottom are similar to Figure 5.67. During the main phase, all the observatories show strong depression on ΔH -component. The level of depression for ISK, GNA, TRW and GUI were -120, -90, -100 and -180 nT respectively. Similarly, at the time of HILDCAA, the fluctuations are almost below zero for all observatories. However at some places, GNA and GUI show slightly positive values and ISK shows some data gap. As previous event, the signatures recorded by each magnetic observatory are quite dissimilar.

Figure 5.74 depicts the scalograms for ΔH -component from (a) ISK (b) GNA (c) TRW and (d) GUI during the HILDCAA event on 12-15 February 2004. In this figure, all the observatories show the wavelet power areas of higher and lower intensities on both medium and higher time scales. As compared to all, GNA shows wavelet powers at lower time scales.

Figure 5.75 and Figure 5.76 are similar to Figure 5.69 and Figure 5.70 but refer to the HILDCAA preceded by the CIR-storm which occurred on 12-15 February 2004. In both events, it was possible to identify singularity patterns and larger and

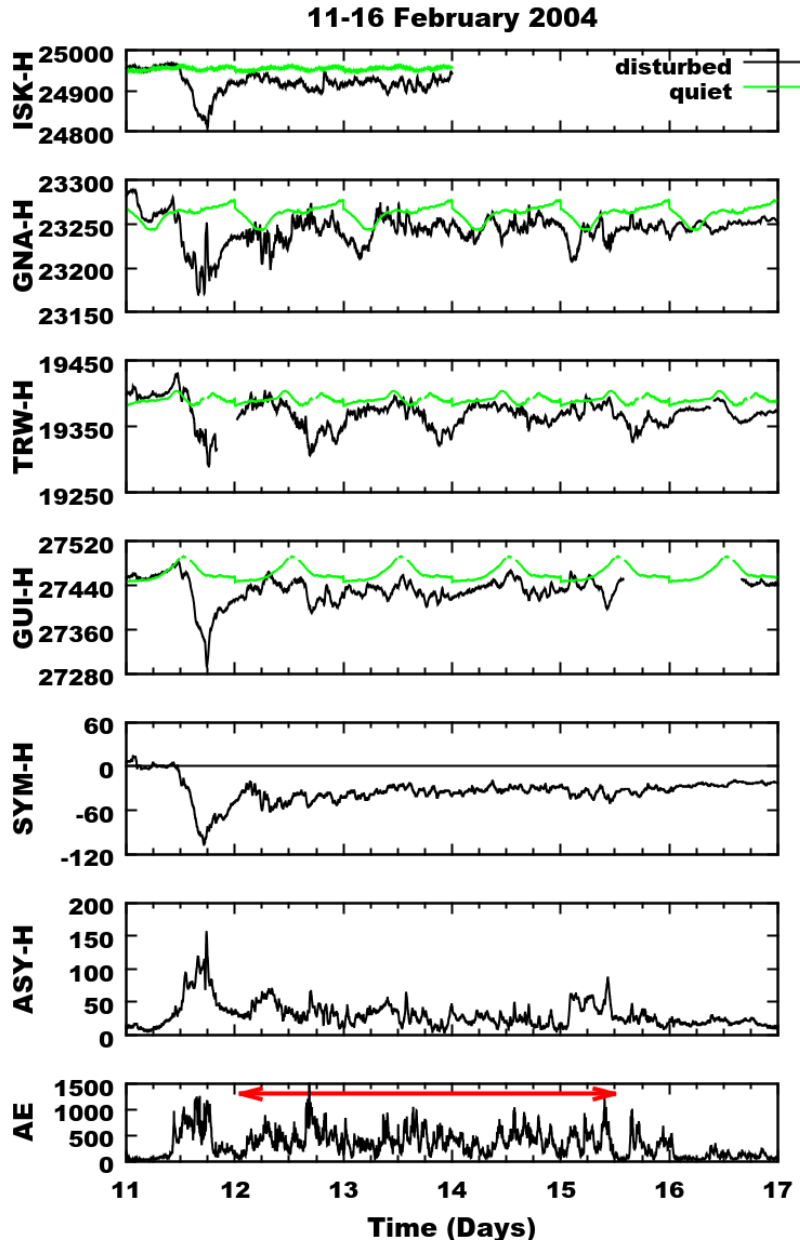


Figure 5.72 - From top to bottom, the panels show variations of H-component (nT) at the observatories ISK, GNA, TRW, GUI along with the geomagnetic indices SYM-H (nT), ASY-H (nT) and AE (nT) respectively during the HILDCAA event on 12-15 February 2004. The green line represents the average quietest day variation, the black line represents the disturbed day variation and the red horizontal arrow in AE panel indicates the HILDCAA interval.

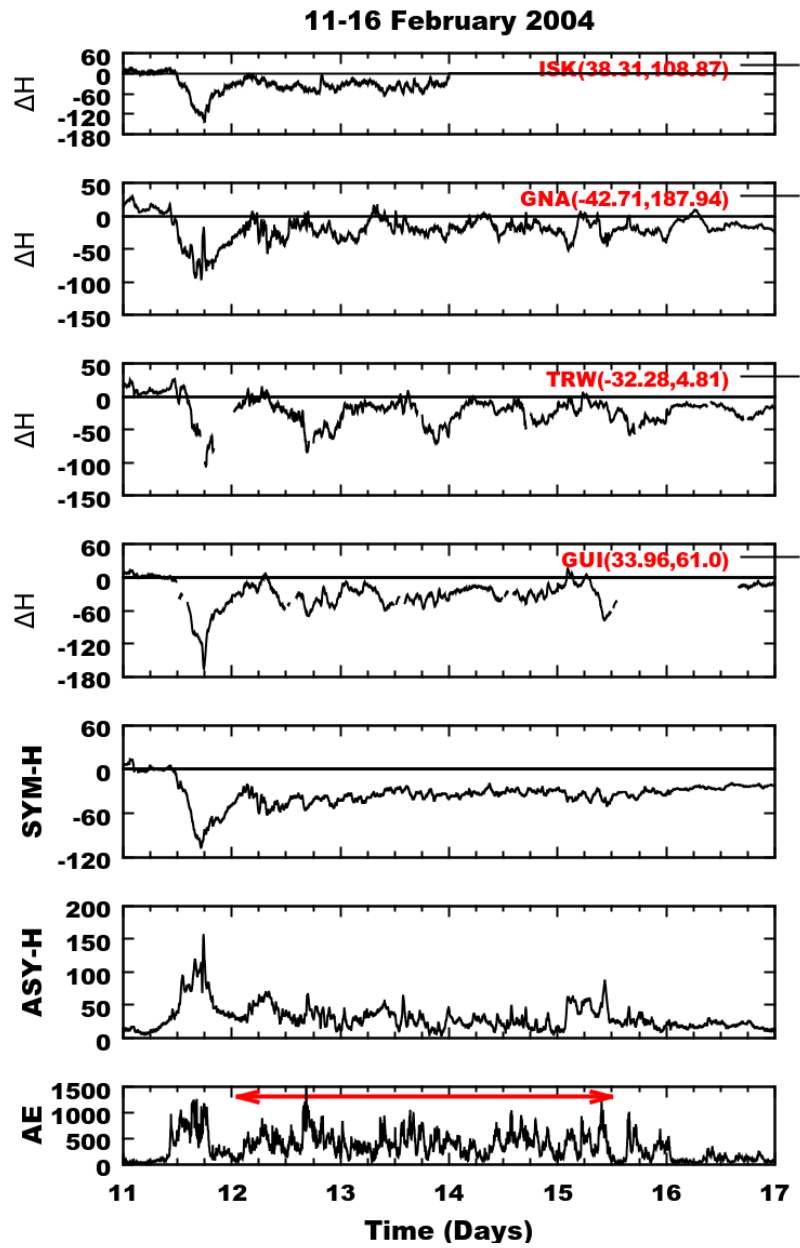


Figure 5.73 - From top to bottom, the panels represent the variation of ΔH signatures from ISK, GNA, TRW, GUI and geomagnetic indices SYM-H (nT), ASY-H (nT) and AE (nT) during HILDCAA event during 12-15 February 2004. The red horizontal arrow in AE panel represents the HILDCAA interval.

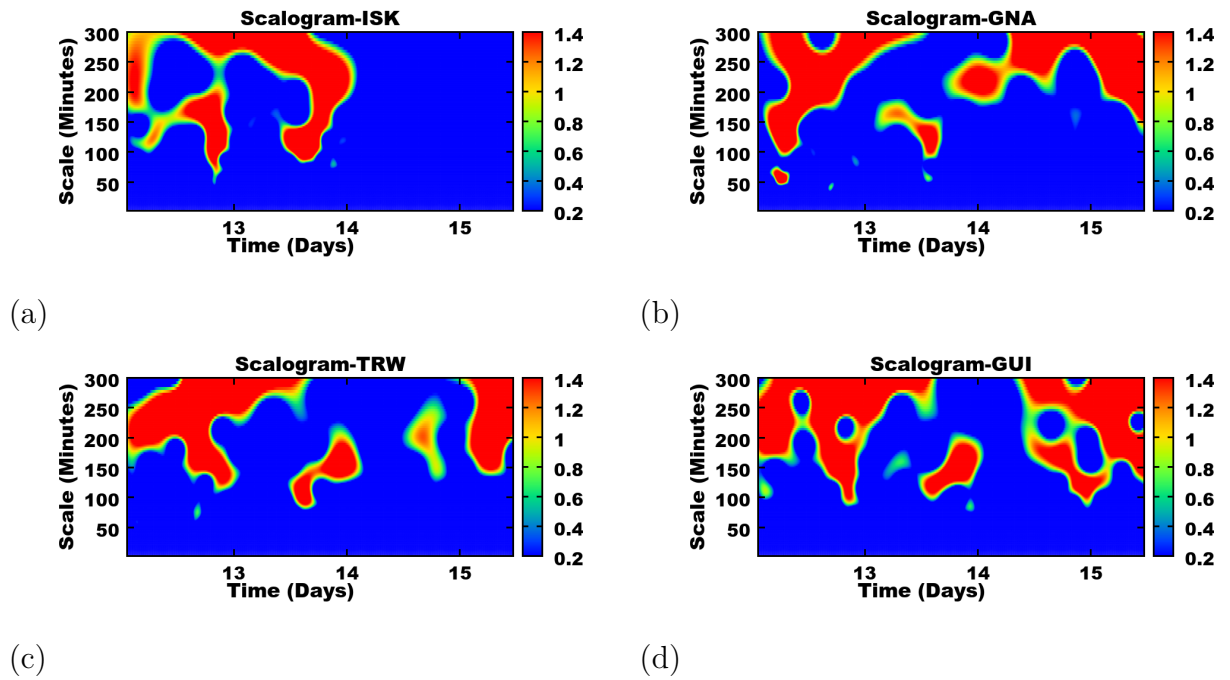


Figure 5.74 - Scalograms for ΔH -component from (a) ISK (b) GNA (c) TRW and (d) GUI during HILDCAA event on 12-15 February 2004.

smaller amplitudes of the wavelet coefficients related to HILDCAAs intervals in the magnetograms of the magnetic observatories considered, where the larger amplitudes of the wavelet coefficients indicate that the whole magnetosphere is globally affected.

Figure 5.77 shows the result of wavelet modulus correlation of ΔH -component from ISK, GNA, TRW and GUI with interplanetary magnetic field (B_z) for the same event. The panels, axis representation and scales are similar as like Figure 5.71. The first panel of this figure shows the peak modulus correlation about 0.7 at time scale approximately 300 minutes for IMF- B_z with ISK. Similarly, the second and the third panels show the peaks modulus correlation about 0.5 and 0.65 at time scale approximately 250 and 180 minutes for IMF- B_z with GNA and GUI respectively. The last panel shows the peak modulus correlation about 0.5 at time scale approximately 180 minutes for IMF- B_z with TRW. As previous event, this event also shows correlation of ΔH -component with IMF- B_z and also shows scale dependent characteristics.

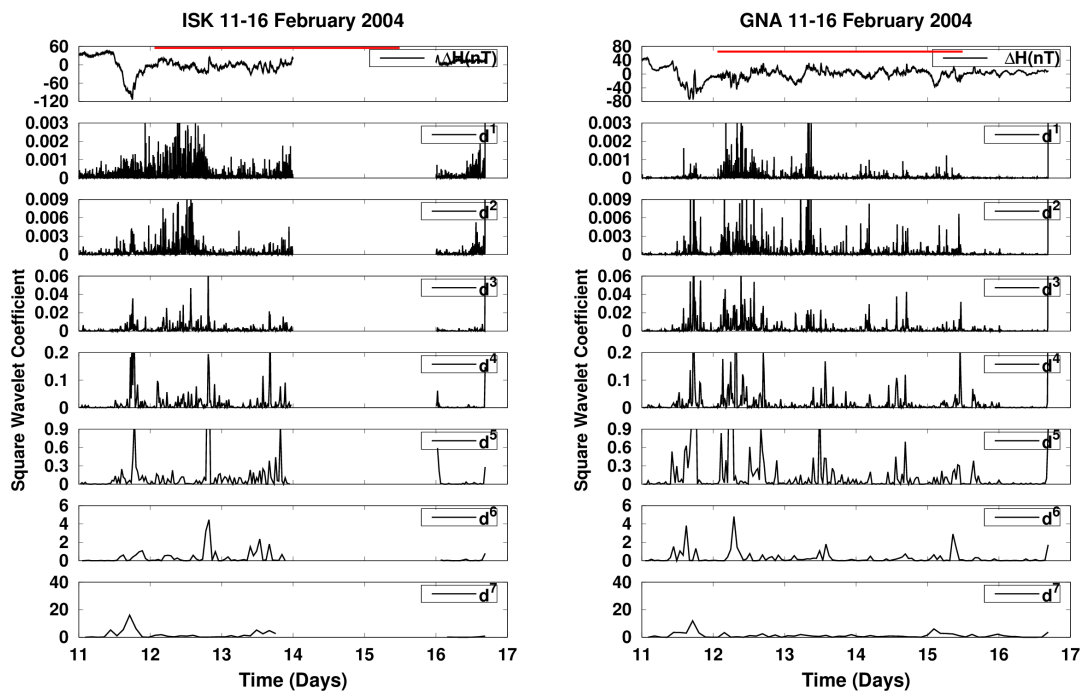


Figure 5.75 - Daubechies Wavelet coefficients d^j (for $j= 1,2,3,\dots,7$) for ΔH -component from ISK (left) and GNA (right) during HILDCAA event occurred on 12-15 February 2004. The red color identifies where the HILDCAA events is happening.

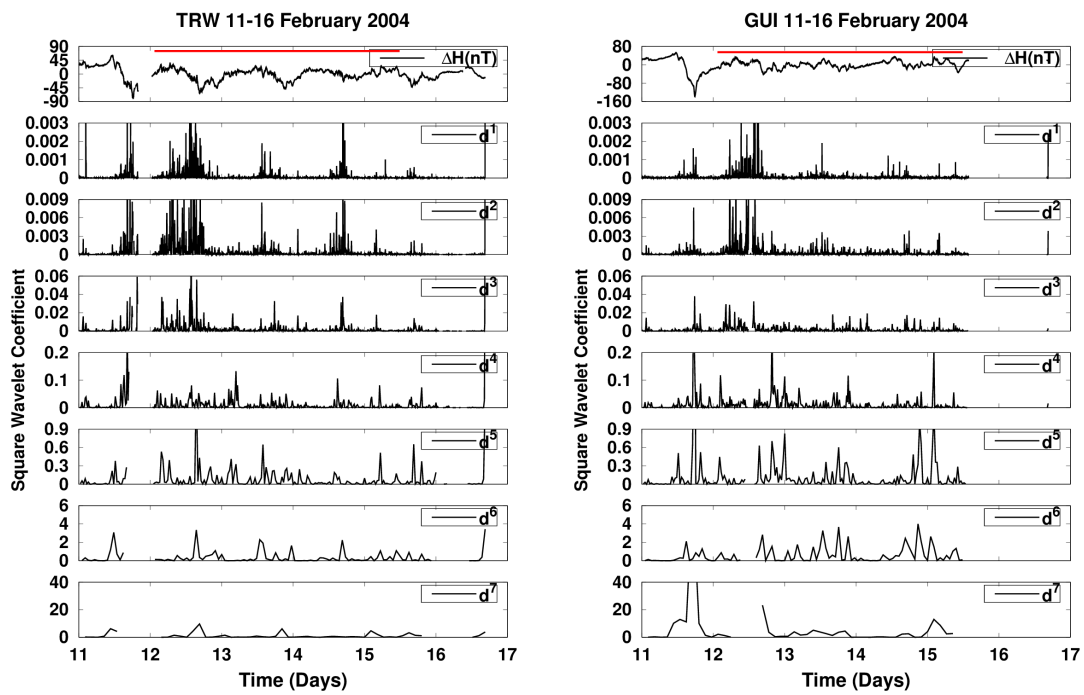


Figure 5.76 - Daubechies Wavelet coefficients d^j (for $j= 1,2,3,\dots,7$) for ΔH -component from TRW (left) and GUI (right) during HILDCAA event occurred on 12-15 February 2004. The red color identifies where the HILDCAA events is happening.

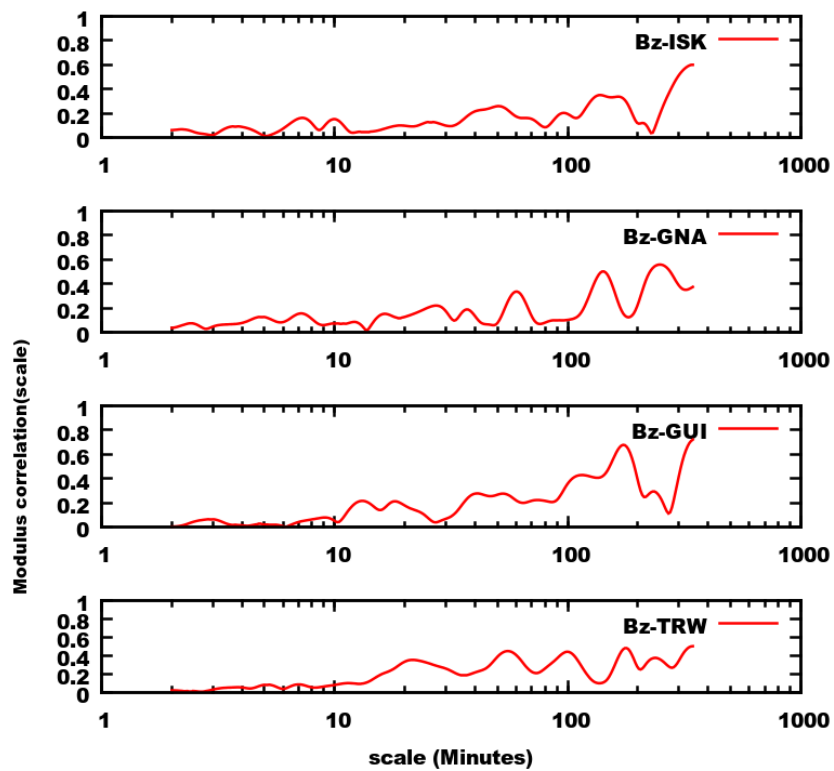


Figure 5.77 - From top to bottom, the panels represent the correlation of IMF-Bz with ΔH -component from geomagnetic observatories ISK, GNA TRW and GUI during the HILDCAA event on 12-15 February 2004.

Case 3: An ICME preceding HILDCAA which occurred on 15-18 May 2005

Figure 5.78 represents the geomagnetic signatures and geomagnetic indices for an ICME preceding HILDCAA occurred on 15-18 May 2005. The panels representation are similar as like Figure 5.66 and Figure 5.72. The interplanetary cause for this storm was the shock driven by an ICME contained a magnetic cloud structure (HAJRA et al., 2013; OJEDA et al., 2013; OJEDA et al., 2014) characterized by large southward IMF-Bz with a peak of $-50nT$. This storm also clearly shows three different phases of storm. During the initial phase, the stage of SSC (sudden storm commencement) can be easily visible on all observatories with positive increment on H-component. During the main phase, all observatories show strong depressions on H-component. At that time, SYM-H, ASY-H and the AE indices show peak value of about -300 nT, 275 nT and 2000 nT respectively. The recovery phase lasts from midday of 15 May to midday of 18 May, about 3 days. During this phase, the differences between the quietest day curve and the disturbed days curve show very large separations. The SYM-H index shows fluctuation between -100 nT to -30 nT. Similarly, ASY-H index shows fluctuation between 100 nT to 30 nT and AE index shows intense activity for the entire event.

Figure 5.79 depicts the ΔH signatures and geomagnetic indices for the same event. The panels representation are similar to Figure 5.67 and Figure 5.73. During the initial phase, all observatories show SSC (sudden storm commencement) on ΔH component. During the main phase, ISK, GNA, TRW and GUI show strong depression on ΔH component about -275 nT, -250 nT, -250 nT and -175 nT respectively. At the time of HILDCAA, all the observatories show fluctuations between -100 nT to -30 nT. Compared to the other two events, the HILDCAA time fluctuations for this event were totally different. However, the signatures recorded by each magnetic observatory are quite dissimilar.

Figure 5.80 depicts the scalograms for ΔH -component from (a) ISK (b) GNA (c) TRW and (d) GUI during the HILDCAA event on 15-18 May 2005. In the figure, ISK, GNA, TRW and GUI show the continuous periodicity of higher intensity at time scale between approximately 130-300 minutes at the beginning of HILDCAA. Like other two events, the wavelet powers of the highest spectral variabilities are seen at time scales between 80-300 minutes.

Figure 5.81 and Figure 5.82 are similar to Figure 5.75 and Figure 5.76 or Figure 5.69 and Figure 5.70 but refer to the HILDCAA preceded by ICME-storm which occurred

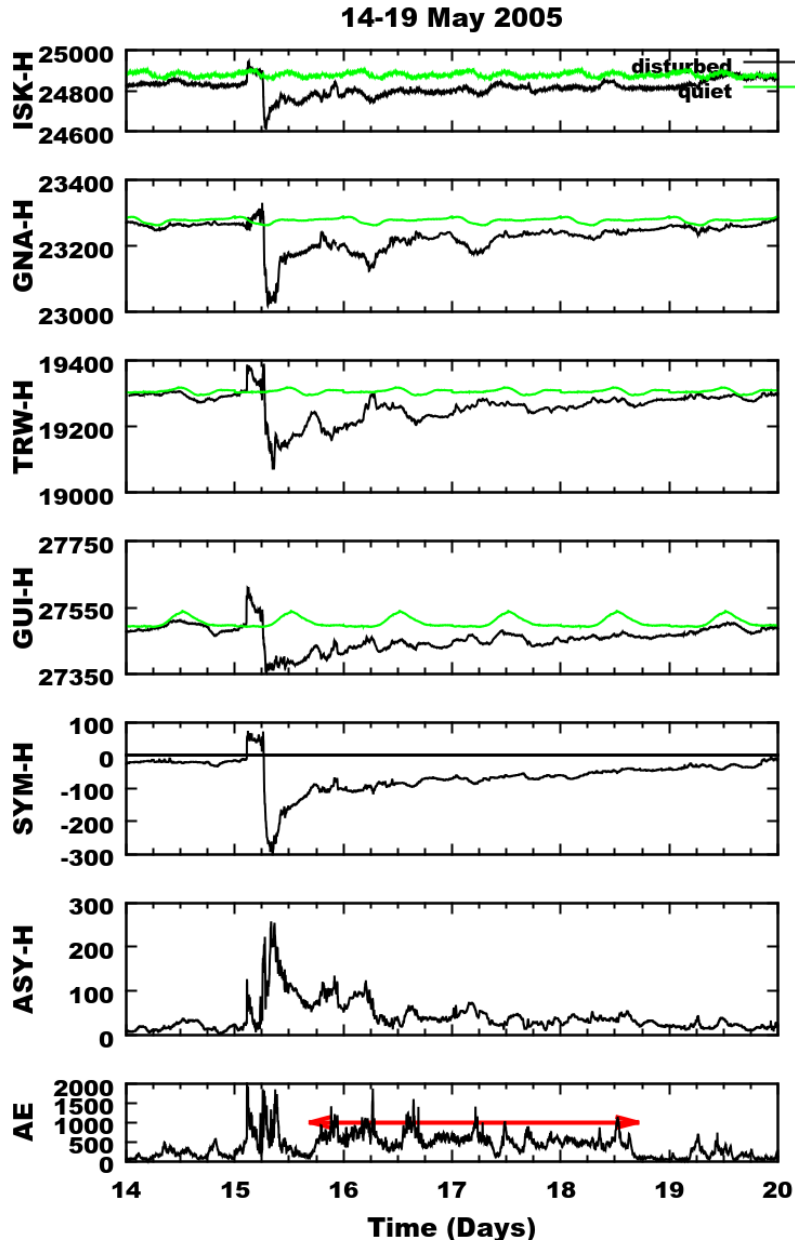


Figure 5.78 - From top to bottom, the panels show variations of H-component (nT) at the observatories ISK, GNA, TRW, GUI along with the geomagnetic indices SYM-H (nT), ASY-H (nT) and AE (nT) respectively during the HILDCAA event on 15-18 May 2005. The green line represents the average quietest day variation, the black line represents the disturbed day variation and the red horizontal arrow in AE panel indicates the HILDCAA interval.

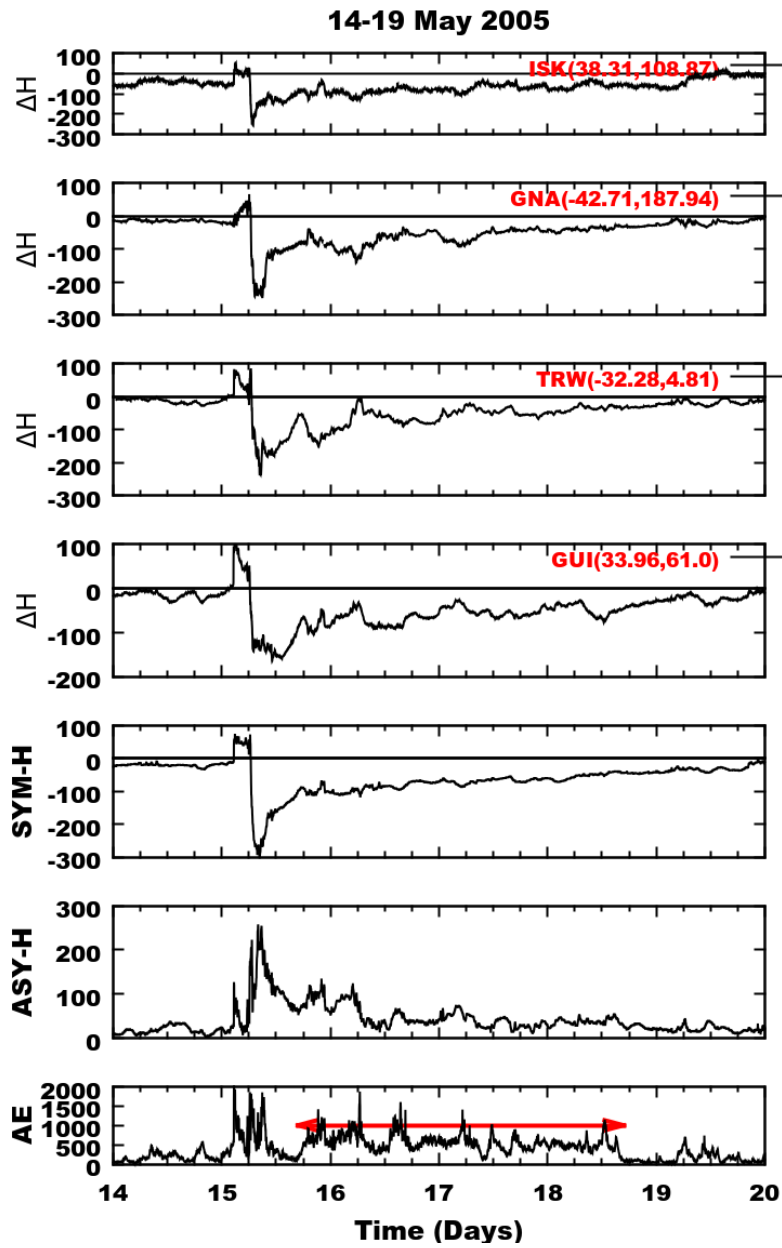


Figure 5.79 - From top to bottom, the panels represent the variation of ΔH signatures from ISK, GNA, TRW, GUI and geomagnetic indices SYM-H (nT), ASY-H (nT) and AE (nT) during HILDCAA event during 15-18 May 2005. The red horizontal arrow in AE panel represents the HILDCAA interval.

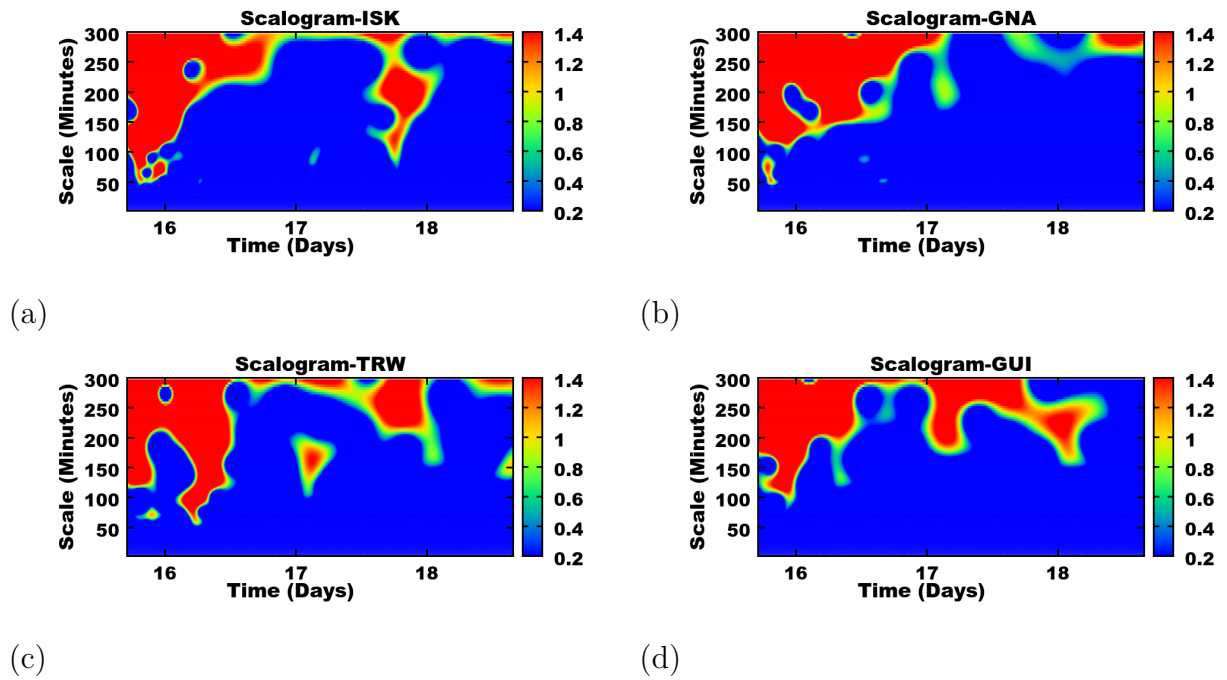


Figure 5.80 - Scalograms for ΔH -component from (a) ISK (b) GNA (c) TRW and (d) GUI during HILDCAA event on 15-18 May 2005.

on 15-18 May 2005. In all observatories, the singularities pattern are present for all levels during the main phase of storm. At the time of HILDCAA, all the observatories show smaller amplitude of square wavelet coefficients. As compared to other, ISK shows relatively larger amplitude of square wavelet coefficients at levels d1 and d2. When observing these results, it can be noticed that there was impulsive energy injection inside the magnetosphere during the main phase of storm. During the recovery phases, the energy injection was weak but continuous. When compared to the results obtained from other two events, it shows completely different results. The main cause for such a difference may be related to interplanetary causes. As we know, the other two events were caused by CIRs where the fluctuation of Alfvén waves were present. These waves are the main causes for freshly injection of charged particles inside the magnetosphere. But this event was caused by the southward IMF (B_z) of the magnetic cloud. When the magnitude of southward IMF (B_z) was very strong, the energy injection was huge. At the time of HILDCAA, the magnitude of B_z was small and continuously southward. Due to this reason, the energy injection was also relatively higher and continuous.

Figure 5.83 is similar to Figure 5.71 and Figure 5.77 but refers to the HILDCAA preceded by ICME-storm which occurred on 15-18 May 2005. In this figure, B_z -ISK,

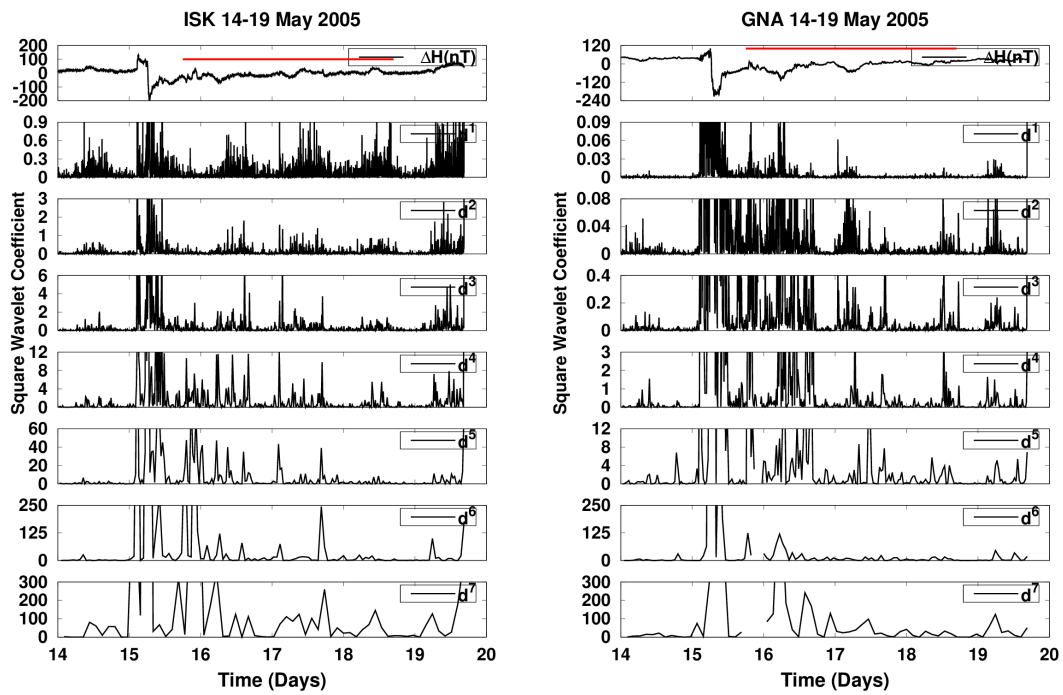


Figure 5.81 - Daubechies Wavelet coefficients d^j (for $j= 1,2,3,\dots,7$) for H-component from ISK (left) and GNA (right) during HILDCAA event occurred on 15-18 May 2005. The red color identifies where the HILDCAA events is happening.

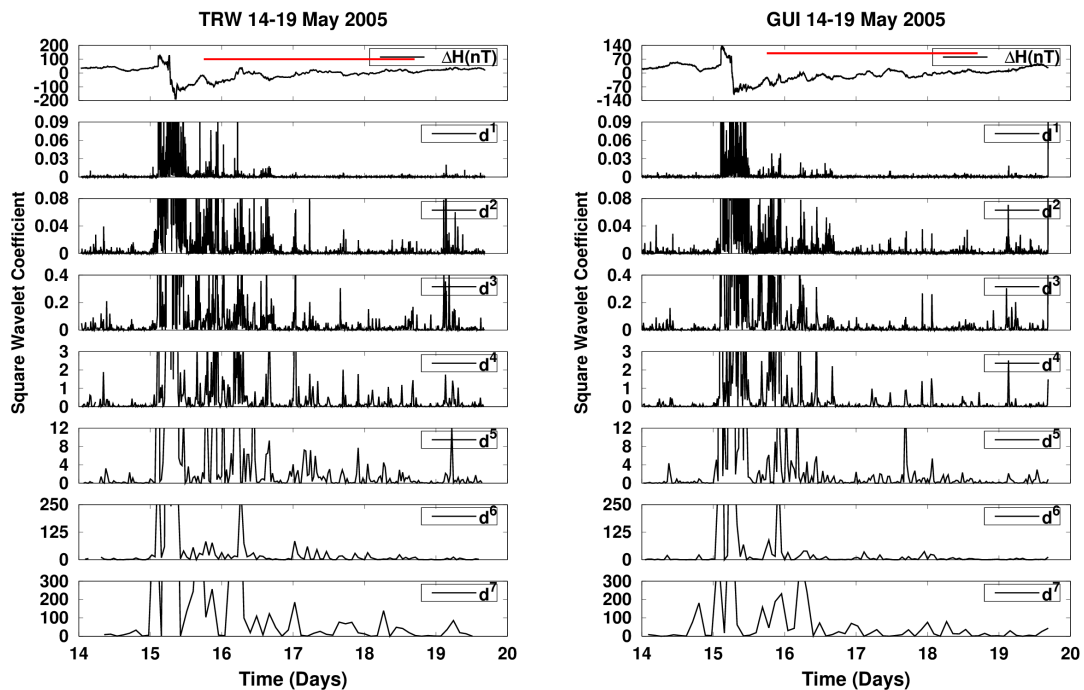


Figure 5.82 - Daubechies Wavelet coefficients d^j (for $j= 1,2,3,\dots,7$) for H-component from TRW (left) and GUI (right) during HILDCAA event occurred on 15-18 May 2005. The red color identifies where the HILDCAA events is happening.

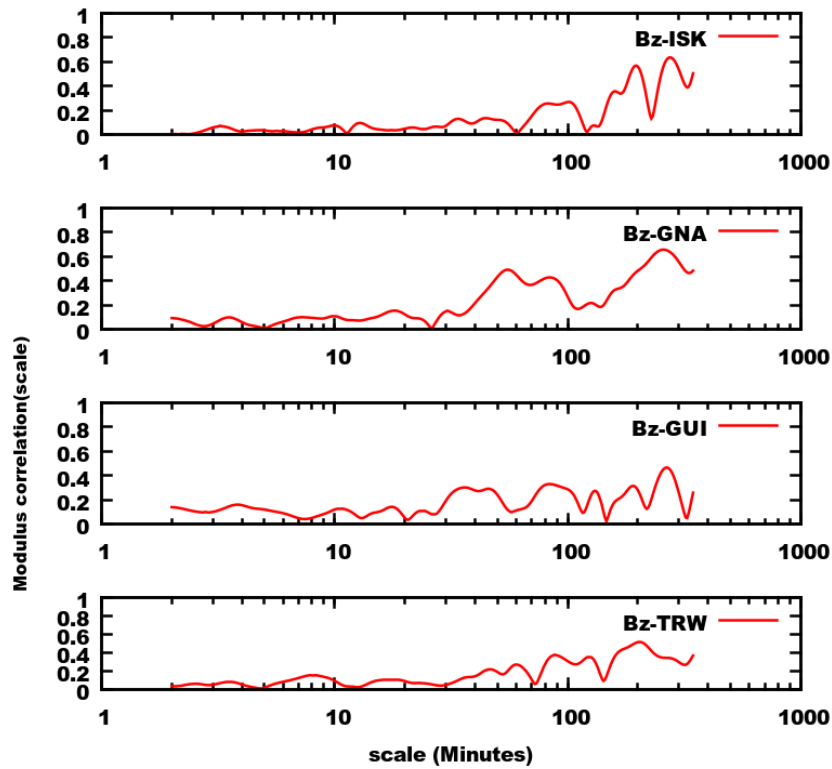


Figure 5.83 - From top to bottom, the panels represent the correlation of IMF-Bz with ΔH -component from geomagnetic observatories ISK, GNA TRW and GUI during the HILDCAA event on 15-18 May 2005.

Bz-GNA, Bz-GUI and Bz-TRW show the wavelet modulus correlation around 0.6, 0.7, 0.5 and 0.5 at time scales approximately 275, 250, 250, 200 minutes respectively. Like the other two events, this event also shows correlation of IMF-Bz with ΔH -component and also shows scale dependent characteristics.

Case 4: quiet periods 18-21 July, 2006

Figure 5.84 represents the geomagnetic signatures and geomagnetic indices for quiet periods from 18 to 21 July, 2006. The panels representations are similar to Figure 5.66, Figure 5.72 and Figure 5.78. In this figure, all the observatories show small scale fluctuations on quiet days curves. Predominantly daily variations are explicitly in the data set due to ionospheric dynamo under the solar irradiation. Existing fluctuations superimposed on the basic curve are due to sources other than ionosphere, for example UV incidence, energetic particles, polar cap heating etc (GONCHAROVA, 2004; BOLAJI et al., 2013)

Figure 5.85 depicts the scalograms for ΔH -component from (a) ISK (b) GNA (c) TRW and (d) GUI during quiet periods from 18 to 21 July, 2006. In this figure, all the observatories show wavelet power areas of lesser amplitudes when compared to the three HILDCAA events above. However, except for GNA, the wavelet powers of the highest spectral variabilities are seen at time scales between 100-300 minutes. Compared to all, ISK shows more scatter wavelet powers at lower to higher time scales. As we know, the nature of average quietest day signatures for equatorial and low latitudes observatories follow the diurnal cycle of solar irradiation. The quiet days signatures depend on the phase of the sunspot cycle, seasons, movement of the solar quiet foci, atmospheric tide and longitude. In order to illustrate the causal analysis, the observatories can be organized from north position towards south position: from ISK, GUI, TRW, and GNA. The period of event occurred during summer season at North Hemisphere. But there may be small scale fluctuations on quiet days curves at high and mid latitudes related to other sources than ionosphere. The last aspect is indicated in the next figure on the DWT analysis.

Figure 5.86 and Figure 5.87 are similar to Figure 5.69 and Figure 5.70 or Figure 5.75 and Figure 5.76 or Figure 5.81 and Figure 5.82 but refer to quiet periods from 18 to 21 July, 2006. In the figures, all observatories show smaller and larger square wavelet coefficients for all levels. Apart from ISK, the other three observatories show smaller amplitude of square wavelet coefficients when compared to HILDCAAs events. From the observation of dataset, ISK seems to be a noisy observatory.

Figure 5.88 is similar to Figure 5.83 or Figure 5.71 or Figure 5.77 during quiet periods from 18 to 21 July, 2006. In this figure, all the observatories show correlation of IMF-Bz with ΔH -component from ISK, GNA TRW and GUI. However, each observatory shows different peak correlation at different time scales.

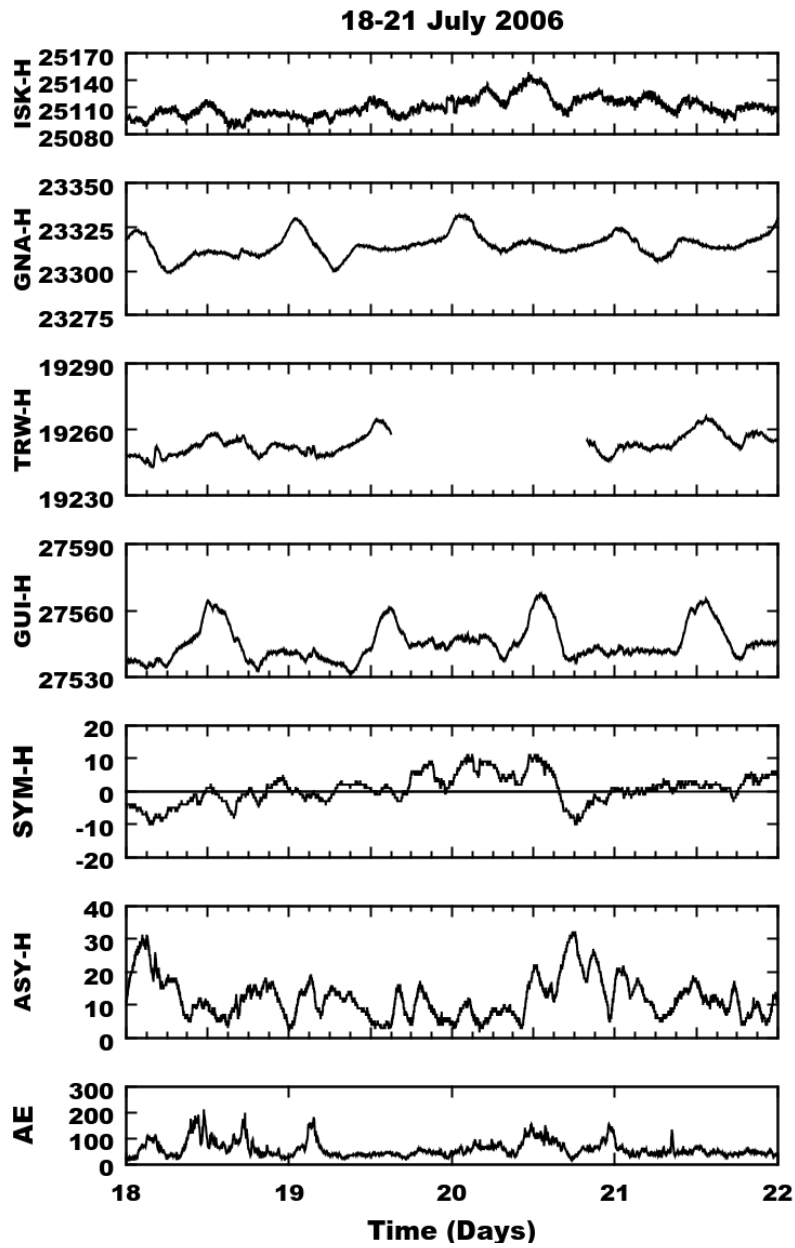


Figure 5.84 - From top to bottom, the panels show variations of H-component (nT) at the observatories ISK, GNA, TRW, GUI along with the geomagnetic indices SYM-H (nT), ASY-H (nT) and AE (nT) respectively during quiet periods from 18 to 21 July, 2006.

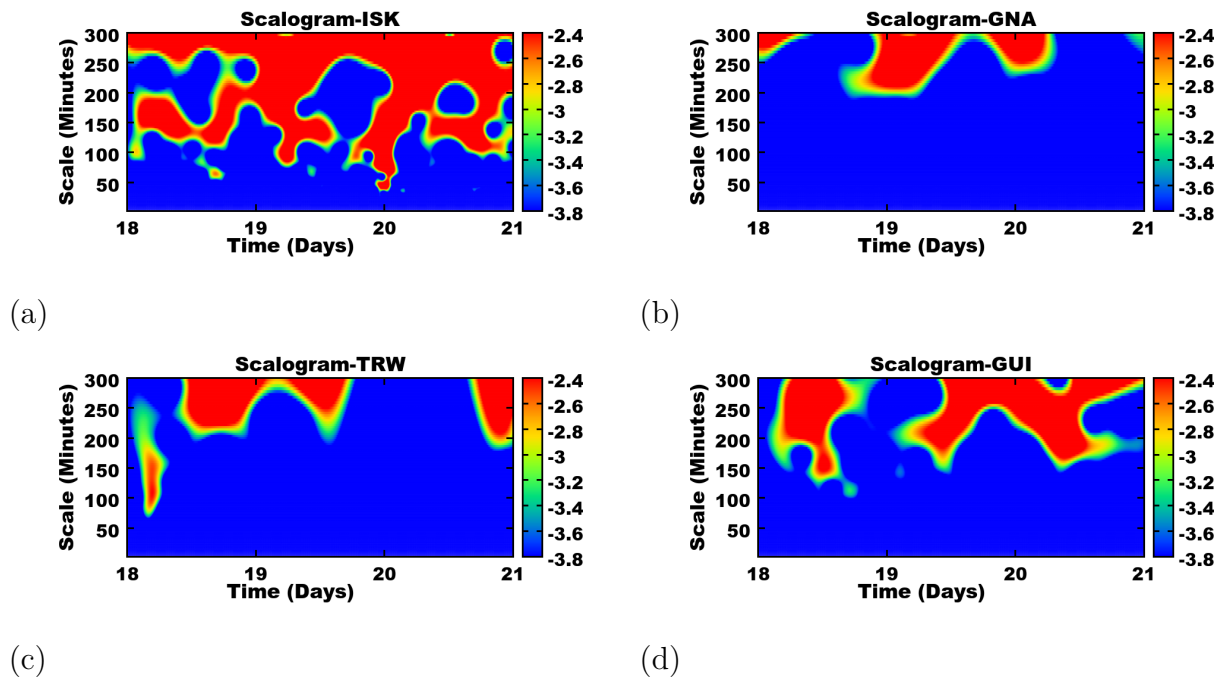


Figure 5.85 - Scalograms for ΔH -component from (a) ISK (b) GNA (c) TRW and (d) GUI during quiet periods from 18 to 21 July, 2006.

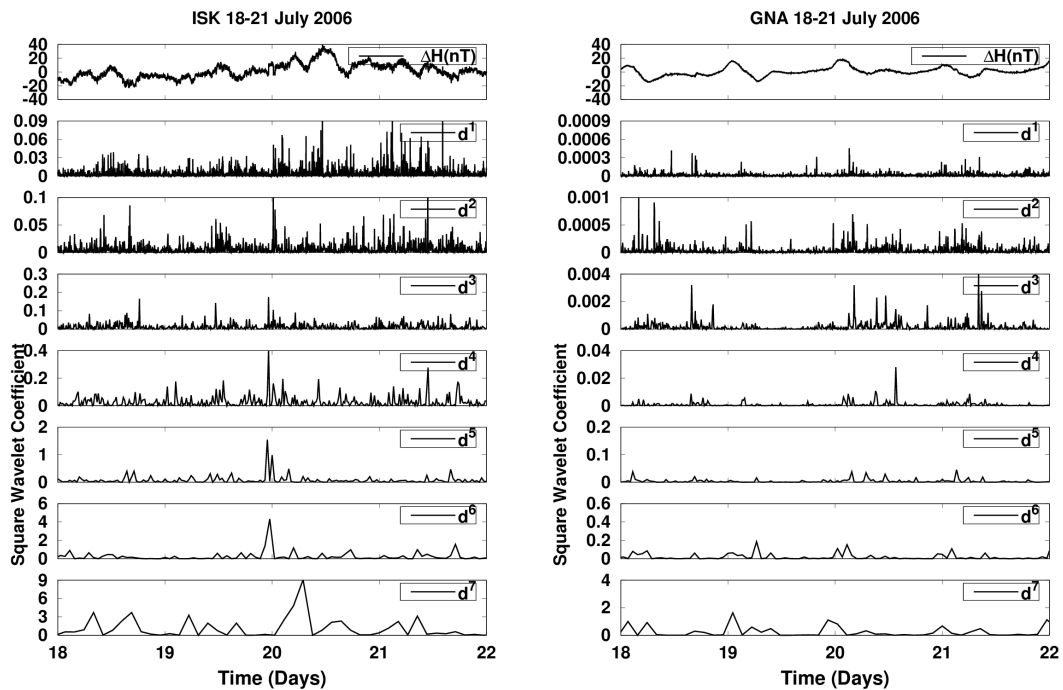


Figure 5.86 - Daubechies Wavelet coefficients d^j (for $j= 1,2,3,\dots,7$) for ΔH -component from ISK (left) and GNA (right) during quiet periods from 18 to 21 July, 2006.

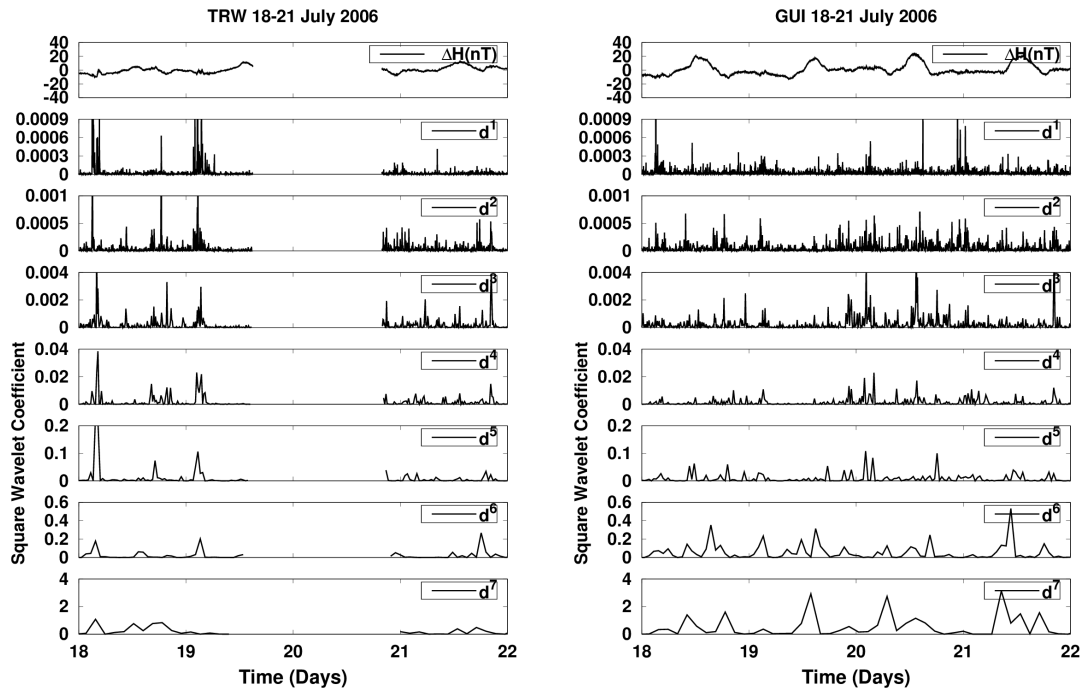


Figure 5.87 - Daubechies Wavelet coefficients d^j (for $j= 1,2,3,\dots,7$) for ΔH -component from TRW (left) and GUI (right) during quiet periods from 18 to 21 July, 2006.

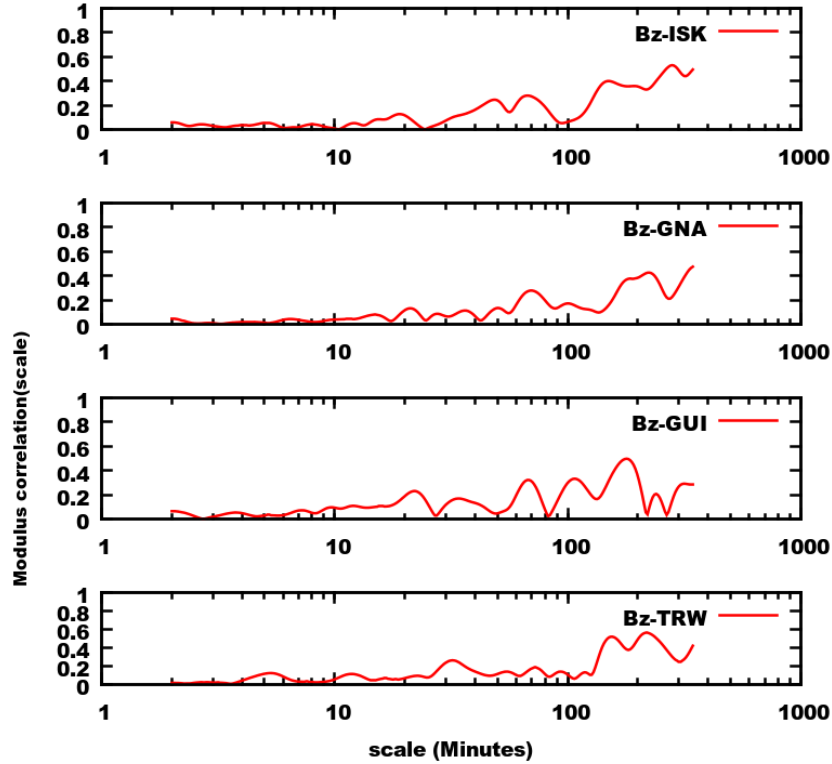


Figure 5.88 - From top to bottom, the panels represent the correlation of IMF-Bz with ΔH -component from geomagnetic observatories ISK, GNA TRW and GUI during quiet periods from 18 to 21 July, 2006.

Partial conclusions

The CWT analysis is an important analysis tool due to its skill of good properties of localization in time and frequency domains. From the analyses of our cases, multi-scale structures and their temporal locations have been easily identified. Embedment of some small-scale features within large-scale feature are noticed.

Using DWT, some similar characteristics effects of HILDCAAs are visible on the results of the wavelet analysis on ΔH -component for all observatories. In the results, the larger amplitude of the wavelet coefficients marks the geomagnetic activity, an indicator of that some process of impulsive energy transfer is going on. By careful inspection, one can observe that magnetic observatories do not show the identical pattern of wavelet coefficients in different decomposition levels. This may be due to several reasons, for example: type of magnetometer used, local time, ground conductivity and Sq current effects. However, the larger amplitudes of the wavelet coefficients presence in magnetic observatories indicate that the whole magnetosphere is globally affected. Hence, by the use of this analysis, the intrinsic processes of energy transfer during HILDCAA at mid latitudes are being surveyed.

Finally, the results of wavelet modulus correlation show correlation of IMF-Bz with ΔH -component from ISK, GNA, TRW and GUI and also show scale dependent characteristic. We use similar procedures for the other two events. Both events show significant perturbations on H and ΔH components at the time of HILDCAAs. However, the level of perturbations for each event show different. This is because we analyze three different events that were caused by different interplanetary structures. The results of wavelet techniques (CWT, DWT and wavelet modulus correlation) observed similar phenomena to the previous events but different trends for each observatory. When observing these results, it can be suggested that during HILDCAAs, mid latitude observatories were dominated by a system of current on magnetosphere known as ring current and its effects were recorded on magnetograms.

5.5 Study of field aligned current (FAC) with D-component (east-west) and interplanetary electric field (E_y) during three different HILDCAA events

According to Sun et al. (1984), the field aligned currents (FACs) are the primary sources for the eastward-westward magnetic field perturbations in the mid latitudes whereas equatorial and auroral electrojets are the main causes at low and high latitudes. Iijima and Potemra (1976) studied the global characteristics of the field aligned currents by using magnetometer observations from TRIAD satellite and discovered two components of FACs. The Region 1 currents are located near the poleward boundary typically at magnetic latitudes 70-75 degrees and flow into the ionosphere in the pre-midnight to forenoon sector (2300-1100 MLT) and away from the ionosphere in the afternoon to pre-midnight sector (1300-2300 MLT). On the other hand, the Region 2 currents are observed near the equatorward boundary and flow into the ionosphere in the afternoon to pre-midnight sector and away from the ionosphere during the pre-midnight to forenoon sector. In this section, we are discussing the low latitude geomagnetic field variations in response to various interplanetary conditions and their associated field aligned currents during three different HILDCAA events. The analysis takes into account only geomagnetic observatory of Vassouras.

Case 1: Non-storm HILDCAA which occurred on 20-23 April 2003

Figure 5.89 depicts the calculated Field Aligned Current density (J_{\parallel} in μAm^{-2}), Interplanetary Electric Field (E_y in mV/m), Declination (ΔD in nT) and Horizontal (ΔH in nT) components of geomagnetic field as recorded at Vassouras for the non-storm HILDCAA which occurred on 20-23 April 2003. The horizontal line with double arrows presented on ΔH component at the last panel of this figure shows the HILDCAA interval. The first panel of this figure shows the FACs density. It is derived as suggested by Iijima and Potemera (1982). During the event, it shows continuous fluctuation approximately between 2 to 4 μAm^{-2} . The characteristics of FACs were studied by Chun and Russel (1997) and explained that during geomagnetic storms the regions of FACs expand and are seen in pre-midnight and post-midnight sectors. The second panel of this figure depicts the interplanetary electric (E_y) field which shows eastward-westward perturbations during the event. The declination component (ΔD) at the third panel of this figure shows just opposite nature with field aligned current. It shows westward when FAC eastward and eastward when FAC westward during the event. The ΔH component at the last panel of

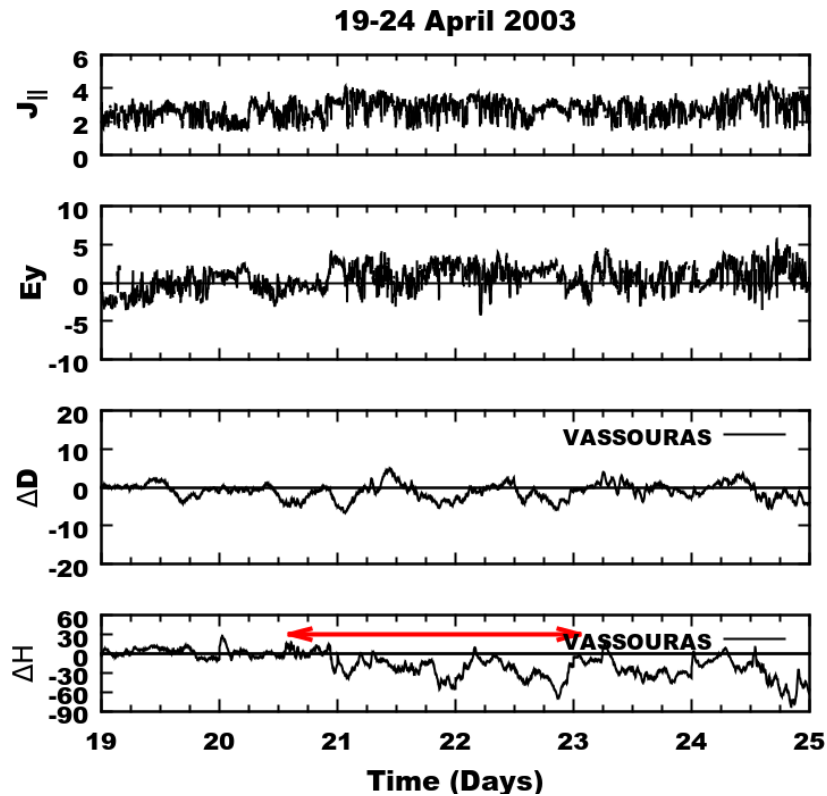


Figure 5.89 - From top to bottom, the panels represent Field Aligned Current density (J_{\parallel} in $\mu A m^{-2}$), Interplanetary Electric Field (E_y in mV/m), Declination (ΔD in nT) and Horizontal (ΔH in nT) components of geomagnetic field as recorded at Vassouras for the non-storm HILDCAA event. The HILDCAA interval is marked by red horizontal arrows in ΔH panel. It occurs during 20-23 April 2003.

this figure also shows negative fluctuation which indicates that smoothly injection of charged particles has been continuously carried on inside the magnetosphere at the time of HILDCAA. A more detailed description about the field aligned current with solar wind conditions can be found in Wang et al. (2006), Cheng et al. (2011). In order to verify the relationship of FAC with component of IMF, interplanetary electric field (E_y) and D-component, we have used some wavelet techniques (CWT, DWT and wavelet modulus correlation) and cross-correlation which are applied as follows.

Figure 5.90 shows the results of the wavelet analysis (scalograms) for FAC (left) and ΔD (right) during the non-storm HILDCAA occurred on 20-23 April 2003. In the figures, the horizontal axes represents the time in days and vertical axes represent the scale in minutes. The color indicated on the right vertical part of each scalogram gives the amplitude of each scale (or frequency). It represents the \log_2 of the squared

wavelet coefficient obtained from the signal analysis. The same dataset that we used above are used but only for HILDCAA interval. When analyzing the scalograms, the characteristic of FAC signal shows highly variable in time. The wavelet powers of the highest spectral variabilities are seen at time scales between 50-300 minutes for FAC and 150-300 minutes for ΔD . These results show that longer periodicities between 150-300 minutes are most continuous on the series. When observing these results, it can be noticed that some characteristics of the solar wind are visible on scalograms. It is in agreement with the equation used to calculate FAC derived from interplanetary parameters. ΔD does not present a continuous behavior, i.e. it occurs as a sporadic behavior triggered by some specific mechanism.

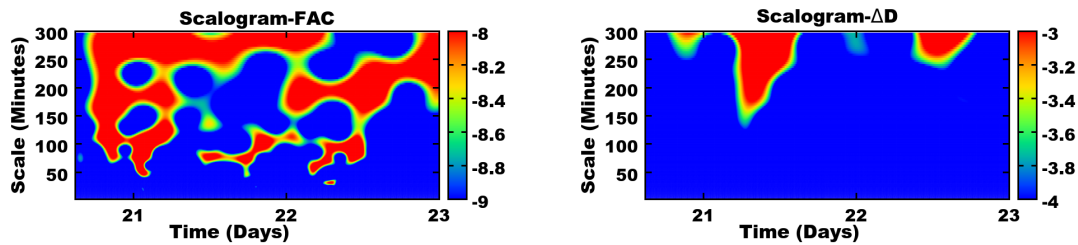


Figure 5.90 - Scalograms for FAC (left) and ΔD (right) during HILDCAA event on 20-23 April 2003.

Figure 5.91 shows the discrete wavelet transform for ΔD for the same event. Here we used Daubechies order 2 orthogonal wavelet transform of seven levels ($j= 1, 2, 3, 4, 5, 6, 7$) denoted by $d^1, d^2, d^3, d^4, d^5, d^6$ and d^7 . For the chosen wavelet of frequency 0.66667 and sampling rate of one minute, the pseudo periods of the seven levels were 3, 6, 12, 24, 48, 96, 192 minutes. The figure shows the amplitude of squared wavelet coefficients. In the panels from top to bottom, the data series and the 7 levels of squared wavelet coefficients are shown. The higher amplitudes of square wavelet coefficients present in this figure indicate singularities during HILDCAA event. On the other-hand, the presence of significant wavelet coefficients indicate freshly injection of charged particle at the time of HILDCAA. The red marked color in each first panel represents the HILDCAA preceding time. The higher and smaller amplitude of squared wavelet coefficients are present for all levels. Taking into account the amplitude of squared wavelet coefficients, it is found that ΔD are continuously affected at the time of HILDCAA through the influence of solar wind and interplanetary magnetic field fluctuations. At that time, there was freshly

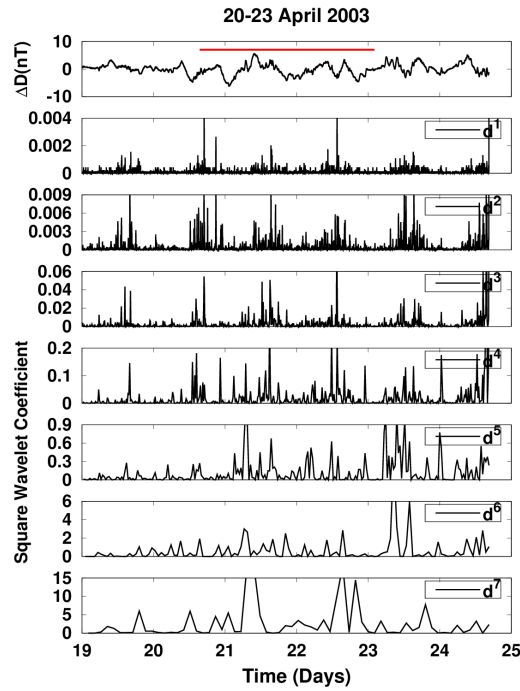


Figure 5.91 - Daubechies wavelet coefficients d^j (for $j= 1, 2, 3, \dots 7$) ΔD during HILDCAA event occurred on 20-23, April 2003. The red color identify where the HILDCAA events are happening.

injection of charged particle inside the mid-low latitudes.

Figure 5.92 shows the results of wavelet modulus correlation of FAC and ΔD with the components of interplanetary magnetic field (B_y and B_z) for the same event. The horizontal axis represents the scale in minutes and the vertical axis represents the modulus correlation (scale). In each panel, the scale of 1, 10, 100 and 1000 are labeled in horizontal axis. The first and the second panels of this figure represent the wavelet modulus correlation for B_y -FAC and B_y - ΔD with peaks modulus correlation about 0.6 and 0.5 at time scales approximately 200 and 190 minutes respectively. Similarly, the third and the fourth panels give the wavelet modulus correlation for B_z -FAC and B_z - ΔD with peaks modulus correlation about 0.8 and 0.5 at time scales approximately 320 and 100 minutes respectively. When observing these results, it is seen that modulus correlations are scale dependent. It is also seen that both FAC and ΔD are correlated with components of interplanetary magnetic fields (B_y and B_z) at the time of HILDCAA.

Figure 5.93 shows the results of classical cross correlation between FAC and ΔD , FAC and E_y and E_y and ΔD during the HILDCAA event on 20-23 April 2003. The

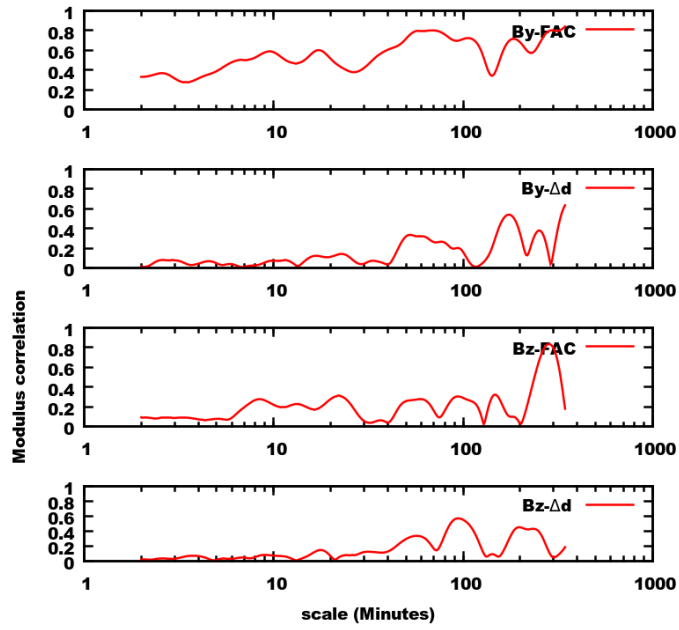


Figure 5.92 - From top to bottom, the panels represent the correlation of FAC and ΔD with the components of interplanetary magnetic field (B_y and B_z) during the HILDCAA event on 20-23 April 2003.

horizontal axis represents the time in minutes and the vertical axis represents the range of cross-correlation. In this figure, FAC and E_y do not show any correlation (less than 0.3) with ΔD during this event. But FAC and E_y show a relative peak correlation about -0.6 at zero time lag. When observing these results, it is noticed that E_y show negative correlation with FAC. The negative cross-correlation are basically associated with the phase shift in the the variation trend in FAC and E_y (RAWAT et al., 2009). Such a correlation of FAC and E_y may be due to the direct causative role of solar wind electric field in the development of high latitude asymmetry (CLAUER; MCPHERRON, 1980), a consequence of the fundamental interplanetary parameters taking part in the mechanisms.

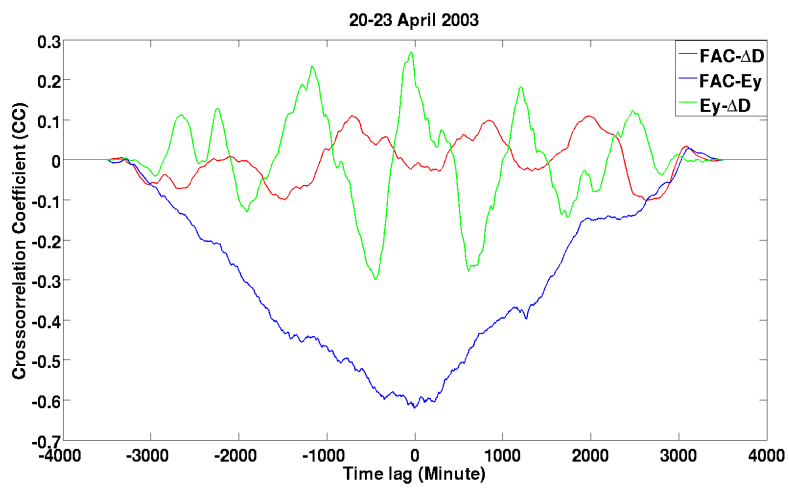


Figure 5.93 - Cross-correlation of FAC and E_y with ΔD during the HILDCAA event on 20-23 April 2003. Where blue, green and red lines represent the cross-correlation for $FAC - E_y$, $E_y - \Delta D$ and $FAC - \Delta D$ respectively.

Case 2: HILDCAA preceded by CIR-storm when occurred on 12-15 February 2004

Figure 5.94 shows the Field Aligned Current density (J_{\parallel} in μAm^{-2}), Interplanetary Electric Field (E_y in mV/m), Declination (ΔD in nT) and Horizontal (ΔH in nT) components of geomagnetic fields as recorded at Vassouras for the HILDCAA event on 12-15 February 2004. Starting from top to bottom, the first panel stands for FAC, the second panel for E_y , the third panel for ΔD and the fourth panel for ΔH . The main phase of this storm is considered the time of sharp depression in ΔH at the last panel of this figure. Similarly, the recovery phase or the HILDCAA interval is characterized by the double arrow present in ΔH . During the main phase, the peak value of FAC was approximately $6 \mu Am^{-2}$ but at the time of HILDCAA, it was fluctuating between 2 to $4 \mu Am^{-2}$. The interplanetary electric field was predominantly eastward having amplitude of $5 mV/m$ during the main phase. But at the time of HILDCAA, it was also highly fluctuating approximately between 3 to $-3 mV/m$. The declination component was also predominantly eastward during the main phase period but at the time of HILDCAA, it shows east-west perturbations.

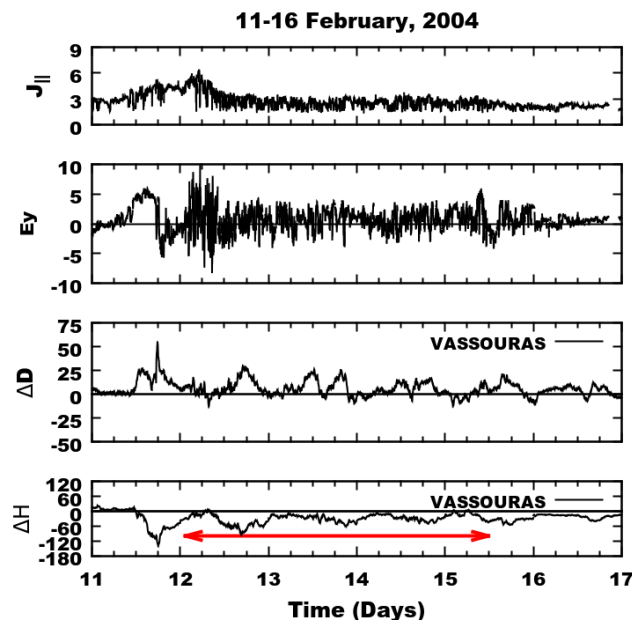


Figure 5.94 - From top to bottom, the panels represent Field Aligned Current density (J_{\parallel} in μAm^{-2}), Interplanetary Electric Field (E_y in mV/m), Declination (ΔD in nT) and Horizontal (ΔH in nT) components of geomagnetic field as recorded at Vassouras for the non-storm HILDCAA event. The HILDCAA interval is marked by red horizontal arrow in ΔH panel. It occurs during 12-15 February 2004.

Figure 5.95 represents the scalogram for FAC and ΔD . Like the scalogram for non-storm HILDCAA, FAC shows different power areas at different times and scales. But during this event, ΔD shows continuous periodicity at time scale between 100-300 minutes.

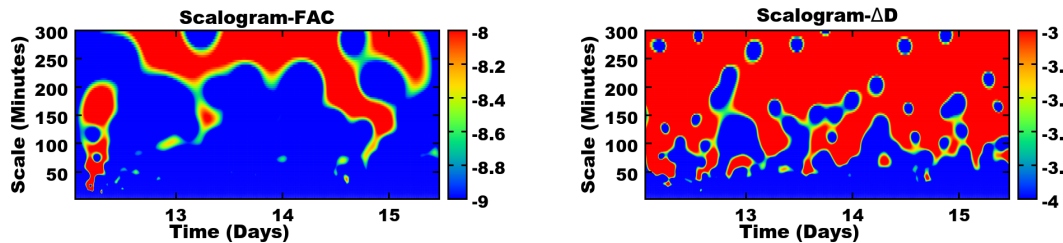


Figure 5.95 - Scalograms for FAC (left) and ΔD (right) during HILDCAA event on 12-15 February 2004.

Figure 5.96 depicts the results obtained from discrete wavelet transform for ΔD for the same event. This figure shows the amplitude of the squared wavelet coefficients for ΔD . Like previous event, this event also shows continuous effect during HILDCAA on ΔD . It means deposition of particles and magnetic effects as consequence. It allows to notice variation of the coupling mechanisms among the several parts of magnetosphere-ionosphere system.

Figure 5.97 represents the wavelet modulus correlation of FAC and ΔD with the components of interplanetary magnetic field (B_y and B_z) for the HILDCAA event on 12-15 February 2004. The first panel of this figure shows the peak modulus correlation about 0.8 at time scale approximately 200 minutes for IMF- B_y with FAC. Similarly, the second panel shows the peak modulus correlation about 0.5 at time scales approximately 150 minutes for IMF- B_y with ΔD -component from VSS. Finally, the third and the fourth panels show the peaks about 0.6 and 0.5 at time scales approximately 150 and 60 minutes for IMF- B_z with FAC and ΔD -component respectively. Observing these results, it is noticed that FAC and ΔD are correlated with the components of interplanetary magnetic field (B_y and B_z) and are scale dependent at the time of HILDCAA.

Figure 5.98 gives the cross-correlation of FAC- ΔD , FAC- E_y and E_y - ΔD for the same event. As like previous event, this event also does not show any correlation of FAC and E_y with ΔD . Similarly, the blue line gives the cross-correlation between

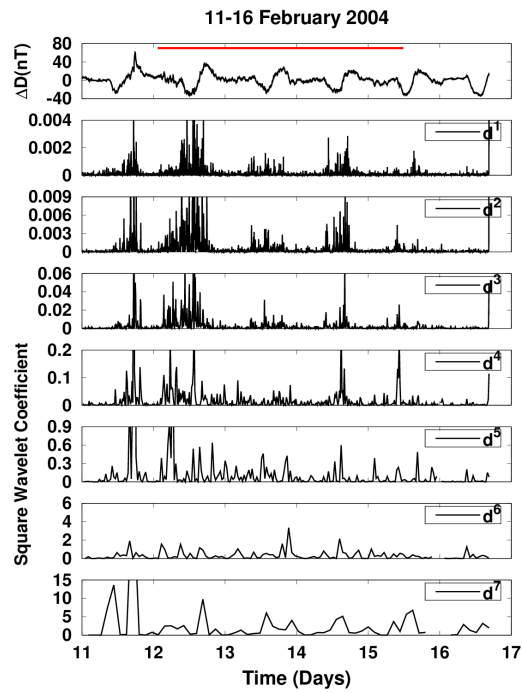


Figure 5.96 - Daubechies wavelet coefficients d^j (for $j= 1, 2, 3, \dots 7$) for ΔD during HILD-CAA event occurred on 12-15 February, 2004. The red color identifies where the HILDCAA events are happening.

FAC and Ey.

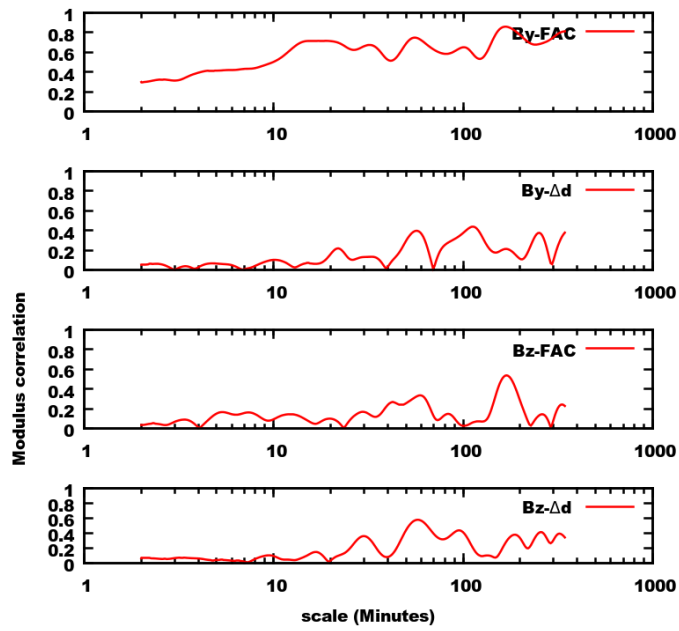


Figure 5.97 - From top to bottom, the panels represent the correlation of FAC and ΔD with the components of interplanetary magnetic field (B_y and B_z) during the HILDCAA event on 12-15 February 2004.

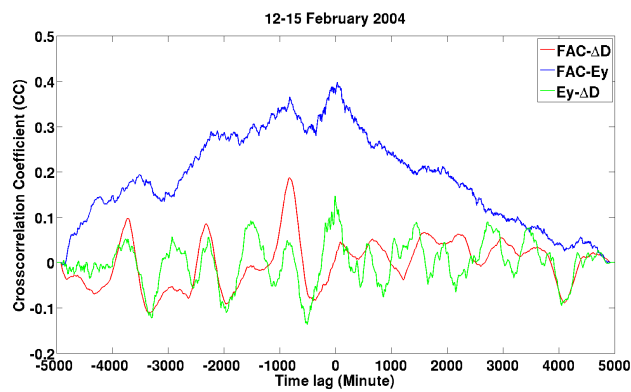


Figure 5.98 - Cross-correlation of FAC and E_y with ΔD during the HILDCAA event on 12-15 February 2004. Where blue, green and red lines represent the cross-correlation for $FAC - E_y$, $E_y - \Delta D$ and $FAC - \Delta D$ respectively

Case 3: An ICME preceding HILDCAA which occurred on 15-18 May 2005

Figure 5.99 gives the Field Aligned Current density (J_{\parallel} in μAm^{-2}), Interplanetary Electric Field (E_y in mV/m), Declination (ΔD in nT) and Horizontal (ΔH in nT) components during the HILDCAA event on 15-18 May 2005. The first panel of this figure gives the FAC in μAm^{-2} . During the main phase, the peak was approximately $10 \mu Am^{-2}$ but at the time of HILDCAA, it was highly fluctuating between 1 to $5 \mu Am^{-2}$. The second panel of this figure gives interplanetary electric field (E_y) in mV/m . It shows peak value of approximately $45 mV/m$ during the storm main phase. But at the time of HILDCAA, it was highly fluctuating approximately between -7 to $7 mV/m$. The third and the fourth panels of this figure represent ΔD and ΔH components of geomagnetic field respectively. During the main phase period, both show sharp depression but at the time of HILDCAA, ΔD shows east-west perturbations and ΔH shows approximately constant negative values except during earlier recovery phase.

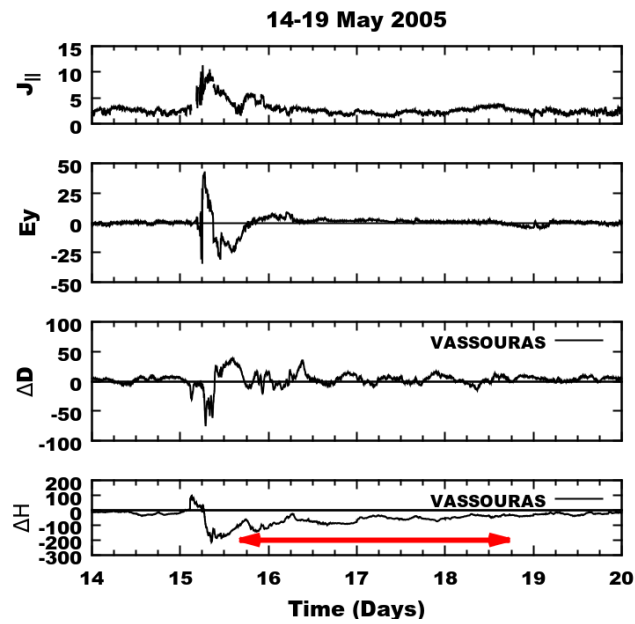


Figure 5.99 - From top to bottom, the panels represent Field Aligned Current density (J_{\parallel} in μAm^{-2}), Interplanetary Electric Field (E_y in mV/m), Declination (ΔD in nT) and Horizontal (ΔH in nT) components of geomagnetic field as recorded at Vassouras for the non-storm HILDCAA event. The HILDCAA interval is marked by red horizontal arrow in ΔH panel. It occurs during 15-18 May 2005.

Figure 5.100 gives the wavelet scalograms for FAC (left) and ΔD (right) for the same event. During this event, FAC shows continuous periodicity at the beginning of HILDCAA. But ΔD shows continuous periodicity as like CIR-preceding HILDCAA. However, the wavelet powers of the highest spectral variabilities are seen at time scales between 50-300 minutes.

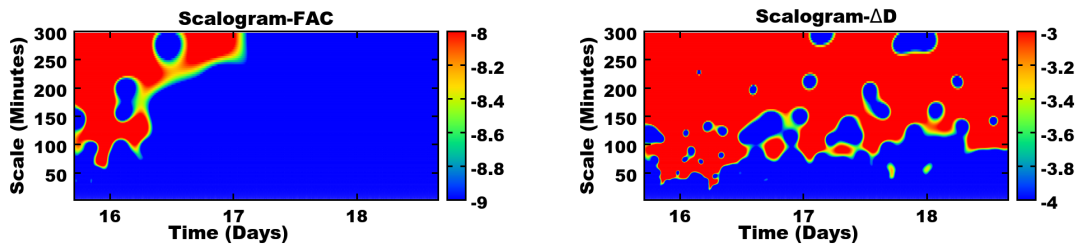


Figure 5.100 - Scalograms for FAC (left) and ΔD (right) during HILDCAA event on 15-18 May 2005.

Figure 5.101 represents the results of DWT for ΔD for the same event. This figure gives the amplitude of squared wavelet coefficients. The interplanetary cause for this storm was the shock driven by an ICME contained a magnetic cloud structure (HA-JRA et al., 2013; OJEDA et al., 2013; OJEDA et al., 2014). The recovery phase begins about 3 days without variations in IMF-Bz. The data series of ΔD shows sharp depression during the main phase period. All the levels except d7 show singularities during this period. It also shows smaller amplitude of squared wavelet coefficients at the time of HILDCAA. This event shows relatively small amplitude of squared wavelet coefficients as compared to other two events. The attenuation of the amplitude of the coefficients during HILDCAA may be connected to the depletion of particles during the coupling processes.

Figure 5.102 gives modulus correlation of FAC and ΔD with the components of interplanetary magnetic field (B_y and B_z) for the HILDCAA event on 15-18 May 2005. B_y -FAC shows peak modulus correlation about 0.9 at time scale approximately 250 minutes. The peak modulus correlation for B_y - ΔD is approximately 0.8 at time scale around 250 minutes. Similarly B_z -FAC shows peak modulus correlation about 0.5 at time scale 190 minutes. Finally B_z - ΔD shows peak modulus correlation about 0.8 at time scale approximately 290 minutes. These results show that FAC and ΔD are correlated with the components of interplanetary magnetic fields (B_y and B_z) during this event.

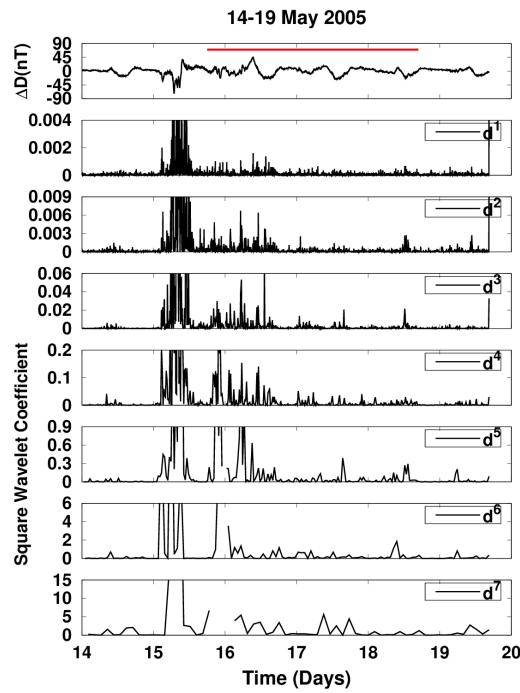


Figure 5.101 - Daubechies wavelet coefficients d^j (for $j= 1, 2, 3, \dots 7$) for ΔD during HILDCAA event occurred on 15-18 May 2005. The red color identify where the HILDCAA events are happening.

Figure 5.103 gives the cross-correlation of FAC and ΔD , FAC and E_y and E_y and ΔD during HILDCAA event occurred on 15-18 May 2005. Like the other two events, this event also does not show any correlation of FAC and E_y with ΔD . But FAC and E_y show very good positive correlation about 0.8 during this event.

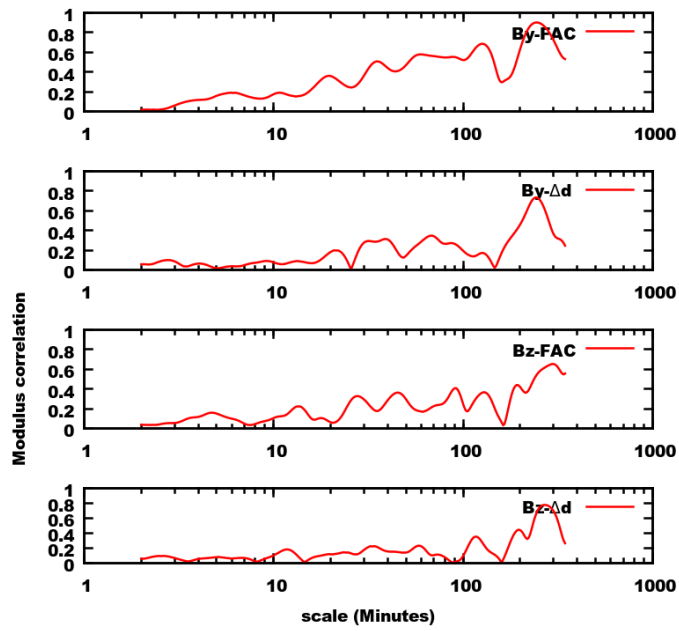


Figure 5.102 - From top to bottom, the panels represent the correlation of FAC and ΔD with the components of interplanetary magnetic field (B_y and B_z) during the HILDCAA event on 15-18 May 2005.

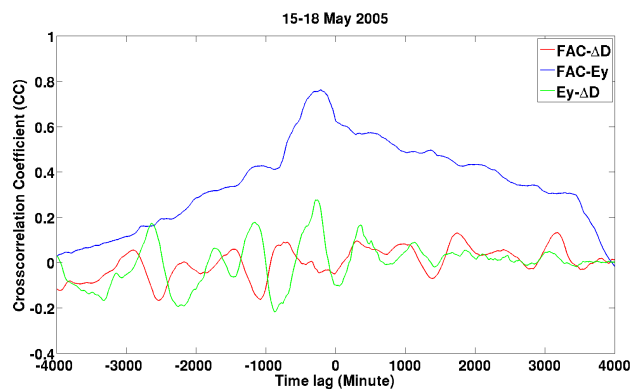


Figure 5.103 - Cross-correlation of FAC and E_y with ΔD during the HILDCAA event on 15-18 May 2005. Where blue, green and red lines represent the cross-correlation for $FAC - E_y$, $E_y - \Delta D$ and $FAC - \Delta D$ respectively

Case 4: quiet periods 18-21 July 2006

Figure 5.104 is calculated by similar procedure to obtain the earlier figures (5.89, 5.94 and 5.99) but refers to a quiet period: 18-21 July 2006. In this figure, we observe a small scale of fluctuations on all parameters. The geomagnetic field variations at low latitude, for instance, to Vassouras observatory, is due to the equatorial electrojet superposed by the ring current affected by a quiescent meridional connection.

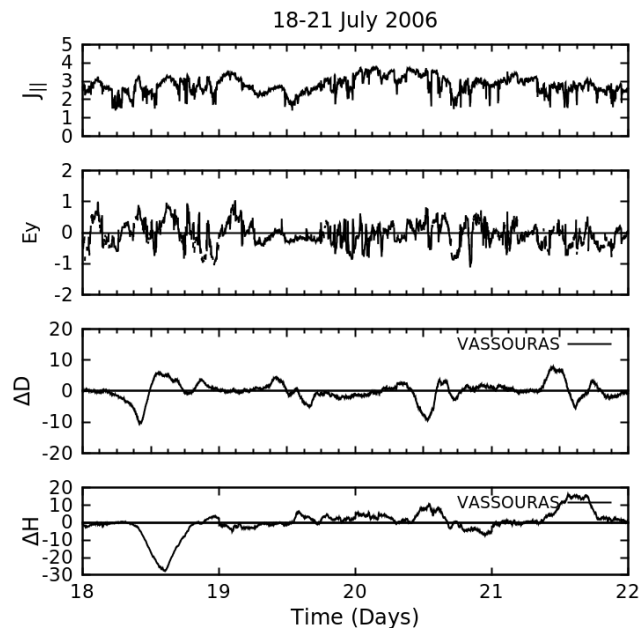


Figure 5.104 - From top to bottom, the panels represent Field Aligned Current density (J_{\parallel} in $\mu A m^{-2}$), Interplanetary Electric Field (E_y in mV/m), Declination (ΔD in nT) and Horizontal (ΔH in nT) components of geomagnetic field as recorded at Vassouras during quiet periods from 18 to 21 July 2006.

Figure 5.105 depicts the wavelet scalograms for FAC (left) and ΔD (right) during this quiet period. In the figures, FAC shows very few scatter wavelet powers at medium to higher time scales while ΔD shows almost continuous periodicity at time scales between 200-300 minutes. Such a small scale fluctuations are related to the sources other than the field aligned currents.

Figure 5.106 represents the results of DWT ΔD during this period. This figure gives the amplitude of squared wavelet coefficients. Compared to the earlier three HILDCAA events, both parameters for the quiet period show the smallest amplitude of squared wavelet coefficients. The reason for that could be attributed basically to

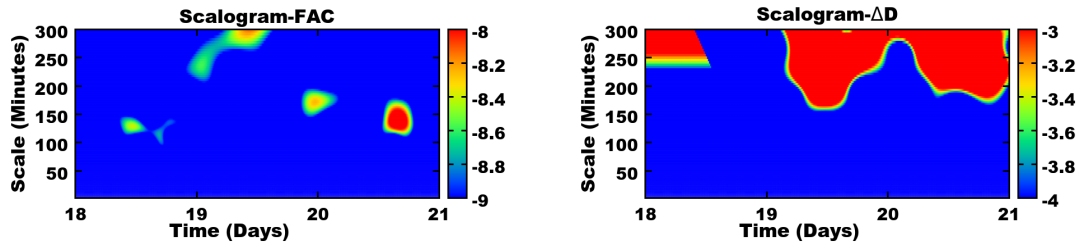


Figure 5.105 - Scalograms for FAC (left) and ΔD (right) during quiet periods from 18 to 21 July 2006.

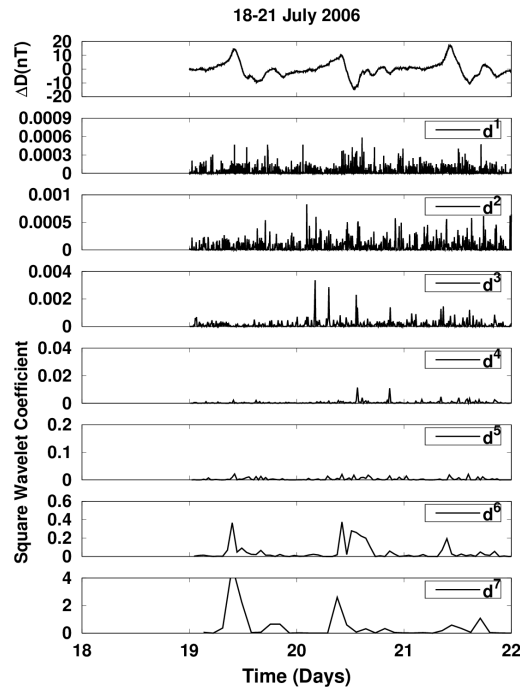


Figure 5.106 - Daubechies wavelet coefficients d^j (for $j= 1, 2, 3, \dots 7$) ΔD during quiet periods from 18 to 21 July 2006.

the background behavior of ring current and ionospheric electrojet.

Figure 5.107 gives modulus correlation of FAC and ΔD with the components of interplanetary magnetic field (B_y and B_z) during quiet periods. As expected, the interplanetary magnetic field components show relative correlation with FAC; but the ΔD presents independence on the magnetic field.

Figure 5.108 gives the cross-correlation of FAC and ΔD , FAC and E_y and E_y and ΔD during the quiet period. Extremely poor correlations were determined using the

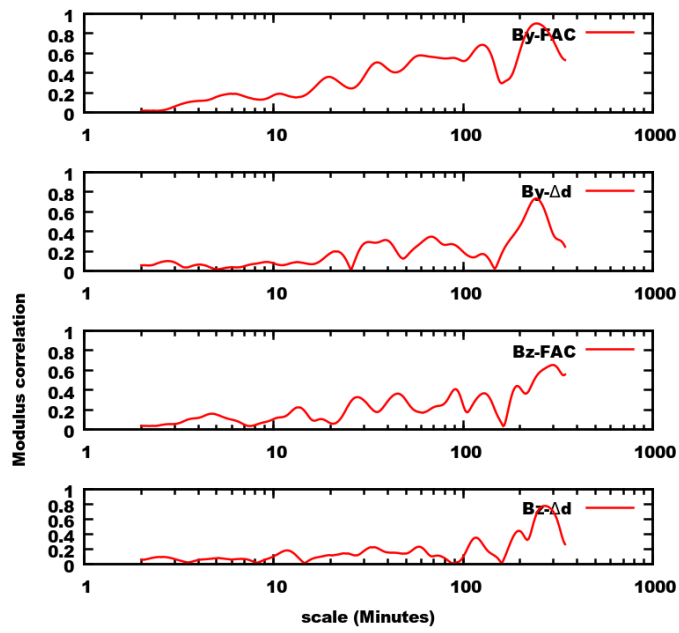


Figure 5.107 - From top to bottom, the panels represent the correlation of FAC and ΔD with the components of interplanetary magnetic field (B_y and B_z) during quiet periods from 18 to 21 July 2006.

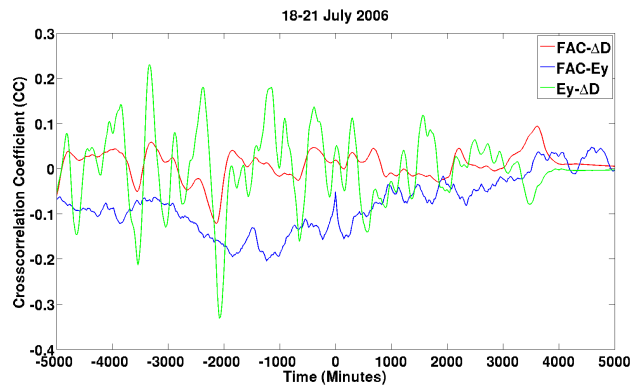


Figure 5.108 - Cross-correlation of FAC and E_y with ΔD during quiet periods from 18 to 21 July 2006. Where blue, green and red lines represent the cross-correlation for $FAC - E_y$, $E_y - \Delta D$ and $FAC - \Delta D$ respectively

parameters.

Partial conclusions

FACs affect the geomagnetic field but with latitudinal and longitudinal peculiarities. In order to study their behavior during HILDCAAs, we have selected the peak and time density of FACs during HILDCAAs and studied its relationship with ΔD component of geomagnetic field from low latitude station Vassouras. They could be examined by using both ground and satellite data. Also, the study is being completed with the use of interplanetary electric field parameter. The conclusion drawn from these studies follows below.

At the time of non-storm HILDCAA, the densities of FACs fluctuated between 0 to $5 \mu Am^{-2}$. The ΔD component shows east-west perturbations between -6 to 5 nT. The analysis of CWT is restricted to the period range 0 to 300 minutes. We use a similar procedure for other two events. For CIR preceding HILDCAA, the peak value of FAC was approximately $5 \mu Am^{-2}$ during the main phase but at the time of HILDCAA, it was fluctuating below $4 \mu Am^{-2}$. The ΔD component shows east-west perturbations between -15 to 30 nT. The results of CWT and DWT show a similar trend to the previous events. The result of wavelet modulus correlation show similar result to the previous events. During this event, only FAC and E_y show positive correlation. Finally for ICME preceding HILDCAA, the peak value of FAC was approximately $20 \mu Am^{-2}$ during the main phase. At the time of HILDCAA, it was highly fluctuating between 0 to $5 \mu Am^{-2}$. The ΔD component shows east-west perturbations between -20 to 40 nT. The CWT and DWT results for this event also show similar trend to the previous events. This event also shows correlation of FAC and ΔD with IMF B_y and B_z . As like HILDCAA preceding by CIR-storm, this event also show positive correlation of FAC with E_y .

As highlighted in the studies of the earlier sections, some peculiar behaviors occur in magnetic records during HILDCAAs. They results are visible from the analysis techniques used.

CWT analysis indicates complex patterns concerning to coupling mechanism between solar wind and the magnetosphere-ionosphere system. The wavelet coefficients highlights possible regions under disturbance on the field aligned currents and ΔD . The highest amplitude of squared wavelet coefficients indicate this disturbance, i.e. freshly injections of charged particle at the time of HILDCAA. All results can be used as characterization of effects evolving during HILDCAAs, sometimes as an indicator that some process of continuous energy transfer is going on and other times as impulsive processes. It confirms how complex these kinds of phenomena evolve in

the magnetosphere-ionosphere system.

Finally, calculations on the cross-correlation for FAC and ΔD with interplanetary magnetic field (B_y and B_z) were evaluated. We also performed this correlation analysis involving interplanetary electric field (E_y). This procedure was done only for HILDCAA interval. It allows understanding the global response at low latitude during HILDCAA. The results are summarized as follows:

- a) FACs intensities are related to HILDCAA interval.
- b) FAC is negatively correlated with E_y during the non-storm HILDCAA but positively correlated during CIR and ICME preceding HILDCAAs.
- c) FAC presents no correlation during geomagnetically quiet interval.
- d) FACs are correlated with the components of interplanetary magnetic field (B_y and B_z) during the events.

Such a correlation of FAC and E_y may be due to the direct causative role of solar wind electric field in the development of high latitude asymmetry.

5.6 Estimation of Polar Cap Potential (PCV) and Merging electric field (Em) during HILDCAAs

The polar cap potential has long been considered as a key parameter for describing the state of the magnetosphere-ionosphere system (BOYLE et al., 1997), which helps to understand the coupling process between solar wind and this system. In this work, we estimated polar cap potential and merging electric field as suggested by Kan and Lee (1979) during three different HILDCAA events. We examine the interplanetary electric field, merging electric field and polar cap potential, and also study the role of PC and AL indices to monitor polar cap activity during HILDCAAs.

Case 1: Non-storm HILDCAA which occurred on 20-23 April 2003

Figure 5.109 shows the variation of interplanetary electric field (E_y in mV/m), merging electric field (E_m in mV/m), polar cap potential (PCV in kv), polar cap index (PCI in mV/m) and AL (nT) for the HILDCAA event on 20-23 April 2003. The horizontal red line with double arrow on AL index at the the last panel shows the HILDCAA interval. During the event, E_y shows significant east-west perturbations. Merging electric field shows high level of fluctuation through out the event and has an average value of 1.83 mV/m. More details about the E_m can be found in Vennerstrqm et al. (1991), Moon (2012). The polar cap potential (PCV) shows continuous variations during the event and has an average of 81.83 kv. The parameters PCV and E_m are derived as suggested by Kan and Lee (1979). In this figure, the nature of variations on both PCI and AL indices are very well-anti-correlated which shows very close relation between them. The HILDCAA time averages for them are -264.98 nT and 2.08 mV/m respectively. In order to verify the role of PCI and AL indices on polar cap potential and merging electric field, we have implemented some wavelet techniques (CWT and DWT) and cross-correlation which are explored below.

Figure 5.110 shows the scalograms for AL (left) and PCI (right) indices for the same event. In this figure, the horizontal axis represents the time in days and the vertical axis represents the scale in minutes. The scale of color on the right side of the second panel has same unit of real data. The scalogram of AL shows different power areas at different times and scales. The power areas of the highest intensity covered by red color are seen at time scales between 150-300 minutes. Similarly, the power areas covered by yellow colors are seen at time scales between 100-300 minutes. The less intense power areas covered by green color are seen at several places. The right side of Figure 5.110 gives the scalogram for PC index. It shows the strong power areas covered by red color at time scales approximately between 80-300 minutes. In both

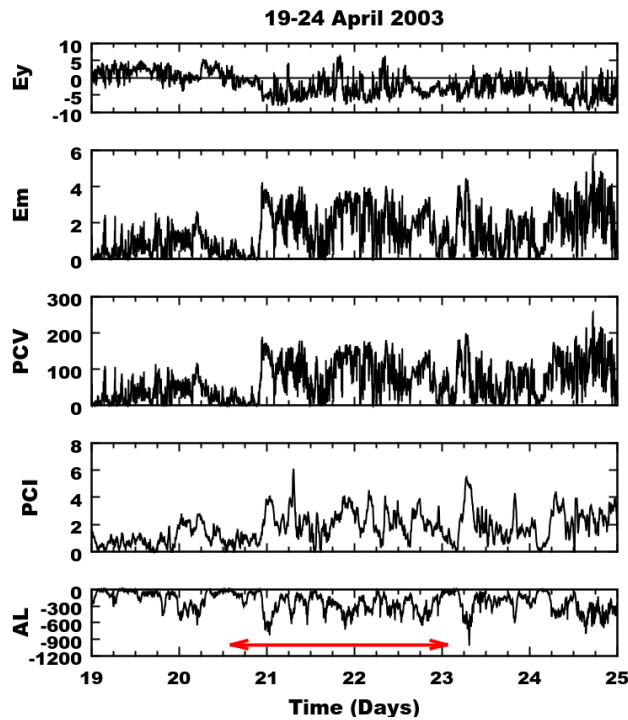


Figure 5.109 - From top to bottom, the panels represent the variations of interplanetary electric field (Ey in mV/m), merging electric field (Em in mV/m), polar cap potential (PCV in kv), and geomagnetic index PC (mV/m) and AL (nT) for the non-storm HILDCAA event. The HILDCAA interval is marked by red horizontal arrow in AL panel. It occurs during 20-23 April 2003.

scalograms, the characteristic of signals with highly variable in time with presence of continuous periodicities are presence at higher time scales between 150-300 minutes. However, the wavelet powers of the highest spectral variabilities are seen at time scales between 10-300 minutes for AL and 80-300 minutes for PCI . These results show that longer periodicities between 150-300 minutes are most continuous on the series. When Observing these results, it can be noticed that some characteristics effects during HILDCAA are seen on both indices. These characteristics show that both AL and PC indices were highly disturbed at the time of HILDCAA.

Figure 5.111 represents the results of discrete wavelet transform for AL and PCI indices for the same event. The Daubechies order 2 orthogonal wavelet transform of seven levels ($j= 1, 2, 3, 4, 5, 6, 7$) has been used for this analysis. The seven levels are denoted by $d^1, d^2, d^3, d^4, d^5, d^6$ and d^7 . For the chosen wavelet of frequency 0.66667 and sampling rate of one minute, the pseudo periods of the seven levels were 3, 6, 12, 24, 48, 96, 192 minutes. The red marked color in 5.110 each first panel represents the HILDCAA preceding time. The left side of this figure gives DWT for AL . It

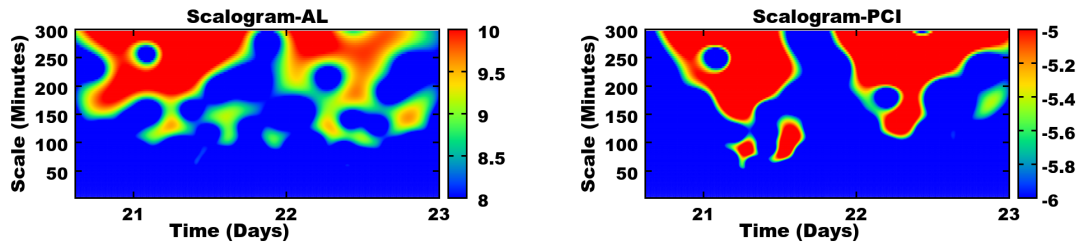


Figure 5.110 - Scalograms for AL (left) and PCI (right) during HILDCAA event on 20-23 April 2003.

shows singularity only at d^2 level. But higher and smaller amplitude of squared wavelet coefficients are present on all levels. However, the amplitude of squared wavelet coefficients for each level are different. Similarly, the right side of this figure gives the result of DWT for PCI. It shows singularities on first four decomposition levels (d^1 , d^2 , d^3 , and d^4) at the time of HILDCAA. It also shows singularities after this event which is related to another HILDCAA event. This index shows relatively larger amplitude of squared wavelet coefficient as compared to AL index. When Observing these amplitude of squared wavelet coefficients, it can be concluded that both indices are highly disturbed and freshly injection of charged particle are carried on at high latitudes during the HILDCAA. A more detailed description about the injection of charged particle inside the low, mid and high latitudes of the ionosphere and magnetosphere during geomagnetic disturbances can be found in Morioka et al. (2003).

The left side of Figure 5.112 shows the results of cross correlation between PCI-AL, PCI-SYM (H), Ey-PCI and Bz-PCI for the same event. The horizontal axis represents the time in minutes and the vertical axis represents the range of cross-correlation. The black line of this figure shows the relationship between PCI-AL, demonstrates the high level of correlation (-0.9). Similarly, the red line shows the relationship between PCI-SYM-H with very good correlation of -0.9. Other two lines, blue and pink represent the cross correlation of Ey-PCI and Bz-PCI with the coefficients of 0.7 and -0.7 respectively. According to this figure, the correlation coefficients of PCI-AL and PCI-SYM-H are higher than Ey-PCI and Bz-PCI. As we have already mention that AL index is used to monitor westward electrojet in the DP2 current system (a current produces by magnetospheric electric convection field and mainly composed of electric Hall currents) (CHAPMAN; BARTELS, 1962; KIKUCHI et al., 2000) whereas PCI is associated to field aligned currents flowing to the polar cap (RIDLEY; KIHN, 2004). The high cross-correlation between PCI-

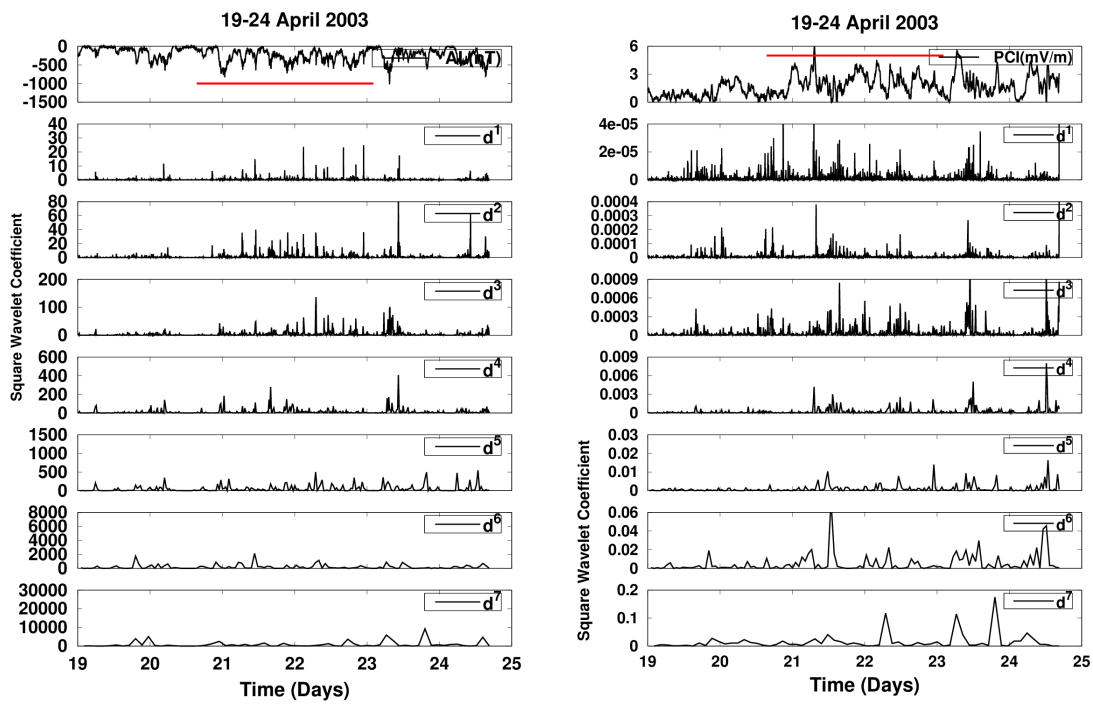


Figure 5.111 - Daubechies Wavelet coefficients d^j (for $j= 1,2,3,\dots,7$) for AL (left) and PC (right) indices during HILDCAA event occurred on 20-23 April 2003. The red color identifies where the HILDCAA events are happening.

AL indicates the link between underlying current systems in the ionosphere during HILDCAA. Similarly, the right side of Figure 5.112 depicts the results of cross correlation between PCV-AL, PCV-SYM (H), Ey-PCV and Bz-PCV for the same event. This figure shows very good relationship of PCV with AL, SYM-H, Ey and Bz with the coefficients of -0.9, -0.9, 0.9 and -0.9 respectively. These results shows that PC and AL indices are well correlated to PCV, Ey and Bz during the HILDCAA interval and provide the weighty argument to support the role for the monitoring the magnetosphere (TROSHICHEV et al., 2011).

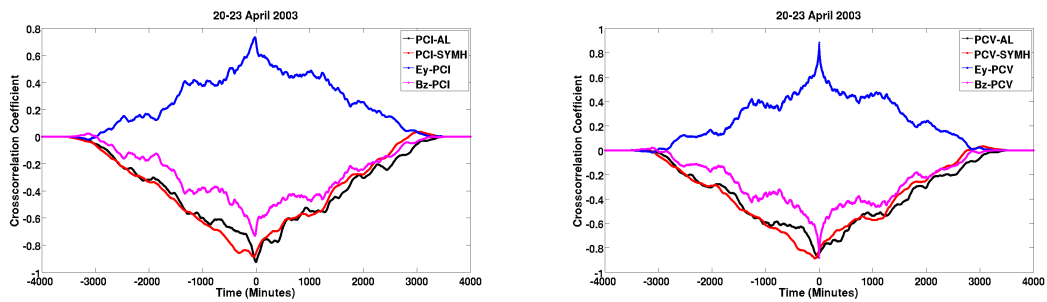


Figure 5.112 - (Left panel) Cross correlation between PCI and AL (black line), PCI and SYM-H (red line), Ey and PCI (blue line) and Bz and PCI (pink line). (right Panel) Cross correlation between PCV and AL (black line), PCV and SYM-H (red line), Ey and PCV (blue line) and Bz and PCV (pink line) for the HILDCAA event on 20-23 April 2003.

Case 2: HILDCAA preceded by CIR-storm which occurred on 12-15 February 2004

Figure 5.113 shows the variation of interplanetary electric field (E_y in mV/m), merging electric field (E_m in mV/m), polar cap potential (PCV in kv), polar cap index (PCI in mV/m) and AL (nT) for the same event. The horizontal red line with double arrow on AL index at the the last panel shows the HILDCAA event. During the main phase, E_y changes from negative value to positive value and reaches the maximum value being $5 mV/m$, the merging electric field was recorded being the maximum value of approximately $7 mV/m$, polar cap potential recorded being approximately $250 kv$, polar cap index had also reached the maximum value recorded as $5 mV/m$ and the AL index reached the minimum value recorded around $-1200 nT$. But at the time of HILDCAA, the IEF (E_y) shows significant east-west perturbation. The merging electric field also shows strong oscillation and the HILDCAA time average is $1.86 mV/m$. The variation in polar cap potential is similar to merging electric field with an average of $83.32 kv$. Both PCI and AL indices show intense activity and the HILDCAA time averages for them are $2.29 mV/m$ and $-284.94 nT$ respectively. The HILDCAA time averages value obtained in this event shows slightly greater than previous event for all parameters. It may be related to higher level of Alfvénic fluctuations in IMF-Bz (GUARNIERI et al., 2006).

Figure 5.114 depicts the scalograms for AL and PCI during HILDCAA event on 12-15 February 2004. In this event, for both indices, the wavelet powers of the highest spectral variabilities are seen at time scales between 80-300 minutes. Like previous event, the longer periodicities between 200-300 minutes are more continuous on the series.

Figure 5.115 is similar to Figure 5.111 but refers to the HILDCAA preceded by CIR-storm occurred on 12-15 February 2004. Like previous results, the singularities present in these figures also represent the discontinuities associated with shocks and higher and smaller amplitude of squared wavelet coefficients represent the energy injection inside the polar cap during the HILDCAA (MENDES et al., 2005; OJEDA et al., 2014; KLAUSNER et al., 2014b). Taking into account the amplitude of squared wavelet coefficients, it is found that PCI index shows relatively higher coefficient of squared wavelet coefficients as compared to AL index.

The left side of Figure 5.116 shows the results of cross correlation between PCI-AL, PCI-SYM-H, E_y -PCI and Bz-PCI for the same event. The representation of horizontal and vertical axes are same as like previous event. When observing this figure,

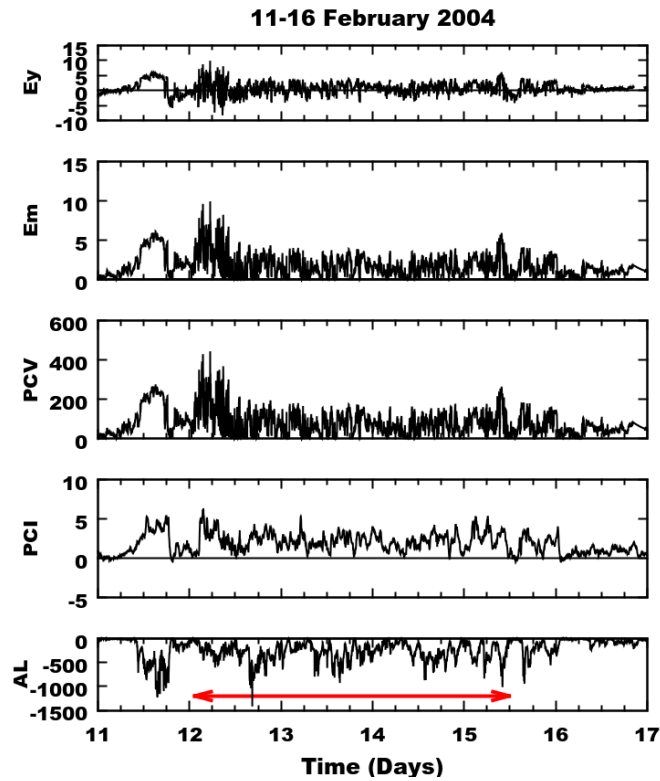


Figure 5.113 - From top to bottom, the panels represent the variations of interplanetary electric field (Ey in mV/m), merging electric field (Em in mV/m), polar cap potential (PCV in kv), and geomagnetic index PC(mV/m) and AL(nT) for the non-storm HILDCAA event. The HILDCAA interval is marked by red horizontal arrow in AL panel. It occurs during 12-15 February 2004.

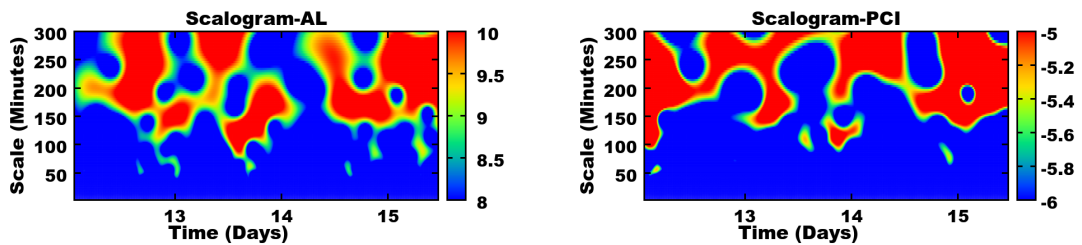


Figure 5.114 - Scalograms for AL (left) and PCI (right) during HILDCAA event on 12-15 February 2004.

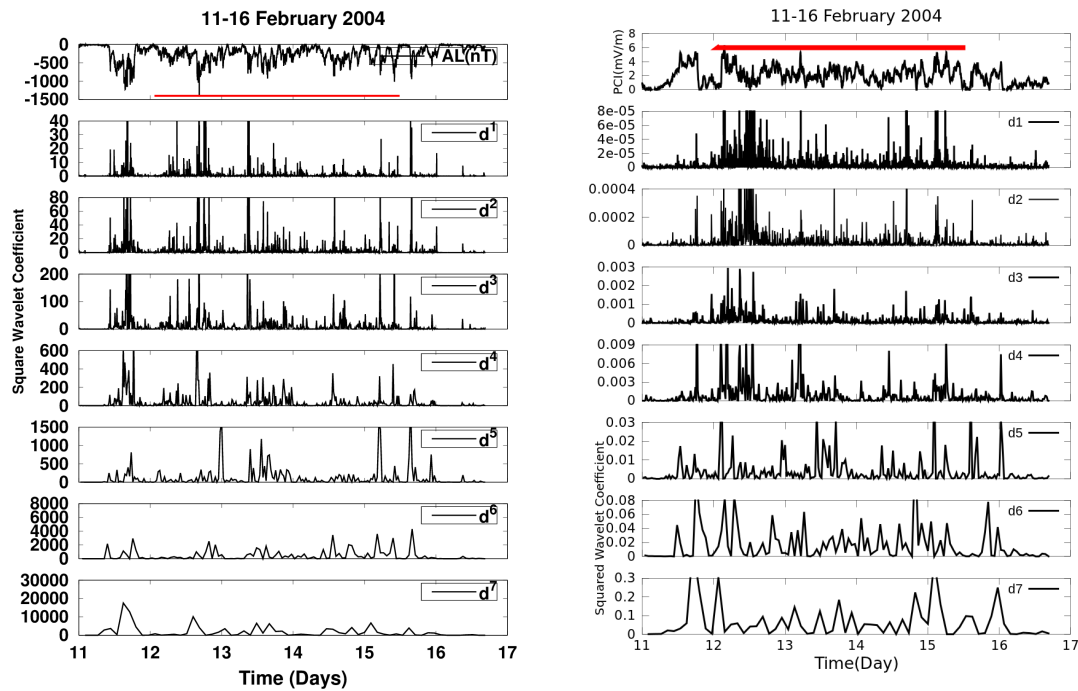


Figure 5.115 - Daubechies Wavelet coefficients d^j (for $j= 1,2,3,\dots,7$) for AL (left) and PC (right) indices during HILDCAA event occurred on 12-15 February 2004. The red color identifies where the HILDCAA events are happening.

the coefficients of cross-correlation for PCI-AL, PCI-SYM-H, Ey-PCI and Bz-PCI are approximately -0.8, -0.9, 0.3 and -0.5 respectively. Compared to previous events, the coefficients of cross correlation for AL shows relatively lower for all parameters. However, in both cases, Bz and Ey show weak correlation with AL. As we know that during the geomagnetic storms, the primary source of the ring current is terrestrial in origin (KRIMIGIS; SARRIS, 1985; HAMILTON et al., 1988; SHELDON; HAMILTON, 1993) and the O^+ ion is the dominant contributor (LENNARTSSON; SHARP, 1982; MOORE et al., 1999; LOTKO, 2007) which shows that magnetospheric processes are capable for energizing low-energy ionospheric ions and transporting them from the ionosphere to the magnetotail and back into the inner magnetosphere (CHAPPELL et al., 1987). Thus, during HILDCAA, the ionosphere may be a significant sources for the development of ring current. Similarly, the right side of Figure 5.116 depicts the results of cross correlation between PCV-AL, PCV-SYM-H, Ey-PCV and Bz-PCV for the same event. In this figure, except for Ey, PCV shows very good correlation with all other parameters.

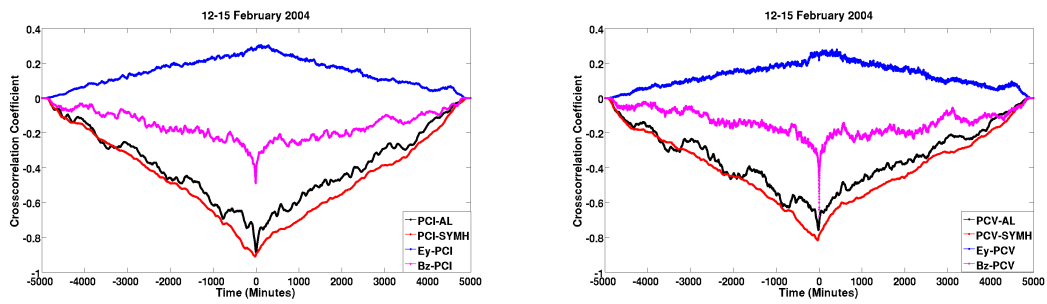


Figure 5.116 - (left panel) Cross correlation between PCI and AL (black line), PCI and SYM-H (red line), Ey and PCI (blue line) and Bz and PCI (pink line). (right panel) Cross correlation between PCV and AL (black line), PCV and SYM-H (red line), Ey and PCV (blue line) and Bz and PCV (pink line) for the HILDCAA event on 12-15 February 2004.

Case 3: An ICME preceding HILDCAA which occurred on 15-18 May 2005

Figure 5.117 shows the variation of interplanetary electric field (E_y in mV/m), merging electric field (E_m in mV/m), polar cap potential (PCV in kv), polar cap index (PCI in mV/m) and AL(nT) for the same event. During the main phase, E_y shows east-west perturbation and reaches the maximum value being approximately 40 mV/m, E_m was recorded being the maximum value of approximately 45 mV/m, PCV recorded being 2000 kv, PCI had reached the maximum value being 10 mV/m and the AL index reached the minimum value around -1500 nT. At the time of HILDCAA, E_y shows east-west perturbation for some hours than after it shows almost eastward oscillation for the entire event, E_m also shows strong eastward oscillation and has an average of 2.8 mV/m, PCV also shows significant variation and has an average of 125 kv, both PCI and AL show intense activity and the averages for them are 2.53 mV/m and -385.44 nT, respectively. These results show that the HILDCAA time average for E_y , PCV, PCI and AL are higher for this event as compared to other two.

Figure 5.118 gives the results obtained from scalograms for AL (left) and PCI (right) for the same event. During this event, AL index show wavelet power of the highest spectral variabilities at time scale between 25-300 minutes while PCI shows at time scale between 100-300 minutes. In this event, AL shows the longer periodicities between 150-300 minutes are more continuous on the series. But PCI shows wavelet powers of lesser and higher intensities only at higher time scales.

Figure 5.119 represents the results obtained from DWT for AL (left) and PCI (right) for the same event. During the main phase, AL shows singularities for all levels except d_7 . At the time of HILDCAA, the singularities are present at d^1 , d^2 , d^3 , d^4 , d^5 and d^6 levels. At that time, higher and smaller amplitude of squared wavelet coefficients are present for all levels. Similarly, PCI shows singularities for all levels during the main and earlier recovery phases. It shows relatively very small amplitude of squared wavelet coefficients at the time of HILDCAA. These results shows that both indices are severely affected during the main phase period but at the time of HILDCAA, AL shows relatively higher amplitude of squared wavelet coefficients.

The left side of Figure 5.120 gives the results obtained from cross-correlation for the same event. When observing this figure, it is noticeable that the peaks cross-correlation between PCI-AL, PCI-SYM-H, E_y -PCI and Bz-PCI are approximately -0.9, -0.95, 0.7 and -0.7 respectively. Where E_y and Bz show time lag of some minutes

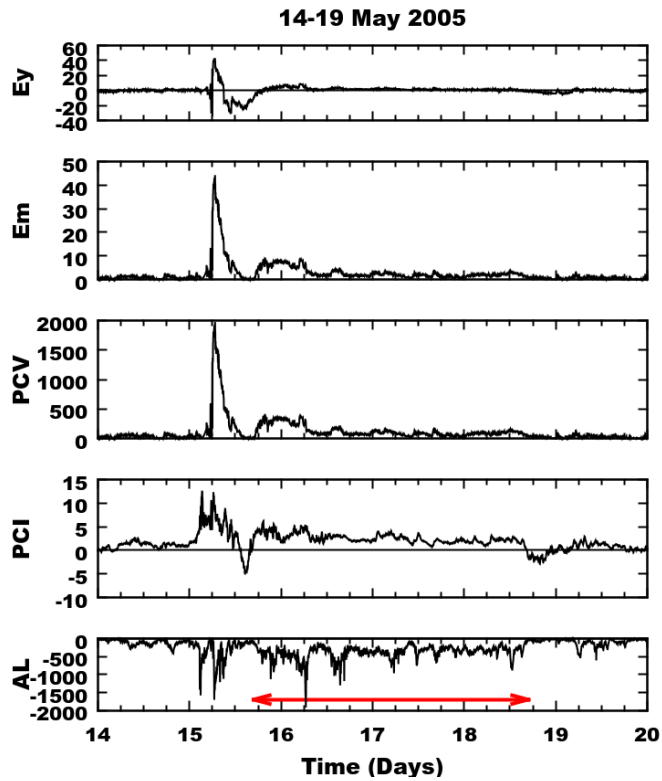


Figure 5.117 - From top to bottom, the panels represent the variations of interplanetary electric field (E_y in mV/m), merging electric field (E_m in mV/m), polar cap potential (PCV in kv), and geomagnetic index PC (mV/m) and AL (nT) for the non-storm HILDCAA event. The HILDCAA interval is marked by red horizontal arrow in AL panel. It occurs during 15-18 May 2005.

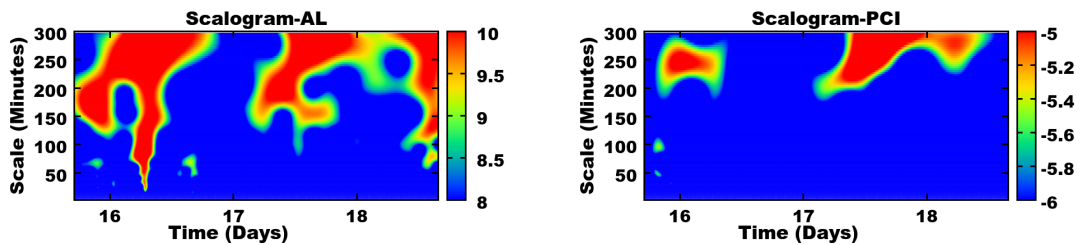


Figure 5.118 - Scalograms for AL (left) and PCI (right) during HILDCAA event on 15-18 May 2005.

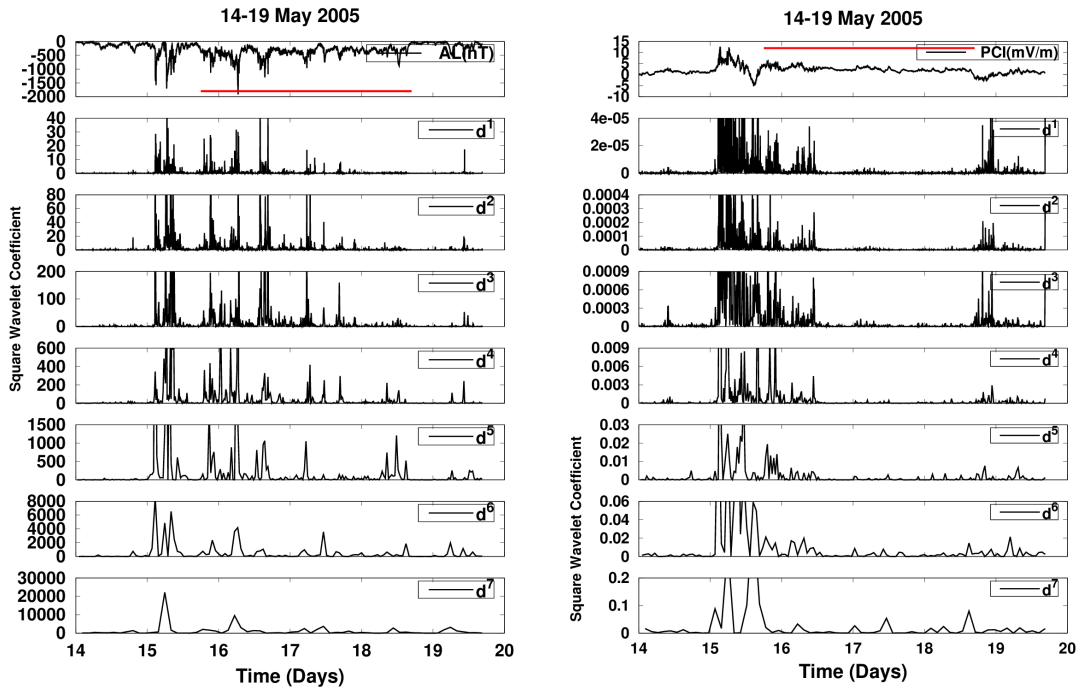


Figure 5.119 - Daubechies Wavelet coefficients d^j (for $j= 1,2,3,\dots,7$) for AL (left) and PC (right) indices during HILDCAA event occurred on 15-18 May 2005. The red color identifies where the HILDCAA events are happening.

but AL and SYM-H show zero time lag with PCI. It is because the euclidean distance from L1 (Lagrangian point) to magnetopause cause a lag time of $\approx 35min$ between the interplanetary parameters and geomagnetic indices (WEIMER *et al.*, 2001). Similarly, the right side of Figure 5.119 gives the cross-correlation results of PCV with the same parameters. In this figure, the correlations coefficients for PCV with AL, SYM-H, E_y and B_z are approximately -0.9, -0.95, 0.7 and -0.7 respectively. Like PCI, PCV also shows time lag of some minutes with E_y and B_z . All these results show that PCI and PCV are highly correlated with AL, SYM-H, E_y and B_z at the time of HILDCAA.

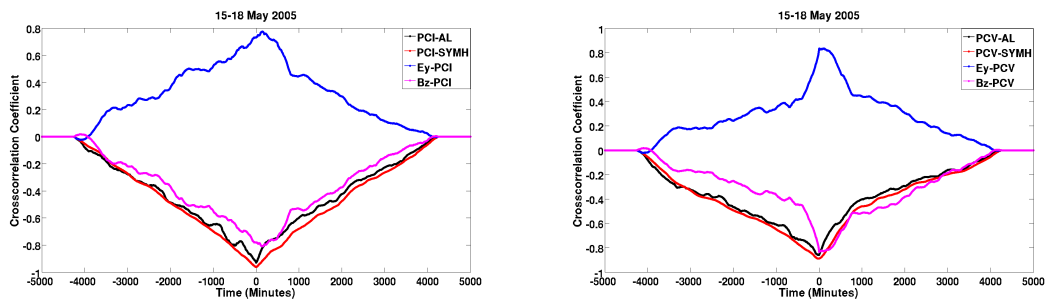


Figure 5.120 - (Left panel) Cross correlation between PCI and AL (black line), PCI and SYM-H (red line), Ey and PCI (blue line) and Bz and PCI (pink line). (right panel) Cross correlation between PCV and AL (black line), PCV and SYM-H (red line), Ey and PCV (blue line) and Bz and PCV (pink line) during HILDCAA event occurred on 15-18 May 2005.

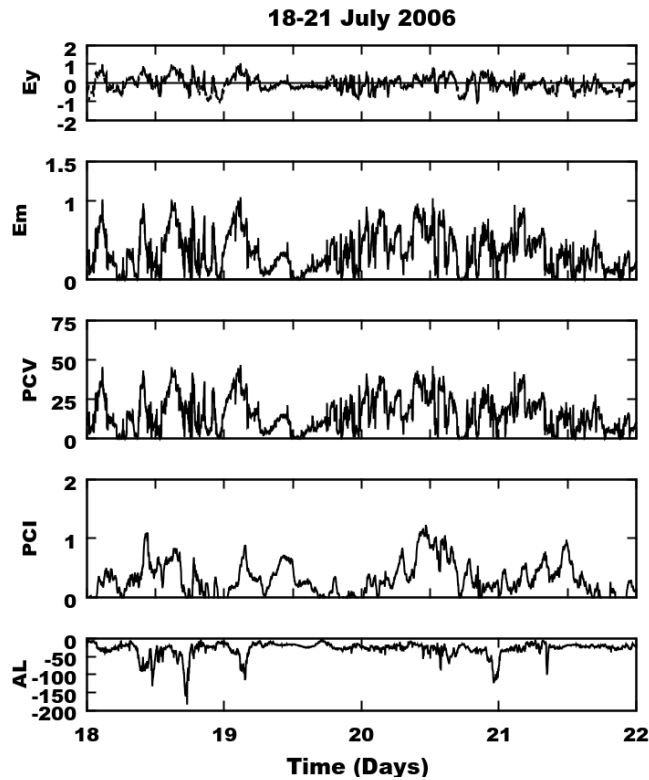


Figure 5.121 - From top to bottom, the panels represent the variations of interplanetary electric field (Ey in mV/m), merging electric field (Em in mV/m), polar cap potential (PCV in kv), and geomagnetic index PC(mV/m) and AL(nT) during the quiet periods from 18-21 July 2006.

Case 4: quiet periods 18-21 July 2006

In this case study, we take three quiet days to compare the results obtained from HILDCAAs. Figure 5.121 is obtained in similar calculation to earlier figures (5.109 or 5.113 or 5.117) but refers to quiet periods from 18-21 July 2006.

Figure 5.122 gives the results obtained from scalograms for AL (left) and PCI (right) during the quiet periods from 18-21 July 2006. In the figure, both indices show less intensities than one of HILDCAA events. The latitudinal positions and the Sun's location of the observatories affect the quiet days curves and the small scale perturbations on AL and PC indices during these day at high auroral latitudes may related to the sources other than ionosphere, for example magnetosphere, polar cap etc. As a consequence, AL and PC indices show the wavelet powers of different intensities at different time scales during these quiet days.

Figure 5.123 is the result of a similar procedure to obtain the earlier figures (as 5.111

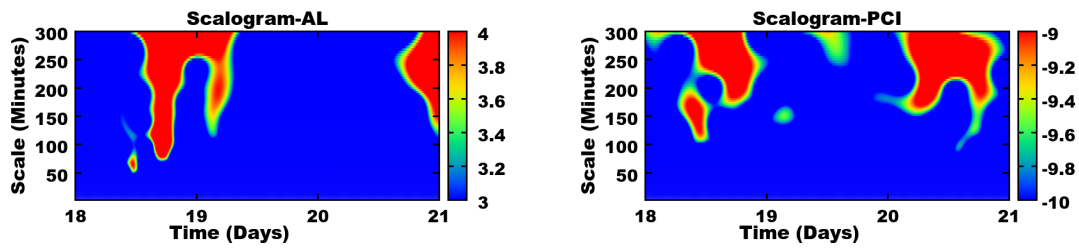


Figure 5.122 - Scalograms for AL (left) and PCI (right) during the quiet periods from 18-21 July 2006.

or 5.115 or 5.119) but refers to quiet periods from 18-21 July 2006. The left side of this figure shows the results of DWT for AL index. It shows larger coefficients for larger values on the time series. Similarly, the right side of this figure shows the results of DWT for PC index. It shows small scale of fluctuations between -1 (mv/m) to 1 (mv/m). When it changes direction, at that time, the squared wavelet coefficients observe relatively higher than its background smooth levels. However, the amplitude of squared wavelet coefficients are smaller as compared to above three HILDCAA events.

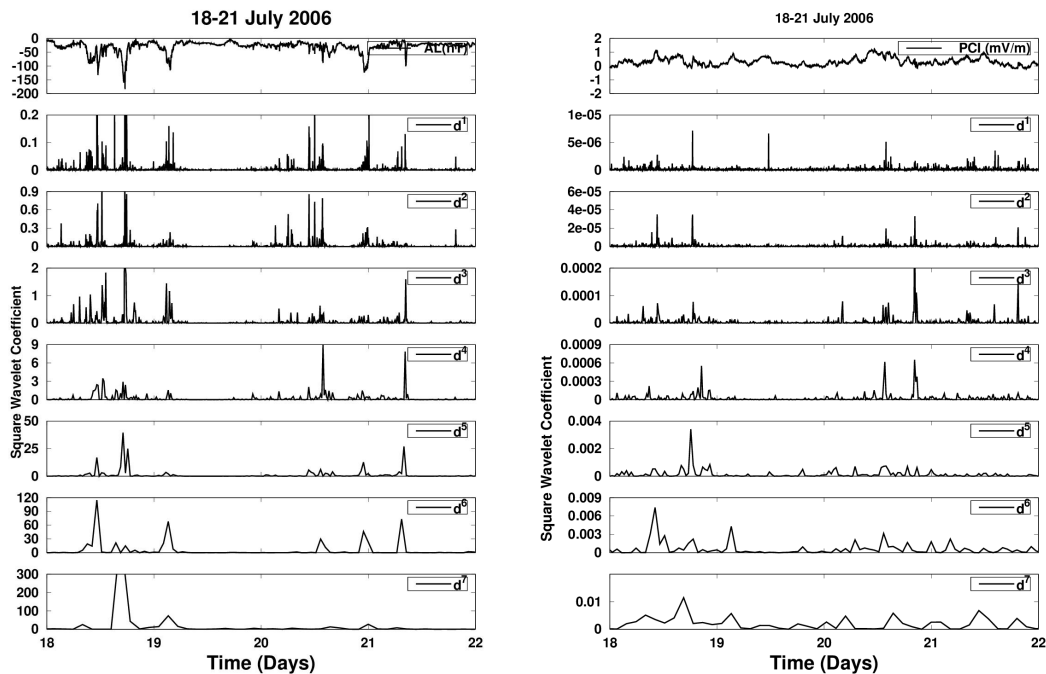


Figure 5.123 - Daubechies Wavelet coefficients d^j (for $j= 1,2,3,\dots,7$) for AL (left) and PC (right) indices during the quiet periods from 18-21 July 2006.

The Figure 5.124 is similar to earlier figures (5.120 or 5.116 or 5.112) but refers to quiet periods from 18-21 July 2006. During these days, except by for $PCV - SYM(H)$, others show very poor correlation.

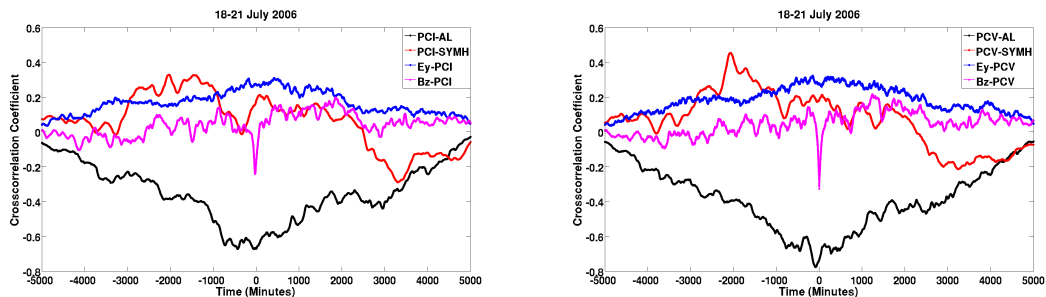


Figure 5.124 - (Left panel) Cross correlation between PCI and AL (black line), PCI and SYM-H (red line), Ey and PCI (blue line) and Bz and PCI (pink line). (right panel) Cross correlation between PCV and AL (black line), PCV and SYM-H (red line), Ey and PCV (blue line) and Bz and PCV (pink line) during the quiet periods from 18-21 July 2006.

Partial conclusions

The polar cap potential has long been widely considered as an important parameter in characterizing the interaction between solar wind and magnetosphere. However, the measurement of polar cap geomagnetic activity through PCI still is in controversial topic (MOON, 2012). However, recently, it has been discussed at the International Association of Geomagnetism and Aeronomy meeting. we have estimated the polar cap potential and merging electric field during three different HILDCAA events. To calculate polar cap potential and merging electric field, we have used the relation as suggested by Kan and Lee (1979). We have also studied the role of PC and AL indices with the polar cap potential and merging electric field during HILDCAAs. In this work, we have studied three HILDCAA events having different interplanetary causes and observed solar wind parameters, magnitude of IMF and components, interplanetary electric field, polar cap potential, merging electric field and geomagnetic indices SYM-H, AE, PCI and AL individually. The results obtained from this work are summarized below.

Related to the events, typical values calculated in this work are compiled at the tables. In the tables, 2003 refers to non storm HILDCAA, 2004 HILDCAA preceded by CIR, 2005 by ICME, and 2006 is an interval of geomagnetically quiet days. First,

Table 5.2 presents the Average values of AL, PCI, PCV and Em during HILDCAA and quiet-day intervals. Following, Table 5.3 presents the cross-correlation coefficients for PCI with AL, SYM-H, Ey and Bz only for HILDCAA period. Finally, Table 5.4 presents the cross-correlation coefficients for PCV with AL, SYM-H, Ey and Bz only for HILDCAAs period.

Table 5.2 - Average values of AL, PCI, PCV and Em during HILDCAAs and quiet-day interval

Events	AL(nT)	PCI (mV/m)	PCV (kv)	Em (mV/m)
2003-04-20to23	-264.98	2.0808	81.83	1.83
2004-02-12to15	-284.94	2.2925	83.32	1.86
2005-05-15to18	-385.44	2.53	125.0	2.8
2006-07-18to21	-29.32	0.31	15.6	0.000035

Table 5.3 - Cross-correlation coefficient for PCI with AL, SYM-H, Ey and Bz only for HILDCAAs interval

Events	PCI-AL	PCI-SYM (H)	Ey-PCI	Bz-PCI
2003-04-20to23	-0.9	-0.9	0.7	-0.7
2004-02-12to15	-0.8	-0.9	0.3	-0.5
2005-05-15to18	-0.9	-0.95	0.7	-0.7
2006-07-18to21	-0.7	–	–	–

Table 5.4 - Cross-correlation coefficient for PCV with AL, SYM-H, Ey and Bz only for HILDCAAs interval

Events	PCV-AL	PCV-SYM(H)	Ey-PCV	Bz-PCV
2003-04-20to23	-0.9	-0.9	0.9	-0.9
2004-02-12to15	-0.8	-0.8	0.3	-0.75
2005-05-15to18	-0.9	-0.95	0.7	-0.7
2006-07-18to21	-0.8	–	–	–

For the event which occurred on 20-23 April 2003, the interplanetary electric field shows significant east-west perturbations, merging electric field also shows significant oscillations and has an average value of 1.83 mV/m , the polar cap potential also shows similar trend to a merging electric field and has an average of 81.83 kv ,

both *AL* and *PCI* show intense activity and have an average of -264.98 nT and 2.08 mV/m respectively. Similarly, for the event on 12-15 February 2004, all these parameters show significant variations like previous events. Averaged values taking along the HILDCAA time interval are seen in the second column of Table 5.2. Finally, the averaged values along the HILDCAA time interval for the event of 15-18 May 2005, are seen in third of Table 5.3. For all events, both the results of CWT and DWT support the fact that *PCI* and *AL* show intense activity during the events. The results obtained from cross-correlation provide the weighty argument to support the role of *PCI* and *AL* indices to monitor geomagnetic disturbances (TROSHICHEV et al., 2011).

In conclusion, we have estimated the polar cap potential (PCV) and merging electric field (Em) and study the role of polar cap (PC) and AL indices during High Intensity Long Duration Continuous Auroral Activity (HILDCAAs), with the major statements:

- a) We got significant variations in polar cap potential and merging electric field during the HILDCAAs interval and got different averages for different events.
- b) We got very good cross correlation of PCI and PCV with AL, SYM-H indices at the time of HILDCAAs.
- c) All these results suggest that the polar cap was severely affected at the time of HILDCAAs.
- d) Also, the results obtained from cross-correlation provide weighty argument to support the role of *PCI* and *AL* indices to monitor the geomagnetic disturbances (TROSHICHEV et al., 2011).

6 CONCLUSIONS

The major solar sources in the interplanetary medium responsible for geomagnetic disturbances are identified as coronal mass ejection (ICMEs), in which are included the magnetic cloud and interplanetary shock; the co-rotating interaction region (CIR), in which are included heliospheric current sheet and sector boundary; and Alfvén waves. Thus, the interaction between those interplanetary structures with the Earth's magnetosphere-ionosphere system can produce effects such as geomagnetic storms, substorms, and a more recent type so-called HILDCAAs (high intensity long duration continuous AE activity).

This work presents a comprehensive study of the effects on geomagnetic records during HILDCAA events. Though a subtle phenomenon, it affects the environment of the Earth and analyses on them could help diagnose the coupling mechanism between solar wind and magnetosphere-ionosphere.

As methodology, an extensive analysis was done with a large number of datasets obtained from different geomagnetic observatories along with solar wind and interplanetary parameters during three basic HILDCAA events and a case of geomagnetically quiet interval. Wavelet techniques (composed by CWT, DWT, and wavelet modulus correlation) and the usual cross-correlation technique were applied to reveal features on the records during HILDCAA events.

The original contribution of this work is related to extending the earlier analyses of other researchers to obtain results concerning geomagnetic measurements recorded at middle-low latitudes during HILDCAAs. Studies on the characteristics of geomagnetic effects that examined the latitude and longitude influences are also carried out. We did complementary investigations by taking into account the effects of field aligned currents associated to the periods of HILDCAAs. Also, we estimated the polar cap potential and the merging electric field during the same events for a comprehensive view.

The results of HILDCAA-related phenomena are obtained by using geomagnetic and solar wind/interplanetary datasets. Out of three events, two were associated with interplanetary high speed streams (HSSs). The HILDCAAs events related to HSSs were typically associated with large-amplitude IMF-Bz variances. The remaining one occurred after the passage of ICME. The ICME-related HILDCAA was characterized by a long steady southward Bz interval marked by low-frequency fluctuations.

The major conclusions obtained from this study can be presented as:

1. There are indeed effects on middle-low latitude magnetic records during HILD-CAA events, as consequence of the coupling between the solar wind plasma and the magnetosphere-ionosphere system.
2. From the analysis of three case studies and the use of a quiet case as background control, we were able to identify common features among the different events for the middle-low latitude geomagnetic records.
3. From the analysis of magnetograms, the geomagnetic indices AE, and the interplanetary Bz components, characteristic signals were identified along the HILD-CAA time interval, whose periods vary from 50 to 300 min.
4. However, there are peculiarities in those identifications, which demonstrate the complexity that exists in the coupling mechanism between the incident solar plasma and the Earth's magnetosphere-ionosphere system.
5. The peculiarities that appeared among the events are attributed to the different conditions of the interplanetary environment and the answers of the magnetosphere-ionosphere system.
6. The evaluation of the local regularity level on middle-low latitude records for each event indicates that there were impulsive energy injections superposed to the smooth background process during HILDCAA events.
7. The north or south turning of IMF-Bz plays a significant role for the intensity of records during HILDCAAs.
8. The comparison of results using several observatories located spread out the globe confirm effects depending on latitude and longitude.
9. The comparison of results using several observatories located spread out the globe confirm effects depending on latitude and longitude.
10. Field aligned currents (FACs) as well as polar cap potential (PCP) seem to take an important part in the middle-low latitude effects, and it deserves more studies.

6.1 Perspectives for future work:

- Evaluation of the results for a large amount of events in order to characterize in a deep way the physics involved and tabulate typical parameters for the different interplanetary causes;

- Investigation of coupling mechanism for some well identified cases in order to allow some modeling of the magnetosphere-ionosphere electrical current system during pure HILDCAA in low latitudes.

REFERENCES

- ABBAS, M.; SALIHU, M. Variability strength of the equatorial electrojet over africa during low solar activity. **International Journal of Marine, Atmospheric and Earth Sciences**, v. 2(1), p. 28–40, 2014. 105, 107
- ABRY, P. Ondelettes et turbulences - multirésolutions, algorithmes de de compositions, invariance de chelle et signaux de pression. **Diderot, Editeurs des sciences et des arts, Paris**, 1997. 57
- AKASOFU, S. I. The development of the auroral substorm. **Planetary and Space Science**, v. 12, p. 273–282, 1964. 17
- _____. Energy coupling between the solar wind and the magnetosphere. **Space Science Reviews**, v. 28, p. 121–190, 1981. 28
- AKASOFU, S. I.; CHAPMAN, S. The development of the main phase of magnetic storms. **Journal of Geophysical Research**, v. 68, 1963. 18, 98
- ALEXEEV, I. I.; KIRILLOV, A. A.; A., C. T. Current system of the geomagnetic tail. **Geomagnetizm Aeronomiya**, v. 15, p. 508, 1975. 23
- ALFVEN, H. Existence of electromagnetic-hydrodynamic waves. **Nature**, v. 150, p. 405–406, 1942. 16
- _____. Electric current in cosmic plasma. **Journal of Geophysical Research**, v. 15, p. 271, 1977. 16
- ALVES, M.; ECHER, E.; GONZALEZ, W. D. Geoeffectiveness of corotating interaction regions as measured by dst. **Journal of Geophysical Research**, v. 111, p. A07S05, 2006. 4, 15, 20
- ANTOINE, J. P.; MURENZI, R.; P., V.; Twareque Ali, S. **Two-Dimensional Wavelets and their Relatives**. [S.l.]: Cambridge University Press, 2008. 48, 50, 52
- ARAKI, T. Global structure of geomagnetic sudden commencements. **Planetary and Space Science**, v. 25, p. 373, 1977. 9, 17, 98
- AXFORD, W. I.; HINES, C. O. A unifying theory of high-latitude geophysical phenomena and geomagnetic storms. **Canadian Journal of Physics**, v. 39, p. 1433, 1961. 2, 17

BAKER, D. What is space weather *qm*? **Advances in Space Research**, v. 22, p. 7–16, 1998. 3, 17, 38

BAKER, D. N.; KLIMAS, A. J.; VASSILIADIS, D.; PULKKINEN, T. I.; MCPHERRON, R. L. Re-examination of driven and unloading aspects of magnetospheric substorms. **Journal of Geophysical Research**, v. 102, p. 7169–7177, 1997. 18

BAKER, D. N.; PULKKINEN, T. I.; HESSE, M.; MCPHERRON, R. L. A quantitative assessment of energy storage and release in the earth's magnetotail. **Journal of Geophysical Research**, v. 102, p. 7159–7168, 1997. 18

BALLATORE, P.; MACLENNAN, C. G. Significance of the high-latitude geomagnetic index AES–80: comparison with the pc index. **Earth Planets Space**, v. 51, p. 425–430, 1999. 40

BALOGH, A.; GOSLING, J. T.; JOKIPII, J.; KALLENBACH, R.; KUNOW, H. Corotating interaction regions. **Space science series of ISSI**, v. 7, 1999. 10

BARTELS, J. Potsdamer erdmagnetische kennziffern, 1 mitteilung. **Zeitschrift für Geophysik**, v. 14, p. 699–718, 1938. 35

BAUMJOHANN, W.; BLANC, M.; FEDOROV, A.; GLASSMEIER, K. H. Current systems in planetary magnetospheres and ionospheres. **Space Science Reviews**, v. 152, p. 99–134, 2010. 22, 23

BELCHER, J. W.; DAVIS, L. Large amplitude alfvén waves in the interplanetary medium. **Journal of Geophysical Research**, v. 76, p. 3534, 1971. 16

BIRKELAND, K. **The norwegian aurora polaris expedition**. [S.l.]: Aschehoug, H. and Oslo, Co., 1908. 24

BOLAJI, O. S.; ADIMULA, I. A.; ADENIYI, J. O.; YUMOTO, K. Variability of horizontal magnetic field intensity over nigeria during low solar activity. **Earth Moon Planets**, v. 110, p. 91–103, 2013. 82, 105, 113, 137, 171

BOROVSKY, J. E.; LAVRAUD, B.; KUZNETSOVA, M. M. Polar cap potential saturation, dayside reconnection, and changes to the magnetosphere. **Journal of Geophysical Research**, v. 114, 2009. 27

BOTHMER, V.; SCHWENN, R. The structure and origin of magnetic clouds in the solar wind. **Annals of Geophysics**, v. 16, p. 1–24, 1998. 13

BOYLE, C. B.; REIFF, P. H.; HAIRSTON, M. R. Empirical polar cap potentials. **Journal of Geophysical Research**, v. 102, p. 111, 1997. 25, 195

BRACEWELL, R. N. **The Fourier Transform and Its Applications**. 3, illustrated. ed. [S.l.]: McGraw Hill, 2000, 2000. 45, 47

BRUECKNER, G. E.; HOWARD, R. A.; KOOMEN, M. J.; KORENDYKE, C. M.; MICHELS, D. J.; MOSES, J. D.; SOCKER, D. G.; DERE, K. P.; LAMY, P. L.; LLEBARIA, A.; BOUT, M. V.; SCHWENN, R.; SIMNETT, G. M.; BEDFORD, D. K.; EYLES, C. J. The large angle spectroscopic coronagraph. **Solar Physics**, v. 162, p. 357–402, 1995. 12

BURLAGA, L. F. Interplanetary magnetohydrodynamics. In: **Interplanetary Magnetohydrodynamics**. New York: Oxford Univ. Press, 1995. 7

BURLAGA, L. F.; LEPPING, R. P.; JONES, J. A. Global configuration of a magnetic cloud. in: physics of magnetic flux ropes. In: .RUSSELL, C. T.; PRIEST, E. R.; LEE, L. C. (Ed.). **Geophysical Monograph Series**. [S.l.]: Washington DC: American Geophysical Union, 1990. v. 58, p. 373–377. 13

BURLAGA, L. F.; SITTER, E.; MARAINI, F.; SCHWENN, R. Magnetic loop behind an interplanetary shock: Voyager, helios and imp-8 observations. **Journal of Geophysical Research**, v. 86, p. 66–73, 1981. 9, 13, 61

BURLAGA, L. J. Magnetic clouds and force-free fields with constant alpha. **Journal of Geophysical Research**, v. 93, p. 7217–7224, 1988. 13, 61

BUTI, B.; TSURUTANI, B. T.; NEUGEBAUER, M.; GOLDSTEIN, B. E. Generation mechanism for magnetic holes in the solar wind. **Geophysical Research Letters**, v. 28, p. 1355, 2001. 16

CAMP, C. D.; TUNG, K. K. Surface warming by the solar cycle as revealed by the composite mean difference projection. **Geophysical Research Letters**, v. 34, p. L14703, 2007. 8

CAMPBELL, W. H. **Introduction to geomagnetic field**. [S.l.]: Cambridge university press, 1997. 31, 105

CAMPBELL, W. H.; SCHIFFMACHER, E. R. Quiet ionospheric currents of the southern hemisphere derived from geomagnetic records. **Journal of Geophysical Research**, v. 93, p. 933–944,, 1988. 21

- CASTILHO, J. E.; DOMINGUES, M. O.; MENDES, O.; PAGAMISSE, A. Introdução ao mundo das wavelets. **Notas em Matemática Aplicada, SBMAC**, 2012. 47, 56
- CHANDRASEKHAR, E.; OSHIMAN, N.; YUMOTO, K. On the role of oceans in the geomagnetic induction by Sq along the 210 degree magnetic meridian region. **Earth Planets Space**, v. 55, p. 315–326, 2003. 21
- CHAPMAN, S. The normality of geomagnetic disturbance at Huancayo. **Geofísica Pura e Aplicata**, v. 14, p. 151–158, 1951. 82
- CHAPMAN, S.; BARTELS, J. **Geomagnetism**. [S.l.]: Clarendon Press Oxford, 1940. 18, 20, 98, 105
- _____. _____. [S.l.]: Clarendon Press, Oxford, 1962. 1, 31, 197
- CHAPMAN, S. C.; RAJARAO, K. S. The H and Z variation along and near the equatorial electrojet in India, Africa and Pacific. **Journal of Atmospheric and Solar–Terrestrial Physics**, v. 27, p. 559–581, 1965. 21
- CHAPPELL, C.; MOORE, T.; Waite Jr, J. The ionosphere as a fully adequate source of plasma for the earth’s magnetosphere. **Journal of Geophysical Research**, v. 92(A6), p. 5896–5910, 1987. 23, 24, 202
- CHATFIELD, C. **The Analysis of Time Series—An Introduction**. [S.l.]: Chapman and Hall, London, 1989. 47
- CHEN, J. Theory of prominence eruption and propagation: Interplanetary consequences. **Journal of Geophysical Research**, v. 101, p. 27499–27520, 1996. 13
- CHENG, Z. W.; SHI, J. K.; ZHANG, T. L.; WANG, S. G.; LIU, Z. X. Field-aligned currents at the PSBL on 17 August 2001 storm: Relationships with solar wind conditions. **Chinese Physics Letters**, v. 28, p. 9, 2011. 177
- CHUN, F. K.; RUSSEL, C. T. Field-currents in the magnetosphere in the inner magnetosphere: control by geomagnetic activity. **Journal of Geophysical Research**, v. 102, p. 2261–2270, 1997. 24, 176
- CHUN, L.; LIN, A. Tutorial of the wavelet transform. 2010. 48
- CLAUER, C. R.; MCPHERRON, R. L. The relative importance of the interplanetary electric field and magnetospheric substorms on partial ring current development. **Journal of Geophysical Research**, v. 85, p. 6747–6759, 1980. 180

COLEMAN, P. J. Turbulence, viscosity and dissipation in the solar wind plasma. **Astrophysical Journal**, v. 153, p. 371, 1968. 16

COOLEY, J. W.; LEWIS, P.; WELCH, P. The fast fourier transform and its applications. **IEEE Trans on Education**, v. 12(1), p. 28–34, 1969. 45

COOLEY, J. W.; TUKEY, J. W. An algorithm for the machine calculation of complex fourier series. **Mathematical Computation**, v. 19, p. 297–301., 1965. 45

CREMADES, H.; BOTHMER, V. On the three-dimensional configuration of coronal mass ejections. **Astronomy and Astrophysics**, v. 422, p. 307–322, 2004. 12

CYR, O. C. S.; HOWARD R. A. ANDSHEELEY, N. R.; PLUNKETT, S. P.; MICHELS, D. J.; PASWATERS, S. E.; KOOMEN, M. J.; SIMNETT, G. M.; THOMPSON, B. J.; GURMAN, J. B.; SCHWENN, R.; WEBB, D. F.; HILDNER, E.; LAMY, P. L. Properties of coronal mass ejections: SOHO LASCO observations from January 1996 to June 1998. **Journal of Geophysical Research**, v. 105, p. 18169–18186, 2000. 12

da COSTA, A. M.; DOMINGUES, M. O.; MENDES, O.; BRUM, C. G. M. Interplanetary medium condition effects in the south atlantic magnetic anomaly: A case study,. **Journal of Atmospheric and Solar-Terrestrial Physics**, v. 73(11–12), p. 1478–1491, 2011. 57

DAGLIS, I. A.; THORNE, R. M.; BAUMJOHANN, W.; ORSINI, S. The terrestrial ring current: Origin, formation, and decay. **Reviews of Geophysics**, v. 37, p. 407–438, 1999. 4, 9, 19, 23, 38

DAUBECHIES, I. **Ten lectures on wavelets**. [S.l.]: Society for Industrial and Applied Mathematics,PA, USA, 1992. 47, 48, 54, 118

DAVID, T. . W. Investigation into quiet and magnetic storms periods above Magadan during October–December 2003. **Indian Journal of Radio & Space Physics**, v. 42, p. 89–96, 2013. 60

DAVIS T. N. ANDSUGIURA, M. Auroral electrojet activity index AE and its universal time variations. **Journal of Geophysical Research**, v. 71, p. 785, 1966. 3, 36, 40

de Lucas, A.; GONZALEZ, W. D.; ECHER, E.; GUARNIERI, F. L.; Dal Lago, A.; da SILVA, M. R.; VIEIRA, L. E. A.; SCHUCH, N. J. Energy balance during

intense and super-intense magnetic storms using an akasofu e parameter corrected by the solar wind dynamic pressure. **Journal of Atmospheric and Solar–Terrestrial Physics**, v. 69, p. 1851–1863, 2007. [28](#), [29](#), [72](#)

DEMOULIN, P.; DASSO, S. Causes and consequences of magnetic cloud expansion. **Astronomy and Astrophysics**, v. 498, p. 551–566, 2009. [61](#)

DEVI, B.; DUBEY, S.; SAINI, S.; DEVI, R.; WAHI, R.; DHAR, A.; VIJAY, S. K.; GWAL, A. K. Geomagnetic field variation during winter storm at localized southern and northern high latitude. **Journal of Astrophysics and Astronomy**, v. 29, p. 275–280, 2008. [83](#), [86](#), [110](#)

DOMINGUES, M. O. **Análise Wavelet na Simulação Numérica de Equações Diferenciais Parciais com Adaptabilidade Espacial**. PhD Thesis (PhD) — Tese de Doutorado. Universidade de Campinas, 2001. [54](#), [56](#)

DOMINGUES, M. O.; KAIBARA, M. k. wavelet, ondinhas, ondeletas, ondaletas, ôndulas, ondículas, análise de multirresolução, wavelets, multiresolution analysis. **Revista Brasileira de Ensino de Física**, v. 34, p. 1–16, 2013. [56](#)

DOMINGUES, M. O.; MENDES, O.; da COSTA, A. M. Wavelet techniques in atmospheric sciences. **Advances in Space Research**, v. 35, n. 5, p. 831–842, 2005. [48](#), [49](#), [54](#), [57](#)

DRYER, M. Interplanetary shock waves: recent development. **Space Science Reviews**, v. 17, p. 277, 1975. [14](#)

DUNGEY, J. W. Interplanetary magnetic field and the auroral zones. **Physical Review Letters**, v. 6, p. 47–48, 1961. [1](#), [2](#), [9](#), [17](#), [18](#), [24](#), [27](#)

ECHER, E.; ALVES, M. V.; GONZALEZ, W. D. Geoeffectiveness of interplanetary shocks during solar minimum (1995–1996) interplanetary shocks during solar minimum (1995–1996) and solar maximum (2000). **Solar Physics**, v. 221, p. 361–380, 2004. [14](#)

ECHER, E.; GONZALEZ, W. D.; TSURUTANI, B. T.; VIEIRA, L. E. A.; ALVES, M. V.; CLUA-GONZALEZ, A. L. On the preferential occurrence of interplanetary shocks in July and November: Causes (solar wind annual dependence) and consequences (intense magnetic storms). **Journal of Geophysical Research**, v. 110, 2005. [13](#)

ECHER, E.; GONZALEZ, W. D.; TSURUTANI, B. T.; CLUA-GONZALEZ, A. L. Interplanetary conditions causing intense geomagnetic storms ($Dst \leq -100$ nT) during solar cycle 23 (1996–2006). **Journal of Geophysical Research**, v. 113, 2008. 13, 17

ECHER, E.; GONZALEZ, W. D.; VIEIRA, L. E. A.; Dal Lago, A.; GUARNIERI, F. L.; PRESTES, A.; CLUA-GONZALEZ, A. L.; SCHUCH, N. J. On the preferential occurrence of interplanetary shocks in July and November: Causes (solar wind annual dependence) and consequences (intense magnetic storms). **Brazilian Journal of Physics**, v. 33, 2003. 14

EDDY, J. A. Observation of a possible neutral sheet in the corona. **Solar Physics**, v. 30, p. 385, 1973. 16

_____. A nineteenth-century coronal transient. *astronomy and astrophysics*. **Astronomy and Astrophysics**, v. 34, p. 235, 1974. 12

_____. The maunder minimum. **Science**, v. 19, p. 1189–1202, 1976. 7

EGEDAL, J. The magnetic diurnal variation of the horizontal force near the magnetic equator. **Terr. Magn. Atmos. Electr**, v. 52, p. 449–451, 1947. 82

ELLIOTT, H. A.; COMFORT, R. H.; CRAVEN, P. D.; CHANDLER, M. O.; MOORE, T. E. Solar wind influence on the oxygen content of ion outflow in the high-altitude polar cap during solar minimum conditions. **Journal of Geophysical Research**, v. 106, p. 6067–6084, 2001. 23

FAIRFIELD, D. H. Magnetic field signatures of substorms on high-latitude field lines in the nighttime magnetosphere. **Journal of Geophysical Research**, v. 78, p. 1553–1562, 1973. 25

FARGE, M. Wavelet transform and their applications to turbulence. **Annual Reviews of Fluid Mechanics**, v. 24, p. 395–457, 1992. 48, 50

FEDDER, J. A.; LYON, J. G. The solar wind-magnetosphere-ionosphere current-voltage relationship. **Geophysical Research Letters**, v. 14, p. 880–883, 1987. 26

FELDMAN, W. C.; TOKAR, R. L.; BIRN, J.; HONES, E. W.; BAME, S. J.; RUSSEL, C. T. Structure of slow mode shock observed in the plasma sheet. **Journal of Geophysical Research**, v. 92, p. 83–94, 1987. 13

FINCH, I.; M., L. Solar wind-magnetosphere coupling functions on timescales of 1 day to 1 year. **Annals of Geophysics**, v. 25, p. 495–506, 2007. 46

FOK, M. C.; MOORE, T.; GREENSPAN, M. Ring current development during storm main phase. **Journal of Geophysical Research**, v. 101(A7), p. 5311–5322, 1996. 38

FRANK, L. A. On the extraterrestrial ring current during geomagnetic storms. **Journal of Geophysical Research**, v. 72(15), p. 3753–3767, 1967. 38

FRICK, P.; BALIUNAS, S. L.; GALYAGLN, D.; SOKOLOFF, D.; SOON, W. Wavelet analysis of stellar chromospheric activity variations. **Astrophys Journal**, v. 483, p. 426, 1997. 50, 52, 54

FRICK, P.; BECK R. ANDBERKHUIJSEN, E. M.; PATRICKEYEV, I. Scaling and correlation analysis of galactic images. **Monthly Notices of the Royal Astronomical Society**, v. 327(4), p. 1145–1157, 2001. 52

GARRET, H. B.; DESSLER, A. J.; HILL, J. W. Influence of solar wind variability on geomagnetic activity. **Journal of Geophysical Research**, v. 79, p. 4603, 1974. 10, 16

GOLDESTSTEIN, M. L.; ROBERTS, D. A.; DEANE, A. E.; GHOSH, S.; WONG, H. K. Numerical simulations of alfvénic turbulence in the solar wind. **Journal of Geophysical Research**, v. 104, p. 14437, 1999. 16

GOMBOSI, T. I. **Physics of the Space Environment**. [S.l.]: New York, NY Cambridge University Press, 1998. 22

GONCHAROVA, M. Y. A peculiarity of the sq variation with high altitude. In: PHYSICS OF AURORAL PHENOMENA ANNUAL SEMINAR. **Proceedings...** Apatity, 2004. p. 27–30. 72, 82, 105, 113, 137, 171

GONZALEZ, W.; TSURUTANI, B.; CLUA-GONZALEZ, A. L.; SMITH, E. J.; TANG, F.; AKASOFU, S. I. Solar wind–magnetosphere coupling during intense magnetic storms (1978–1979). **Journal Geophysical Research**, v. 94, p. 8835–8851, 1989. 27

GONZALEZ, W. D. **A quantitative three dimensional model for magnetopause reconnection. Ph.D. Thesis**. PhD Thesis (PhD) — University of California, Berkeley, 1973. 28

GONZALEZ, W. D. A unified view of solar wind–magnetosphere coupling functions. **Planetary and Space Science**, v. 38 (5), p. 627–632, 1990. 27, 29

GONZALEZ, W. D.; CLUA-GONZALEZ, A. L. Solar wind energy and electric field transfer to the earth's magnetosphere via magnetopause reconnection. **Geophysical Research Letters**, v. 8(3), p. 265–268, 1981. 28

_____. Energy transfer by magnetopause reconnection and the substorm parameter ϵ . **Planetary and Space Science**, v. 32 (8), p. 1007–1012, 1984. 28

GONZALEZ, W. D.; GUARNIERI, F. L.; CLUA-GONZALEZ, A. L.; ECHER, E.; ALVES, M. V.; OGINOO, T.; TSURUTANI, B. T. Magnetospheric energetics during HILDCAAs, in recurrent magnetic storms: Corotating solar wind streams,. In: AL, B. T. et (Ed.). **Geophysical Monograph Series**. [S.l.]: AGU, Washington, 2006. v. 167, p. 175–182. 20

GONZALEZ, W. D.; JOSELYN, J. A.; KAMIDE, Y.; KROEHL, H. W.; ROSTOKER, G.; TSURUTANI, B. T.; VASYLIUNAS, V. M. What is a geomagnetic storm *qm*? **Journal of Geophysical Research**, v. 99, p. 5771–5792, 1994. 1, 3, 4, 9, 10, 17, 18, 19, 27, 38, 60, 83, 91, 98, 110, 151

GONZALEZ, W. D.; MOZER, F. S. A quantitative model for the potential resulting from reconnection with an arbitrary interplanetary magnetic field. **Journal of Geophysical Research**, v. 79, p. 4186, 1974. 24, 28

GONZALEZ, W. D.; TSURUTANI, B. T. Criteria of interplanetary parameters causing intense magnetic storms ($dst < -100$ nt). **Planetary and Space Science**, v. 35, p. 1101, 1987. 3, 4, 5, 19

GONZALEZ, W. D.; TSURUTANI, B. T.; CLUA-GONZALEZ, A. L. Interplanetary origin of geomagnetic storms. **Space Science Reviews**, v. 88, p. 529–562, 1999. 2, 3, 10, 14, 27, 34

GOPALSWAMY, N.; YASHIRO, S.; AKIYAMA, S. Geoeffectiveness of halo coronal mass ejections. **Journal of Geophysical Research**, v. 112, 2007. 12

GOSLING, J. T. Coronal mass ejections and magnetic flux ropes in interplanetary space, in physics of magnetic flux ropes. In: RUSSELL, C. T.; PRIEST, E. R.; LEE, L. (Ed.). **Geophysical Monograph Series**. [S.l.]: American Geophysical Union, Washington, DC, 1990. v. 58, p. 343–364. 13, 14

_____. Coronal mass ejections: An overview, in coronal mass ejections. **Geophys. Monograph**, v. 99, p. 9, 1997. 13

GOSLING, J. T.; MCCOMAS, D. J.; PHILLIPS, J. L.; BAME, S. J. Geomagnetic activity associated with earth passage of interplanetary shock disturbances and coronal mass ejections. **Journal of Geophysical Research**, v. 96, p. 7831, 1991. 14

GOSLING, J. T.; PIZZO, V. J. Formation and evolution of corotating interaction regions and their three dimensional structure. **Space Science Reviews**, v. 89, p. 21–52, 1999. 11, 14

GREENER, J. G.; SCHLAPP, D. M. A study of day to day variability of Sq over Europe. **Journal of Atmospheric and Solar-Terrestrial Physics**, v. 41, p. 217–223, 1979. 20

GREENWALD, R. A.; RUOHONIEMI, J. M.; BAKER, K. B.; BRISTOW, W. A.; SOFKO, G. J.; VILLAIN, J. P.; LESTER, M.; SLAVIN, J. Convective response to a transient increase in dayside reconnection. **Geophysical Research Letters**, v. 104, p. 10007–10016, 1999. 26

GUARNIERI, F. F.; TSURUTANI, B. T.; GONZALEZ, W. D.; CLUA-GONZALEZ, A. L.; GRANDE, M.; SORAAS, F.; ECHER, E. Icmc and cir storms with particular emphasis on hildcaa events. In: GOPALSWAMY, N.; BHATTACHARYYA, A. (Ed.). **Proceedings...** [S.l.]: ILWS Workshop, 2006. p. 266. ISBN: 81-87099-40-2. 3, 5, 20, 60, 61, 70, 91, 158, 200

HAAR, A. Zur theorie der orthogonalen funktionen–systeme. **Mathematische Annales**, v. 69, p. 331–371, 1910. 47

HAIRSTON, M. R.; DRAKE, K. A.; SKOUG, R. Saturation of the ionospheric polar cap potential during the october–november 2003 superstorms. **Journal of Geophysical Research**, v. 110, p. A09S26, 2005. 25

HAIRSTON, M. R.; WEIMER, D. R.; HEELIS R. A. ANDRICH, F. J. Analysis of the ionospheric cross polar cap potential drop and electrostatic potential distribution patterns during the january 1997 cme event using dmsp data. **Journal of Atmospheric and Solar-Terrestrial Physics**, v. 61, p. 195–206, 1999. 26

HAJRA, R.; ECHER, E.; TSURUTANI, B. T.; GONZALEZ, W. D. Solar cycle dependence of High-Intensity, Long-Duration, Continuous AE Activity (HILDCAA) events. **Journal of Geophysical Research**, v. 118, p. 1–12, 2013. 3, 5, 20, 44, 60, 61, 70, 91, 98, 132, 165, 187

_____. Solar wind-magnetosphere energy coupling efficiency and partitioning: Hildcaas and preceding cir storms during solar cycle 23. **Journal of Geophysical Research**, v. 119, 2014. 3, 5, 20, 91

HAJRA, R.; TSURUTANI, B. T.; ECHER, E.; GONZALEZ, W. D. Relativistic electron acceleration during high-intensity, long-duration, continuous ae activity (hildcaa) events: Solar cycle phase dependences. **Geophysical Research Letters**, v. 41, 2014. 3, 5, 20, 91

HAMILTON, D. C.; GLOECKLER, G.; IPAVICH, F. M.; STUDEMANN, W.; WILKEN, B.; KREMSER, G. Ring current development during the great geomagnetic storm of february 1986. **Journal of Geophysical Research**, v. 93(A12), p. 14343–14355, 1988. 23, 202

HARGREAVES, J. K. **The solar-terrestrial environment**. [S.l.]: Cambridge University Press, Cambridge, 1992. 2

HARVEY, K.; SUESS, S.; ASCHWANDEN, M.; GUHATHAKURTA, M.; HARVEY, J.; HATHAWAY, D.; LABONTE, B.; SHEELEY, N.; TSURUTANI, B. T. A NASA workshop on coronal holes near solar maximum and over the solar cycle. In: . Washington: NASA: [s.n.], 2000. 7, 10, 14

HEELIS, R. A. The effects of interplanetary magnetic field orientation on dayside high-latitude ionospheric convection. **Journal of Geophysical Research**, v. 89, p. 2873, 1984. 25

HEPPNER, J. P.; MAYNARD, N. C. Empirical high-latitude electric field models. **Journal of Geophysical Research**, v. 92, p. 4467, 1987. 25

HILL, T. W. Magnetic merging in a collisionless plasma. **Journal of Geophysical Research**, v. 80, p. 4689–4699, 1975. 26

_____. Mercury and mars: The role of ionospheric conductivity in the acceleration of magnetospheric particles. **Geophysical Research Letters**, v. 3, p. 429–432, 1976. 26

HOLLWEG, J. V. Some physical processes in the solar wind. **Reviews of Geophysics and Space Physics**, v. 16, p. 689, 1978. 16

_____. Cyclotron resonance in corona holes: Heating and acceleration of protons, 0^{5+} , mg^{9+} . **Journal of Geophysical Research**, v. 104, p. 24781, 1999. 16

HOWARD, R. A.; MOSES, J. D.; VOURLIDAS, A.; NEWMARK, J. S.;
SOCKER, D. G.; PLUNKETT, S. P.; KORENDYKE, C. M.; COOK, J. W.;
HURLEY, A.; DAVILA, J. M.; THOMPSON, W. T.; CYR, O. C. S.;
MENTZELL, E.; MEHALICK, K.; LEMEN, J. R.; WUELSER, J. P.; DUNCAN,
D. W.; TARBELL, T. D.; WOLFSON, C. J.; MOORE, A.; HARRISON, R. A.;
WALTHAM, N. R.; LANG, J.; DAVIS, C. J.; EYLES, C. J.; MAPSONMENARD,
H.; SIMNETT, G. M.; HALAIN, J. P.; DEFISE, J. M.; MAZY, E.; ROCHUS, P.;
MERCIER, R.; RAVET, M. F.; DELMOTTE, F.; AUCHERE, F.;
DELABOUDINIÈRE, J. P.; BOTHMER, V.; DEUTSCH, W.; WANG, D.; RICH,
N.; COOPER, S.; STEPHENS, V.; MAAHS, G.; BAUGH, R.; MCMULLIN, D.;
CARTER, T. Sun earth connection coronal and heliospheric investigation (secchi).
Space Science Reviews, v. 136, p. 67–115, 2008. 12

HUBBARD, B. B. **The World According to Wavelets: The Story of a
Mathematical Technique in the Making**. [S.l.]: A K Peters Ltd, 1997. 47, 54
_____. _____. [S.l.: s.n.], 1998. 47, 48

HUNDHAUSEN, A. J. **Coronal Expansion and Solar Wind**. [S.l.]:
Springer-Verlag, Berlin, 1972. 14

HUNDHAUSEN, A. J.; SAWYER, C. B.; HOUSE, L.; ILLING, R. M. E.;
WAGNER, W. J. Coronal mass ejections observed during the solar maximum
mission -latitude distribution and rate of occurrence. **Journal of Geophysical
Research**, v. 89, p. 2639–2646, 1984. 11, 12

IJIMA, T.; POTEMERA, T. A. The relationship between interplanetary
quantities and birkeland current densities. **Journal of Geophysical Research**,
v. 9, p. 442, 1982. 25, 176

IJIMA, T.; POTEMERA, T. A. Field-aligned currents in the dayside cusp observed
by triad. **Journal of Geophysical Research**, v. 81, p. 5971–5979, 1976. 24, 25,
176

IWAI, K.; SHINYA, K.; TAKASHI, K.; MOREAU, R. Pressure change
accompanying alfvén waves in a liquid metal. **Magnetohydrodynamics**, v. 39, p.
245–250, 2003. 16

JAMES, M. E.; TRIPATHI, D.; RASTOGI, R. G. Day to day variability of
ionospheric current system. **Indian Journal of Radio and Space Physics**,
v. 25, p. 36–43, 1996. 105, 107

JANKOVICOVA, D.; DOLINSKY, P.; VALACH, F.; VOROS, Z. Neural network-based nonlinear prediction of magnetic storms. **Journal of Atmospheric and Solar-Terrestrial Physics**, v. 64 (5–6), p. 651–656, 2002. [83](#), [110](#), [112](#), [146](#), [151](#)

JANKOWSK, I. J.; SUCKSDORFF, C. Guide for magnetic measurements and observatory practice. In: **IAGA, Warsaw**. [S.l.: s.n.], 1996. p. 56–64. [32](#)

KAMIDE, Y.; RICHMOND, A. D.; MATSUSHITA, S. Estimation of ionospheric electric fields, ionospheric currents, and field-aligned currents from ground magnetic records. **Journal of Geophysical Research**, v. 86, p. 801–813, 1981. [26](#)

KAMIDE, Y.; YOKOYAMA, N.; GONZALEZ, W. D.; TSURUTANI, B. T.; DAGLIS, I. A.; BRAKKE, A.; MASUDA, S. Two-step development of geomagnetic storms. **Journal of Geophysical Research**, v. 103, p. 6917–6921, 1998. [2](#), [3](#), [83](#), [110](#), [112](#), [146](#)

KAN, J. R.; LEE, L. C. Energy coupling function and solar wind magnetosphere dynamo. **Geophysical Research Letters**, v. 6, p. 577–580, 1979. [26](#), [27](#), [195](#), [210](#)

KENNEL, C. F. Nonlinear evolution of slow waves in the solar wind. **Journal of Geophysical Research**, v. 90, p. 531, 1985. [8](#)

KIKUCHI, T.; PINNOCK, M.; RODGER, A.; LUEHR, H.; KITAMURA, T.; TACHIHARA, H.; WATANABE, M.; SATO, N.; RUOHONIEMI, M. Global evolution of a substorm-associated dp2 current system observed by superdarn and magnetometers. **Advances in Space Research**, v. 26 (1), p. 121–124, 2000. [197](#)

KIM, H. J.; LEE, D.; LYONS, L. H. Are repetitive particle injections during high-speed solar wind streams classic substorms *qm*. **Journal of Geophysical Research**, v. 113, p. A08205, 2008. [5](#)

KIM, H. J.; LYONS, L.; BOUDOURIDIS, A.; PILIPENKO, V.; RIDLEY, A. J.; WEYGAND, J. M. Statistical study of the effect of ulf fluctuations in the imf on the cross polar cap potential drop for northward imf. **Journal of Geophysical Research**, v. 116, 2011. [25](#)

KIVELSON, M. G.; RUSSEL, C. T. **Introduction to Space Physics**. [S.l.]: Cambridge University Press, 1995. [2](#), [7](#), [24](#), [32](#), [36](#), [40](#)

KLAUSNER, V. .; DOMINGUES, M. O.; MENDES, O.; PAPA, A. R. R. Tsunami effects on the z component of the geomagnetic field. **Journal of Atmospheric and Solar–Terrestrial Physics**, v. 92, p. 124–136, 2013. [52](#), [72](#), [119](#), [139](#), [155](#)

KLAUSNER, V.; MENDES, O.; DOMINGUES, M. O.; PAPA, A. R. R.; TYLER, R. H.; FRICK, P.; KHERANI, E. A. Advantage of wavelet technique to highlight the observed geomagnetic perturbations linked to the chilean tsunami (2010). **Journal of Geophysical Research**, v. 119, p. 3077–3093, 2014. [57](#)

_____. _____. **Journal of Geophysical Research**, v. 119, p. 3077–3093, 2014. [70](#), [88](#), [118](#), [154](#), [200](#)

KLEIN, L. W.; BURLAGA, L. F. Interplanetary magnetic clouds at 1 au. **Journal of Geophysical Research**, v. 87, p. 613–624, 1982. [2](#), [8](#), [9](#), [13](#), [61](#)

KOGA, D.; SOBRAL, J. H. A.; GONZALEZ, W. D.; ARRUDA, D. C. S.; ABDU, M. A.; de Castilho, V. M.; MASCARENHAS, M.; GONZALEZ, A. C.; TSURUTANI, B. T.; DENARDINI, C. M.; ZAMLUTTI, C. J. Electrodynamic coupling processes between the magnetosphere and the equatorial ionosphere during a 5-day hildcaa event. **Journal of Atmospheric and Solar-Terrestrial Physics**, v. 73, p. 148–155, 2011. [5](#), [20](#)

KOZYRA, J. U.; LIEMOHN, M. W. Ring current energy input and decay. **Space Science Reviews**, v. 109, p. 105–131, 2003. [23](#)

KRIEGER, A. S.; TIMOTHY, A. F.; ROELOF, E. C. A coronal hole and its identification as the source of a high velocity solar wind stream. **Solar Physics**, v. 29, p. 505–525, 1973. [10](#)

KRIMIGIS, S. M.; GLOECKLER, G.; MCENTIRE, R. W.; POTEMRA, T. A.; SCARF, F. L.; SHELLEY, E. G. Magnetic storm of september 4, 1984: A synthesis of ring current spectra and energy densities measured with ampte/cce. **Geophysical Research Letters**, v. 12, p. 329–332, 1985. [23](#)

KRIMIGIS, S. M.; SARRIS, E. T. Acceleration of ions and electrons to near-cosmic ray energies in a perpendicular shock: The January 6, 1978 event, In NASA. Goddard Space Flight Center 19th intern. In: **International Cosmic Ray Conference**. [S.l.: s.n.], 1985. v. 4, p. 170–173. [202](#)

KUMAR, A.; RUST, D. M. Interplanetary magnetic clouds, helicity conservation, and current-core flux-ropes. **Journal of Geophysical Research**, v. 101, p. 15667–15684, 1996. [13](#)

- KUMAR, P.; FOUFOULA, E. Wavelet analysis for geophysical applications. **Reviews of Geophysics**, v. 35, p. 385–412, 1997. 151
- LAKHINA, G. S.; ALEX, S.; MUKHERJEE, S.; VICHARE, G. On magnetic storms and substorms. In: **ILWS WORKSHOP 2006, GOA**. [S.l.: s.n.], 2006. 18
- LARIO, D.; ROELOF, E. C. Energetic particles during the first and third Ulysses southern high-latitude excursions: probing global corotating interaction region structure beyond 5 AU. **Journal of Geophysical Research**, v. 112, p. 9107, 2007. 14
- LEE, D. Y.; LYONS, L. R.; KIM, K. C.; BAEK, J. H.; KIM, K. H.; KIM, H. J.; WEYGAND, J.; MOON, Y. J.; CHO, K. S.; PARK, Y. D. .; HAN, W. Repetitive substorms caused by alfvénic waves of the interplanetary magnetic field during high-speed solar streams. **Journal of Geophysical Research**, v. 111, p. A12214, 2006. 5
- LENNARTSSON, O. W.; SHARP, R. D. A comparison of the 0.1–17 keV/e ion composition in the near equatorial magnetosphere between quiet and disturbed conditions. **Journal of Geophysical Research**, v. 87 (A8), p. 6109–6120, 1982. 23, 202
- LEWIS, R. V.; FREEMAN, M. P.; RODGER, A. S.; REEVES, G. D.; MILLING, D. K. The electric field response to the growth phase and expansion phase onset of a small isolated substorm. **Annales Geophysicae**, v. 15, p. 289–299, 1997. 18
- LINDSAY, G. M.; RUSSELL, C. T.; LUHMANN, J. G. Coronal mass ejection and stream interaction region characteristics and their potential geomagnetic effectiveness. **Journal of Geophysical Research**, v. 100, p. 16, 1995. 13
- LOTKO, W. The magnetosphere–ionosphere system from the perspective of plasma circulation: A tutorial. **Journal of Atmospheric and Solar-Terrestrial Physics**, v. 69, p. 191–211, 2007. 23, 202
- LOVE, K. J.; REMICK, J.; PERKINS, D. M. Statistical modeling of storm level kp occurrences: Solar cycle modulation. **Space Weather**, v. 5, p. S12005, 2007. 36
- LYATSKY, V. B.; MALTSEV, Y. P. Steady magnetosphere convection as a cause of sq-variation. **Geomagnetizm I Aeronomiya**, v. 15, p. 118–123, 1975. 72
- MALLAT, S. Multiresolution approximations and wavelets orthonormal bases. **Transaction of American Mathematical Society**, v. 315, p. 334–351, 1991. 56

MALLAT, S. G. Multiresolution approximations and wavelet orthonormal bases of $l_2(\mathbb{R})$. **American Mathematical Society**, v. 315 (1), p. 69–87, 1989. 48, 54, 55, 118

MANNUCCI, A. J.; TSURUTANI, B. T.; ABDU, M. A.; GONZALEZ, W. D.; KOMJATHY, A.; ECHER, E.; IJIMA, B. A.; CROWLEY, G.; ANDERSON, D. Superposed epoch analysis of the dayside ionospheric response to four intense geomagnetic storms. **Journal of Geophysical Research**, v. 113, p. A00A02, 2008. 46

MANSILLA, G. A. Solar cycle and seasonal distribution of geomagnetic storms with sudden commencement. **Earth Science Research**, v. 3, 2014. 21

MAYAUD, P. N. **Derivation meaning and use of geomagnetic indices**. Union,22,Washington,DC: Geophysics. Monogr. Am Geophys, 1980. 154 p. 34, 36

MCELHINNY, M. W. **Palaeomagnetism and Plate Tectonics**. [S.l.]: Cambridge, London, 1973. 1

MCPHERRON, R. L. **Physical Processes Producing Magnetospheric Substorms and Magnetic Storms, in Geomagnetism**. [S.l.]: Academic Press, London, 1991. 18

MEDVEDEV, M. V.; DIAMOND, P. H. Fluid models for kinetic effects on coherent nonlinear alfvén waves. i. fundamental theory. **Physics of Plasmas**, v. 3, p. 863, 1995. 16

MEDVEDEV, M. V.; SHEVCHENKO, V. I.; DIAMOND, P. H.; GALINSKY, V. L. Fluid models for kinetic effects on coherent nonlinear alfvén waves. ii. numerical solutions. **Physics of Plasmas**, v. 4, p. 1257, 1997. 16

MENDES, O. **A origem interplanetaria e o desenvolvimento da fase principal das tempestades geomagnéticas moderadas (1978-1979)**. PhD Thesis (PhD) — INPE–Instituto Nacional de Pesquisas Espaciais, 1992. 40, 42, 60

MENDES, O.; DOMINGUES, M. O.; da COSTA, A. M. Wavelet analysis applied to magnetograms. **Journal of Atmospheric and Solar-Terrestrial Physics**, v. 67, p. 1827–1836, 2005. xiv, 2, 50, 57, 70, 88, 113, 118, 147, 154, 200

MonrealMacMahon, R.; GONZALEZ, W. D. Energetics during the main phase of geomagnetic superstorms. **Journal of Geophysical Research**, v. 102 (A7), p. 14199–14207, 1997. 28, 71

- MOON, G. H. Estimation of polar cap potential and the role of pc index. **Astrophysics and Space Science**, v. 29(3), p. 259–267, 2012. [40](#), [195](#), [210](#)
- MOORE, T. E.; DELCOURT, D. C. Large-scale structure of magnetospheric plasma. **Surveys in Geophysics**, v. 16, p. 363–387, 1995. [23](#)
- MOORE, T. E.; PETERSON, W. K.; RUSSELL, C. T.; CHANDLER, M. O.; COLLIER, M. R.; AND, H. L. C.; CRAVEN, P. D.; FITZENREITER, R.; GILES, B. L.; POLLOCK, C. J. Ionospheric mass ejection in response to a CME. **Geophysical Research Letters**, v. 26, p. 239, 1999. [23](#), [202](#)
- MOOS, N. A. F. **Magnetic observations made at the government observatory Bombay for the period 1846 to 1905 and their discussions, Part II The phenomenon and its discussions.** Bombay, 1910. [82](#)
- MORIOKA, A.; MIYOSHI, Y.; SEKI, T.; TSUCHIYA, F.; MISAWA, H.; OYA, H.; MATSUMOTO, H.; HASHIMOTO, K.; MUKAI, T.; YUMOTO, K.; NAGATSUMA, T. AKR disappearance during magnetic storms. **Journal of Geophysical Research**, v. 108 (A6), p. 1226–1235, 2003. [118](#), [147](#), [197](#)
- NAGATSUMA, T. Conductivity dependence of cross-polar potential saturation. **Journal of Geophysical Research**, v. 109, p. A04210, 2004. [27](#)
- NesmeRibes, E.; FRICK, P.; SOKOLOFF, D.; ZAKHAROV, V.; RIBES, J. C.; VIGOUROUX, A.; LACLARE, F. Wavelet analysis of the maunder minimum as recorded in solar diameter data. **Comptes Rendus de l'Academie des Sciences, Ser. II, Fasc. b, Tome**, v. 321(12), p. 525–532, 1995. [52](#)
- NEUGEBAUE, M. Heliospheric sector boundaries: Single or multiple *qm*. **Journal of Geophysical Research**, v. 113, 2008. [16](#)
- NIKOLAEVA, N. S.; YERMOLAEV, Y. I.; LODKINA, I. G. Dependence of the cross polar cap potential saturation on the type of solar wind streams. **Journal of Geophysical Research**, 2013. [27](#)
- NISHIDA, A. **Geomagnetic Diagnosis of the Magnetosphere (Physics and Chemistry in Space)**. [S.l.]: Springer-Verlag; First Edition edition, 1978. [9](#), [14](#)
- O'BRIEN, T. P.; MCPHERRON, R. L. An empirical phase space analysis of ring current dynamics: Solar wind control of injection and decay. **Journal of Geophysical Research**, v. 105, 2000. [2](#)

OJEDA, G. A.; GONZALEZ, W. D.; MENDES, O.; DOMINGUES, M. O.; ROSA, R. R. Nonlinear fluctuation analysis for a set of 41 magnetic clouds measured by the advanced composition explorer (ace) spacecraft. **Nonlinear Processes in Geophysics**, v. 21, p. 1059–1073, 2014. 57, 61, 70, 88, 98, 118, 132, 154, 165, 187

OJEDA, G. A.; MENDES, O.; CALZADILLA, M. A.; DOMINGUES, M. O. Spatio-temporal entropy analysis of the magnetic field to help magnetic cloud characterization. **Journal of Geophysical Research**, v. 118, p. 5403–5414, 2013. 61, 70, 98, 132, 165, 187

OJEDA, G. A.; MENDES, O.; DOMINGUES, M. O.; MENCONI, V. E. Daubechies wavelet coefficients: a tool to study interplanetary magnetic fluctuations. **Geofísica internacional**, v. 53, p. 101–115, 2014. 200

OLSEN, N.; HULOT, G.; SABAKA, T. J. **Sources of the Geomagnetic Field and the Modern Data That Enable Their Investigation**. [S.l.]: Springer Berlin Heidelberg, 2010. 1

ONWUMECHILI, C. A. **The Equatorial Electrojet**. [S.l.]: Gordon and Breach, New York, 1997. 21

OWOLABI, T. P.; RABIU, A. B.; OLAYANJU, G. M.; BOLAJI, O. S. Seasonal variation of worldwide solar quiet of the horizontal magnetic field intensity. **Applied Physics Research**, v. 6, 2014. 20

PAPITASHVILI, V.; RICH, F. J.; HEINEMANN, M. A.; HAIRSTON, M. R. Parametrization of the defense meteorological satellite program ionospheric electrostatic potentials by the interplanetary magnetic field strength and direction. **Journal of Geophysical Research**, v. 104, p. 177–184, 1999. 26

PARKER, E. N. Dynamics of the interplanetary gas and magnetic fields. **Astrophysical Journal**, v. 128, p. 664, 1958. 15

_____. **Interplanetary dynamical processes**. [S.l.]: Wiley Interscience, New York, 1963. 24

PARKS, G. K. **Physics of Space Plasmas, An Introduction**. [S.l.]: Redwood City-CA: Addison-Wesley Publishing Company, 1991. 16

_____. **Physics of Space Plasmas**. [S.l.]: Westview Press, 2004. 7

PERREAULT, P.; AKASOFU, S. I. A study of geomagnetic storms. **Journal of Geophysical Research**, v. 54, p. 547–573, 1978. 26, 27, 71, 72, 81

- PIZZO, V. J. Interplanetary shocks on the large scale, in collisionless shock in the heliosphere: A tutorial review. In: STONE, R. G.; TSURUTANI, B. T. (Ed.). **Geophysical Monograph Series**. [S.l.]: AGU, Washington, 1985. v. 34, p. 51. [10](#)
- RAEDER, J.; LU, G. Polar cap saturation during large geomagnetic storms. **Advances in Space Research**, v. 36, p. 1804, 2005. [27](#)
- RASTOGI, R. G. Westward equatorial electrojet during daytime hours. **Journal of Geophysical Research**, v. 79, p. 1503–1512, 1974. [21](#)
- _____. Signatures of storm sudden commencements in geomagnetic h, y and z fields at indian observatories during 1958–1992. **Annales Geophysicae**, v. 17, p. 1426, 1999. [82](#), [83](#), [105](#), [117](#)
- _____. Magnetic storm effects in h and d components of the geomagnetic field at low and middle latitudes. **Journal of Atmospheric and Solar-Terrestrial Physics**, v. 67, p. 665, 2005. [82](#), [105](#), [113](#), [117](#), [137](#), [151](#)
- _____. Day-to-day variability of the equatorial electrojet current in the south american sector. **Earth Planets Space**, v. 59, p. 459–461, 2007. [20](#)
- RASTOGI, R. G.; IYER, K. N. Quiet day variation of geomagnetic h-field at low latitudes. **Journal of Geomagnetism and Geoelectricity**, v. 28, p. 461–479, 1976. [20](#)
- RAWAT, R.; ALEX, S.; LAKHINA, G. S. Low-latitude geomagnetic response to the interplanetary conditions during very intense magnetic storms. **Advances in Space Research**, v. 43, p. 1575–1587, 2009. [180](#)
- REIFF, P.; LUHMANN, J. G. Solar wind control of the polar cap potential. In: KAMIDE, Y. in.; SLAVIN, J. E. (Ed.). [S.l.]: Terra Scientific Publishing Company, Tokyo, 1986. Solar Wind Magnetosphere Coupling., p. 453–468. [26](#)
- RICH, F. J.; HAIRSTON, M. Large-scale convection patterns observed by dmsp. **Journal of Geophysical Research**, v. 99, p. 3827, 1994. [25](#)
- RICHMOND, A. D.; KAMIDE, Y. Mapping electrodynamic features of the high-latitude ionosphere from localized observations: Technique. **Journal of Geophysical Research**, v. 93, p. 5741, 1998. [25](#)
- RIDLEY, A. J.; KIHN, E. A. Polar cap index comparisons with AMIE cross polar cap potential, electric field, and polar cap area. **Geophysical Research Letters**, v. 31, p. L07801, 2004. [197](#)

RILEY, P.; LINKER, J. A.; MIKIC, Z. An empirically-driven global MHD model of the corona and inner heliosphere. **Geophysical Research Letters**, v. 106, p. 15889, 2001. 15

ROSTOKER, G. Geomagnetic indices. **Reviews of Geophysics and Space Physics**, v. 10, p. 935–950, 1972. 3, 24, 34, 35, 36, 38

_____. Magnetic signatures of precursors to substorm expansive phase onset. **Journal of Geophysical Research**, v. 92, p. 5845–5856, 1987. 18

RUOHONIEMI, J. M.; BAKER, K. B. Large-scale imaging of high latitude convection with super dual auroral radar network hf radar observation. **Journal of Geophysical Research**, v. 103, p. 797, 1998. 25

RUOHONIEMI, J. M.; GREENWALD, R. A. Observations of IMF and seasonal effects in high-latitude convection. **Geophysical Research Letters**, v. 22, p. 1121–1124, 1995. 26

RUSSELL, C. T. Geophysical coordinate transformations. **Cosmic Electrodynamic**, v. 2, p. 184–196, 1971. 40

RUSSELL, C. T.; LUHMANN, J. G. **EARTH: MAGNETIC FIELD AND MAGNETOSPHERE**. [S.l.]: Encyclopedia of Planetary Sciences, 1997. 22

SABA, M.; GONZALEZ, W. D.; CLUA-GONZALEZ, A. L. Relationships between the AE, ap and Dst indices near solar minimum (1974) and at solar maximum (1979). **Annales Geophysicae**, v. 15, p. 1265–1270, 1997. 35

SCHLAPP, D. M. World-wide morphology of day to day variability of sq. **Journal of Atmospheric and Solar-Terrestrial Physics**, v. 30, p. 1761–1776, 1968. 20

SCHULZ, M. Interplanetary sector structure and the heliomagnetic equator. **Astrophysics and Space Science**, v. 24, p. 371–383, 1973. 16

SCHWENN, R. Space weather the solar perspective. **Living Review Solar Physics**, v. 3, p. 1–72, 2006. 11

SHELDON, R.; HAMILTON, D. Ion transport and loss in the earth's quiet ring current, 1. data and standard model. **Journal of Geophysical Research**, v. 98(A8), p. 13491–13508, 1993. 23, 202

SHELLEY, E.; JOHNSON, R.; SHARP, R. Satellite observations of energetic heavy ions during a geomagnetic storm. **Journal of Geophysical Research**, v. 77, p. 6104–6110, 1972. 23

SHEPHERD, S. G.; GREENWALD, R. A.; RUOHONIEMI, J. M. A possible explanation for rapid, large-scale ionospheric responses to southward turnings of the imf. **Geophysical Research Letters**, v. 26, p. 3197–3200, 1999. 26

SIMOES, M. C. **Identificação de distúrbios em magnetogramas associados a tempestades geomagnéticas utilizando técnicas wavelets**. Master Thesis (Mestrado) — Instituto Nacional de Pesquisas Espaciais, 2011. 57

SMITH, E. J.; WOLF, J. H. Observation of interaction region and corotating shocks between one and five au: Pioneer 10 and 11. **Geophysical Research Letters**, v. 3, p. 137, 1976. 10

_____. Observations of interaction regions and corotating shocks between one and five au: Pioneers 10 and 11. **Geophysical Research Letters**, v. 3, p. 137, 1976. 14

SOBRAL, J. H. A.; MANGALATHAYIL, A. A.; GONZALEZ, W. D.; CLUA-GONZALEZ, A. L.; TSURUTANI, B. T.; da SILVA, R. R. L.; BARBOSA, I. G.; ARRUDA, D. C. S.; DENARDINI, C. M.; ZAMLUTTI, C. J.; GUARNIERI, F. Equatorial ionospheric responses to high-intensity long duration auroral electrojet activity (hildcaa). **Journal of Geophysical Research**, v. 111, 2006. 5, 20

SONNERUP, B. U. O. Magnetopause reconnection rate. **Geophysical Research Letters**, v. 79, p. 1546–1549, 1974. 26

SORAAS, F.; AARSNESA, K.; OKSAVIKA, K.; SANDANGERA, M. I.; EVANS, D. S.; GREERB, M. S. Evidence for particle injection as the cause of Dst reduction during HILDCAA events. **Journal of Atmospheric and Solar-Terrestrial Physics**, v. 66, p. 177–186, 2004. 4, 16, 19, 20, 91

STENING, R. J. Variation in the strenght of Sq current system. **Annales Geophysicae**, v. 13, p. 627–632, 1995. 21

STENING, R. J.; REZTSOVA, T.; MINH, L. H. Variation of Sq focus latitudes in the Australian Pacific region during a quiet sun year. **Journal of Atmospheric and Solar-Terrestrial Physics**, v. 69(6), p. 734–740, 2007. 149

SUGIURA, M. Hourly values of equatorial Dst for the IGY. **Annals of the International Geophysical Year**, v. 35, p. 9, 1964. 3, 24, 38, 83, 110

- _____. Identification of polar cap boundary and the auroral belt in the high-altitude magnetosphere: a model for field-aligned current. **Journal of Geophysical Research**, v. 80, p. 2057, 1975. 25
- SUGIURA, M.; KAMEI, T. Equatorial Dst index 1957-1986. **IAGA Bulletin**, v. 40, 1991. 3, 17, 38
- SUN, W.; AND, B. H. A.; AKASOFU, S. I.; KAMIDE, Y. A. Comparison of the observed mid-latitude magnetic disturbance fields with those reproduced from the high-latitude modeling current system. **Journal of Geophysical Research**, v. 89, p. 10880–10881, 1984. 176
- SZABO, A.; LARSON, D. E.; LEPPING, R. P. The heliospheric current sheet on small scale, in solar wind nine. In: AL., S. R. H. et (Ed.). **AIP Conf. Proc.** [S.l.: s.n.], 1999. v. 471, p. 589. 15
- TAKAHASHI, S.; IYEMORI, T.; TAKEDA, M. Ring current response to impulsive southward IMF: a cause of second development of the Dst index. **Journal Geomagnetism Geoelectricity**, v. 42, p. 1325–1331, 1990. 3, 38
- TROSHICHEV, O.; ANDREZEN, V. G.; VENNERSTROM, S.; Friis-Christensen, E. Magnetic activity in the polar cap– a new index. **Planetary and Space Science**, v. 36, p. 1095, 1988. 38, 40
- TROSHICHEV, O.; HAYAKAWA, H.; MATSUOKA, A.; MUKAI, T.; TSURUDA, K. Cross polar cap diameter and voltage as a function of pc index and interplanetary quantities. **Journal of Geophysical Research**, v. 101, p. 13429–13436, 1996. 27
- TROSHICHEV, O. A.; DMITRIEVA, N. P.; KUZNETSOV, B. M. Polar cap magnetic activity as a signature of substorm development. **Planetary and Space Science**, v. 27, p. 217, 1979. 40
- TROSHICHEV, O. A.; PODOROZHKINA, N. A.; JANZHURA, A. S. Invariability of relationship between the polar cap magnetic activity and geoeffective interplanetary electric field. **Annals of Geophysics**, v. 29, p. 1479–1489, 2011. 198, 212
- TSUNOMURA, S. Characteristics of geomagnetic sudden commencement observed in middle and low latitudes. **Earth, Planets and Space**, v. 50, p. 755, 1998. 151

TSURUTANI, B. T.; GONZALEZ, W. D. The cause of high-intensity long duration continuous AE activity (HILDCAAS): interplanetary alfvén wave trains. **Planetary and Space Science**, v. 35, p. 400–412, 1987. 3, 4, 5, 19, 20, 44, 60, 91, 110, 113, 149

_____. The interplanetary causes of magnetic storms. **A review, in Magnetic Storms, AGU monograph**, v. 98, p. 77, 1997. 2, 27

TSURUTANI, B. T.; GONZALEZ, W. D.; CLUA-GONZALEZ, A. L.; TANG, F.; ARBALLO, J. K.; OKADA, M. Interplanetary origin of geomagnetic activity in the declining phase of the solar cycle. **Journal of Geophysical Research**, v. 100, p. 21717, 1995. 4, 15, 18

TSURUTANI, B. T.; GONZALEZ, W. D.; CLUA-GONZALEZ, A. L.; GUARNIERI, F. L.; GOPALSWAMY, N.; GRANDE, M.; KAMIDE, Y.; KASAHARA, Y.; LU, G.; MANN, I.; MCPHERRON, R.; SORAAS, F.; VASYLIUNAS, V. Corotating solar wind streams and recurrent geomagnetic activity: a review. **Journal of Geophysical Research**, v. 11, p. A07S01, 2006. 10

TSURUTANI, B. T.; GONZALEZ, W. D.; GUARNIERI, F.; KAMIDE, Y.; ZHOUA, X.; ARBALLO, J. K. Are high-intensity long-duration continuous AE activity (HILDCAA) events substorm expansion events *qm*. **Journal of Atmospheric and Solar-Terrestrial Physics**, v. 66, p. 167–176, 2004. 3, 4, 5, 18, 19, 20, 37, 91

TSURUTANI, B. T.; GOULD, T.; GOLDSTEIN, B. E.; GONZALEZ, W. D.; SUGIURA, M. Interplanetary alfvén waves and auroral (substorm) activity: Imp-8. **Journal of Geophysical Research**, v. 95, p. 2241, 1990. 4, 20

TSURUTANI, B. T.; SMITH, E. J.; GONZALEZ, W. D.; TANG, F.; AKASOFU, S. I. Origin of interplanetary southward magnetic fields responsible for major magnetic storms near solar maximum (1978–1979). **Journal of Geophysical Research**, v. 93, p. 8519–8531, 1988. 8, 13, 17

TSURUTANI, B. T.; THORNE, R. M. Diffusion processes in the magnetopause boundary layer. **Geophysical Research Letters**, v. 9, p. 1247, 1982. 2, 17

TSURUTANI, B. T.; VERKHOGLYADOVA, O. P.; MANNUCCI, A. J.; LAKHINA, G. S.; LI, G.; ZANK, G. P. A brief review of solar flare effects on the ionosphere. **Radio Science**, v. 44, 2009. 14

TSURUTANI, B. T.; ZHOU, X. Y.; ARBALLO, J. K.; GONZALEZ, W. D.; LAKHINA, G. S.; VASYLIUNAS, V.; PICKETT, J. S.; ARAKI, T.; YANG, H.; ROSTOKER, G.; HUGHES, T. J.; LEPPING, R. P.; BERDICHEVSKY, D. Auroral zone dayside precipitation during magnetic storm initial phases. **Journal of Atmospheric and Solar-Terrestrial Physics**, v. 63, p. 513–522, 2001. [9](#), [17](#), [18](#), [98](#)

VALDIVIA, J. A.; VASSILIADIS, D.; KLIMAS, A. Spatiotemporal activity of magnetic storms. **Journal of Geophysical Research**, v. 104, p. 12239–12250, 1999. [151](#)

VANDAS, M.; FISCHER, S.; PELANT, P. A. Evidence for a spheroidal structure of magnetic clouds. **Journal of Geophysical Research**, v. 98, p. 21061–21069, 1993. [13](#)

VASQUEZ, B. J.; HOLLWEG, J. V. Formation of pressure balance structures and fast waves from nonlinear alfvén waves. **Journal of Geophysical Research**, v. 104, p. 4681, 1999. [16](#)

_____. Evolution and dissipation of imbedded rotational discontinuities and alfvén waves in nonuniform plasma and the resultant proton heating. **Journal of Geophysical Research**, v. 106, p. 5661, 2001. [16](#)

VASYLIUNAS, V. M.; KAN, J. R.; SISCOE, G. L.; AKASOFU, S. I. Scaling relations governing magnetospheric energy transfer. **Planetary and Space Science**, v. 30 (4), p. 359–365, 1982. [28](#), [71](#)

VENNERSTRQM, S.; Friis-Christensen, E.; TROSHICHEV, O. A.; ANDRESEN, V. G. Comparison between the polar cap index pc and the auroral electrojet indices AE , AL , and AU . **Journal of Geophysical Research**, v. 96, p. 101–113, 1991. [195](#)

VERBANAC, G. .; MANDEA, M.; VRSNAK, B.; SENTIC, S. Evolution of solar and geomagnetic activity indices, and their relationship: 1960 – 2001. **Solar Physics**, v. 271, p. 183–195, 2011. [34](#), [38](#)

VICHARE, G.; ALEX, A. S.; LAKHINA, G. S. Influence of solar wind parameters on ground magnetic field near equator during intense storms. **Journal of Atmospheric and Solar Terrestrial Physics**, v. 71, p. 1814–1823, 2009. [46](#)

- VICHARE, G.; RAWAT, R.; HANCHINAL, A.; SINHA, A. K.; DHAR, A.; PATHAN, B. M. Seasonal evolution of Sq current system at sub-auroral latitude. **Earth Planets Space**, v. 64, p. 1023–1031, 2012. [149](#)
- VORONKOV, I. O.; KUZNETSOV, B. M. The relationship of mid-latitude Sq variation to the solar wind velocity. **Geomagnetizm I Aeronomiya**, v. 29, p. 319–321, 1989. [72](#)
- VOURLIDAS, A.; HOWARD, R. A.; ESFANDIARI, E.; PATSOURAKOS, S.; YASHIRO, S.; MICHALEK, G. J. Comprehensive analysis of coronal mass ejection mass and energy properties over a full solar cycle. **Astrophysical Journal**, v. 722, p. 1522–1538, 2010. [12](#)
- WANG, H.; LUHR, H.; MA, S. Y.; WEYGAND, J.; SKOUG, R. M.; YIN, F. Field-aligned currents observed by champ during the intense 2003 geomagnetic storm events. **Annales Geophysicae**, v. 24, p. 311–324, 2006. [177](#)
- WEBB, D. F.; CLIVER, E. W.; CROOKER, N. U.; CYR, O. C. S.; THOMPSON, B. J. Relationship of halo coronal mass ejections, magnetic clouds, and magnetic storms. **Journal of Geophysical Research**, v. 105, p. 7491–7508, 2000a. [11](#)
- WEI, F.; LIU, R.; FENG, X.; ZHONG, D.; YANG, F. Identification of the magnetic cloud boundary layers. **Journal of Geophysical Research**, v. 108(A6), p. 1263, 2003. [2](#)
- WEIMER, D. R. Models of high-latitude electric potentials derived with a least error fit of spherical harmonic coefficients. **Journal of Geophysical Research**, v. 100, p. 595, 1995. [25](#), [26](#)
- WEIMER, D. R.; OBER, D. M.; MAYNARD, N. C.; BURKE, W. J.; COLLIER, M. R.; MCCOMAS, D. J.; NESS, N. F.; SMITH, C. W. Variable time delays in the propagation of the interplanetary magnetic field. **Journal of Geophysical Research**, v. 107, p. A8, 2001. [206](#)
- WEIMER, D. R.; REINLEITNER, L. A.; KAN, J. R.; ZHU, L.; AKASOFU, S. I. Saturation of the auroral electrojet current and the polar cap potential. **Journal of Geophysical Research**, v. 95, p. 18981–18987, 1990. [26](#)
- ZMUDA, A. J.; ARMSTRONG, J. C. The diurnal variation of the region with vector magnetic field changes associated with field-aligned currents. **Journal of Geophysical Research**, v. 79, p. 2501–2502, 1974. [25](#)

ZMUDA, A. J.; MARTIN, J. H.; HEURING, F. T. Transverse magnetic disturbances at 1100 kilometers in the auroral region. **Journal of Geophysical Research**, v. 71, p. 5033–5045, 1966. 24

ZONG, Q. G.; ZHOU, X. Z.; WANG, Y. F.; AND, X. L.; SONG, P.; BAKER, D. N.; FRITZ, T. A.; DALY, P. W.; DUNLOP, M.; PEDERSEN, A. Energetic electron response to ULF waves induced by interplanetary shocks in the outer radiation belt. **Journal of Geophysical Research**, v. 114, 2009. 13

PUBLICAÇÕES TÉCNICO-CIENTÍFICAS EDITADAS PELO INPE

Teses e Dissertações (TDI)

Teses e Dissertações apresentadas nos Cursos de Pós-Graduação do INPE.

Manuais Técnicos (MAN)

São publicações de caráter técnico que incluem normas, procedimentos, instruções e orientações.

Notas Técnico-Científicas (NTC)

Incluem resultados preliminares de pesquisa, descrição de equipamentos, descrição e ou documentação de programas de computador, descrição de sistemas e experimentos, apresentação de testes, dados, atlas, e documentação de projetos de engenharia.

Relatórios de Pesquisa (RPQ)

Reportam resultados ou progressos de pesquisas tanto de natureza técnica quanto científica, cujo nível seja compatível com o de uma publicação em periódico nacional ou internacional.

Propostas e Relatórios de Projetos (PRP)

São propostas de projetos técnico-científicos e relatórios de acompanhamento de projetos, atividades e convênios.

Publicações Didáticas (PUD)

Incluem apostilas, notas de aula e manuais didáticos.

Publicações Seriadas

São os seriados técnico-científicos: boletins, periódicos, anuários e anais de eventos (simpósios e congressos). Constam destas publicações o Internacional Standard Serial Number (ISSN), que é um código único e definitivo para identificação de títulos de seriados.

Programas de Computador (PDC)

São a seqüência de instruções ou códigos, expressos em uma linguagem de programação compilada ou interpretada, a ser executada por um computador para alcançar um determinado objetivo. Aceitam-se tanto programas fonte quanto os executáveis.

Pré-publicações (PRE)

Todos os artigos publicados em periódicos, anais e como capítulos de livros.